Asymmetries of Radio Galaxies

Dissertation

zur

Erlangung des Doktorgrades (Dr. rer. nat.)

der

Mathematisch-Naturwissenschaftlichen Fakultät

der

Rheinischen Friedrich-Wilhelms-Universität Bonn

vorgelegt von

Sohn, Bong Won

aus

Seoul, Korea

Bonn März 2003

Angefertigt mit Genehmigung der Mathematisch-Naturwissenschaftlichen Fakultät der Rheinischen Friedrich-Wilhelms-Universität Bonn

1. Referent : Prof. Ulrich Klein

2. Referent : Prof. Ulrich Mebold

Tag der Promotion : 19. März. 2003

to my parents

나면서 어리석고 生而大癡
자라서는 병도 많아 壯而多疾
중간에 어쩌다 학문을 즐겼는데 中何嗜學

학문은 구할수록 멀어지고 學求愈邈

산은 산은 높고 높으며 有山祥祥
물은 깊고 또 깊어라 有水源源

퇴계 이황이 스스로 쓴 명문에서 (退溪自銘)

Born stupid
Grown weak
Happened to joy studies

The road to the truth became longer and longer

Mountains are high and high
Waters are deep and deep

from `Self-written epitaph' of Lee Hwang, A.D. 1570

범을 그리되 가죽은 그릴 수 있으나 뼈를 그리기는 어렵고 畫虎畫皮難畫骨
사람을 알되 얼굴은 알 수 있으나 마음을 알기는 어렵다 知人知面不知心

명심보감 성심편 상 십구장에서 (明心寶鑑 省心篇 上)

Shape of tiger can be easily drawn
Not the tiger's bone
One's face can be easily read
Not the shape of mind

from `A book making mind clear for children',
Edited by Chu Jeok, late 13th century

Contents

List of Figures

List of Tables

Chapter 1

Introduction

Since the discovery of radio galaxies in the late 40's (Bolton et al., 1949), synchrotron radiation in radio galaxies has been proposed (Shklovskii, 1953; Burbidge, 1966) in order to explain the radiation over a wide frequency range. Due to their large projected extent, the transport of energy has become a common and important theme. In the early 70's the beaming model was suggested by Rees (1971); Blandford & Rees (1974); Scheuer (1974) which describes a symmetric beam created by a central active galactic nucleus (AGN). Curiously these symmtrically shaped sources have been known to have one-sided jets. The process of relativistic beaming in radio galaxies can explain one-sided jets in many powerful radio galaxies (Rees, 1971; Blandford & Rees, 1974; Scheuer, 1974). Since that time, people have been looking for systematic asymmetries in radio galaxies which can possibly be connected to the jet asymmetries. Now it is known that not only powerful FR II-, but also many FR I-type radio galaxies have jet asymmetries (Morganti et al., 1997b). Four asymmetries are known in radio galaxies from decades of observations: these are the depolarization, spectral index (Liu & Pooley, 1991; Garrington et al., 1991), the lobe length (Scheuer, 1995), and emission line asymmetry (McCarthy et al., 1991). The last two of them are known to be not related (at least directly) to the jet asymmetry. The first two asymmetries are known to be related to the jet asymmetry.

The first one is also known as the 'Laing-Garrington effect' (Laing, 1988; Garrington et al., 1988). The idea is that a magneto-ionic medium having a King density profile surrounds the radio galaxies, e.g. Garrington & Conway (1991). The radiation from the jet-side lobe travels through fewer cells of the magneto-ionic medium to us than that of the counter-jet side lobe. This idea is based on the assumption that the magnetic field scale-length in the magneto-ionic medium is unresolved by the telescope beam used. The second one is the spectral index asymmetry, which means that the jet-side lobe has a flatter spectral index than the counterjet-side lobe. A possible explanation is the frequency-shift effect. The jet-side lobe is advancing to us and has a blue-shifted spectrum, while the counterjet-side lobe is receding, and thus has a redshifted spectrum (Blundell & Alexander, 1994).

There are weaknesses in the theories of the two asymmetries which must be tested. In the depolarization asymmetry, the depolarization measure, DP, is obtained from the fractional polarization of two radio frequencies. At low signal-to-noise, the fractional polarization is severely biased. This is known as the 'Ricean bias'. In order to reduce the problem, the integrated fractional polarization, $m = \Sigma P/\Sigma I$, is more frequently used than the pixel-to-pixel fractional polarization, $m = \Sigma(P/I)$. As a result, DP contains more information about the intrinsic fractional polarization than the foreground medium information, and the DP maps are severely biased in extended lobes. This can lead to

a wrong interpretation of the DP trend in sources.

A further question about the foreground magnetic field is if there is any relation between the Rotation Measure dispersion, ΔRM, and the DP asymmetry. To answer this question, one must have a reliable pixel-to-pixel DP estimate, rather than the integrated DP. In case of the spectral index asymmetry, the frequency shift effect requires a relativistic speed of the advancing hotspot, which seems to be an unrealistic assumption. Furthermore, the spectral index steepening from a two-frequency observation can be also feasible through multiple injection spectra, the distribution of the magnetic field strength, or spectral ageing. For the estimate of a pixel-to-pixel DP, we suggest a less biased correction method, and with this new correction we have investigated the DP asymmetry and DP trend in sources and the ΔRM - DP relation in giant radio galaxies (GRGs) and B2 radio galaxies. This is the first part the thesis.

The second part deals with the spectral index asymmetry. Most of the spectral index studies are based on two-frequency analyses. A recent study of 3C 449 (Katz-Stone & Rudnick, 1997) shows that there are possibly more than one injection spectra in 3C 449. If this is a general property of radio galaxies, the spectral index asymmetry must be influenced by it. We suggest an improved technique to analyze multi-frequency spectra of radio galaxies and to extract injection spectra. Using this technique, we have investigated GRGs and compact steep-spectrum (CSS) sources in order to find out if there are indeed multiple injection spectra in GRGs and if CSS sources have a universal injection spectrum or not. In the last section, we will check if there is any connection between the spectral and the DP variation in GRGs.

First results - overview

Depolarization occurs only at low frequencies (e.g. ≤ 1.6 GHz). The depolarization asymmetry is also strong. However, there is only little connection to the RM dispersion. The scale lengths of RM patches or the mean field strength in GRGs and in B2 sources seems to be completely different. In GRGs, we find a high mean RM, a DP-spectral curvature relation as well as multiple injection spectra. All of this leads us to the conclusion that GRGs are not just a larger version of B2 sources, but a result of the interaction with their environment.

The lack of any clear connection between DP and ΔRM suggests that RM structures in radio galaxies are not multi-cellar as those of DP. Considering the lack of depolarization at high frequencies, even with a large beam size and considering the fact that RM structures are due to a stronger field and to larger scale lengths, a possible interesting scenario is the *small-scale weak magnetic field* which causes the depolarization to be stretched and strengthened in the vicinity (or at the surface) of radio galaxies through the interaction between radio galaxies and their environment. It implies different RM scale-lengths in GRGs and B2 sources. It indicates that the interaction with the environment is more important in GRGs than in B2 sources, since we detect a higher mean RM in GRGs. In particular, the magnetic field is dynamically important in GRGs. This idea is worth further scrutiny.

Due to the lack of any spectral curvature information of B2 sources, it is an open question whether or not B2 sources have such a trend in their spectra. This should be studied with new-generation instruments such as the 9-mm array-receiver at the 100-m Effelsberg telescope.

Part I

Polarization Asymmetries

Chapter 2

Depolarization of Giant Radio Galaxies

2.1 (De)-polarization

Synchrotron radiation from radio galaxies is known to be linearly polarized. Even unresolved sources show measurable linear polarization. Using this linear polarization property, we can measure the fractional polarization and the polarization angle of the radiation after traversing the Faraday medium (e.g. a magnetized thermal plasma between the polarized source and us). First investigations of the Galatic Faraday medium were made by Simard-Normandin et al. (1981) and others using the integrated polarization of extragalactic sources. With increased sensitivity and angular resolution of radio telescopes and telescope arrays, the investigation of the Faraday medium of radio galaxies has become one of the main interests of this field. Burn (1966) and Laing (1985) have shown that deciphering the geometry of the Faraday medium is very complex. In general, there are two basic geometric configurations.

- The Faraday medium is 'internal' to the source, and physically mixed with the emitting volume (e.g. a thermal cloud surrounded by a shell of relativistic electrons).
- A foreground Faraday medium (in front of the synchrotron source) has a fine structure that is unresolved by the telescope.

Decades of multi-frequency observations have shown that the Faraday rotation is highly linear in λ^2 when the spatial resolution is good enough. This linearity is the property of the resolved slab and the external (resolved) Faraday medium (Burn, 1966). The difference between the internal slab geometry and the external medium becomes evident in the fractional polarization. In the internal case, we will see the secondary maxima of the fractional polarization in the low-frequency regime. In the external case, we will see no depolarization at low frequencies. The observational results seem to be 'in between'. The achievement of full frequency-sampled data is virtually impossible. While a depolarization trend is seen, it is not easy to distinguish between the internal slab and the unresolved external component.

The Faraday rotation of supernova remnants and spiral galaxies is an example of the first case. In this case, the Faraday rotation profile is non-linear in λ^2. On the other hand, the observational results of radio galaxies over the last decades, especially multi-frequency observations with high angular resolution, have proven that Faraday rotation

in radio galaxies does follow a λ^2 law. Therefore, it must be concluded that the Faraday-rotating media do not permeate the lobes of radio galaxies. Recently obtained sensitive X-ray images (e.g. with *ROSAT*, *Chandra*) exhibit cavities in the hot gas towards the lobes of radio galaxies. This confirms that the thermal electrons of the X-ray halos and the relativistic electrons of the radio lobes are not mixed. Physically, this could imply pressure balance between the thermal and the relativistic electrons. Alternatively, it could mean rapid acceleration of the thermal electrons in the radio lobes and rapid cooling of the relativistic electrons in the X-ray halo. In any case, the λ^2 behaviour of the Faraday rotation of radio galaxies indicates that the differential depolarization (DP) and the Rotation Measure (RM) of radio galaxies are due to an 'external' Faraday medium. It also implies that the Faraday media are almost or even fully resolved. This should lead to a low differential de-polarization.

In the case of fully resolved Faraday cells and assuming that radio galaxies reside in the centre of X-ray halos with King profiles, we expect an RM asymmetry instead of a depolarization asymmetry. Although the scale length of the Faraday cells is not definitely known yet, the λ^2 behaviour suggests that we do resolve the Faraday screen. On the other hand, the asymmetry of the differential depolarization (i.e. the 'Laing-Garrington effect' Laing (1988); Garrington et al. (1988)) is known to be the best proof of the relativistic beaming effect of jets in radio galaxies. The Laing-Garrington effect means that a non-negligable amount of (magnetic) energy is contained in small-scale (unresolved) magnetic field structures. In that case, Faraday rotation will deviate from the λ^2 behaviour and will be saturated at $\Delta\chi < \pi/3$ (Burn, 1966).

In this work, we study the RM and the DP distribution of various radio galaxies. The fractional polarization of a radio source is determined by the pitch angle distribution of the relativistic electrons, the geometry of the magnetic field, and by the energy distribution function of the relativistic electrons

$$N(E) \propto E^{-p}, \text{ with } \alpha_{\rm inj} = (p-1)/2.$$

The general power-law distribution is known from radio observations, cosmic-ray experiments, and from theory. The theoretical fractional polarization of the radio intensity is (almost) independent of frequency. On the other hand, the measured fractional polarization of the flux density is additionally dependent on the depolarization due to differential Faraday Rotation, i.e. on the distribution of thermal electrons along the line-of-sight, as well as the line-of-sight component of the magnetic field. This way, the polarized component of the radiation undergoing Farady rotation becomes frequency dependent.

For decades, one-sided jets of AGNs have been observed. The most succesful explanation of this phenomenon is Doppler boosting caused by the relativistic bulk motion of the jet material. Since the radio lobes are connected to, and fed by, the jets, large efforts have been made in order to look for independent projection effects which do or do not support the interpretation in terms of projection effects of the relativistic jets. As far as the radio lobes are concerned, the depolarization asymmetry, i.e. the Laing-Garrington effect, is the strongest support of this view. The other asymmetries of the radio lobes, the lobe length and the spectral index asymmetry, do not show any clear connection to the projection effect of the relativistic jets. To conclude, the Laing-Garrington effect is interpreted in terms of differential depolarizaiton. In case of such an *internal* differential depolarization, the foreground medium should also have magnetic field reversals along the line-of-sight.

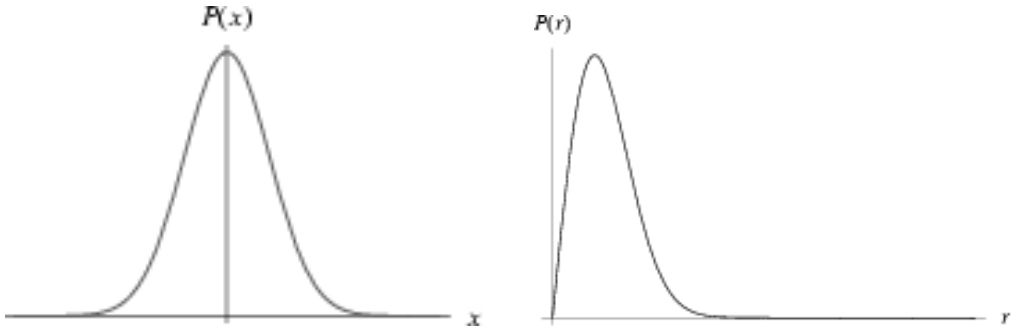

(a) A Gaussian distribution (b) A Rayleigh distribution

Figure 2.1: Two distributions

2.2 The Ricean bias in linear polarization

In this section we discuss the Ricean bias in the polarization intensity and suggest a new correction method. The linearly polarized intensity is obtained from Stokes parameters U and Q according to

$I_{P_{obs}} = \sqrt{U^2 + Q^2}$. It follows a Ricean distribution (Vinokur, 1965):

$$f(I_{P_{obs}}; I_P, \sigma^2_{I_P}) = I_{P_{obs}}/\sigma^2_{I_P} B_0(I_{P_{obs}} I_P/\sigma^2_{I_P}) e^{-0.5(I_P^2+I^2_{P_{obs}})/\sigma^2_{I_P}}$$

where $I_{P_{obs}}$ is the observed polarized intensity, I_P is the intrinsic polarized intensity, B_0 is the modified Bessel function of zero order and σ_{I_P} is the noise level. For $I_P \gg \sigma_{I_P}$ and $I_P \sim \sigma_{I_P}$, the Rice distribution is approximated by the well known statistical forms. In the case of $I_P \gg \sigma$, the Rice distribution of $I_{P_{obs}}$ asymptotically approaches a Gaussian distribution (see Fig. 2.1). Since the Gaussian is a symmetric distribution, the most probable value and the peak value, $df/dI_P = 0$ are the same. Therefore, the most probable $I_{P_{obs}}$ is the real I_P in this case(see Fig.2.1(a)).

In the other case, $I_P \sim \sigma_{I_P}$, the Rice distribution of $I_{P_{obs}}$ is a Rayleigh distribution (see Fig.2.1(b)). In this case, the most probable value is larger than the peak value, $df/dI_P = 0$, $I_{P_{obs}} = \sqrt{\pi/2}\,\sigma\,(= I_P)$. The reason is that the Rayleigh distribution is an asymmetric distribution. This has become known as the Ricean bias in the literature, and is caused by the positivity of the noise in $I_P = \sqrt{U^2 + Q^2}$. Different from the polarized intensity, the distribution function of the polarization angles remains symmetric, and no Ricean bias correction is needed (Wardle & Kronberg, 1974), since there is no positivity problem in $\chi = \tan^{-1}(U/Q)$.

2.2.1 The two known solutions

In practic, two solutions of the Ricean bias correction are widely used.

The solution of Wardle & Kronberg

Wardle & Kronberg (1974) have suggested a solution based on the mode of the equation, namely, $\frac{df}{dI_{P_{obs}}} = 0$.

$$(1 - I_{P_{obs}}^2/\sigma_{I_P}^2)B_0(I_{P_{obs}}I_P/\sigma_{I_P}^2) + I_{P_{obs}}I_P/\sigma_{I_P}^2 I_1(I_{P_{obs}}I_P/\sigma_{I_P}^2) = 0$$

A good approximation of this solution is

$$I_P \sim \sqrt{I_{P_{obs}}^2 - \sigma_{I_P}^2}$$

Conventionally, $I_P \sim \sqrt{I_{P_{obs}}^2 - c_1\sigma_{I_{obs}}^2}$ with $c_1 = 1.2$. As seen above, $I_{P_{obs}} = \sigma_{I_P}\sqrt{\pi/2} \sim 1.25\,\sigma_{I_P}$ is the Rayleigh distribution.

The solution of Killeen et al.

The other solution which is based on a more solid statistical reasoning, viz. the Maximum Likelihood method, $\frac{df}{dI_P} = 0$, was suggested by Killeen et al. (1986). With increasing signal-to-noise, the Maximum Likelihood estimate approaches the value of I_P more rapidly:

$$I_{P_{obs}}I_P/\sigma_{I_P}^2 B_0(I_{P_{obs}}I_P/\sigma_{I_P}^2) - I_{P_{obs}}^2/\sigma_{I_P}^2 I_1(I_{P_{obs}}I_P/\sigma_{I_P}^2) = 0$$

A good approximation of this solution is

$$I_P \sim I_{P_{obs}} - 0.5\,\sigma_{I_{P_{obs}}}^2/I_{P_{obs}},$$

which is implemented in the AIPS task POLCO as such.

Pros and Cons of the solutions

The performance of the Maximum Likelihood (ML) estimation is better at high signal-to-noise, $I_P/\sigma_{I_P} > 5$, but does not yield any significant effect, since the difference to the solution of Wardle & Kronberg (1974) is much less than 1% (see Fig.2.2 and 2.3). This is because the probability distribution of $I_{P_{obs}}$ becomes a (symmetric) Gaussian at high signal-to-noise. On the contrary, the difference at low signal-to-noise, i.e. the overestimate of the Maximum Likelihood solution, is significant. As mentioned in the help tool to AIPS task POLCO, one should assume an underestimate of up to about a factor of 2 of the noise level, due to the so-called 'magic blanking'. Therefore, if one wants to go down to a 3-σ_{I_P} level, the choices of the solution and of c_1 become critical.

In the Wardle & Kronberg (1974) solution, $I_P \sim \sqrt{I_{P_{obs}}^2 - c_1\sigma_{I_{P_{obs}}}^2}$, c_1 should be carefully selected. As we are not interested in values of I_P as low as $I_{P_{obs}} \sim \sigma_{I_P}$, c_1 should be lower than $\sqrt{\pi/2}$ for a better performance in the range $3 < I_{P_{obs}}/\sigma_{I_P} < 6 \sim 10$. Above $6\,\sigma_{I_P}...10\,\sigma_{I_P}$, we can expect the best performance using the ML solution. From our experiments, we conclude that $c_1 = 0.9$ is a reasonable choice (Fig.2.2 and Fig.2.3).

2.3 The 'hybrid' solution

Our goal is to improve the performance of the Ricean correction such that $m' = \frac{I_P}{I}$ should be reliable down to $3\,\sigma_{I_P}$ and $3\,\sigma_I$. In the next subsection, we will show the importance of the areal mean m' and the position information of DP. Our scheme is simple. We make a hybrid solution of the two solutions explained in the former subsection. At high signal-to-noise, we will still use the scheme of Killeen et al. (1986). At low signal-to-noise, the solution of (Wardle & Kronberg, 1974) is better, but with $c_1 = 0.9$.

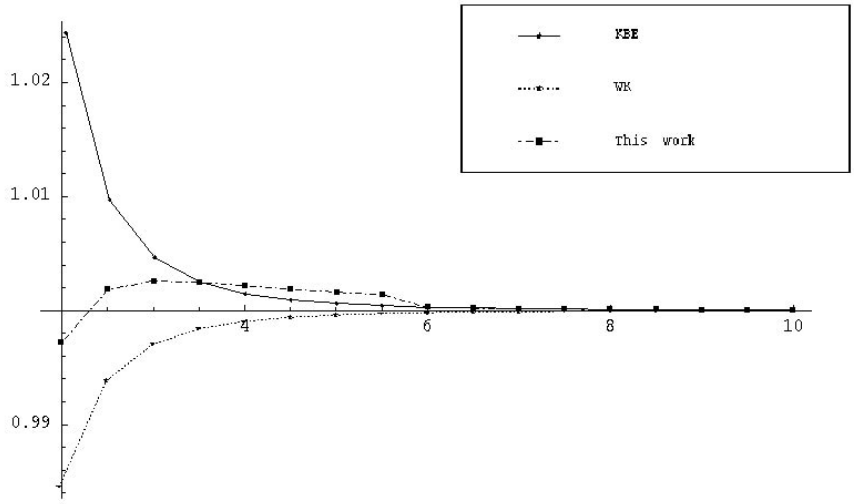

Figure 2.2: The simulation shows the case $\sigma = \sigma_{I_{P_{obs}}}$, an ideal case. The abscissa is $I_{P_{obs}}/\sigma_{I_{P_{obs}}}$ and the ordinate is $I_{P_{obs}}/I_P$. 'WK' denotes the solution of $I_{P_{obs}}$ following Wardle & Kronberg (1974), 'KBE' that of Killeen et al. (1986), and 'this work' that of this thesis. In practice, one should bear in mind that $I_{P_{obs}}$ will NOT be the mathematical solution of the former section, but rather the distribution around this mean value. Therefore, fluctuations of DP and FPOL if obtained from low polarized intensities are largely purely statistical but not physically meaningful. The new solution shows an enhanced performance at low signal-to-noise. Between $4 < I_P/\sigma_{I_P} < 6$, the old solutions are better, but the difference is less than 0.1 percent.

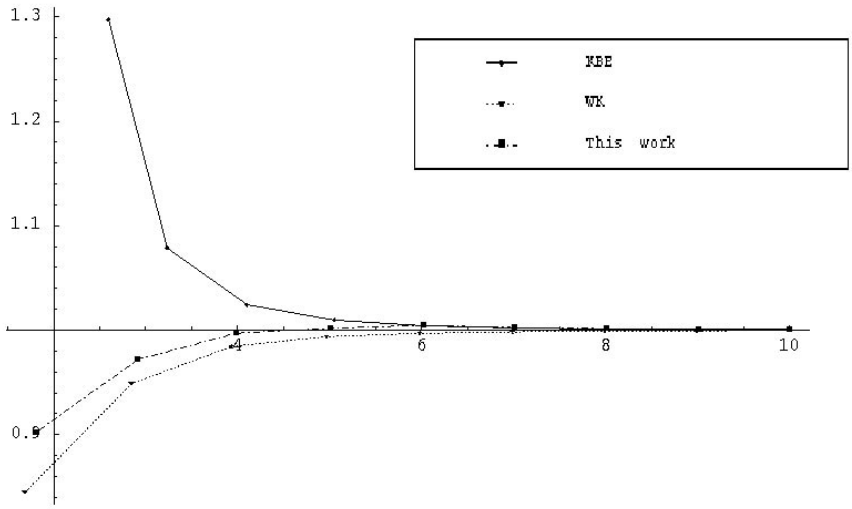

Figure 2.3: The simulation shows the case $\sigma_{I_P} = 2\,\sigma_{I_{P_{obs}}}$. A underestimate of σ by a factor of 2 of σ_{I_P} could be possible ,due to the blanked values ((*AIPS Cookbook*, 1999), see also AIPS HELP). In view of the underestimate of σ_{I_P}, our new solution is the best one. The solution implemented into AIPS task POLCO Killeen et al. (1986) strongly overestimates the polarization intensity, while the Wardle & Kronberg (1974) solution underestimates it. The difference is much larger than that to our solution visible in Fig.2.2.

The selection of c_1 has been done numerically, considering the fact that one should take account of the underestimation of the noise by up to factor of 2 in the intensity (*AIPS Cookbook*, 1999), due to the blanked values. Further minor estimation errors could be caused, for example, through a wrong selection of the noise estimation area, which could further underestimate σ_{I_p}. We combine the two solutions (Wardle & Kronberg, 1974; Killeen et al., 1986). Our solution accepts the Maximum Likelihood over $I_{P_{obs}} \sim 6\,\sigma_{I_P}$; below this, it uses $I_P \sim \sqrt{I^2_{P_{obs}} - c_1\sigma^2_{I_P}}$ with $c_1 = 0.9$, which is a good choice for $\sigma_{I_P}/I_{P_{obs}}$ between 1.5 to 6. Using this new fractional polarization, we can estimate DP with the positional information and can study any correlation between RM and DP.

2.3.1 Integrated fractional polarization

Before working out a new method to estimate the fraction of polarization, we discuss the integrated fractional polarization as published in the literature, motivating this new correction method. There are two ways to estimate the fractional polarization of a region of interest. One can first integrate the polarized and the total intensity and divide them:

$$m' = \frac{\Sigma I_P}{\Sigma I}.$$

There are pros and cons to this integrated estimate. The pro is that the Ricean bias problems are largely removed by the integration. The obtained m' reflects the fractional

polarization of bright source structures, such as cores, hotspots and jets. The con is the loss of the positional information. Conventionally, DP maps are presented after one of the Ricean bias corrections, i.e. (Wardle & Kronberg, 1974; Killeen et al., 1986), down to $3\,\sigma_{I_P}$ of the total intensity. This will lead to significant over- and underestimates of the low-$\sigma_{I,P}$ regions, such as the lobes. Therefore, in order to estimate the fractional polarization including the positional information, an estimate $m' = \Sigma(\frac{I_P}{I})$ is desirable.

In polarization studies, other important informations are the polarization angle and the Rotation Measure. Since they are independent of the brightness, the use of DP as obtained from $m' = \frac{\Sigma P}{\Sigma I}$ could lead to a wrong interpretation.

2.3.2 Underestimates of σ_{I_P} in the literature

In this subsection, we discuss the propagation of the systematic error as due to the insufficient Ricean bias correction in published DP maps. The discussion is based on the solution of Killeen et al. (1986). For the solution of Wardle & Kronberg (1974), this should be interpreted in an opposite sense. In that case, the systematic error in regions with low polarization intensity is less important, unless the signal-to-noise is too low in the absence of any σ_{I_P} cut-off.

We consider the problem of underestimating σ_{I_P} for two cases, namely for well resolved and for unresolved sources. We assume a power-law distribution for I_ν. When the source and the Faraday medium are resolved, the overestimate caused by the $3\,\sigma_{I_P}$ cut is serious at the highest frequencies. In this case, the fractional polarization of regions with low I_p could be overestimated. The other case is that of low anular resolution. Because of the Faraday Rotation in the foreground medium, depolarization will be significant. In the most depolarized regions, a cut at $3\,\sigma_{I_P}$ is serious at the lowest frequencies. Then the fractional polarization of such regions is overestimated at the lowest compared to the highest frequencies. In effect, the depolarization trend will thus be reduced.

In depolarization studies, the integrated DP is rather independent of the polarized and total intensity, but rather depends on $\int m'(S)\cdot S\,dS$, where S is the projected surface. The first case (resolved source) overestimates DP, while the second (unresolved source) underestimates it. Let us discuss this in the light of the Laing-Garrington effect. If one can assume that the jet side is brighter and more polarized, the two arguments will be more important for the counterjet lobe. In the first case, the Laing-Garrington effect will be emphasized through the overestimate of DP, whereas it will be reduced in the second case because of the under-estimation.

One more word of caution seems to be necessary regarding DP structures. Patchy distributions of DP in regions with low I_p which are frequently seen should be interpreted with utter care. One can mis-interprete such a patchy structure as real turbulence or fluctuations. Unless such patchy structures are confirmed independently, e.g. also in RM maps, they could be soley statistical.

2.3.3 The normalized DPm

We use the normalized DP defined by

$$DP = \frac{m'_{high} - m'_{low}}{m'_{high} + m'_{low}},$$

where m'_{high} and m'_{low} are the fractional polarizations at the higher and lower fre-

quency, respectively. Between DPm and DP, we have the relation,

$$DPm = \frac{1-DP}{1+DP} \text{ or } DP = \frac{1-DPm}{1+DPm}.$$

Then, σ_{DP} is

$$\sigma_{DP}^2 = (\frac{\partial DP}{\partial m'_{high}})^2 \sigma_{m'_{high}}^2 + (\frac{\partial DP}{\partial m'_{low}})^2 \sigma_{m'_{low}}^2$$

and

$$\sigma_{m'}^2 = (\frac{\partial I_P/I}{\partial I})^2 \sigma_I^2 + (\frac{\partial I_P/I}{\partial I_P})^2 \sigma_{I_P}^2.$$

In practice, these will be

$$\sigma_{m'}^2 = (\frac{I_P}{I^2})^2 \sigma_I^2 + I^{-2} \sigma_{I_P}^2$$

and

$$\sigma_{DP}^2 = 4\frac{m'^2_{high}+m'^2_{low}}{(m'_{high}+m'_{low})^4}(m'^2_{low}\sigma^2_{m'_{high}} + m'^2_{high}\sigma^2_{m'_{low}}).$$

The merit of a normalized DP shows up when one wants to compare two or more DPs at different frequencies and/or different angular resolutions. One can easily quantify the multi-frequency de- or repolarization. The weakness of the normalized DP is that there is no direct connection to the Faraday depth. Since our aim in the next section will be to compare DP maps, the normalized DP turns out to be a useful tool. If one wants to estimate the Faraday depth, one should go back to the conventional DP. The estimated error will be seen in the section dealing with the DP-RM connection.

2.4 DP maps of Giant Radio Galaxies

Using our new Ricean bias correction, we have estimated the fractional polarization (m) of five GRGs, namely NGC 315, DA 240, 3C236, 3C 326 and NGC 6251. These were observed by Mack et al. (1997b). We have made the maps of fractional polarization at three different frequencies, namely 10.6, 4.8 and 610 MHz. As described in the previous section, the main improvement of our new 'hybrid' Ricean bias correction is the higher reliability provided by the positional information at low signal-to-noise.

We present DP maps of each GRG if necessary in up to three maps with different angular resolution. The higher resolution maps, which have an angular resolution of $69'' \times 69''$, contain the depolarization measure at 610 and 10.6 GHz, $DP_{0.6}^{10.6}$. An exception is 3C 326 where an angular resolution of $82'' \times 69''$ is used. In order to calculate the DP maps, the 610 MHz maps of Mack et al. (1998) were convolved to a Gaussian beam of $69'' \times 69''$, using the AIPS task CONVL.

The $DP_{4.8}^{10.6}$ maps have an angular resolution of $150'' \times 150''$. For 3C 326, a beam of $161'' \times 150''$ was used for the convolution. 3C 326 is the most distant GRG, with $z = 0.0895$. For 3C 326, $82'' \times 69''$ corresponds to 131 kpc $\times$ 110 kpc, and $161'' \times 150''$ to 256 kpc $\times$ 239 kpc [1]. The nearest GRG is NGC 315, with $z = 0.0167$. For NGC 315, $69'' \times 69''$ corresponds to 22 kpc $\times$ 22 kpc, and $150'' \times 150''$ to 48 kpc $\times$ 48 kpc.

2.4.1 Integrated Properties

The integrated fractional polarizations of the five GRGs at 10.6 GHz are presented in Tab. 2.2 at two different resolutions. Two (DA 240 and NGC 6251) out of the five GRGs exhibit integrated fractional polarizations that appear to go into the 'wrong' direction. This is due to the beam convolution. The repolarization does not happen all over the sources, but is seen in the counter-hot spot of NGC 6251 and within the diffuse extension of DA 240. They appear highly polarized in the higher-resolution map. The bracketed values in Tab. 2.2 are the FPOLs and DPs of DA 240 and NGC 6251, excluding these regions. In the higher-resolution map at 10.6 GHz, the projected area of the eastern lobe of DA 240 and of the western jet plus lobe are representative. Therefore, we use the values in brackets for the further estimates.

In Tab. 2.2, DP_{beam} denotes the beam depolarization. If the scale length of the Faraday medium is universal and the Faraday depth is more or less uniform, then the nearer source should be less depolarized than the farther. This simple idea fails to explain the integrated DP_{beam} of five GRGs, in that the two most distant sources (3C 236 and 3C 326) are the least depolarized ones. This is not the long-wavelength saturation effect which is expected from Burn's law. The integrated values of fractional polarization in 3C 236 and 3C 326 are in the same range as those in the other three GRGs, and they were computed at 10.6 GHz.

We should point out once more that the fractional polarization FPOL (m), DPm and DP as estimated here do not derive from $m = (\Sigma P)/(\Sigma I)$, but rather from $m = \Sigma(P/I)$. This means that at positions where either P or I cannot be computed m is not available. Since we are aiming at studying the properties of the Faraday media in this chapter and not the sources' intrinsic polarization properties, this fact is an advantage.

The beam polarization is most significant in the two nearest sources (NGC 315 and NGC 6251). In Tab. 2.2, there is a clear correlation between the distance and the beam depolarization. Since the two least beam depolarized sources, 3C 236 ($l \sim 4.5$ Mpc) and

[1] $H_0 = 75$ km s^{-1} Mpc^{-1}, $q_0 = 1$

Table 2.1: Coordinates of the five GRGs

Name	z	RA(J2000)	DEC(J2000)	l	b
NGC 315	0.016485	$00^h57^m48\overset{s}{.}9$	$+30°21'09''$	$24\overset{\circ}{.}56$	$-32\overset{\circ}{.}49$
DA 240	0.036000	$07^h47^m34\overset{s}{.}14$	$+55°41'34\overset{''}{.}4$	$162\overset{\circ}{.}03$	$+29\overset{\circ}{.}88$
3C 236	0.100500	$10^h06^m01\overset{s}{.}74$	$+34°54'10\overset{''}{.}4$	$190\overset{\circ}{.}06$	$+53\overset{\circ}{.}98$
3C 326	0.089500	$15^h52^m09\overset{s}{.}1$	$+20°05'24''$	$33\overset{\circ}{.}26$	$+48\overset{\circ}{.}22$
NGC 6251	0.024881	$06^h32^m31\overset{s}{.}97$	$+82°32'16\overset{''}{.}5$	$115\overset{\circ}{.}76$	$+31\overset{\circ}{.}19$

Table 2.2: $\overline{m}$ and the beam depolarization.

Name	d (Mpc)	$m_{69''}(\%)$	$m_{150''}(\%)$	DP_{beam}	Notes
NGC 315	66	23.9	19.3	0.81	
DA 240	137	21.2 (19.7)	26.8 (17.5)	1.26 (0.89)	(E lobe)
3C 236	359	19.3	17.9	0.93	
3C 326	328	22.4	20.4	0.91	
NGC 6251	91	14.8 (13.3)	15.1 (10.5)	1.02 (0.79)	(W lobe)

3C 326 ($l \sim 2.6$ Mpc), are the two largest GRGs in the sample and are the two most distant sources at the same time, it is too early to decide whether or not this is just due to beam depolarization. One could argue that the extremities of 3C 236 and 3C 326 are far outside of the X-ray cluster environment and that there could be a difference between Mpc-sized sources and those that are larger. We do not yet draw any conclusion here as to the scale length of the Faraday medium based only on beam depolarization. For a final discussion, the distribution of DP and RM should be also considered. These will be the subjects of the next sections.

2.4.2 NGC 315

At first glance, our two DP_m maps of NGC 315 (Fig. 2.4) do not show any significant polarization asymmetry, but a rather random fluctuation across the whole structure. The statistical fluctuation is unavoidable at low signal-to-noise. The complex structure in the core is largely an instrumental artefact (Mack et al., 1997b). The values of DP and DP_m for the core are hence unreliable. The integrated depolarization measures ($DPm_{0.6}^{10.6}$ and $DP_{0.6}^{10.6}$) show that the Faraday screen of the source is well resolved by the $69''$ beam (Tab. 2.3). There is no λ^4 dependence (Burn's law) visible, in fact $m_{10.6} \sim m_{0.6}$. The regions labelled in Tab. 2.3 refer to those given by Mack et al. (1998). The beam depolarization between $69''$ and $150''$ is, however, clearly visible in Tab. 2.2. The scale length of the Faraday medium seems to be between 22 kpc ($69''$) and 48 kpc ($150''$) in NGC 315.

2.4.3 DA 240

DA 240 (Fig. 2.5) exhibits a high fractional polarization (Tab.2.2). This could be misinterpreted such that DA 240 is a highly polarized source on the whole. In fact, the 'fat double' lobes are very weakly polarized, and we cannot estimate their fractional polarization. The highest values of m are found along the major axis. The 'fat double' lobes disappear at high frequencies. In the SCP-α analysis (the second part of this thesis), the source shows a so-called 'JP' spectrum, characterized by an isotropic pitch

Table 2.3: DPm and DP of NGC 315

	$DPm_{0.6}^{10.6}$	$\Delta DPm_{0.6}^{10.6}$	$DP_{0.6}^{10.6}$	$\Delta DP_{0.6}^{10.6}$
total source	-0.03	0.26	0.94	0.59
core, jets	0.0	0.30	1.00	0.54
inter jet	-0.10	0.19	1.22	0.68
NW hotspot	-0.03	0.26	1.06	0.59
NW bow	0.07	0.23	0.87	0.63
N relic 1	-0.19	0.20	1.47	0.67
N relic 2	-0.38	0.26	2.22	0.59
SE lobe	-0.04	0.20	1.08	0.67

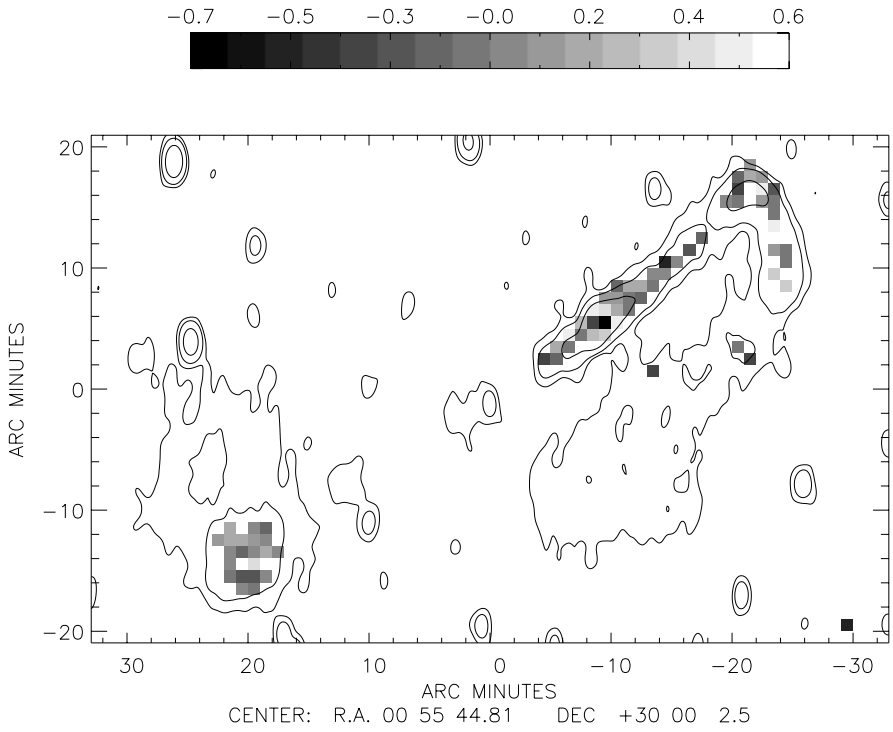

Figure 2.4: $DP_{0.6}^{10.6}$ map of NGC 315. The contours represent the total intensity at 326 MHz. The contour lines are 3, 10 and 50 σ_I.

Table 2.4: DPm and DP of DA 240

	$DPm_{0.6}^{10.6}$	$\Delta DPm_{0.6}^{10.6}$	$DP_{0.6}^{10.6}$	$\Delta DP_{0.6}^{10.6}$
total source	0.12	0.28	0.79	0.56
NE lobe	0.02	0.24	0.96	0.61
SW lobe	0.33	0.19	0.50	0.68
Core	0.55	0.12	0.29	0.79
B.G.	0.51	0.05	0.32	0.90

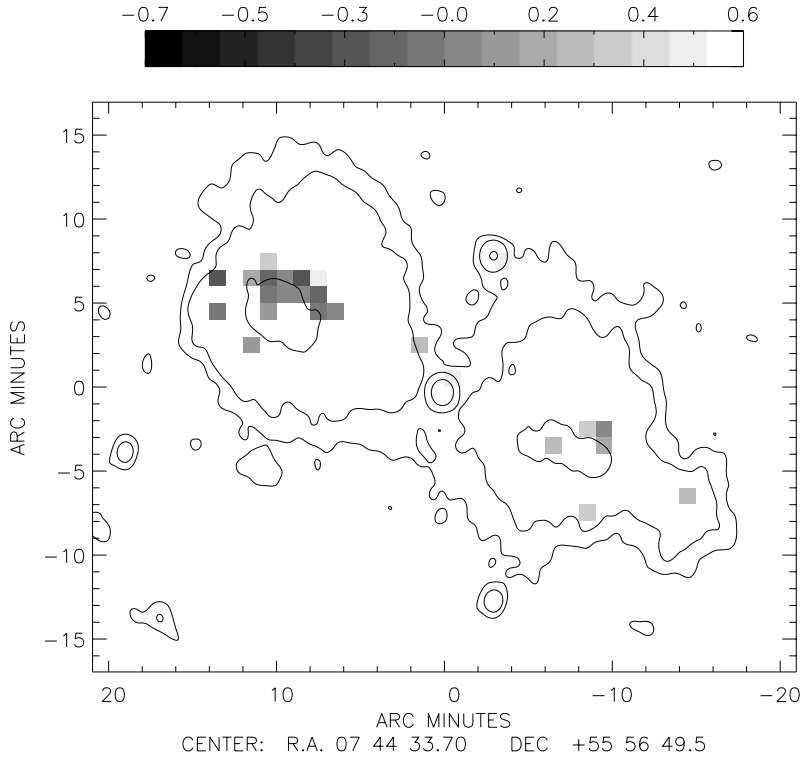

Figure 2.5: $DP_{0.6}^{10.6}$ map of DA 240. The contours represent the total intensity at 326 MHz. The contour lines are 3, 10 and 50 σ_I.

Table 2.5: DPm and DP of 3C 236

	$DPm_{0.6}^{10.6}$	$\Delta DPm_{0.6}^{10.6}$	$DP_{0.6}^{10.6}$	$\Delta DP_{0.6}^{10.6}$
int. source	0.24	0.30	0.61	0.54
Core	0.67	0.26	0.20	0.59
NE back lobe	0.21	0.16	0.65	0.72
NE hot spot	0.30	0.17	0.54	0.71
SW back lobe	0.03	0.22	0.94	0.64
SW hot spot	0.06	0.26	0.89	0.59

angle distribution. We conclude that the low fractional polarization in the 'fat double' lobes is intrinsic. The remaining high values of FPOL show a clear depolarization asymmetry. The NE lobe is not depolarized, while the SW one is (see Tab. 2.4 and Fig. 2.5).

2.4.4 3C 236

3C 236 (Fig. 2.6) at a distance of ~ 4.5 Mpc, is the largest known radio galaxy, and has an FR II morphology, with hotspots at its extremities. The fractional polarizations indicate that the source is highly polarized, $30\% \sim 40\%$, also in the back lobe. Between angular resolutions of $69''$ and $150''$, beam depolarization is not significant (see Tab. 2.2). On the contrary, there is clear evidence for wavelength-dependent depolarization (see Tab. 2.5). The depolarization asymmetry is obvious, too. Taken together, this indicates that the Faraday medium is unresolved and Burn's λ^4 law (which requires an unresolved Faraday foreground) and that the Laing-Garrington effect (which needs a λ^4 law) is working.

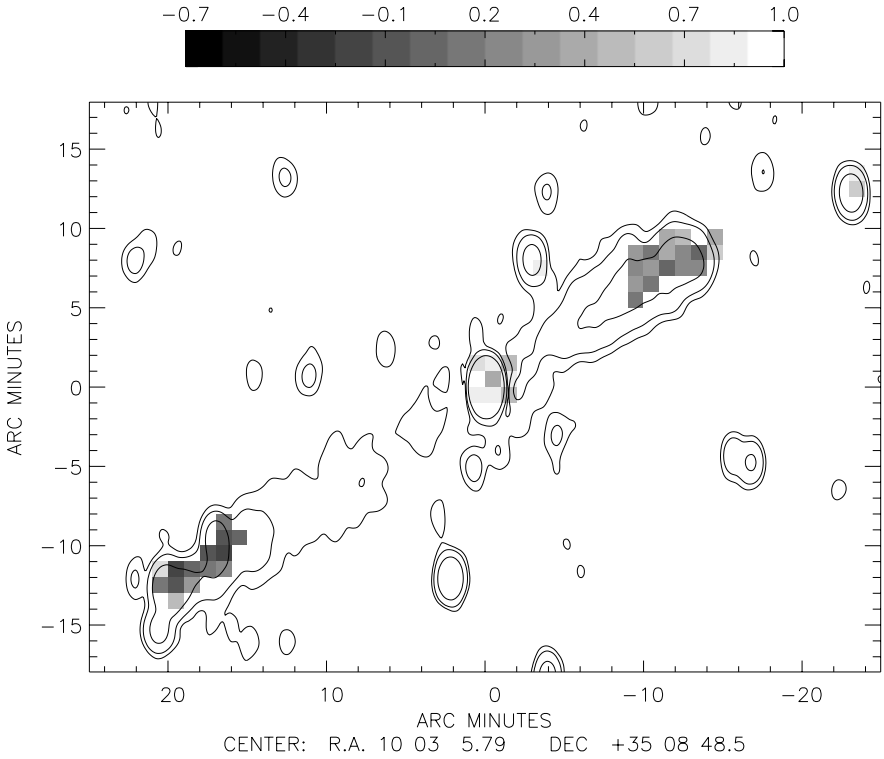

Figure 2.6: $DPm_{49}^{6.3}$ map of 3C 236. The contours represent the total intensity at 326 MHz. The contour lines are 3, 10 and 50 σ_I.

Table 2.6: DPm and DP of 3C 326

	$DPm_{0.6}^{10.6}$	$\Delta DPm_{0.6}^{10.6}$	$DP_{0.6}^{10.6}$	$\Delta DP_{0.6}^{10.6}$
int. source	0.31	0.22	0.53	0.64
E lobe	0.25	0.23	0.60	0.63
Centre	0.42	0.15	0.41	0.74
W lobe	0.20	0.20	0.67	0.67

2.4.5 3C 326

3C 326 (Fig. 2.7) has a complex structure, with several brightness peaks along the major axis. The source is highly polarized, with values up to $\sim 60\%$ in the W lobe, and up to $\sim 30\%$ in the E lobe. The field structure is surprisingly well ordered, which is even evident at 4.8 GHz. At this frequency the resolution corresponds to ~ 110 kpc, yet high fractional polarization is not lost (Mack et al., 1998). The source has a weakly polarized, low-intensity radio lobe around the centre.

In this second largest and second farthest (next to 3C 236) radio galaxy in our sample, beam depolarization is not obvious. The wavelength dependent depolarization is significant as well. The depolarization asymmetry is only marginal, while the centre-to-lobe variation of the depolarization is more pronounced. Our preliminary conclusion is that the Faraday medium is not resolved and that there is a correlation between the Faraday depth and the distance from the centre.

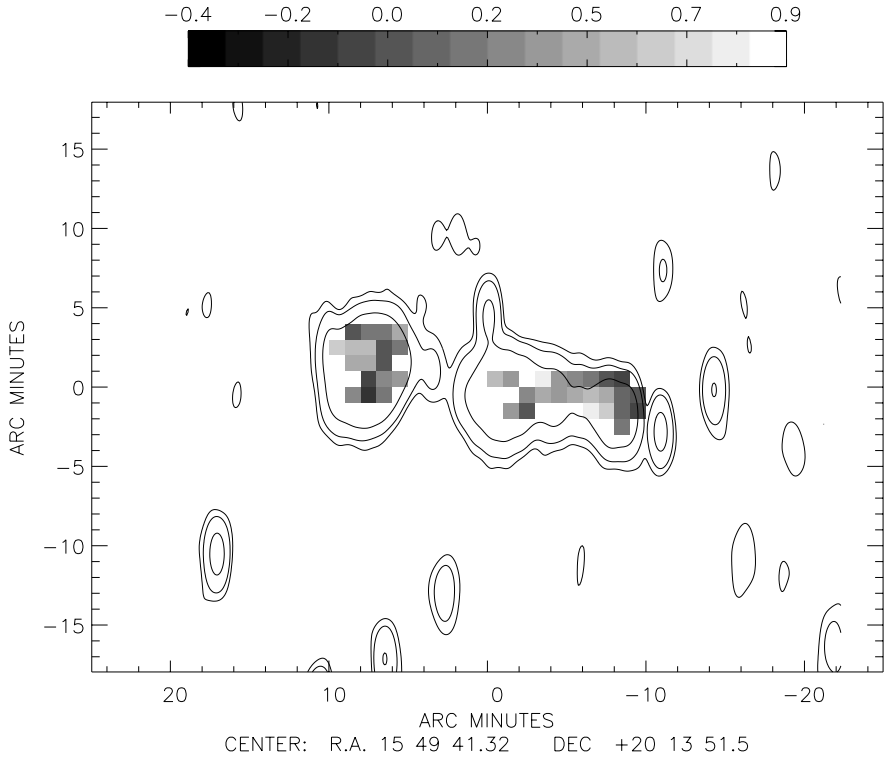

Figure 2.7: $DP_{49}^{2.8}$ map of 3C 326. The contours represent the total intensity at 326 MHz. The contour lines are 3, 10 and 50 σ_I.

Table 2.7: DPm and DP of NGC 6251

	$DPm_{0.6}^{10.6}$	$\Delta DPm_{0.6}^{10.6}$	$DP_{0.6}^{10.6}$	$\Delta DP_{0.6}^{10.6}$
int. source	0.27	0.31	0.57	0.53
Core, jets	0.25	0.37	0.60	0.46
NW hot spot	0.27	0.25	0.57	0.60
SE hot spot	0.40	0.21	0.43	0.65

2.4.6 NGC 6251

The extended lobes are only weakly polarized over the whole frequency range considered here. In this respect, NGC 6251 (Fig. 2.8) is similar to DA 240. From the few values of FPOL (in the jet, the hotspot and the counter-hotspot), clear evidence for beam depolarization is found. The wavelength-dependent depolarization is significant, too. Comparing the two hotspots, depolarization is also seen there. Since the wavelenth dependent and the beam depolarization are working together in NGC 6251, internal depolarization is an alternative (indeed, thermal X-ray emssion has been reported (Mack et al., 1997a)). Otherwise, we would need a more complicated Foreground model such as the quadratic model of Tribble (1991).

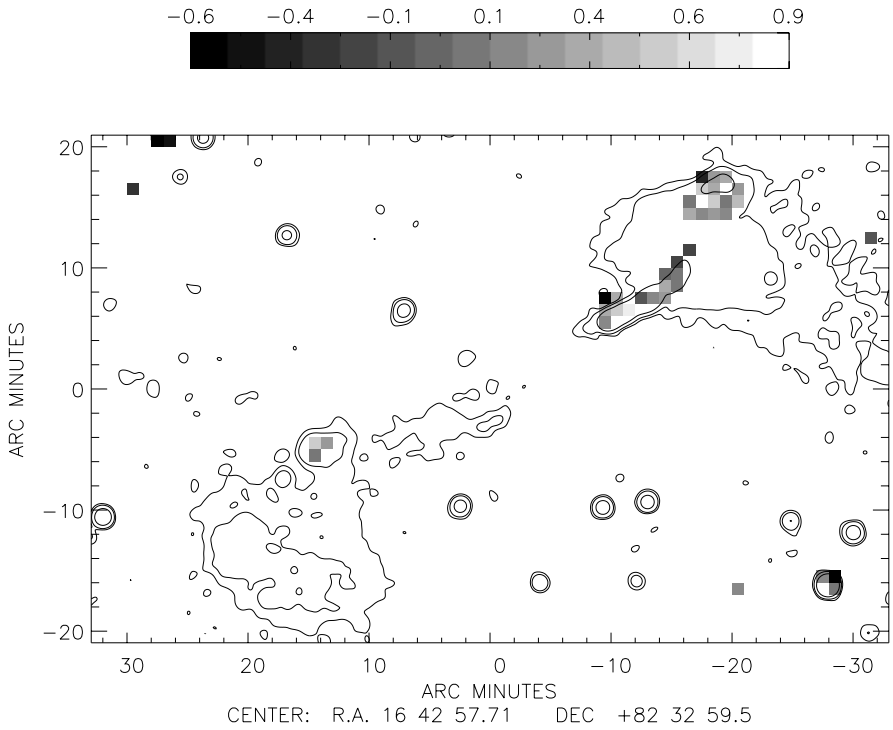

Figure 2.8: DPm and DP of NGC 6251. The contours represent the total intensity at 326 MHz. The contour lines are 3 σ_I, 10 σ_I and 50 σ_I.

Chapter 3

Rotation Measures of Giant Radio Galaxies

3.1 Rotation Measures of GRGs

In this section we present the rotation measure (RM) estimates for the five GRGs. We assume that Faraday rotation occurs in the foreground as claimed in the literature (Clarke et al., 2001; Eilek & Owen, 2002). If needed, the 'internal' case will be discussed. From the RM data, we expect to obtain two pieces of information about the Faraday medium. These are its scale length, $d_{\rm RM}$, and the product $< B_{||} \cdot n_e >$, obtained from

$$\mathrm{RM} \;=\; 8.1 \cdot 10^8 \int \frac{B_{||}}{G} \frac{n_e(l)}{cm^{-3}} \frac{dl}{kpc} \;=\; 810 \cdot \int \frac{B_{||}}{\mu G} \frac{n_e(l)}{cm^{-3}} \frac{dl}{kpc} \ \mathrm{rad\,m^{-2}}.$$

3.1.1 Error estimation

From the rms noise in the Stokes parameters U and Q, σ_U and σ_Q, we obtain σ_χ^2 and σ_{RM}^2 as follows. The position angle of each pixel is

$$\chi = 0.5 \tan^{-1}(\tfrac{U}{Q}).$$

Then, its error will be

$$\sigma_\chi^2 = (\tfrac{\partial \chi}{\partial U})^2 \sigma_U^2 + (\tfrac{\partial \chi}{\partial Q})^2 \sigma_Q^2.$$

Let $f \equiv \frac{U}{Q}$. Then

$$\tfrac{\partial \chi}{\partial f} \tfrac{\partial f}{\partial U} = 0.5 \tfrac{1}{(1+f^2)Q}$$

and

$$\tfrac{\partial \chi}{\partial f} \tfrac{\partial f}{\partial Q} = 0.5 \tfrac{1}{1+f^2} \tfrac{-U}{Q^2}$$

Assuming $\sigma_Q \approx \sigma_U \approx \sigma_{I_P}$, we obtain

$$\sigma_\chi^2 = \tfrac{\sigma_{I_P}^2}{4 I_P^2}.$$

This is exactly the same result as in Wardle & Kronberg (1974) who used a statistical analysis of Vinokur (1965). Then, σ_{RM} is

$$\sigma^2_{RM} = \frac{1}{4(\lambda_1^2-\lambda_2^2)^2}(\sigma^2_{\chi 1} + \sigma^2_{\chi 2}),\ \lambda_1 > \lambda_2.$$

If we go down to $I_p = 3\,\sigma_{I_P}$ and if the noise is an ideal Gaussian distribution, the equations show that the uncertainty of the polarization angle will reach up to $\sigma_\chi \sim 9.5°$. The uncertainty in RM depends on the observing frequencies. In case of a two-frequency estimate between 10.6 and 4.8 GHz, $RM^{10.6}_{4.8}$, $\sigma_{RM} \sim 74$ rad m^{-2}. We should be careful in interpreting pixel-scale polarization angles and RM structures. The pixel-scale variation could be purely due to the noise in the U and Q maps. Therefore, we begin with the histograms of the distribution in order to judge the reliability of the data sets. If there is any substructure or grouping of polarization angles, this must be verified in the histograms. Subsequently, if verified, the positional information will be taken from the RM maps.

3.2 Polarization angle distribution

3.2.1 NGC 315

In Fig. 3.1, we show our results in histogram form. At 10.6 GHz, the polarization angle histogram shows several peaks. From 10.6 to 4.8 GHz, the histograms of the polarization angles have a dominant first peak. At 10.6 GHz, the first peak is at $-51°$ and the second peak is at $-62°$. At 4.8 GHz, the first peak is at 72°. There is a well defined second peak at $-87°$. At 610 MHz, the histogram does not show any significant feature. The first peak is at $-75°$.

The two frequency-based RM was made using the 10.6 and the 4.8 GHz data. The two-frequency RM based on high-frequency measurements has an ambiguity of $-493 < RM < 493$ rad m^{-2}. Less ambiguity is implied for sources which reside in a cluster-core with a cooling flow environment (Clarke et al., 2001; Eilek & Owen, 2002). The RM histogram shows a prominent single peak at -230 rad m^{-2}, with broad shoulders, $\Delta RM \sim 100$ rad m^{-2}. The multiple peaks in the polarization angle histograms at 10.6 and 4.8 GHz are obviously due to the angular variation at different positions. The broad shoulders imply that there is a multi-component Faraday screen. The zero-frequency polarization angle distribution calculated from the RM and the 10.6 GHz data exhibits two clear peaks at $-33°$ and at $-54°$.

We have generated the distributions of the polarization angle at 610 MHz from the RM and the zero frequency. This data is more 'noisy', i.e. there are no peaks, as compared to the observed 610 MHz polarizations. The low-frequency polarization angles resemble somewhat the source structure, which means that they are kind of 'saturated'. The saturation can happen in the presence of an internal Faraday medium or by an unresolved Foreground medium (Laing, 1985). But the effect is only marginal. On the whole, the observed 610 MHz polarization angle histogram is far from a feature that would be expected for full saturation. Internal Faraday rotation and an unresolved Faraday screen do not appear to be major contributors to the RM.

3.2.2 DA 240

In Fig. 3.2, we show our results in histogram form. At 10.6 GHz, the polarization angle histogram shows one clear peak at 59°. At 4.8 GHz, two peaks are seen at $-2°$ and

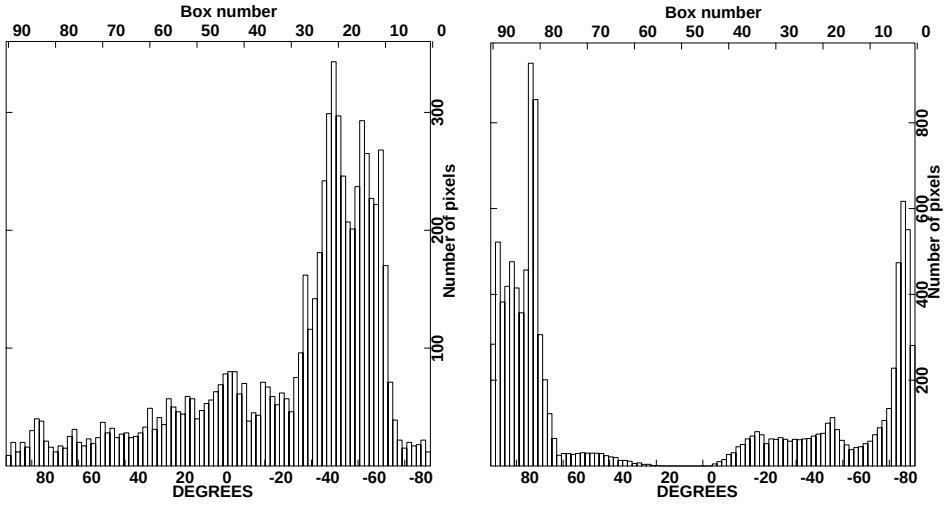

(a) 10.6 GHz

(b) 4.8 GHz

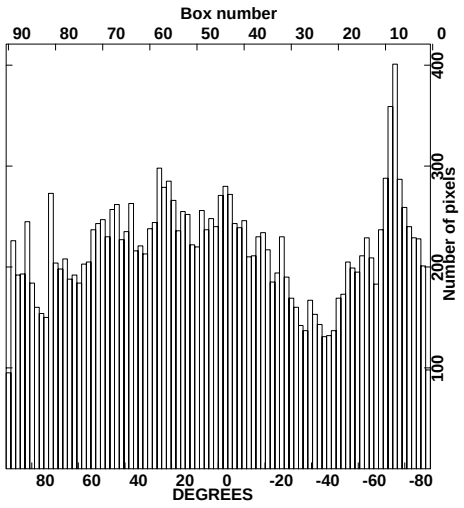

(c) 610 MHz

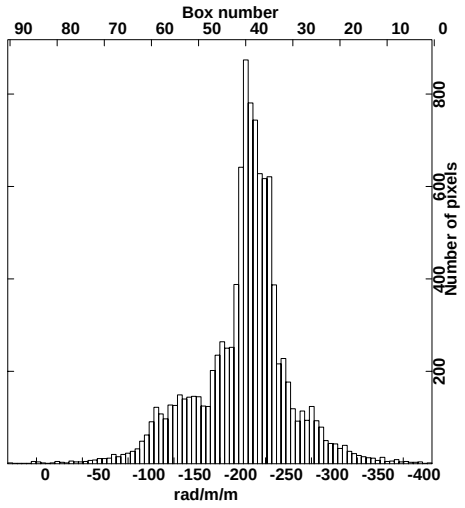

(d) RM

Figure 3.1: Distribution of polarization angles in NGC 315. [a] Polarization angle distribution at 10.6 GHz. [b] Polarization angle distribution at 4.8 GHz. [c] Polarization angle distribution at 610 MHz. [d] RM estimated between 10.6 and 4.8 GHz. [e] Distribution of the λ_0 angle from the RM [d]. [f] Estimated polarization angle distribution at 610 MHz from [e] and [d].

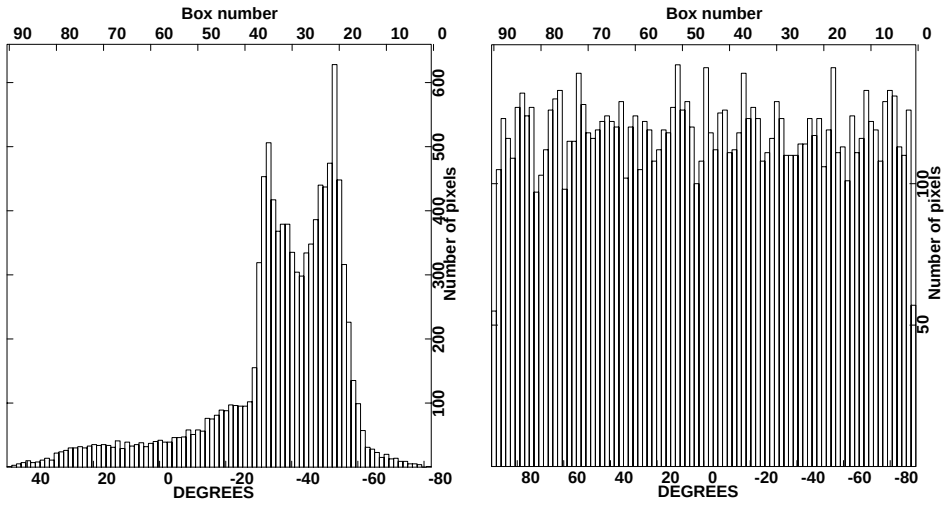

(e) λ_0 (f) 610 MHz from λ_0

Figure 3.1: continued.

$-84°$. The histogram at 610 MHz does not contain any clear trend. The RM histogram has two peaks at 140 rad m^{-2} and at 220 rad m^{-2}. Their wings are about 30 rad m^{-2} broad. The RM estimate of $|2|$ rad m^{-2} by Tsien (1982) at low frequencies appears to be wrong. The zero-wavelength distribution of polarization angles calculated from the RM and the 10.6 GHz data exhibits two clear peaks at 48° and at $-30°$.

Neither the generated 610 MHz polarization angle data nor the observed 610 MHz polarization angle data exhibit any peaks. The lack of any trend in the observed 610 MHz polarization angle data implies that the internal Faraday Rotation or the unresolved foreground screen has no major impact on the RM structure of DA 240.

3.2.3 3C 236

In Fig. 3.3, we show our results in histogram form. At 10.6 GHz, the polarization angle histogram shows a strong peak at 40°, while a second peak at 8° is much weaker. The trend seen at 4.8 GHz is the same as that at 10.6 GHz. At 4.8 GHz, a first strong peak is seen at 10°, and a second, weak peak, at 78°. The histogram at 610 MHz shows a 'zone of avoidance' between $-20°$ and $+20°$. The RM histogram has one peak at 45 rad m^{-2}, with $\Delta RM \sim |100|$ rad m^{-2}. The RM of the hotspot in the SE lobe cannot be estimated, since the hotspot is strongly beam-depolarized at 4.8 GHz.

The zero wavelength distribution of polarization angles calculated from the RM and the 10.6 GHz data exhibits two clear peaks at 48° and at 30°. The generated 610 MHz polarization angle data do not show any peaks. The trend in the observed 610 MHz polarization angle histogram could come from internal Faraday rotation or from an unresolved foreground screen. In fact, 3C 236 is the farthest GRG in our sample. The resolved scale length at 10.6 GHz is 261 kpc (69″). Beam depolarization will be most significant in 3C 236 among the whole sample.

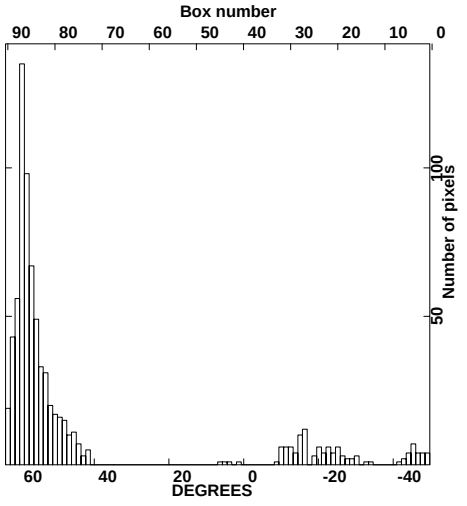

(a) 10.6 GHz

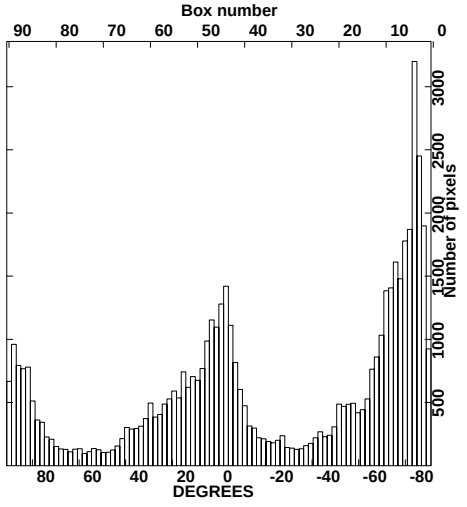

(b) 4.8 GHz

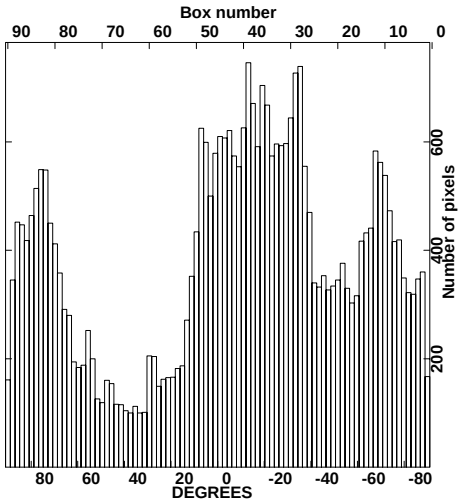

(c) 610 MHz

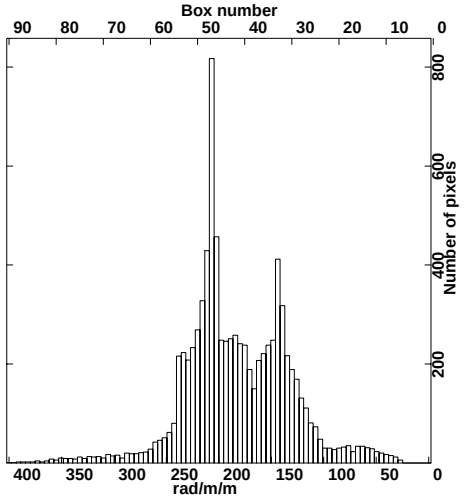

(d) RM

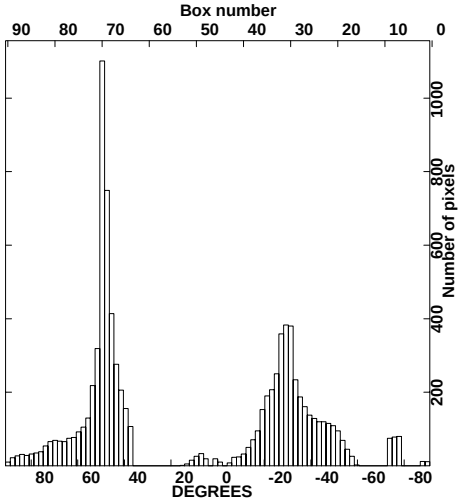

(e) λ_0

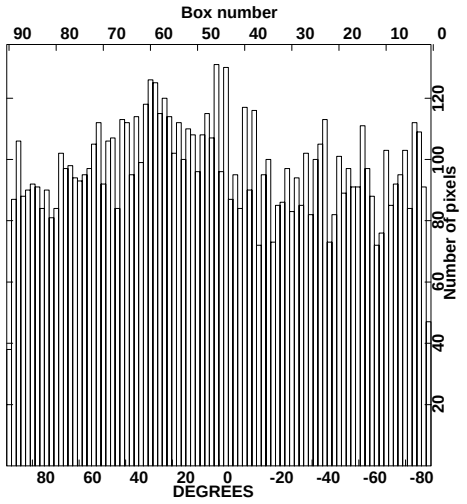

(f) 610 MHz from λ_0

Figure 3.2: Distribution of Polarization angles in DA 240. See Fig. 3.1.

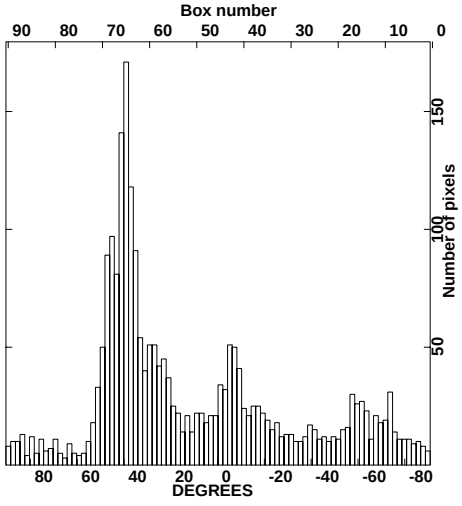

(a) 10.6 GHz

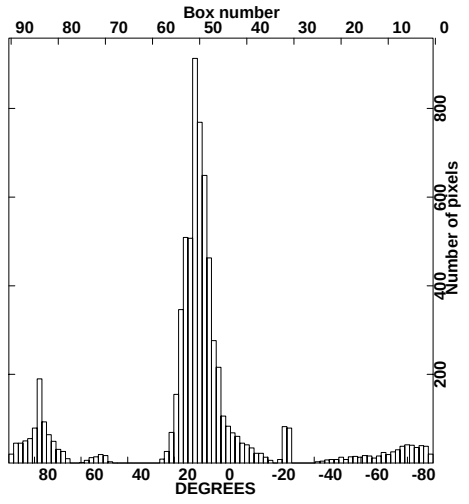

(b) 4.8 GHz

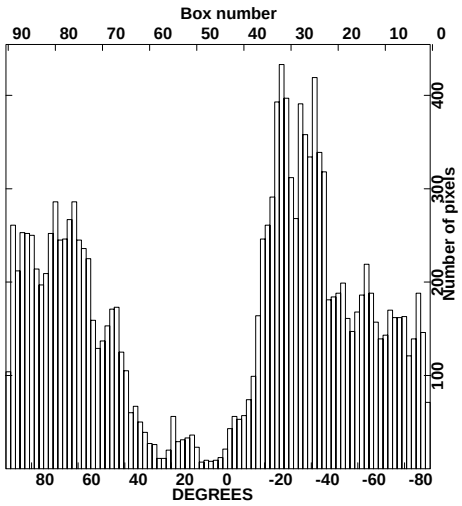

(c) 610 MHz

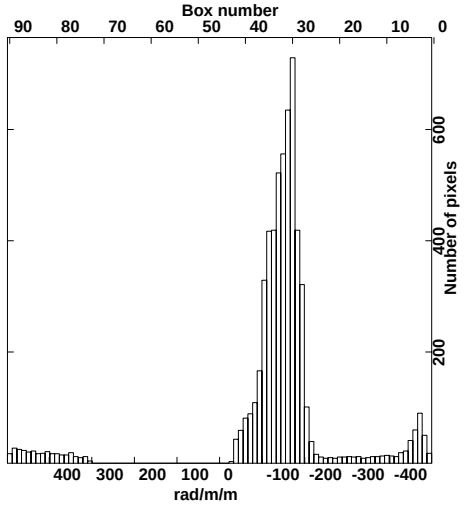

(d) RM

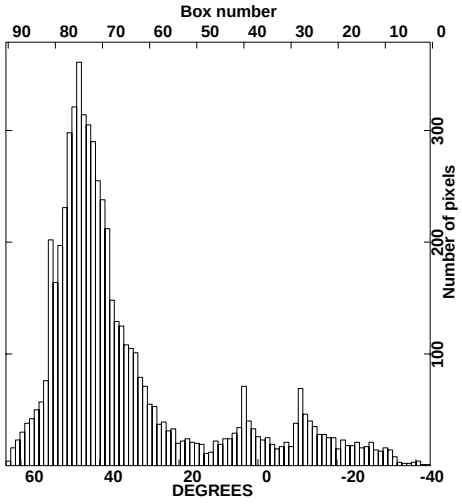

(e) λ_0

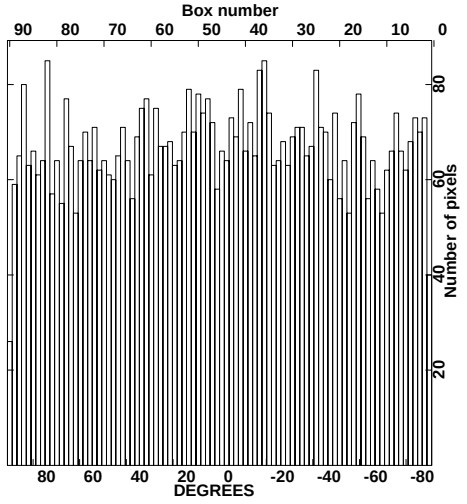

(f) 610 MHz from λ_0

Figure 3.3: Distribution of polarization angles in 3C 236. See Fig. 3.1.

3.2.4 3C 326

In Fig. 3.4, we show our results in histogram form. At 10.6 GHz, the polarization angle histogram shows a strong single peak at $-14°$. There is a weak second peak at 6°. Two peaks are well distinguished at 4.8 GHz, the first strong one being seen at $-7°$, with a second broad component peaking at 20°. The 610 MHz histogram shows structure. The peak at 10° is obvious, and there are also secondaries. The RM histogram has two peaks at 120 rad m^{-2} and at 55 rad m^{-2}. Their shoulders are about 20 rad m^{-2} broad. The RM of the hotspot in the SE lobe was not estimated, since the hotspot is strongly beam-depolarized at 4.8 GHz.

The zero-wavelength polarization angle distribution calculated from the RM and the 10.6 GHz data exhibits two peaks at $-17°$ and at $-6°$, which are better distinguished than the peaks in the 10.6 GHz histogram. The generated 610 MHz polarization angle data do not show any peaks. The trend in the observed 610 MHz polarization angle histogram could come from internal Faraday rotation or from an unresolved Foreground screen. In fact, 3C 326 is the second farthest GRG in our sample. The resolved scale length at 10.6 GHz is 256 kpc (69″), similar to 3C 236, the beam used here is $69'' \times 82''$, rather than $69'' \times 69''$.

3.2.5 NGC 6251

In Fig. 3.5, we show our results in histogram form. At 10.6 GHz, the polarization angle histogram shows a peak at 11°. In contrast to the other sources in our sample, NGC 6251 has very strongly depolarized lobes and a steep spectrum. Therefore, the polarization angle histogram shows only the jets, the hotspots and the central core. The first peak is seen at $-30°$ in the 4.8 GHz histogram. Two secondaries are at $+52°$ and $-56°$. The RM histogram has two peaks at -170 rad m^{-2} and at -260 rad m^{-2}. Their shoulders are about $20 \cdots 40$ rad m^{-2} broad. No RM information of the lobes is available, due to the above mentioned reasons.

The zero-wavelength distribution of the polarization angles calculated from the RM and 10.6 GHz data exhibits a main peak at 24°, and secondary peaks at 2° and at $+86°$. These are more pronounced than the peaks in the 10.6 GHz histogram. The generated 610 MHz polarization angle data do not show any peaks. The trend in the observed 610 MHz polarization angle histogram could come from internal Faraday rotation or from an unresolved Foreground screen.

3.3 The properties of Faraday medium - first step

Although the histograms do not provide any positional information, there are some general trends we can catch from the figures. The first thing is that the 4.8 GHz histogram of each source is more or less similar to that at 10.6 GHz, but with a significant phase difference. At high frequencies, the Faraday medium is well resolved. The second thing we found is that the 610 MHz distribution of polarization angles is not really flat. Considering the possible variation of parameters of the Faraday rotating medium (scale length, field strength of cells), it is hard to believe that the 610 MHz polarization angles were ordered in the presence of a high RM measured at high frequencies. For example, a Faraday cell of 100 rad m^{-2} with a moderate dispersion of 10 rad m^{-2} provides 7.6 π turns of the angle and a dispersion of 140° at 610 MHz. In order to explain the somehow ordered polarization angles at 610 MHz, we need an internal Faraday medium

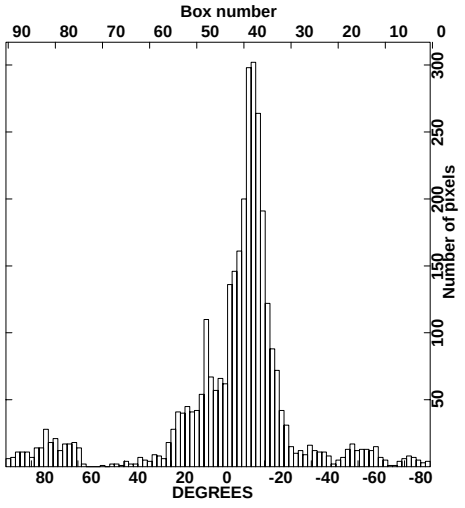

(a) 10.6 GHz

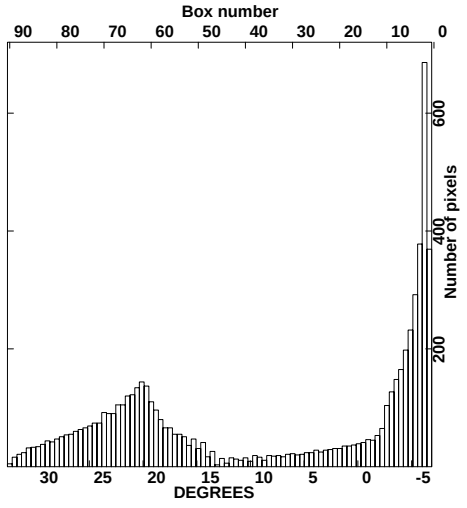

(b) 4.8 GHz

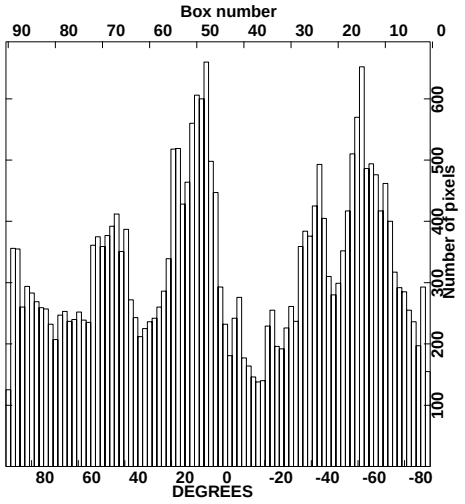

(c) 610 MHz

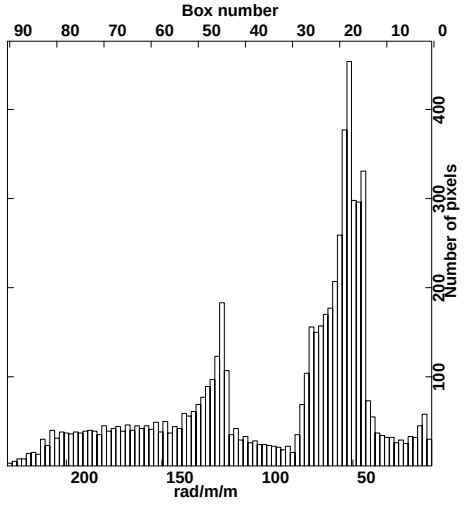

(d) RM

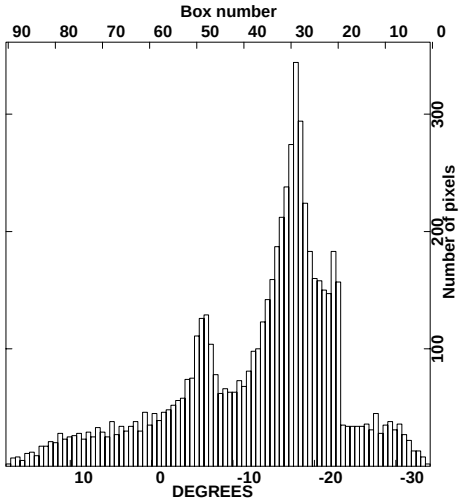

(e) λ_0

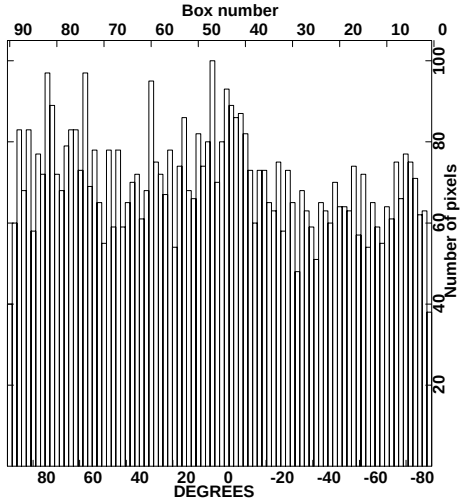

(f) 610 MHz from λ_0

Figure 3.4: Distribution of polarization angles in 3C 326 (see Fig. 3.1).

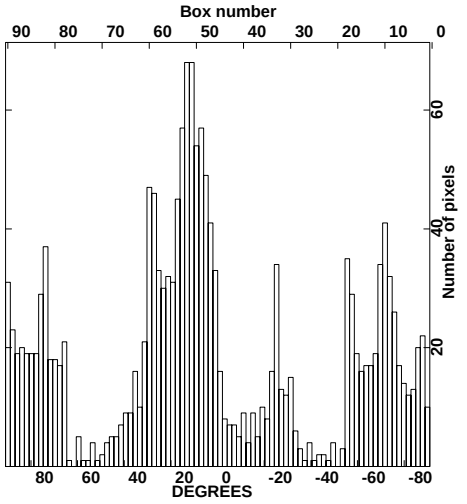

(a) 10.6 GHz

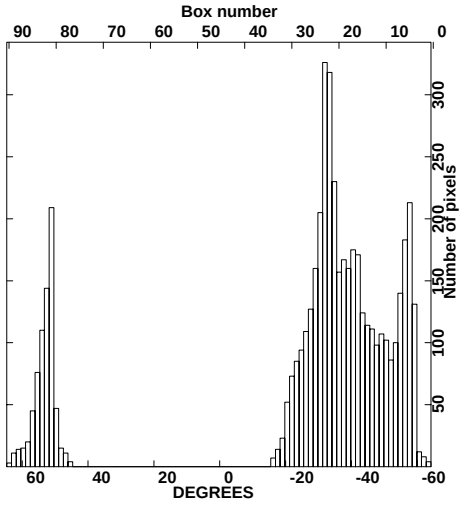

(b) 4.8 GHz

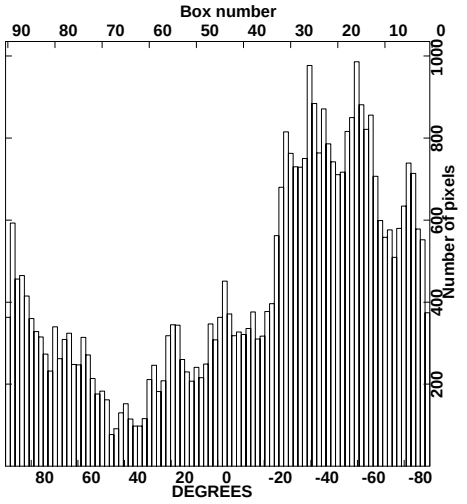

(c) 610 MHz

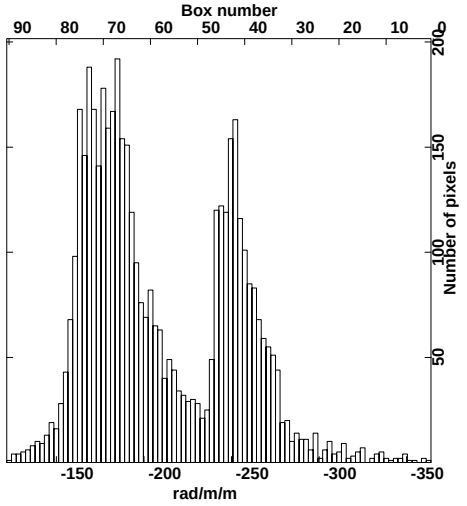

(d) RM

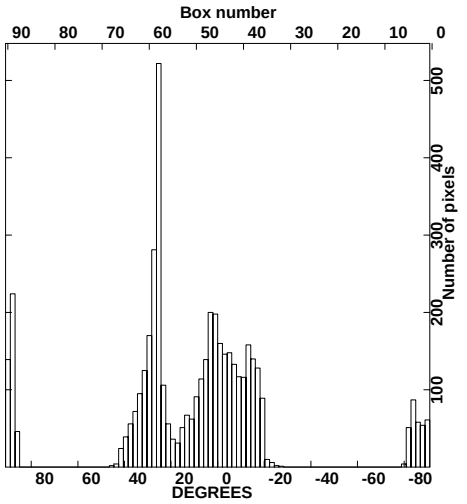

(e) λ_0

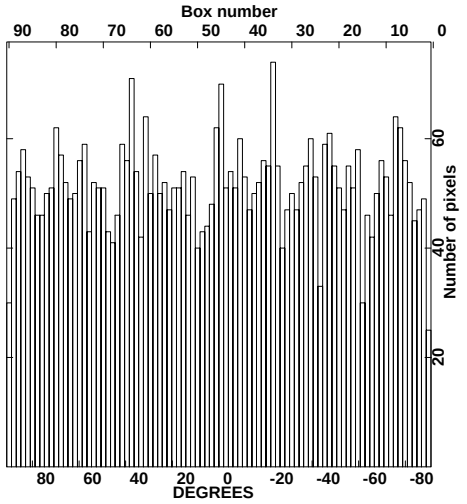

(f) 610 MHz from λ_0

Figure 3.5: Distribution of polarization angles in NGC 6251 (see Fig. 3.1).

or a multi-cell foreground.

Internal Faraday rotation can be discarded with the argument of low depolarization at 610 MHz. If the high estimated RM were internal, the fractional polarization at 610 MHz should show significant depolarization. This is not the case for our sample. The other possibility is a two- or more-phase foreground screen. If we introduce a weak, small-scale multi-cell Faraday screen besides the strong, large-scale Faraday screen which is seen at the high frequencies, it can be explained. In the next section we check this possibility.

3.3.1 λ_0 map

Our RM estimate is based on two frequencies. In the previous section we have shown that the polarization angle at 610 MHz cannot be used as a third frequency. We have an ambiguity $-490 \cdots +490$ rad m^{-2}, which is acceptable if the sources do not reside in a dense environment (Clarke et al., 2001; Eilek & Owen, 2002). In this subsection we perform a further test. From the estimated RM we can get the intrinsic polarization angle at λ_0. We have created maps at $\lambda = 0$ by extrapolating the polarization angles to zero wavelength using the derived two frequency RMs. We will henceforth call them λ_0 maps for brevity. If the ambiguity in our RM data is sufficiently small, then the λ_0 polarization angle maps will show a good correlation with the total intensity structure, e.g. tangential, perpendicular or circumferential.

Figs. 3.6 to 3.10 show the results. The lines represent the E-field direction, their length being proportional to their depolarization measure between 10.6 and 610 MHz, $DP_{0.6}^{10.6} = m_{0.6}/m_{10.6}$. A length of $5'$ of the line corresponds to $DP = 1$, i.e. no depolarization. Every sixth to eighth pixel has been plotted. Except for 3C 326 whose Faraday medium is probably not well-resolved, the other four have their RM peaks at $> |100|$ rad m^{-2}, or $\Delta RM > |100|$ rad m^{-2}. This implies that the polarization angles at 10.6 GHz will be $> 5^\circ$ different from the intrinsic polarization angle. In all five sources including 3C 326, the λ_0 angle is well correlated with the sources' total intensity structure.

NGC 315

The E-field is parallel to the major axis along the jets, and circumferential at both extremities (hotspots). The interesting point is that the polarization angle in the northern relic lobe is not parallel to the major axis but to the direction of the relic extension. This implies a secondary shock perpendicular to the extension direction, which revives the old electrons and the field (see Fig. 3.6).

DA 240

The field configurations in the two lobes of DA 240 are completely different from each other. The polarization angles in the NE lobe are parallel to the major axis in the hotspot and become slightly circumferential in the outer envelope. The SW lobe is significantly depolarized except for its extremity where the E field is perpendicular to the major axis (see Fig. 3.7).

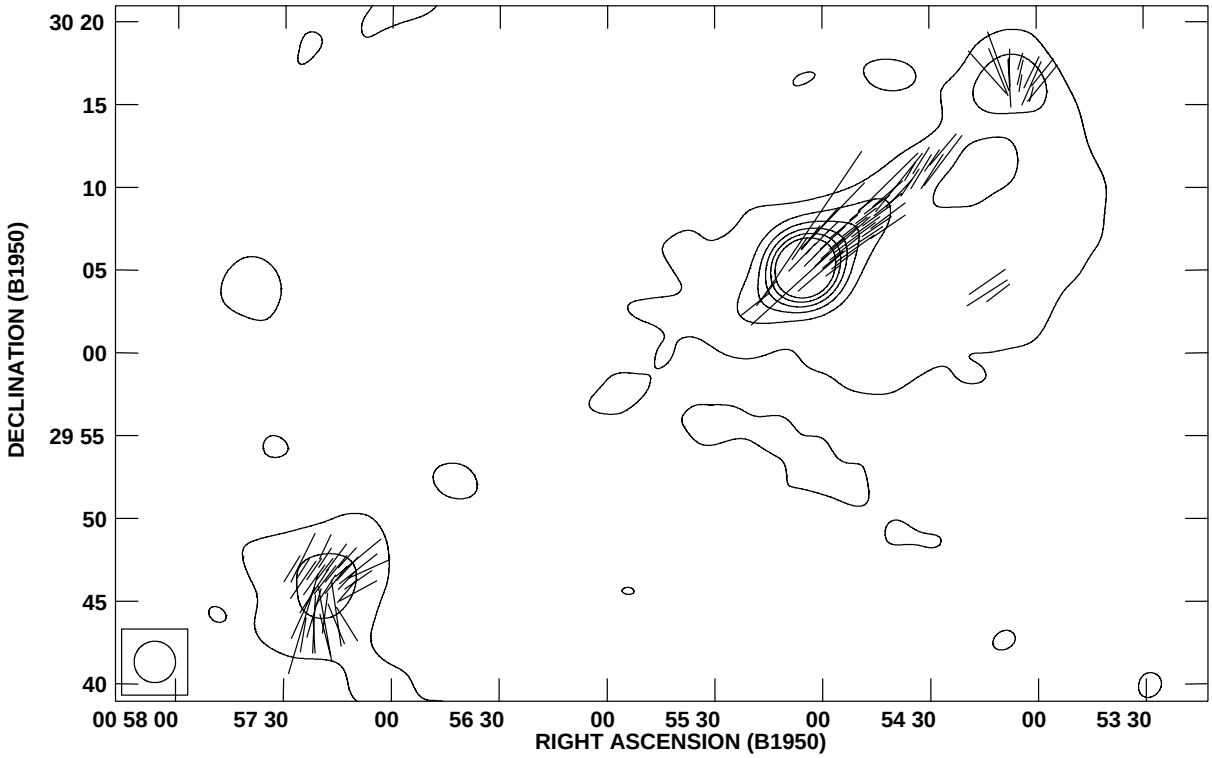

Figure 3.6: λ_0 polarization angle map of NGC 315. The vectors represent the linear polarization direction of the E-vector. The length of the vectors is proportional to $DP_{0.6}^{10.6}$. $DP = 1$ corresponds to a length of $5'$. The contour map is the convolved total intensity map, with a beam of $150'' \times 150''$, at 10.6 GHz. The contour levels are 3, 12, 27, 48 and $75\sigma_I$.

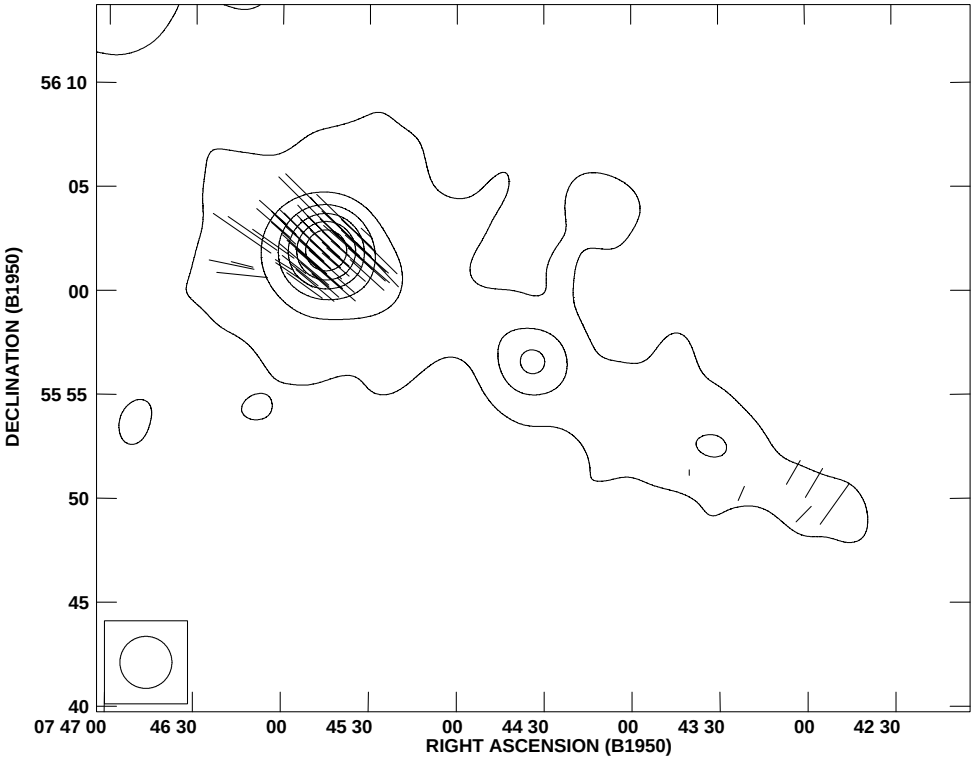

Figure 3.7: λ_0 polarization angle map of DA 240. Vectors and contours are the same as in Fig. 3.6.

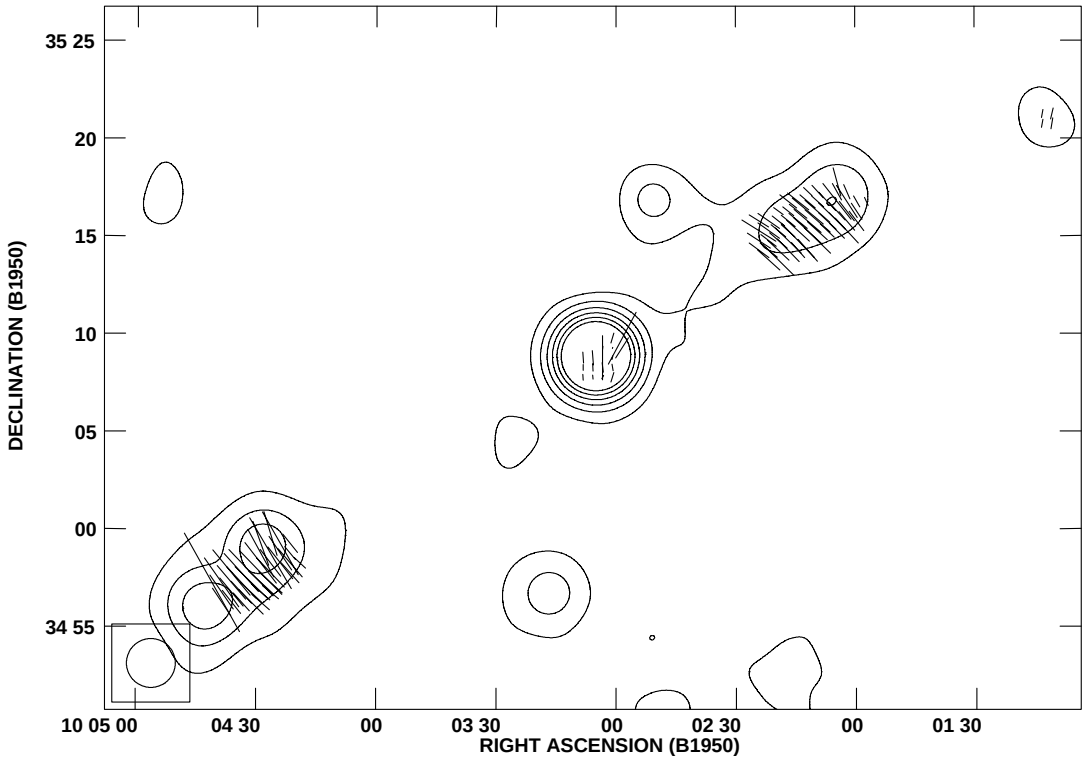

Figure 3.8: λ_0 polarization angle map of 3C 236. Vectors and contours are the same as in Fig. 3.6.

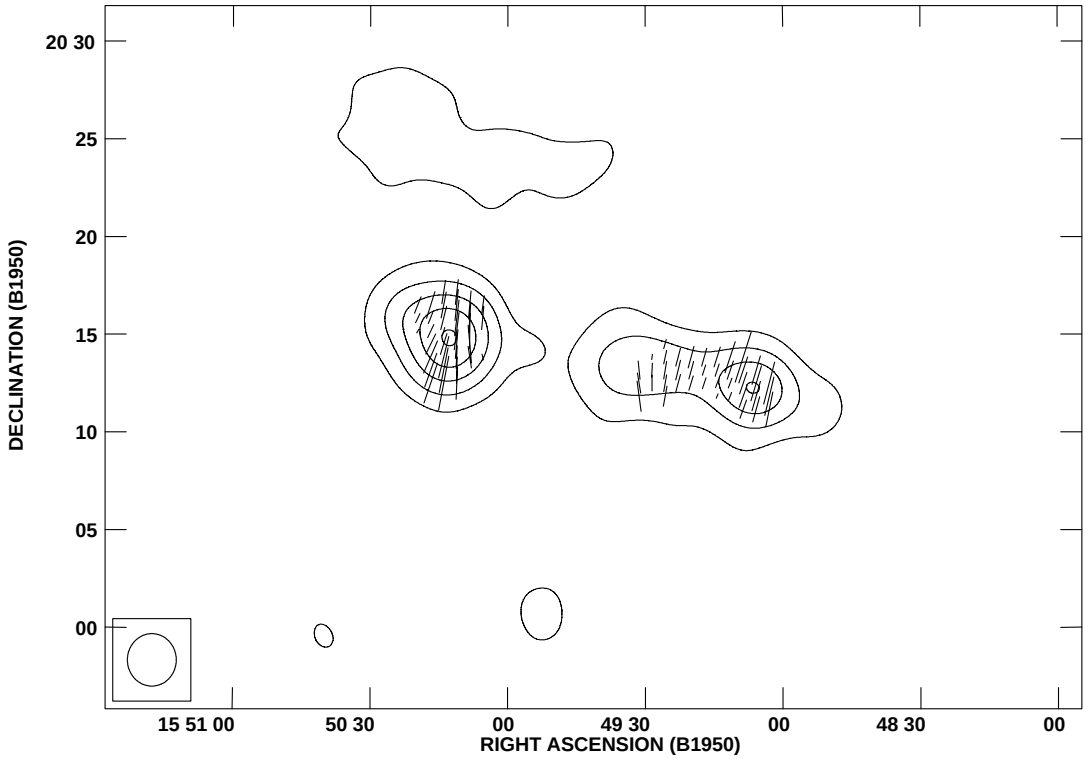

Figure 3.9: λ_0 polarization angle map of 3C 326. Vectors and contours are the same as in Fig. 3.6.

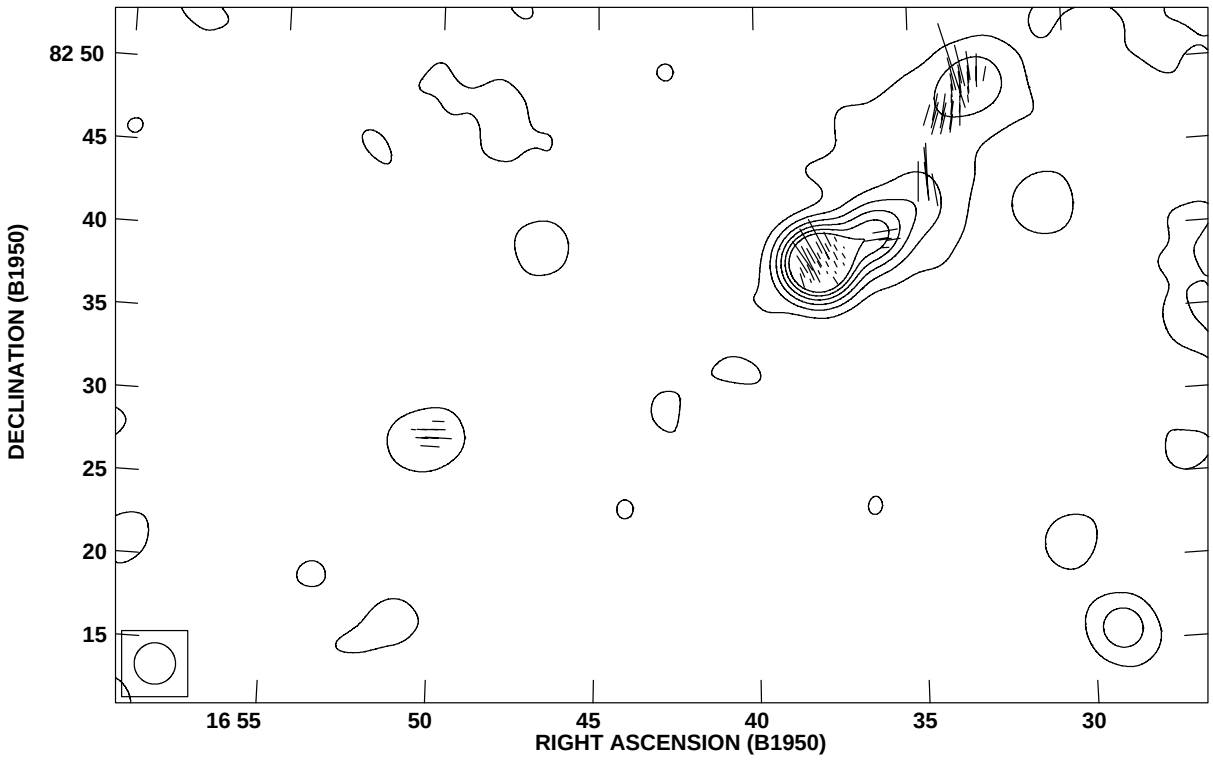

Figure 3.10: λ_0 polarization angle map of NGC 6251. Vectors and contours are the same as in Fig. 3.6.

3C 236

The E-fields in the two lobes are perpendicular to the major axis. At their extremities, there are signs of field direction changes. Unfortunately, the resolution at 4.8 GHz is not sufficient. At the extremities, linear polarization vanishes completely due to beam depolarization at 4.8 GHz (see Fig. 3.8).

3C 326

On the whole, depolarization is significant and the λ_0 angle does not represent the source structure well (in general perpendicular to the major axis). The RM values are quite low and ΔRM is low, too. 3C 326 is suspected to be an 'X-shaped' radio galaxy (Rottmann 2000). If this is true, its field structure is accordingly complicated. Furthermore, 3C 326 is the second farthest source, $d \sim 328\,Mpc$, while 3C 236 is slightly more distant, at $d \sim 359$ Mpc (see Fig. 3.9).

NGC 6251

The field direction in the jet of this famous GRG follows the ridge of the total intensity like a well-defined flow. This is quite different from the low-frequency estimate made by Perley et al. (1984) (see Fig. 3.10).

General remarks

Our maps of polarization angles at λ_0 of the five GRGs show a good correlation with the source structure. A high RM value (e.g. > 100 rad m^{-2}) is usual in GRGs as in cluster radio galaxies. As a result, the Faraday rotation around about 5 GHz - a standard radio frequency for radio galaxies - is $> 20°$. We emphasize that the polarization angle at 5 GHz is NOT representing the intrinsic polarization angle, even in GRGs.

3.3.2 3 frequency fitting

We performed RM fitting test using 3 wavelengths data. In addition to the 2.8 cm and 6.3 cm polarization angle data of the previous sections, 11 cm polarization angle data of the five GRGs are engaged. The results are shown from Fig. 3.11 to Fig. 3.15.

The fitting is processed as below. For 2.8 cm and 6.3 cm, $150''$ angular resolution data are used. We used the available $260''$ angular resolution data at 11 cm. Pixels are interpolated with $5''$ grid. After that we looked for the high polarization region of each lobes in all five sources. In the case of NGC 315, we performed the fitting to the jet additionally. The pixels are chosen in order that the polarization intensity at all three frequencies are much stronger than 3σ noise level. In the figures, we present three different 3 frequency fit results and the two frequency extrapolation results together. The three different fits are done in order to test '$n\pi$' ambiguity at 11 cm and in some case at 6.3 cm too. In all five GRGs, the two frequency extrapolation is in good agreement with the best 3 frequency fit result.

GRGs with rather complex polarization structure such as NGC 315 and NGC 6251 show larger discrepancy between the two frequency extrapolation and the best 3 frequency fit result, although the best 3 frequency fit result remains the nearest fit to the two frequency extrapolation. We reckon that this is because of the beam smearing effect inherent to the 11cm data. There is a measurable decrease of the fractional polarization at 11 cm in NGC 315 and NGC 6251.

The results of the 3-frequency fit indicate that the polarization angle at 11 cm rotated by $\pm(1 \cdots 2) \cdot \pi$ turned by the Faraday rotation. One exception is 3C 326 where the best 3-frequency fit indicates no extra (i.e. $n\pi$) rotation of polarization angle at 11 cm. The two-frequency extrapolation result is in good agreement with this fit. In all five GRGs, it is proved that the the RM computed using two frequencies is reliable. In order to present RM maps with higher angular resolution we will use this two-frequency RM in this work.

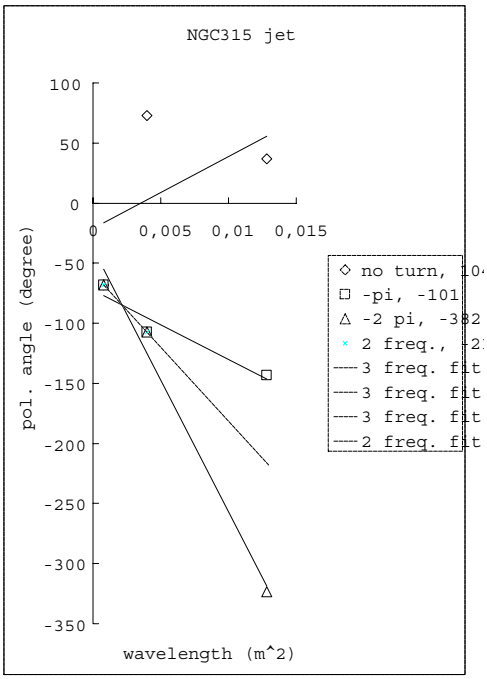

(a) NGC 315 jet

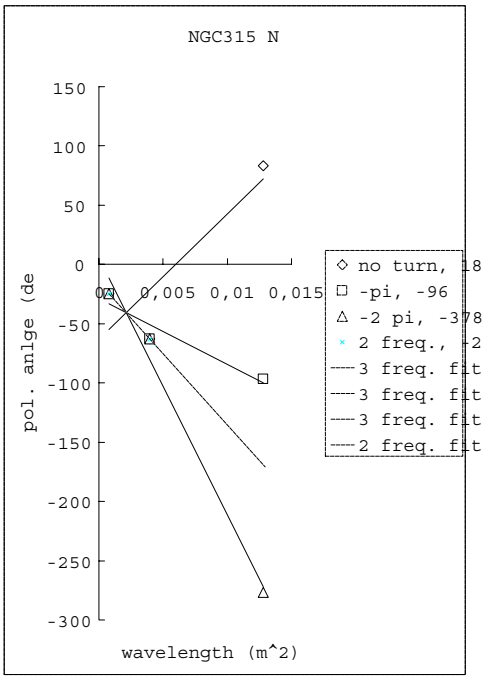

(b) NGC 315 N

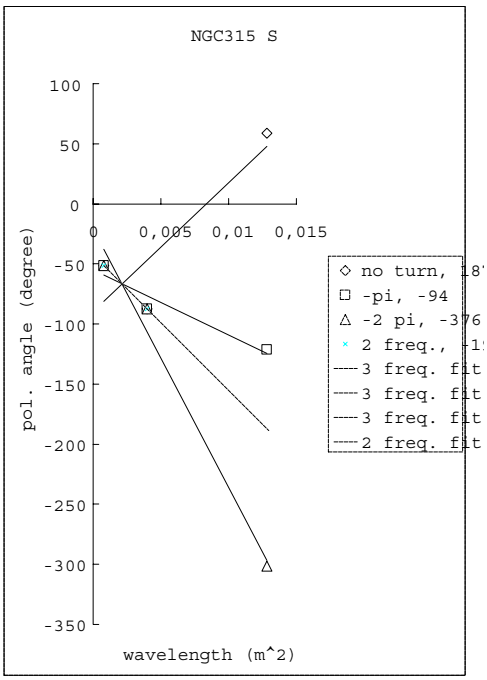

(c) NGC 315 S

Figure 3.11: 3 frequency RM fit of NGC 315

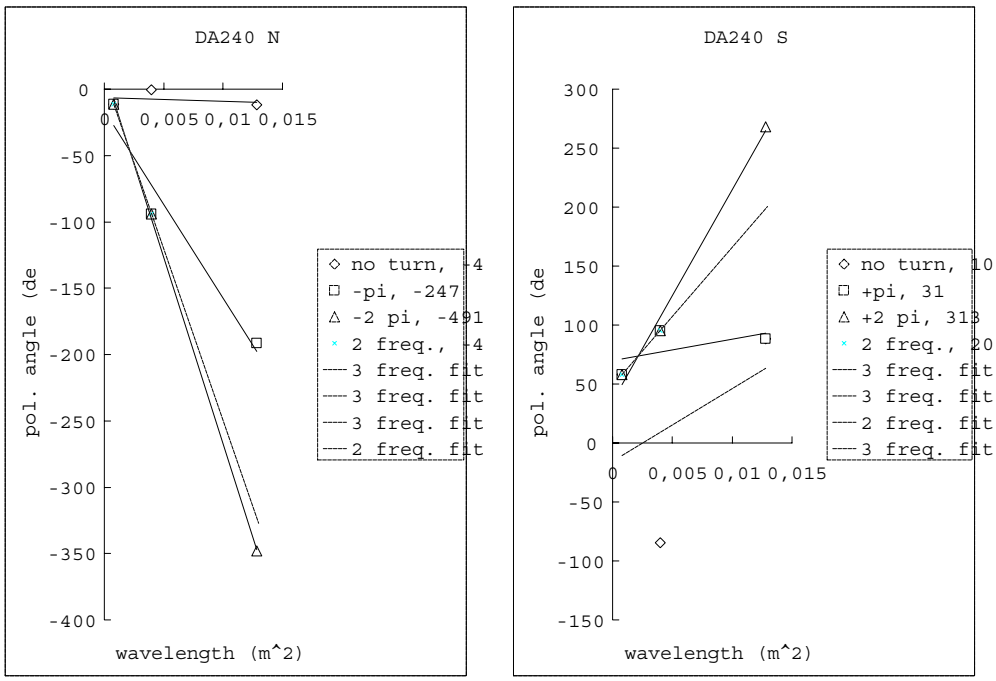

(a) DA 240 N (b) DA 240 S

Figure 3.12: 3 frequency RM fit of DA 240

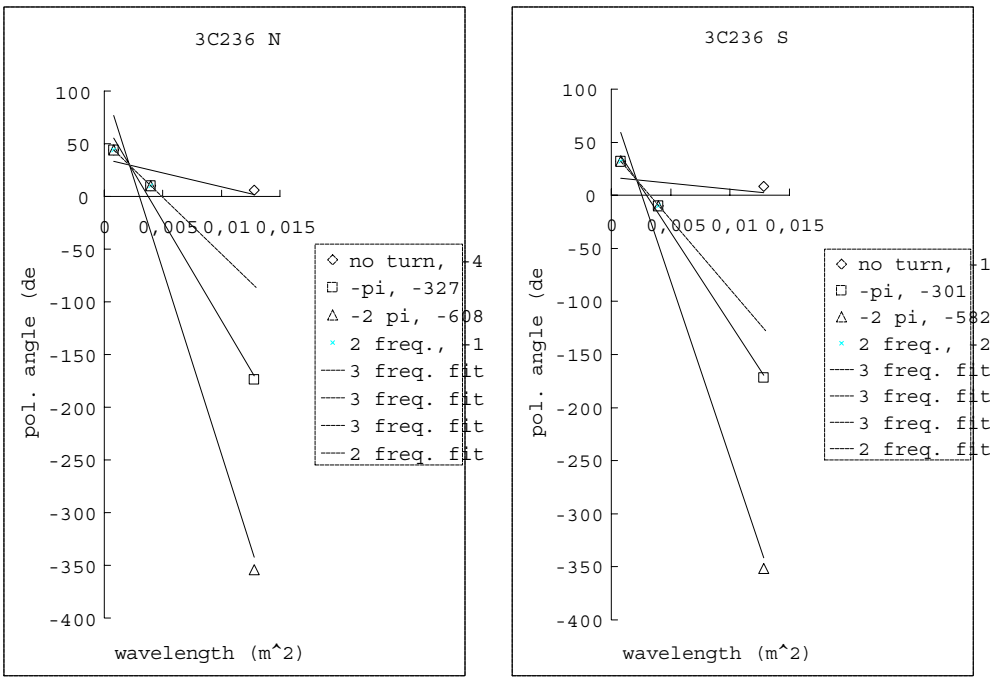

(a) 3C 236 N (b) 3C 236 S

Figure 3.13: 3 frequency RM fit of 3C 236

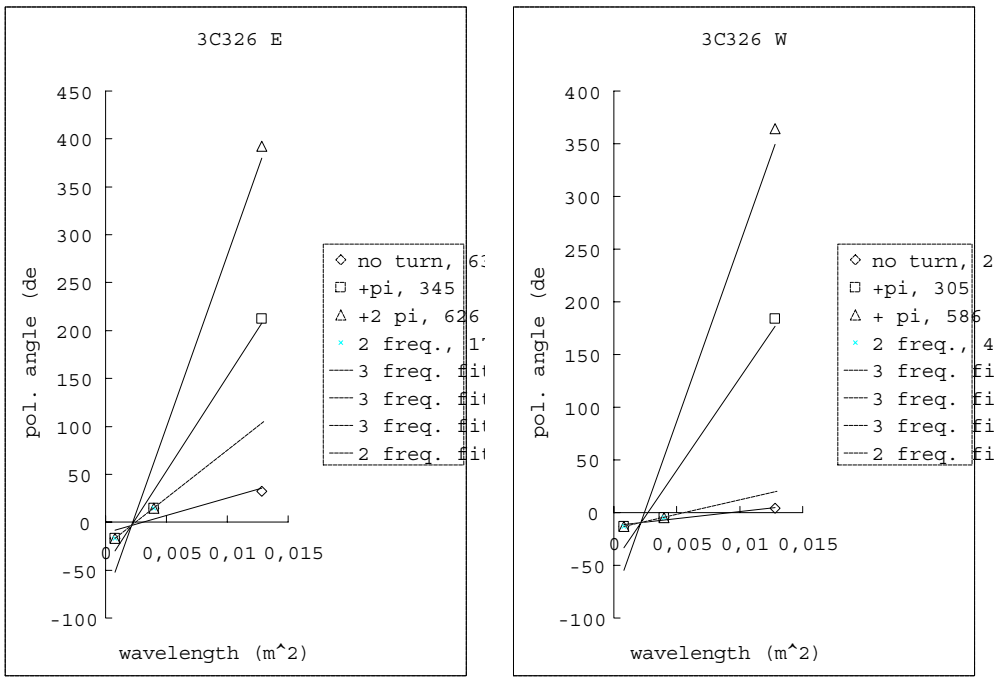

(a) 3C 326 E (b) 3C 326 W

Figure 3.14: 3 frequency RM fit of 3C 326

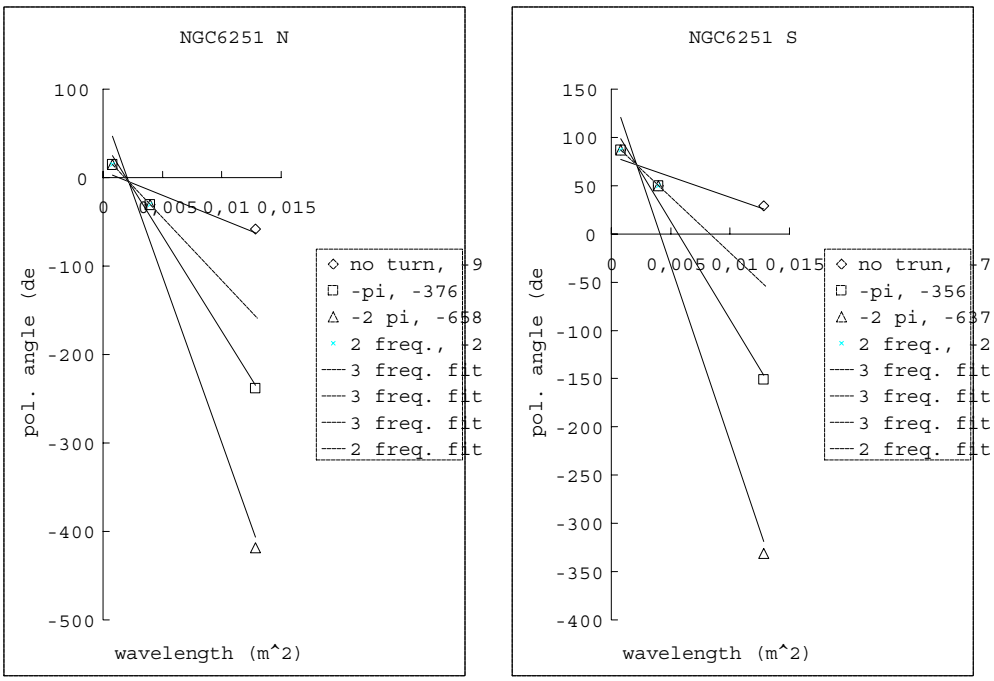

(a) NGC 6251 N (b) NGC 6251 S

Figure 3.15: 3 frequency RM fit of NGC 6251

3.4 Rotation Measure maps of the five GRGs

A difficult part of estimating RM and other physical parameters is the extraction of the Galactic RM. We consider two possibilities to extract the Galactic RM. The first one is the simple subtraction of the mean RM of a source from the RM in each pixel of the map, i.e.

$$RM_{c1} = RM - RM_{mean}.$$

RM_{mean} is obtained using the AIPS task TVSTAT. This correction assumes that the mean RM is the pure Galactic contribution. Since the distribution of RM in GRGs is non-Gaussian and bimodal, the simple mean RM obtained is between the two peaks. After the above correction, two peaks will represent opposite signs of the magnetic field (towards and away from us). As a consequence, the RM variation in a source is translated into field reversals, i.e. alternating field directions. If we take the absolute value of RM_{c1}, a large part of the RM substructures in the sources will disappear.

One cannot be sure whether RM_{mean} is genuinely the Galactic contribution. The second method has a correction term which includes the RM of neighbouring extragalactic sources. We use Simard-Normandin et al. (1981)'s catalogue in order to obtain the mean RM of the three nearest extragalactic sources', RM_3. We then estimate

$$RM_{c2} = RM - \frac{RM_{mean}+RM_3}{2}.$$

If the mean RM of source, RM_{mean}, is the pure Galactic contribution and fairly distributed, we will obtain roughly
$RM_{mean} \sim RM_3$ and $RM_{c2} \sim RM_{c1}$.

If the intrinsic contribution to RM_{mean} is large with respect to the Galactic one then, in a statistical sense, $\frac{RM_{mean}+RM_3}{2}$ will be the better choice than the RM_{mean} for the correction. Since RM_{mean} has 'on'-source information of the Galactic RM, we take the weighted mean, $\frac{RM_{mean}+RM_3}{2}$. In contrast to $|RM_{c1}|$, $|RM_{c2}|$ shows the substructures which are seen in RM_{c1}.

3.4.1 NGC 315

A big difference between the maps of RM_{c1} and $|RM_{c2}|$ of NGC 315 (Fig. 3.16) is the RM value near the core. The $|RM_{c2}|$ map exhibits a decrease, $|RM| \sim 50$ rad m^{-2} from its mean $\overline{RM_{c2}} \sim 90$ rad m^{-2}. On the contrary, the RM_{c1} map exhibits an increase, $|RM| \sim 55$ rad m^{-2} from the mean of $\overline{RM_{c1}} \sim 35$ rad m^{-2}. We should mention that the Galactic $RM_{gal} \sim -225$ rad m^{-2} which is assumed for RM_{c1} is exceptionally high in the region of sky compared to the mean RM of three nearest sources $RM_3 = -53$ rad m^{-2} (Simard-Normandin et al., 1981). Therefore, the question why the mean RM, Galactic or inter-galactic, is so high still remains to be answered.

3.4.2 DA 240

Around DA 240 (Fig. 3.17), the Galactic RM seems to be very low, < 10 rad m^{-2}. Tsien (1982) reported a low RM < 4 rad m^{-2}, based on a low-frequency observation, except for one source, 3C 196 ($l \sim 171.^\circ2, b \sim +33.^\circ2$) with -142 rad m^{-2}. Including 3C 196, our estimate of the foreground RM is $RM_3 = -54$ rad m^{-2} and the $\overline{RM}$ of DA 240 is

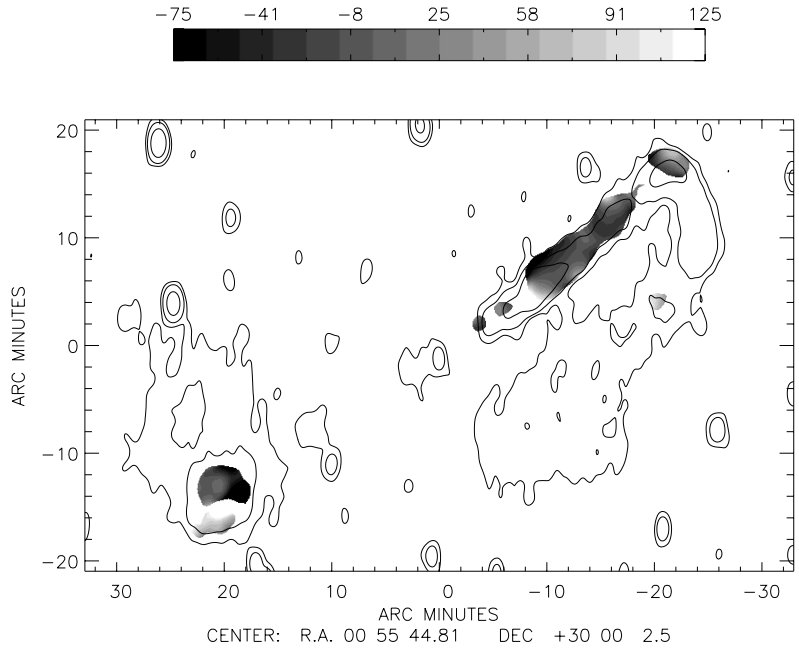

(a) RM_{c1}

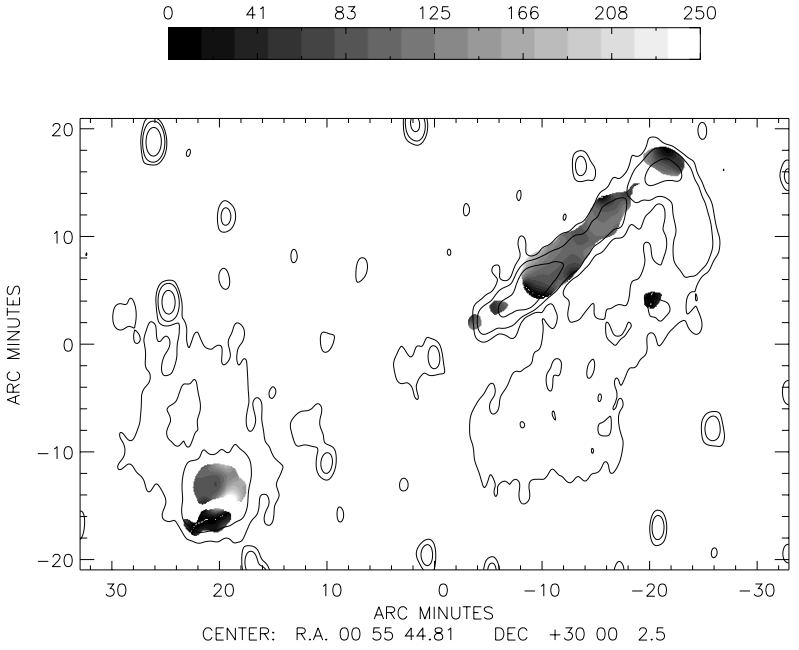

(b) $|RM_{c2}|$

Figure 3.16: RM maps of NGC 315, based on two frequencies (10.6 and 4.8 GHz), the maps corrected for the Galactic foreground, RM_{c1} and RM_{c2}, are shown. The contours represent the total intensity at 610 MHz. The contour lines are 3, 10 and 50 σ_I.

Table 3.1: RM of NGC 315

	RM	ΔRM	$\|RM_{c1}\|$	$\Delta\|RM_{c1}\|$	$\|RM_{c2}\|$	$\Delta\|RM_{c2}\|$
int. source	-225	50	35	35	90	45
core, jets	-235	40	25	25	95	35
inter jet	-235	25	20	15	95	25
NW hotspot	-215	35	30	20	75	35
N relic	-145	20	80	20	15	10
SE lobe	-220	75	55	45	95	60

Table 3.2: RM of DA 240

	RM	ΔRM	$\|RM_{c1}\|$	$\Delta\|RM_{c1}\|$	$\|RM_{c2}\|$	$\Delta\|RM_{c2}\|$
int. source	180	60	40	45	120	55
NE lobe	215	35	40	30	150	35
SW lobe	145	65	45	55	90	50

180 rad m^{-2}. The result of Chapt. 1 implies that there is a significant depolarization asymmetry in DA 240. The SE lobe is more depolarized. If a significant portion of the mean RM is near DA 240 and if this is responsible for the depolarization, then the mean RM should be smaller and ΔRM should be higher than that of the NW lobe. The $\Delta|RM|$ asymmetry is most prominent in RM_{c1}. In DA 240 there is still the question where and how the high mean RM arises.

3.4.3 3C 236

There is a clear polarization asymmetry in 3C 236 (Fig. 3.18), too (Chapt. 1). The NW lobe is more depolarized. All ΔRM values go the wrong direction. The SE lobe has larger ΔRM values. Since RM is not measured in the SE hotspot due to the beam depolarization at 4.8 GHz, the ΔRM values could be different if the SE hotspot were included. Since the central core has a polarization artefact at 10.6 GHz, we also show the integrated values without the core (Table 3.3). The mean RM is much higher than that of the three nearest extragalactic sources, $RM_3 = +27$ rad m^{-2}. We still need an explanation for the large discrepancy between the $\overline{RM}$ and RM_3 of 3C 236, too.

3.4.4 3C 326

On the whole, 3C 326 is the most depolarized GRG in the sample. However, the depolarization asymmetry is not significant. The RM values in the east and west lobe are

Table 3.3: RM of 3C 236

	RM	ΔRM	$\|RM_{c1}\|$	$\Delta\|RM_{c1}\|$	$\|RM_{c2}\|$	$\Delta\|RM_{c2}\|$
int. source	-135	155	80	150	135	115
without core	-145	35	30	20	90	35
core	-95	395	365	160	385	105
NE lobe	-150	30	30	20	95	30
SW lobe	-135	40	35	25	85	40

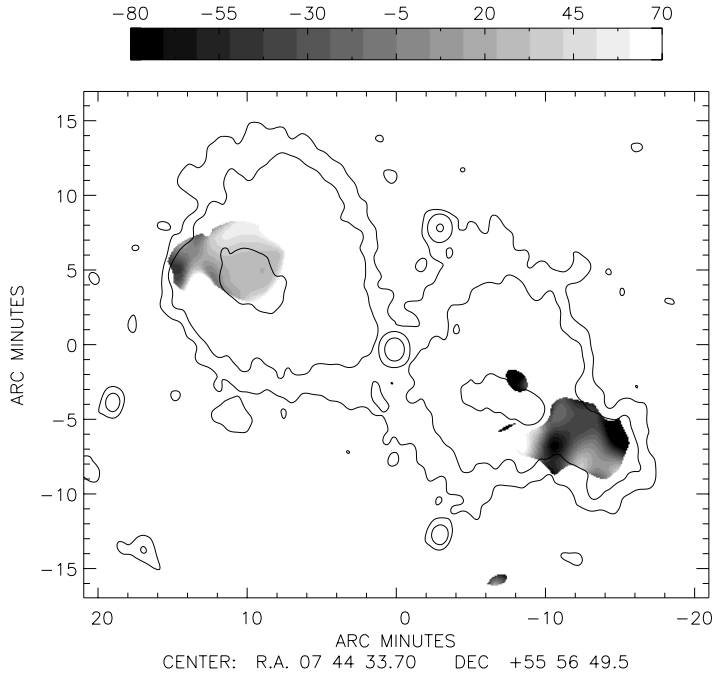

(a) RM_{c1}

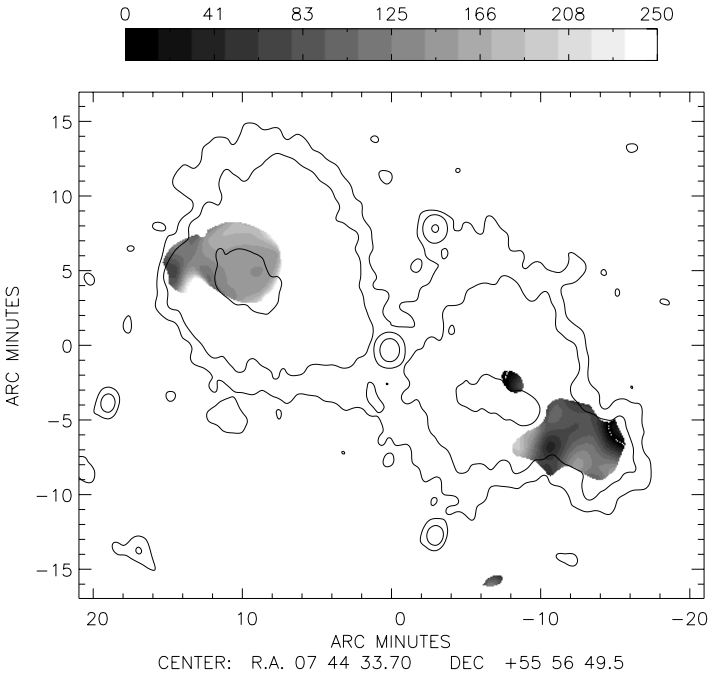

(b) $|RM_{c2}|$

Figure 3.17: RM maps of DA 240. The layout is the same as in Fig.3.16.

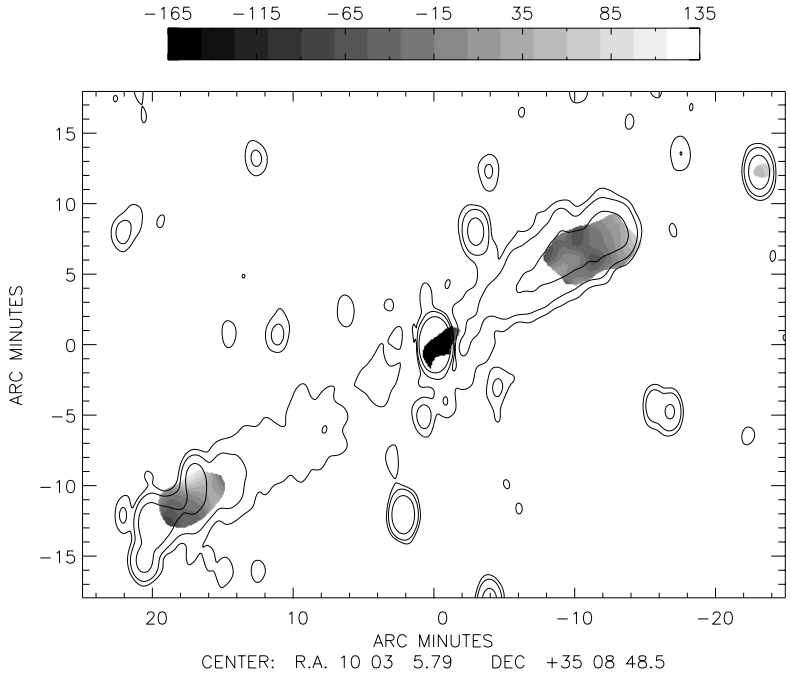

(a) RM_{c1}

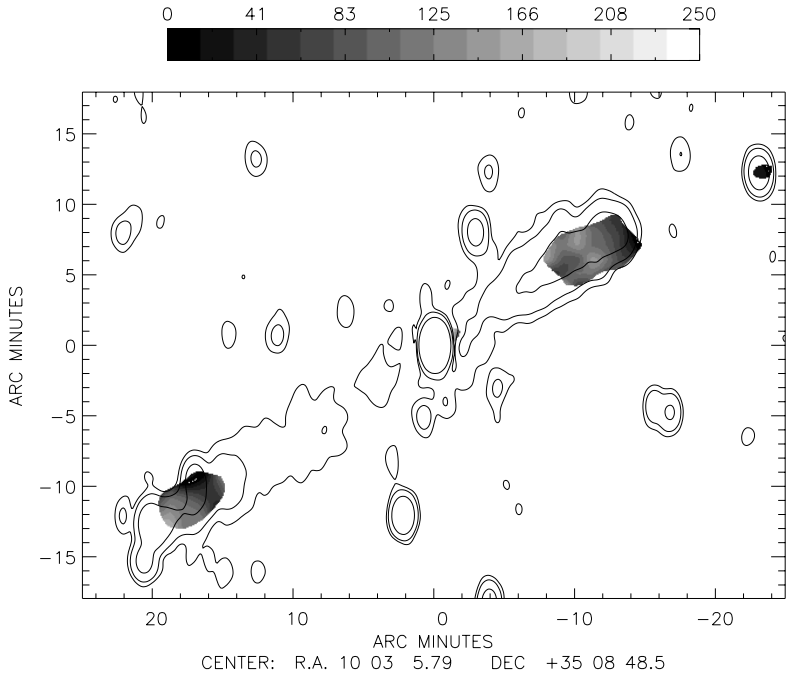

(b) $|RM_{c2}|$

Figure 3.18: RM maps of 3C 236. The layout is the same as in Fig.3.16.

Table 3.4: RM of 3C 326

	RM	ΔRM	$\lvert RM_{c1}\rvert$	$\Delta\lvert RM_{c1}\rvert$	$\lvert RM_{c2}\rvert$	$\Delta\lvert RM_{c2}\rvert$
total source	90	50	45	25	40	40
E lobe	145	40	80	55	35	40
W lobe	50	15	40	15	15	10

Table 3.5: RM of NGC 6251

	RM	ΔRM	$\lvert RM_{c1}\rvert$	$\Delta\lvert RM_{c1}\rvert$	$\lvert RM_{c2}\rvert$	$\Delta\lvert RM_{c2}\rvert$
int. source	-210	40	35	20	90	40
Core, jets	-220	40	40	20	100	40
NW hot spot	-190	20	25	15	70	20
SE hot spot	-160	10	50	10	40	10

completely different (Tab. 3.4). In the east lobe, we can see two completely different RM values resulting from the different methods (Fig. 3.19).

3.4.5 NGC 6251

The source is undergoing strong ageing in its lobe. Hence, an estimate of the polarization is only possible along the ridge of total intensity i.e. at the core, within the jets and the hotspots, which show depolarization. NGC 6251 is different in this respect from the other GRGs in the sample. The contrast between the RM_{c1} and the $|RM_{c2}|$ map is interesting (Fig. 3.20). In the RM_{c1} map, the RM values roughly follow an inverse r relation. In the $|RM_{c2}|$ map, the core has the highest RM value. The discrepancy between $\overline{RM}$ (Table 3.5) and $RM_3 = -26$ rad m^{-2} is huge, which is common to all of the five GRGs.

3.4.6 Remarks

The choice of the extraction is somewhat arbitrary and no 'golden rule' is at hand. The RM_3 and $\overline{RM}$ of all GRGs in the sample have large discrepancies. We cannot conclude yet whether this difference is due to the Galactic contribution or whether it is intrinsic to the GRGs or in between. Maybe the difference is mainly due to the intrinsic field. A connection between the DP asymmetry and ΔRM is not as convincing as expected.

3.5 The RM - DP diagram

How are RM and DP correlated? Burn's law tells us that there should be a λ^4 relation between the fractional polarization and wavelength (λ) such that

$$m_\lambda = m_0 \exp[-2\Delta^2\lambda^4],$$

where m_λ is fractional polarization, and Δ is the standard deviation of the rotation measure, such that

$$\Delta = < n^2B^2 >^{1/2} < Ld >^{1/2} \text{ (Garrington \& Conway, 1991).}$$

Then, the relation between DP and ΔRM is

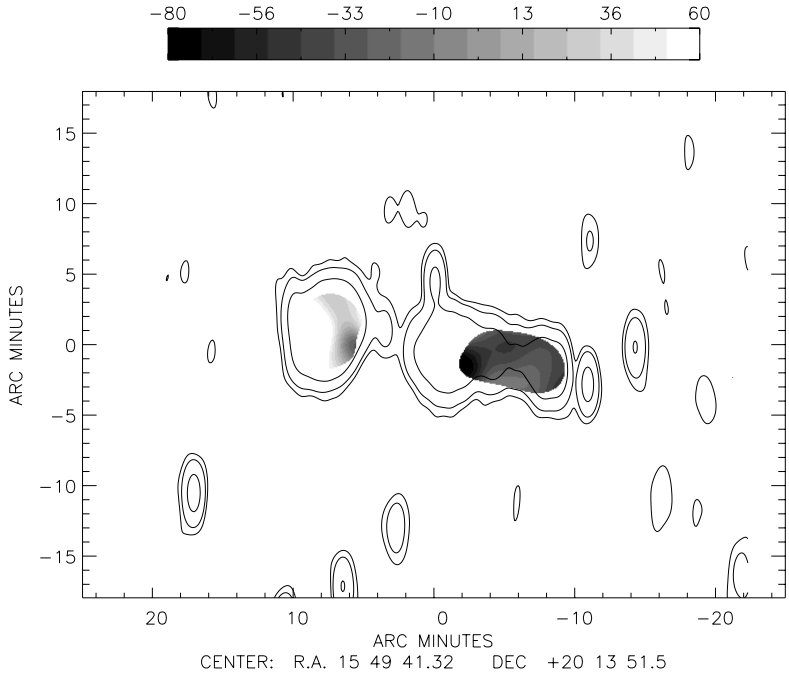

(a) RM_{c1}

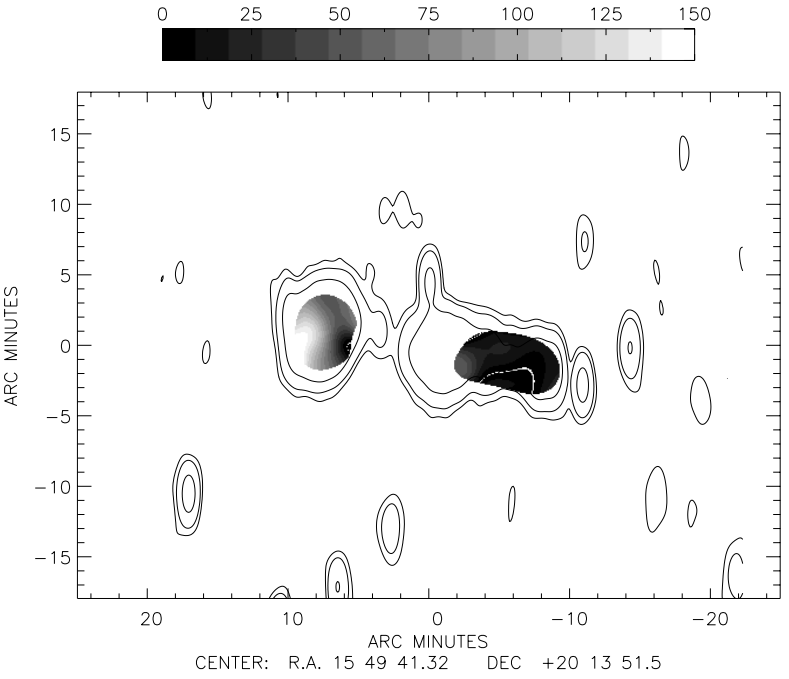

(b) $|RM_{c2}|$

Figure 3.19: RM maps of 3C 326. The layout is the same as in Fig.3.16.

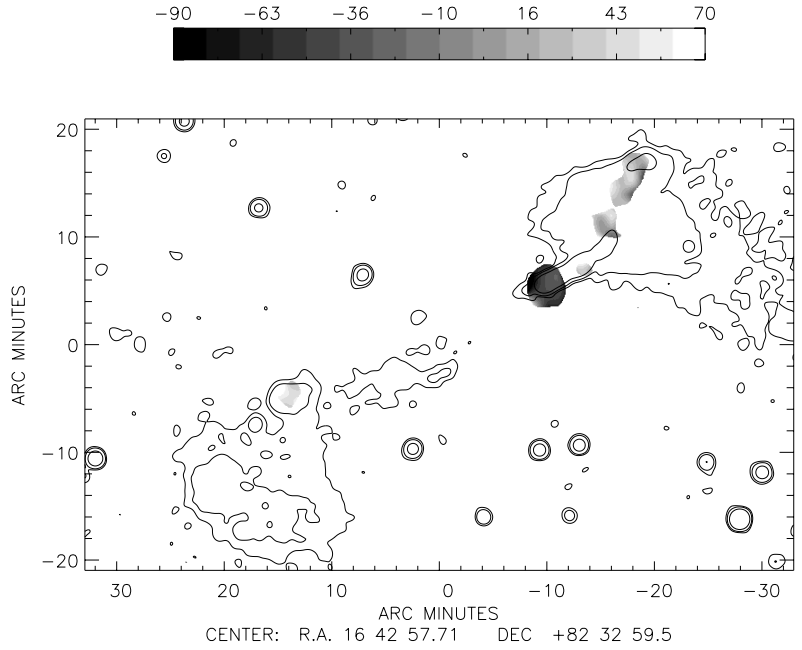

(a) RM_{c1}

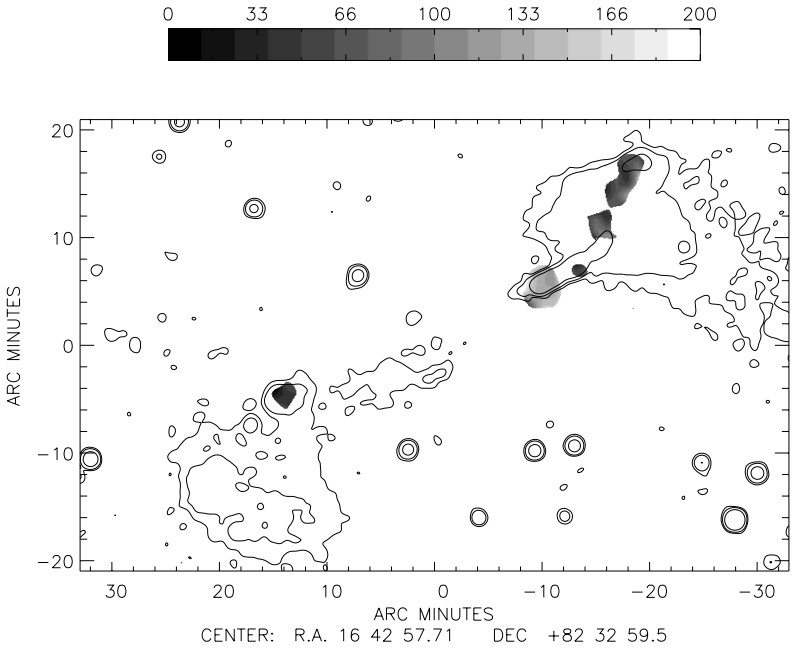

(b) $|RM_{c2}|$

Figure 3.20: RM maps of NGC 6251. The layout is the same as in Fig.3.16.

$$lnDP = c\,\Delta^2.$$

This is only true in the case of a fully unresolved Faraday medium. The more general form of the fractional polarization was given by Tribble (1991). The quadratic approximation of the solution is,

$$m_\lambda^2 = \frac{1-\exp[-S-4\sigma^2\lambda^4]}{1+4\sigma^2\lambda^4/S} + \exp[-S-4\sigma^2\lambda^4],$$

where S is a resolution parameter ($S \equiv s_0^2/2t^2$), s_0 is the scale length of a cell and t is the beam width (HPBW). When $S = \infty$, the RM structure is fully resolved and there is no depolarization. When $S = 0$, the RM structure is fully unresolved and Tribble's solution is approximated exactly by Burn's law. Besides these two extreme cases, there are the partially resolved cases.

We take an example and compare the result with the fully unresolved case. We use $\kappa\Delta = \sigma_{RM} = 50$ rad m^{-2} from the observations. Our estimate in the former section shows that this is common in GRGs. Then from the equations given above, we calculate DP between 10.6 and 610 MHz. From Burn's law, we obtain $DP_{S=0} = 0.0033$. This means that the source must be fully depolarized at 610 MHz, if its Faraday screen is fully unresolved. This is clearly not the case (see Chapt. 1.), the depolarization does not increase as fast as a function of λ as described by Burn's law. In Burn's law, the mean RM is close to 0. Then, not all of the high RMs we measure can be external.

Let us make a calculation for the case $DP_{S=1}$. $S = 1$ means that the source is partially resolved, which is expected both, in terms of the mean field and the depolarization. There can be, especially at high frequencies, an intrinsic mean RM which has a non-zero value. We obtain $DP_{S=1} = 0.28$. The depolarization is also significant, but it is in the range of the observational results. In any case, except for a large S, DP and ΔRM are correlated. More depolarization means a large ΔRM, if they are correlated. If the strength of the correlation depends on S, then with increasing S the RM structure becomes more and more resolved and the DP - ΔRM correlation will become less pronounced. The mean RM signature will reflect the real RM value of the foreground medium. We shall test this idea using the RM_{c1} - DP and RM_{c2} - DP diagrams.

3.5.1 RM_{c1}-DP and RM_{c2}-DP

We have made RM_{c1} - DP and RM_{c2} - DP diagrams in order to search for any DP - ΔRM correlation (Fig. 3.21 and (Fig. 3.22). ΔRM will be preserved in both RM_{c1} - DP and RM_{c2} - DP, but the mean RMs are different, so that a real DP - ΔRM correlation will appear in both planes. In three GRGs, NGC 315, DA 240 and 3C 236 we cannot find any clear trend. If we exclude the core from the diagrams, NGC 6251 shows a clear DP - ΔRM correlation in both the RM_{c1} - DP and the RM_{c2} - DP plane. 3C 326 shows a weak correlation of RM_{c1} - DP. This is not seen in the RM_{c2} - DP plane. The trend in RM_{c1} - DP of 3C 326 can just be an effect of the RM_{c1} correction. Otherwise, ΔRM should be preserved in RM_{c2} - DP plane, too.

3.5.2 Remarks

The underlying idea of RM_{c1} is that the mean RM is not related to GRGs. This implies an intrinsic rotation measure $\overline{RM} \sim 0$. Since a coherent Mpc-scale mean field is difficult to imagine, this idea is quite reasonable. The idea of RM_{c2} is that the mean RM, or at

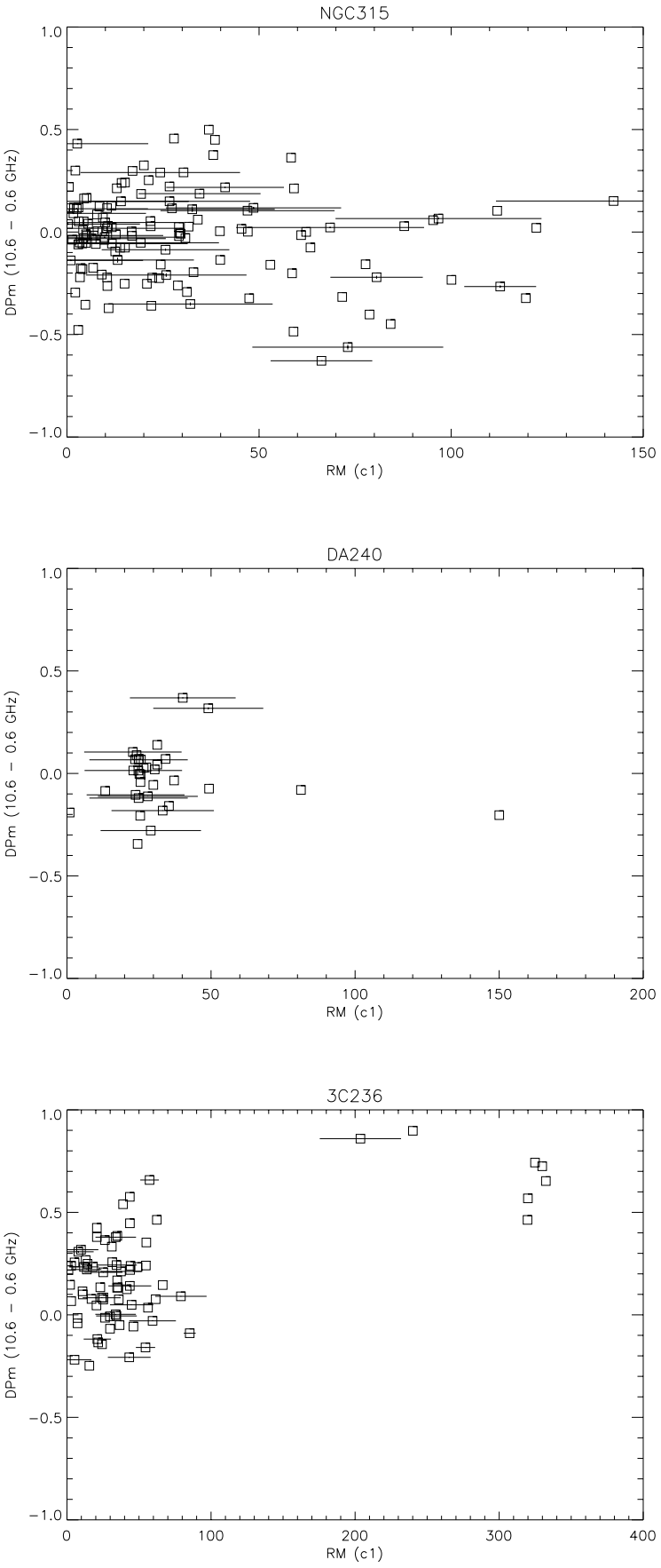

Figure 3.21: RM_{c1}-DPm diagram. The points are plotted on the RM_{c1}- $DPm_{0.6}^{10.6}$ plane.

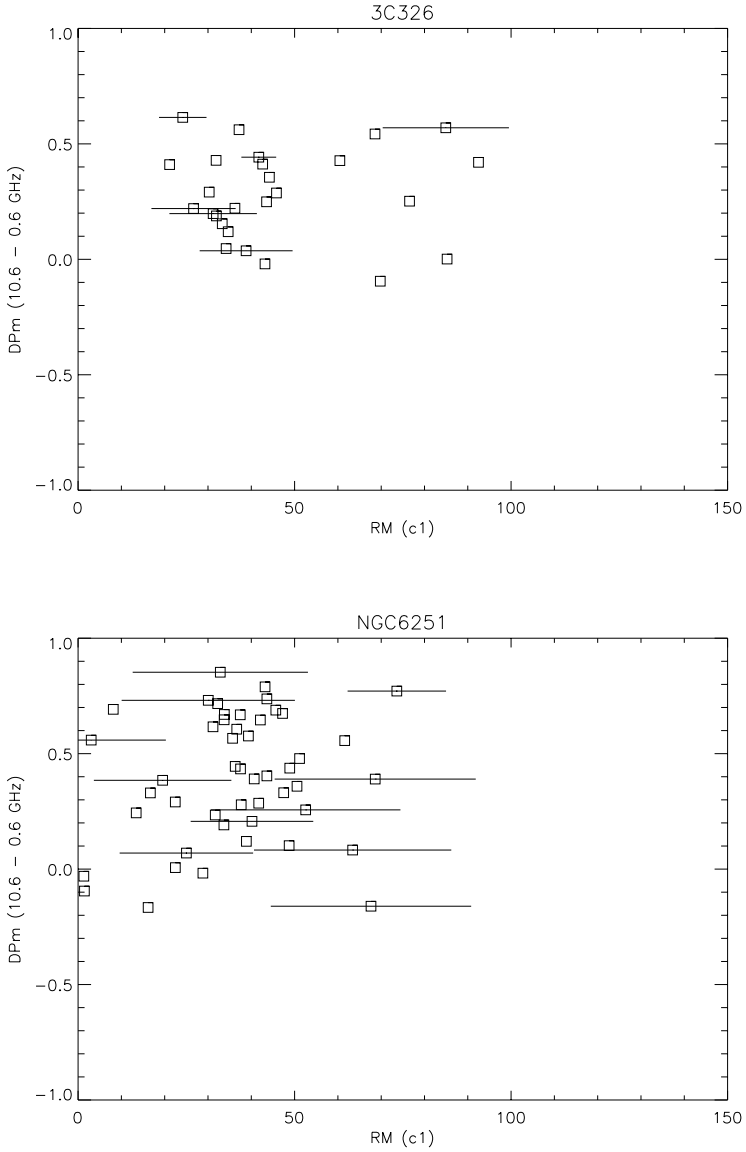

Figure 3.21: continued.

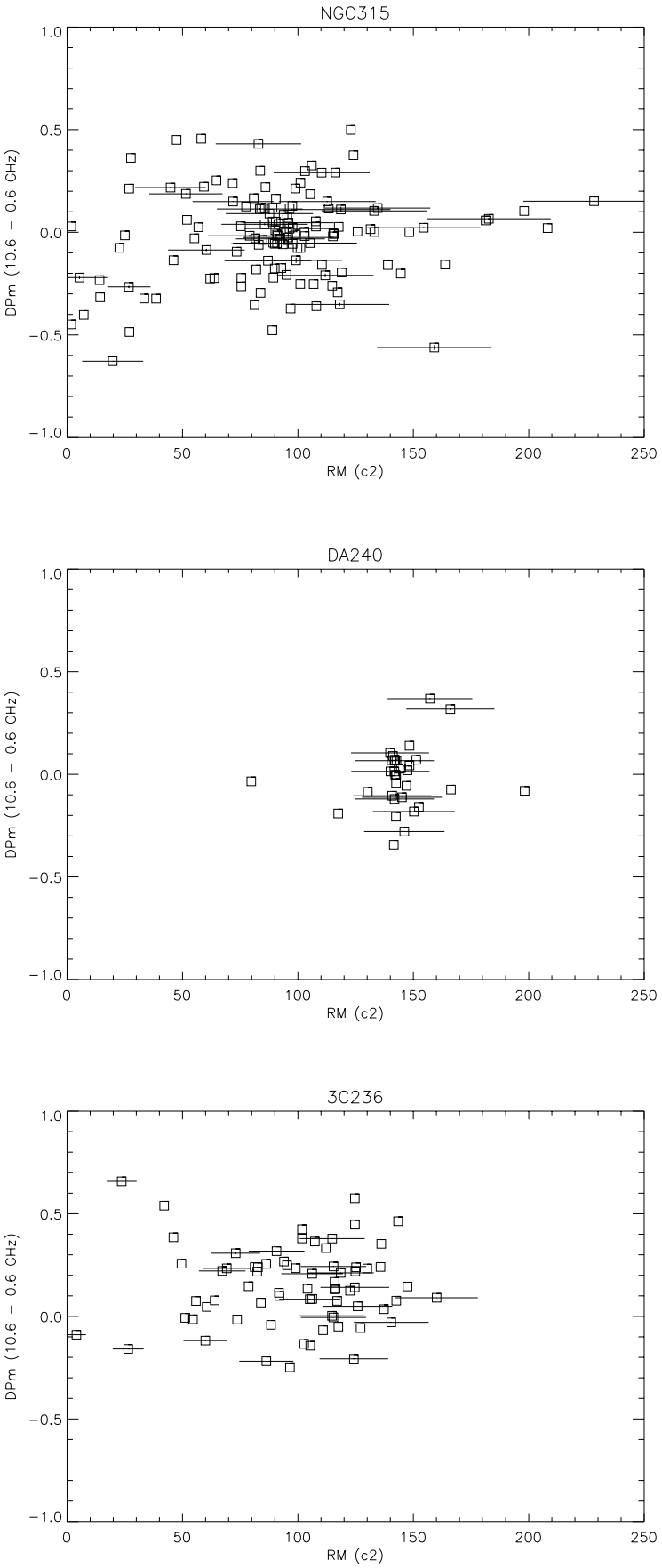

Figure 3.22: RM_{c2}-DPm diagram. The points are plotted on the RM_{c2}- $DPm_{0.6}^{10.6}$ plane.

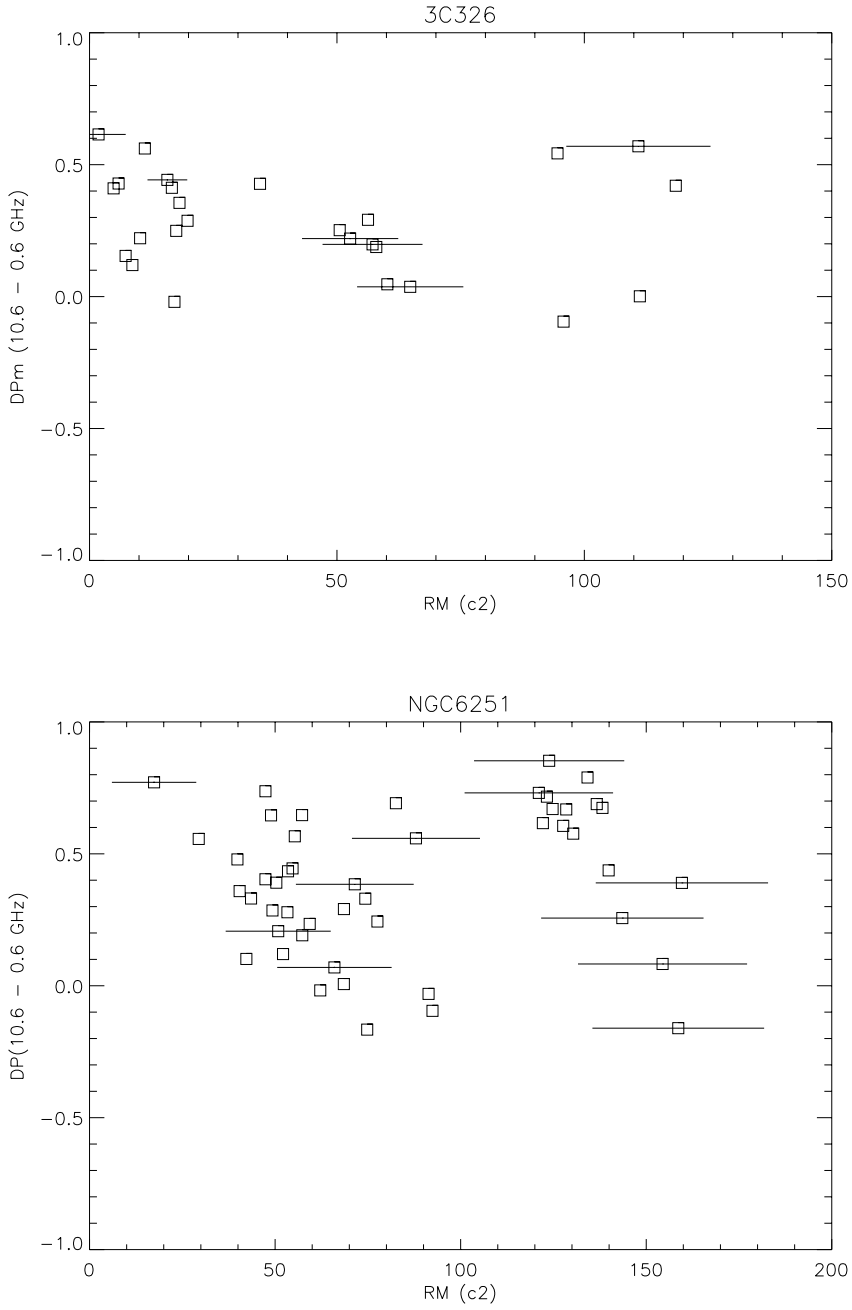

Figure 3.22: continued.

least some portion of it, is intrinsic. There is an argument in favour of this. Burns (1998) shows that there are X-ray clusters which are not relaxed. Even the Coma cluster which was believed to be a prototype of relaxed clusters does have substructure. GRGs can be 'weather stations' of large-scale cosmic flows. This means at least that an energy supply is possible. If this is true we can think about the possibility of an intrinsic large-scale mean field. However, we do not yet have any clear idea of a seed field or of a large-scale mechanism such as a dynamo.

3.6 Discussion: a multi-component Faraday medium?

In the previous sections, we demonstrated that the RM of the GRGs is quite high, and that depolarization exists but is very low. We did not find any clear correlation between DP and ΔRM in the GRGs. In radio galaxies, we are dealing with relativistic- and non-relativistic plasmas and their interaction. It might be no surprise that radio galaxies manifest much more complex processes than supposed. The physical processes in the solar atmosphere are good examples of this complexity and at the same time, this is a source of inspiration.

If we can introduce a second Faraday medium whose characteristic scalelength is smaller than the scale-length of high-RM structure and than the beam size, we can explain the weak, omnipresent DP which has no correlation with the large-scale ΔRM. Two cases are discussed in the subsequent subsections. The first one deals with internal depolarization, the second one with external depolarization.

3.6.1 Can relativistic electrons depolarize GRGs?

This is a classical question which was proved not to be relevant for FR I and FR II sources in the early days of radio galaxy research. Since GRGs are much larger systems than FR I and FR II sources, but were smaller at some time in the past, adiabatic expansion losses must be more important in GRGs than in other types of radio galaxies. Adiabatic expansion produces low-γ electrons and provides kinetic energy. The second aspect will be discussed later.

In order to shed light on the above question we begin with the basic concept of the Faraday Rotation. The equation of motion of a relativistic electron is

$$\gamma\, m\, \ddot{\mathbf{r}} = -e\,(\mathbf{E} + \dot{\mathbf{r}} \times \mathbf{B}),$$

where γ is the Lorentz factor, m the electron rest mass, $\mathbf{E}$ and $\mathbf{B}$ the electric and magnetic field vectors, e the unit charge, and $\dot{\mathbf{r}}$ and $\ddot{\mathbf{r}}$ the instantaneous velocity and acceleration, respectively, of the charged particles. Assuming $\varepsilon \sim 1$, $\mu \sim 1$, the wave number is

$$\kappa_{\pm}^2 = \frac{\omega^2}{c^2}[1 - \frac{\omega_p^2}{\omega(\omega \pm \omega_c)}]$$

Considering γ and a power-series expansion of ω, the phase difference,

$$2\Delta\psi = (\kappa_+ - \kappa_-) \cdot L$$

will be

$$\frac{\omega_p^2 \omega_c}{c^2 \omega^2}.$$

With increasing γ, the difference in the wave numbers, $\kappa_+ - \kappa_-$ decreases $\propto \gamma^{-2}$. This implies that the Faraday Rotation effect vanishes rapidly at high γ.

We now assume pressure balance between the magnetic field and the relativistic particles,, without any consideration of the source evolution.

$$\gamma\, \mathrm{n_e}\, \mathrm{mc}^2 = \mathrm{B}^2/(8\pi).$$

For a demonstrative estimate, we assume a magnetic field strength of 5 μG. If we further assume the lower turn-off frequency of synchrotron radiation at 10 MHz, γ is 1300. For

convenience, we will use $\gamma = 1000$. Particle acceleration theories predict such a high γ cut-off, too. From the above equation, we obtain $n_e = 1.2 \cdot 10^{-9} cm^{-3}$. This is obviously too small and even though the number density is higher, such high-γ electrons with a magnetic field are not a good rotator of the linear polarization at all as shown above. This is why this kind of explanation is irrelevant for the depolarization in the FR-I and -II sources.

In GRGs, the situation may be different. As shown in Chapt. 1, GRGs are only slightly depolarized. They are older than the FR-I and -II type sources, and we can safely assume that GRGs undergo a severe adiabatic loss phase in their lifetime. Now, we consider adiabatic losses in GRGs in order to get low-γ electrons. It is natural to assume that GRGs were once FR I or FR II sources, and compact sources long before. If this is true (which must be), then we can argue that there is an adiabatic loss phase (or more phases) during their lifetime. There are consequences of this adiabatic loss phase. The relativistic electrons of the pre-adiabatic loss phase will lose most of their energy, roughly at a rate $W_0(r_0/r)$, where W_0 is the internal energy before the expansion, r_0 and r are the radii before and the after expansion, respectively. Since they lost most of their energy, they do not significantly contribute to the pressure balance and to the total energy.

In a power-law distribution of relativistic electrons, i.e. $N(\gamma) = N_0 \gamma^{-p}$, where $p \geq 2$, most of the energy is in the lowest possible γ population, since the total energy is $E_{total} = \int N(\gamma) \gamma m_0 c^2 d\gamma$. Therefore, we are interested in electrons with $\gamma = 1000$ from the pre-expansion phase. After the expansion, the relativistic electrons from the pre-expansion phase will have converted most of their energy into the kinetic energy of the expansion, $W_0(r_0/r)$. In this way, low-γ electrons can be generated. Since they are not in pressure balance with the high-γ electrons which are supplied continuously from the central AGN to the lobes, they will be compressed roughly until $\gamma_{low} \cdot n_{low} = \gamma_{high} \cdot n_{high}$. The total number of low-γ electrons depends on the particle number in the pre-expansion phase.

Let $\gamma_{high}/\gamma_{low} \sim 1000$ and $n_{low}/n_{high} = \eta$. If we can further assume pressure balance in the cloud of low-γ electrons after compression, the magnetic field strength will be $5\mu G$ (if they are not in pressure balance, the magnetic energy will be released as in the solar corona and will eventually be in pressure balance). Considering MHD instabilities, we assume the number N_{cloud} of such clouds in a GRG. From the conservation of the total number of particles, we have $N_{cloud} \times V_{cloud} \times n_{low} = \eta \times n_{high} \times V_{GRG}$.

For a simple demonstration, we use $N_{cloud} = 100$, $\eta = 10$ and $V_{GRG} = 1$ Mpc^3. Then the scalelength of each low-γ cloud will be about $V_{cloud}^{1/3} \sim 50$ kpc. This scalelength uncertain and possibly shorter than this, if we consider the instability quantitatively. Fig. 3.23 shows the RM produced by such a cloud. If such clouds exist, they can depolarize GRGs, but will not produce high RMs at all. Since they are independent of the high-RM foreground screen, it is natural that there is no relation between ΔRM and DP.

As mentioned before, adiabatic expansion transforms the internal to kinetic energy, which can be transported into the environment. This is an interesting idea for the high-RM environment, too. The other two major energy loss processes of radio galaxies, i.e. synchrotron and inverse Compton losses, transform the energy to the photon energy at radio and X-ray wavelengths. Since the Faraday medium is supposed to be optically thin, these two loss processes do not contribute to the high RM. This will be discussed in more detail later in this thesis.

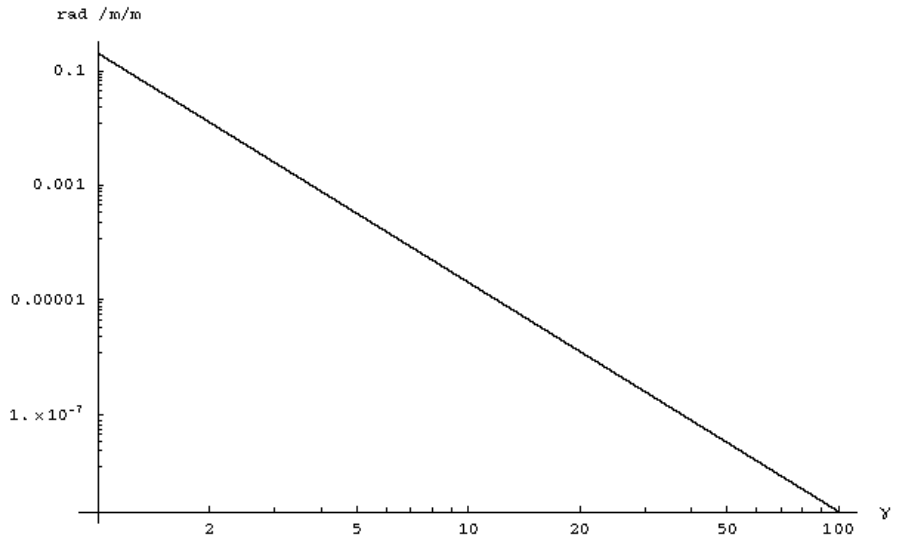

Figure 3.23: Faraday Rotation by a power-law distribution of electrons. At $\gamma = 1$, we assume an electron density of $n_0 = 5 \cdot 10^{-5}\, cm^{-3}$, this assumption needs that the relativitic electron density increases through the compression. At γ, $n_\gamma = n_0 \cdot \gamma^{-p}$. Here p = 2. The line-of-sight component of the magnetic field has a strength of $5\mu G$. The line-of-sight length of the Faraday medium is ~ 1 *kpc*. The resulting Faraday depth is a power-law distribution. There is a high-energy tail (relativistic electron tail) contribution to the integrated Rotation Measure. A discussion of some geometric variation are found in the text.

3.6.2 Depolarization by a turbulent RM structure

The reason to search for an alternative origin of the depolarization is, as mentioned before, that we can not find any significant ΔRM - DP correlation. The idea of a ΔRM - DP correlation comes from the assumption that the Faraday foreground screen is at least partly unresolved, and this Faraday foreground screen has just one characteristic scalelength. This means that the RM distribution is described by some function, e.g. by a Gaussian, a power-law, a quadratic or a delta function. If the screen is unresolved, then Burn's law $\mathrm{m}_\lambda = \mathrm{m}_0 \exp -2\Delta^2\lambda^4$ is valid, regardless of the choice of the RM distribution function.

The situation in GRGs casts some doubt on the validity of a single scalelength. Another possibility is substructure in the RM, but neither with a continuous Gaussian nor with a power-law distribution function. Actually, it sounds natural that a Faraday medium containing a regular magnetic field with a length scale larger than 55 kpc has substructure, e.g. through MHD waves. In order to discuss this effect in the depolarization observations, we have to resort to the RM equation of Tribble (1991) once more.

Faraday dispersion function

Tribble (1991) showed that the quadratic approximation is a good asymptotic solution for a Gaussian and a power-law distribution. We show the Tribble (1991)'s equation again:

$$m_\lambda^2 = \frac{1-\exp[-S-4\,\Delta\mathrm{RM}^2\lambda^4]}{1+4\,\Delta\mathrm{RM}^2\lambda^4/S} + \exp[-S-4\,\Delta\mathrm{RM}^2\lambda^4],$$

When $S = 0$, the RM structure is unresolved, and this equation becomes exactly Burn's law, $m_\lambda = m_0\ \exp[-2\Delta\mathrm{RM}^2\lambda^4]$. Then the DP - ΔRM correlation reads

$$(\ln \mathrm{DP})^{1/2} = -2\,\Delta\mathrm{RM}\,(\lambda_{low}/\lambda_{high})^2.$$

Now, let us consider the case $(B_1/B_0) = (B_{DP}/B_{RM}) = \phi$, where B_0 is the regular field and B_1 is the perturbed field resulting from a small fluid displacement. The whole structure will be perturbed by the MHD wave on a timescale of l_{RM}/v_A, where $v_A = \sqrt{B_0^2/4\pi\rho_0}$ is the Alfvén speed. For a paricle density of few $10^{-4}\,cm^{-3}$ and for a several μG magnetic field, v_A of a few hundreds km/s is obtained. On a $10^6\,yr$ timescale which is much shorter than the source lifetime, the turbulence fills the large-scale RM structure, $l_{RM} < 100$kpc.

3.6.3 Adiabatic Expansion - Internal driver?

The amount of this kinetic energy released will be transported to the environment. This is different from the other two major energy loss processes in radio galaxies, viz. synchrotron radiation and inverse Compton. This will be discussed later in chapter 5.

Chapter 4

Polarization asymmetries of B2 Galaxies

4.1 B2 radio galaxies - First Sample

This section deals with six B2 radio galaxies. Measurements at 10.6 and 4.9 GHz data have been used. The 4.9 GHz data of Morganti et al. (1997a) had to be soothed to the angular resolution of the 10.6 GHz data. The RM unambiguity of the six B2 radio galaxies is therefore consistent with that of the five GRGs treated in the former chapter. The angular resolution of $69'' \times 69''$ is now much more improved over that of the GRGs, thanks to the high resolution at 4.9 GHz.

The study of the B2 sample in this section has two purposes, and it will be a milestone for the coming larger sample of B2 sources. The current B2 sample has better resolution but will be more strongly faced with RM ambiguities, since we are only dealing with two frequencies (4.9 and 1.6 GHz) in the VLA sample. The second purpose of this study is the comparison with the results from the five GRGs. If the bimodality (or multiplicity) in the RM histograms and the high $\overline{RM}$ of the GRGs are due to the Galactic contribution, we should see a similar trend in this section.

4.1.1 DPm maps

We begin with maps of

$$\mathrm{DPm} = \frac{m_{high} - m_{low}}{m_{high} + m_{low}}$$

for six sources. $DPm = -1$ means full repolarization, i.e. no fractional polarization at the higher of the two frequencies and non-zero fractional polarization at the lower one. $DPm = 1$ means full depolarization. The fractional polarization was obtained using the same 'hybrid' method as in the Chapt. 1. In Tab. 4.1, we summarize the integrated DP values. There is a relation between DPm and DP,

$$DPm = \frac{1-DP}{1+DP} \text{ or } DP = \frac{1-DPm}{1+DPm}.$$

For the sake of a clearer display, we use only DPm values between -1 and 1. In the tables, we present the full range of DP values.

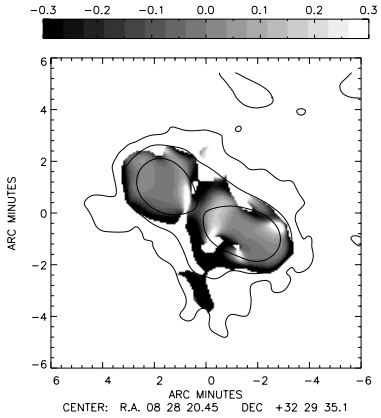

(a) B2 0828+32

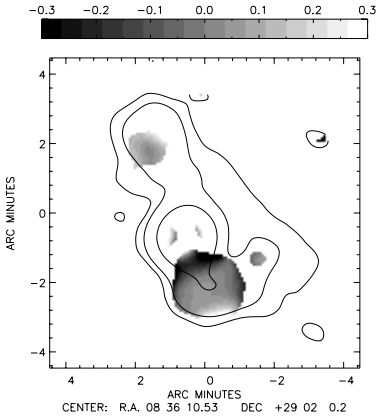

(b) B2 0836+29

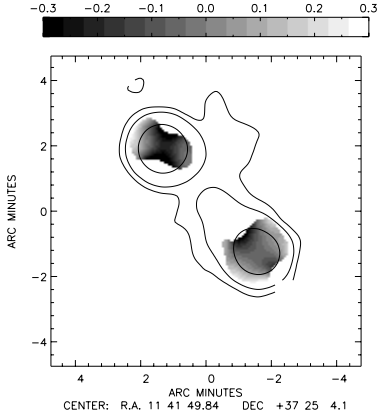

(c) B2 1141+37

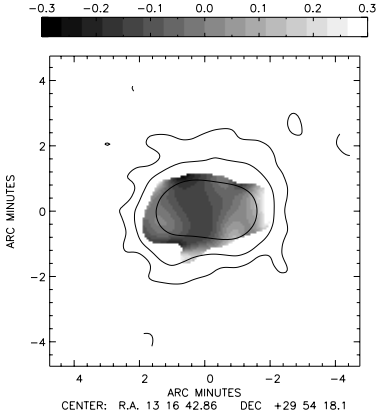

(d) B2 1316+29

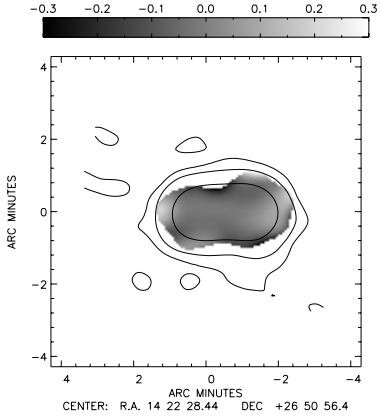

(e) B2 1422+26

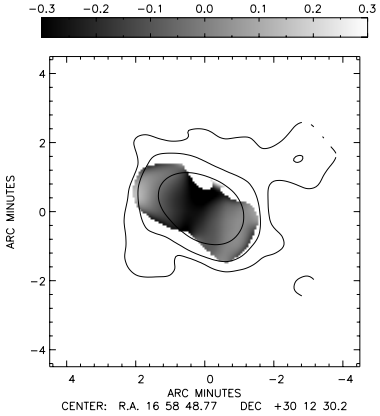

(f) B2 1658+30

Figure 4.1: $DPm_{4.9}^{10.6}$ maps of six B2 sources. The contours delineate the total intensity map at 10.6 GHz represent 3, 10 and $50\sigma_I$.

Table 4.1: The integrated DP of six B2 radio galaxies

B2 name	DP	ΔDP	jet side	DP_j	DP_{cj}
0828+32	≥ 1.2	≥ 0.8	SW	1.39	1.27
0836+29	0.8	0.5	N	0.73	1.08
1141+37	1.1	0.3	NE?	1.27	1.02
1316+29	1.1	0.2	E	1.19	0.99
1422+26	1.0	0.2	W	1.04	1.05
1658+30	1.3	0.4	SW	1.20	1.31

B2 0828+32

This radio galaxy is known as an 'X-shaped' source (Rottmann, 2001). Along the main axis, from the SW to the NE, the depolarization shows a patchy structure, but no clear asymmetry. The core-to-lobe depolarization contrast is more obvious. It is not clear if the high repolarization in the old N lobe is real or an artifact due to missing short spacings at 4.9 GHz (Fig. 4.1 [a]).

B2 0836+29

In the central region of this object, depolarization is seen, with DP = 0.30. The N lobe on the jet- and longer-arm side is more depolarized than the S lobe on the counterjet- and shorter-arm side. From the morphology of this source, one can deduce that it has a very asymmetric environment. Therefore, the physical conditions around the two lobes are probably completely different (Fig. 4.1 [b]).

B2 1141+37

This FR II-type B2 radio galaxy has no jet. Since the Laing-Garrington effect is more frequently expected in FR II-type objects, we consider the less depolarized (or more re-polarized) NE lobe as the jet-side lobe (Fig. 4.1 [c]).

B2 1316+29

The S-shaped two-sided jet (with 'fat double lobes') is not seen at this resolution. Near the core, the E jet is stronger, hence we accept the E lobe as associated with the jet-side lobe. The E lobe is indeed less depolarized (Fig. 4.1 [d]).

B2 1422+26

The W lobe has a stronger jet. At higher resolution, the two lobes are quite identical and symmetric w.r.t. the core.

B2 1658+30

This is another 'fat double' in the high-frequency B2 sample. The SW lobe on the jet side is marginally more depolarized (less re-polarized).

4.1.2 Integrated properties

At the high frequency, the depolarization is very weak in the sample, inspite of the low angular resolution. Given this weak depolarization, it is no surprise that there is a lack of depolarization asymmetry. Only three sources including B2 1141+37 whose jet direction is inferred from the DP asymmetry show the Laing-Garrington effect.

At the low frequency, the $DP_{1.4}^{4.9}$ shows that five of the six sources exhibit the Laing-Garrington effect (Morganti et al., 1997b). Depolarization is probably a genuine low-frequency property. As for the GRGs, DP and RM result from the different distribution functions.

4.1.3 RM of B2 radio galaxies: RM histograms

The histograms of the six B2 radio galaxies show a single distribution and have been well fitted by a Gaussian using AIPS task IMEAN. The peak and mean values in Tab. 4.2 show fairly good agreement. They are quite low, RM $< |50|$ rad m^{-2}, consistent with the RM value at the X-ray cluster periphery (Clarke et al., 2001).

4.1.4 RM maps

Since there is no sub-structure in the RM histograms and $\overline{RM}$ is small in all six B2 radio galaxies studied in this section, we use RM_{c1}, i.e. the simple mean subtraction in order to correct for the Galactic foreground.

4.1.5 λ_0 maps of B2 radio galaxies

Since the $|RM|$ of the B2 radio galaxies is small as seen in their histograms, the λ_0 polarization angle map is very similar to that at 10.6 GHz. In the following, a vector length of $1'$ represents $DP = 1$. A shorter length means depolarization and a longer one means repolarization.

B2 0828+32

The magnetic field in B2 0828+32 is tangential at the lobe periphery. Around the hotspots and the core the field direction is not straight. Since it is not random but has a coherent and bent structure, it is suspected to reflect the complex structure of B2 0828+32, i.e. its X-shaped structure (Rottmann, 2001) (see Figs. 4.5, 4.3 and 4.4) [a].

B2 0836+29

Only the southern jet and the first knot are seen in the RM map. The magnetic field in that region is perpendicular to the jet and does not show any bending along the total intensity ridge. In general, the two lobes are weakly polarized. Therefore, B2 0836+29 is not appropriate to trace its foreground medium (see Figs. 4.5, 4.3 and 4.4) [b].

B2 1141+37

This source has a typical FR II morphology, with two advancing hotspots. Since no jet is detected in this source, we assume the less depolarized N lobe to be on the jet

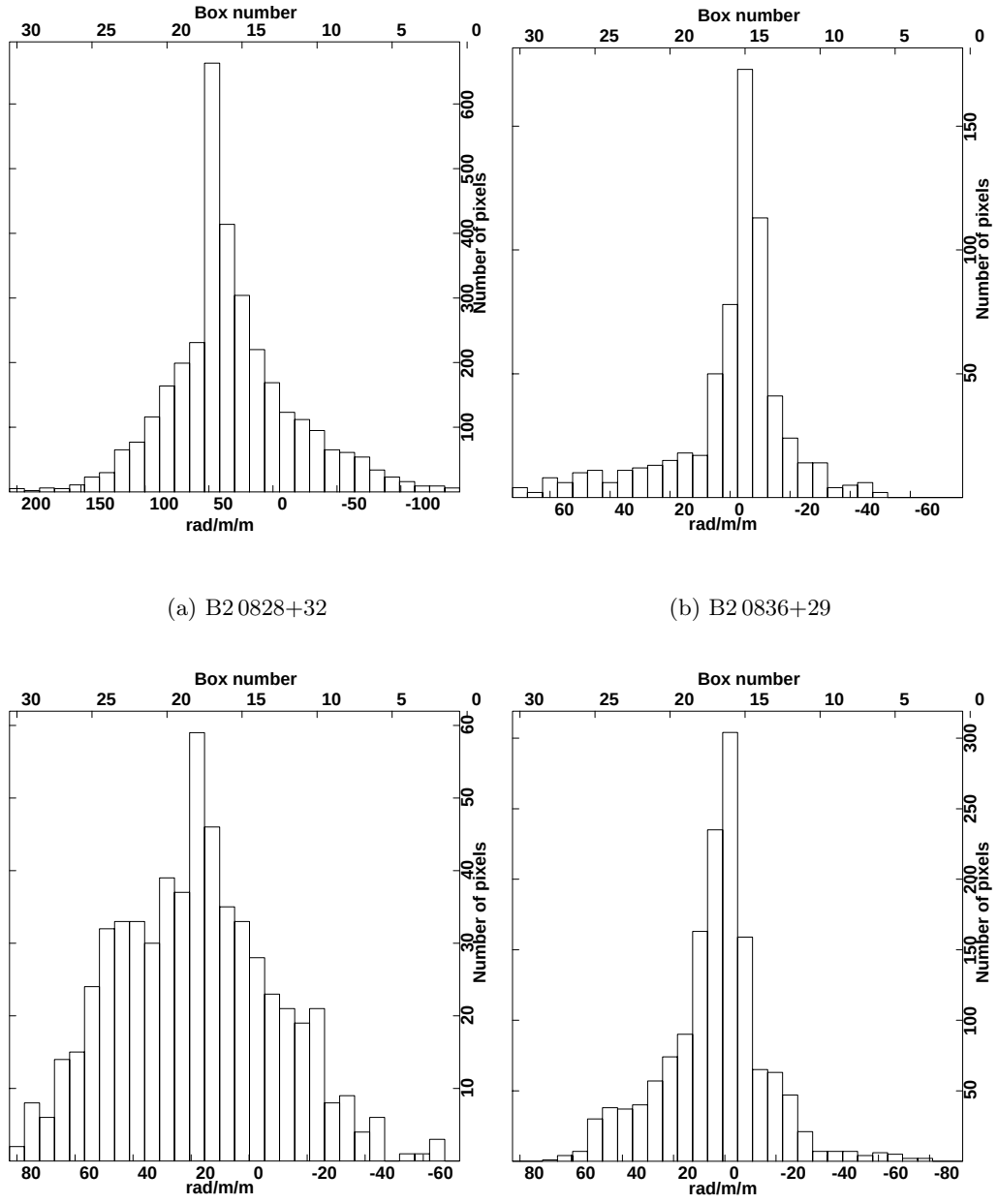

(a) B2 0828+32

(b) B2 0836+29

(c) B2 1141+37

(d) B2 1316+29

Figure 4.2: RM distribution of the six B2 sources. The RM is measured between 10.6 and 4.9 GHz.

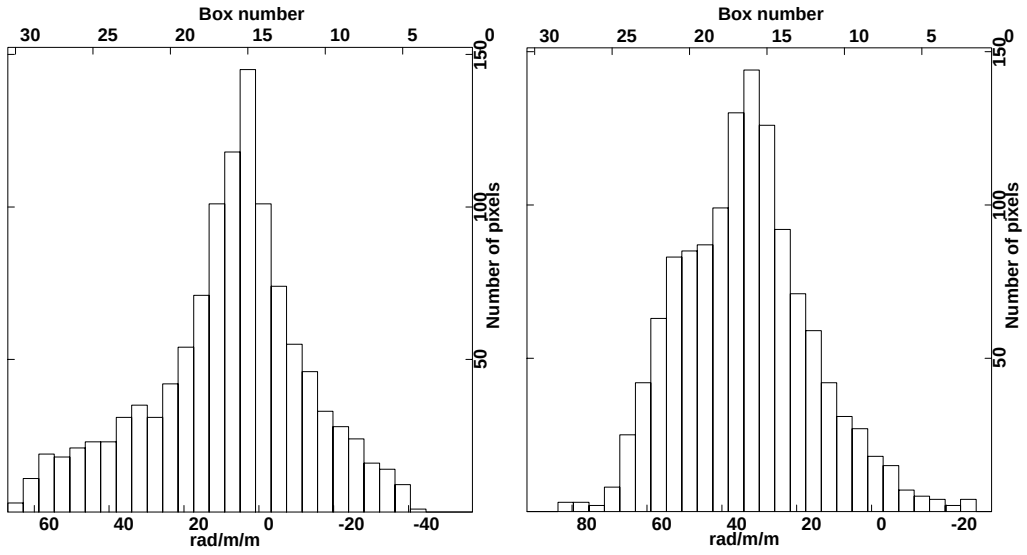

(e) B2 1422+26 (f) B2 1658+30

Figure 4.2: continued.

side. Because of its FR II morphology, the indication of the Laing-Garrington effect in B2 1141+37 is more reliable than in the other B2 sources in this sample.

The two lobes have quite a different magnetic field configuration. The lobe on the jet side (or less polarized N lobe) has a magnetic field structure that is oriented perpendicular to the major axis. In contrast, the S lobe has a B-field structure parallel to the major axis. The maps of RM and $|RM_{c1}|$ exhibit field reversals in the lobes but no clear asymmetric trend (see Figs. 4.5, 4.3 and 4.4) [c].

B2 1316+29

B2 1316+29 is not well resolved by the $69''$ beam. Its DP and RM structure clearly show the Laing-Garrington effect. This could be due to the low resolution, since the Laing-Garrington effect and the DR - ΔRM relation is most pronounced in case of an unresolved foreground (see Figs. 4.5, 4.3 and 4.4) [d].

B2 1422+26

At high resolution, B2 1422+26 shows an S-shaped structure. Besides its highly core-symmetric, total intensity shape, the distribution of RM and ΔRM are symmetric, and so is that of DP. The magnetic field is tangential to the envelope. Along the major axis the magnetic field is slightly oblique (see Figs. 4.5, 4.3 and 4.4) [e].

B2 1658+30

This is a symmetric 'fat double' with a clear jet asymmetry. The polarization trends are not in accord with the Laing-Garrington effect. ΔRM is larger on the jet side. The magnetic field is perpendicular to the major axis along the major axis. At the lobe-extremity the field becomes tangential (see Figs. 4.5, 4.3 and 4.4)[f].

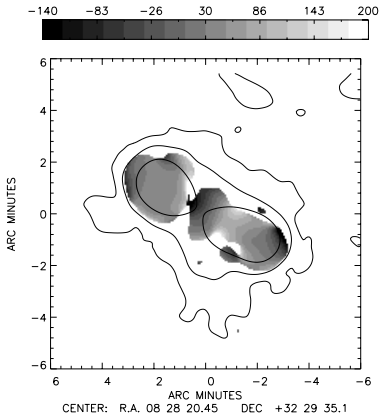

(a) B2 0828+32

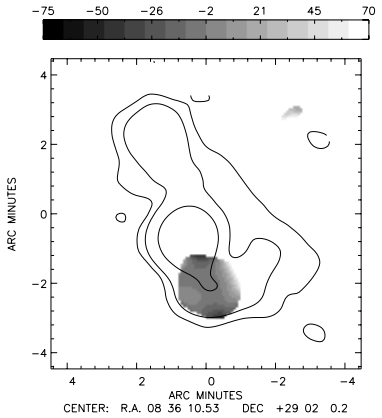

(b) B2 0836+29

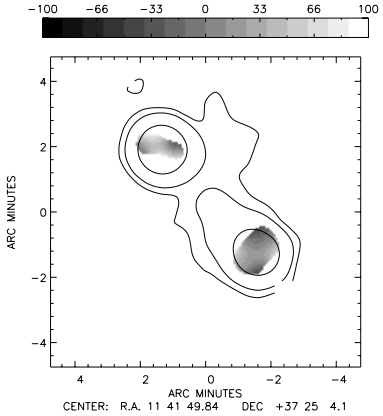

(c) B2 1141+37

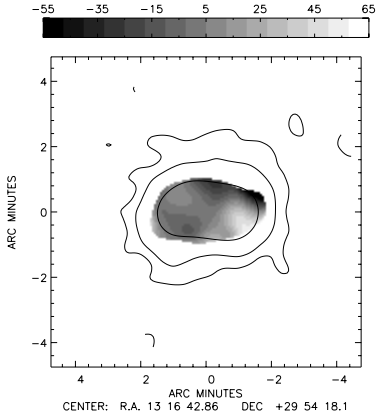

(d) B2 1316+29

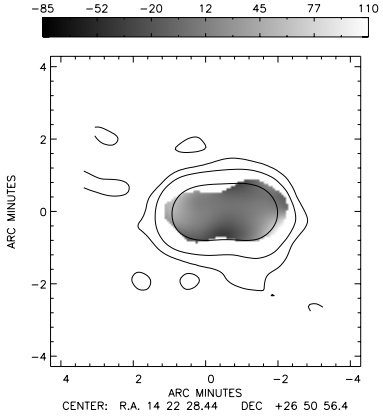

(e) B2 1422+26

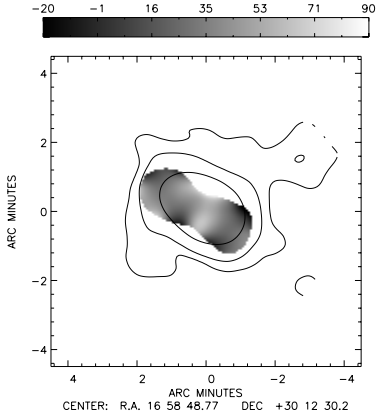

(f) B2 1658+30

Figure 4.3: RM maps of six B2 sources. The ambiguity of RM data is comparable to that of the GRGs.

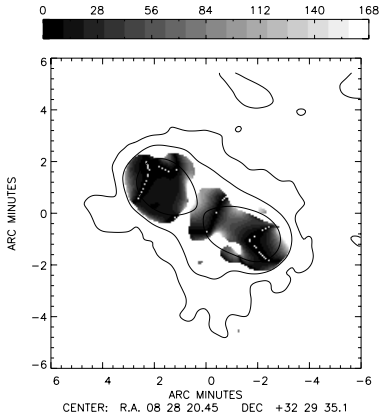

(a) B2 0828+32

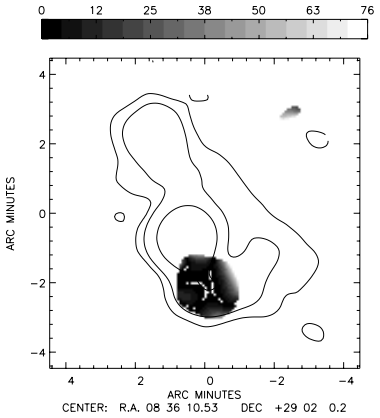

(b) B2 0836+29

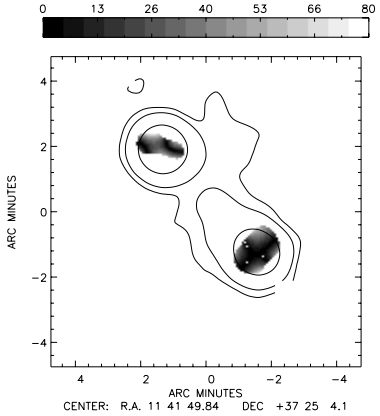

(c) B2 1141+37

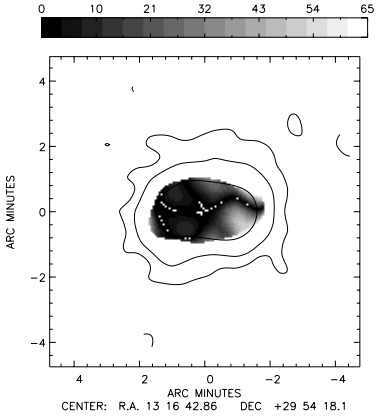

(d) B2 1316+29

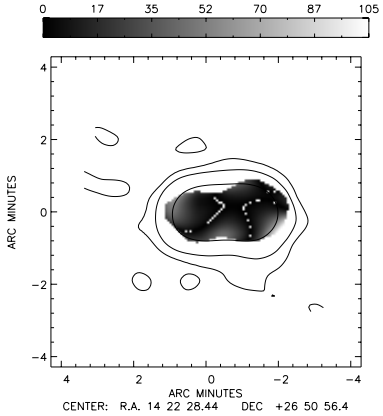

(e) B2 1422+26

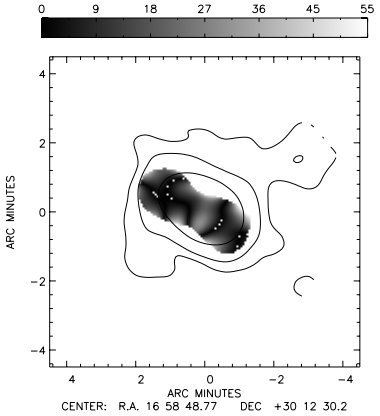

(f) B2 1658+30

Figure 4.4: $|RM_{c1}|$ maps of six B2 sources and the their maps of $|RM|$.

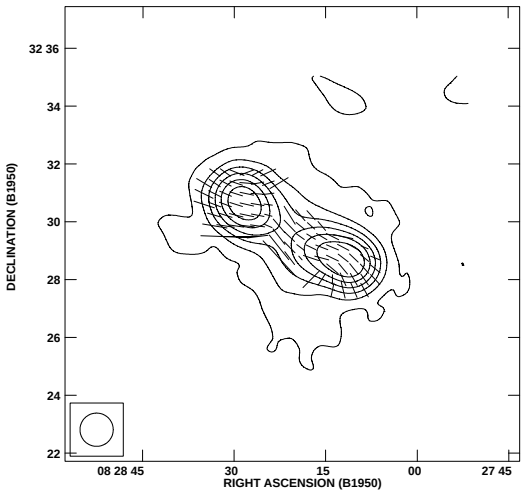

(a) B2 0828+32

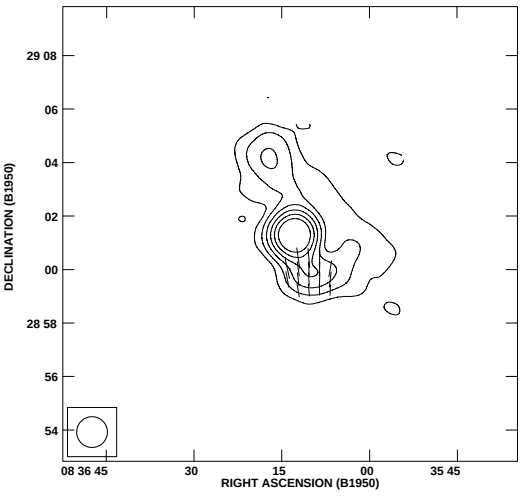

(b) B2 0836+29

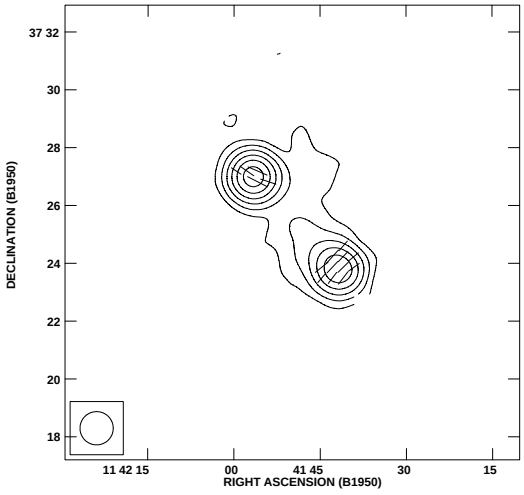

(c) B2 1141+37

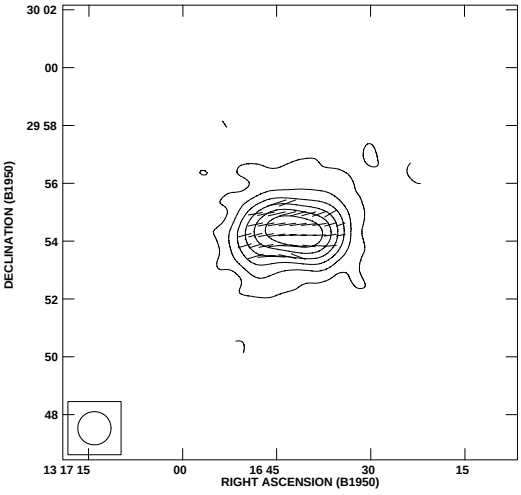

(d) B2 1316+29

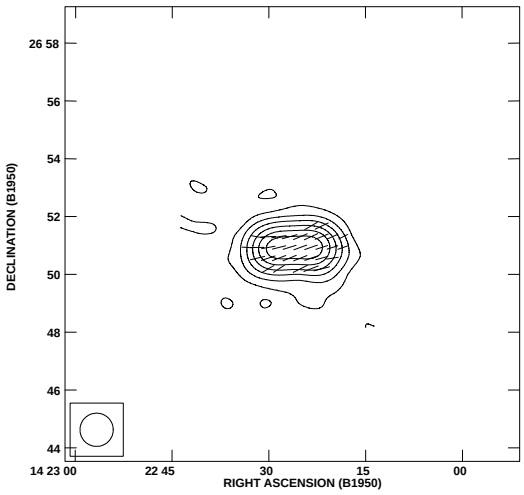

(e) B2 1422+26

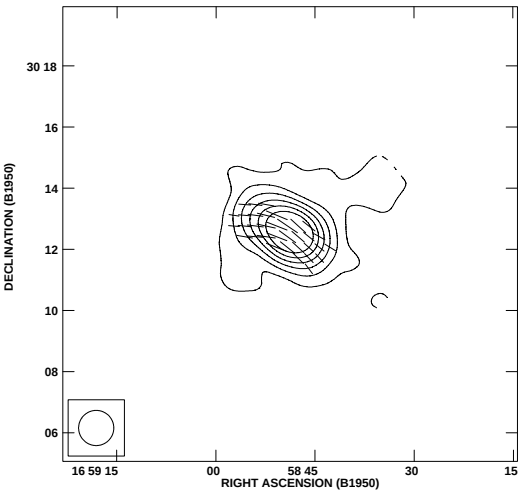

(f) B2 1658+30

Figure 4.5: λ_0 maps of six B2 sources. Using the RM in Fig. 4.3 and the polarization angle at 10 GHz, the zero wavelength (λ_0) polarization angles of the E-vectors are estimated. The length of the vector represents the DP. A vector length of $5'$ means $DP = 1$.

Table 4.2: The integrated $RM_{4.9}^{10.6}$ of six B2 radio galaxies

B2 name	RM_{peak}	ΔRM_{gaus}	$\overline{RM}$	ΔRM_{all}	ΔRM_j	ΔRM_{cj}
0828+32	+42	10	+32	58	58	54
0836+29	-6	5	+2	2	18	-
1141+37	+20	30	-12	106	27	23
1316+29	0	8	+4	20	10	28
1422+26	+5	10	+12	32	24	22
1658+30	+35	17	+34	18	20	15

Summary of the six B2 RGs

Due to the lack of any DP asymmetry at the higher frequency, a ΔRM asymmetry is not expected. However, we find a reversed asymmetric trend, such that ΔRM on the jet side is larger than ΔRM on the counterjet-side (in 4 sources). The difference between the two lobes is marginal in these 4 sources. Since the sample has only 6 members, it is too premature to draw any conclusions.

Only one case, B2 1316+29 shows an exemplary 'Laing-Garrington' effect so far. In this source, the lobe on the jet side is less depolarized and has a smaller ΔRM than the counter-jet lobe.

4.1.6 RM-DP of B2 sources

We now test a possible correlation between the rotation measure and depolarization. If depolarization occurs in the Faraday medium that we see in the RM maps, the RM dispersion as well as DPm (or DP) must be correlated. More strongly depolarized regions should have a larger RM dispersion. In Fig. 4.6, we show the RM – DPm diagrams of the six B2 radio galaxies.

We have checked the dispersion of the most strongly depolarized five points and the most strongly polarized (or re-polarized) five points. In B2 0836+29 and B2 1141+37, this test is not possible, owing to the small number of points. B2 1316+29 exhibits the clearest trend of the DPm(DP) - ΔRM correlation (Fig. 4.6[d]). The most strongly depolarized points have a larger RM dispersion than the most strongly polarized (or re-polarized) five points. B2 1422+26 exhibits a DPm(DP) - RM correlation (Fig. 4.6[e]). The most strongly depolarized points have larger RM values than the most strongly polarized (or re-polarized) five points. This translates to the DPm(DP) - ΔRM correlation if ΔRM is obtained from $|RM_{c1}|$.

4.1.7 Summary and Discussion

Two interesting findings are reported in this section. The mean RMs of B2 sources are very small compared to the GRG sample. From the λ_0 polarization angle maps and the RM histograms, we conclude that the RM of the foreground Faraday medium is unambiguously determined. Based on this knowledge, we will study the better resolved VLA sample in the next section, which however bears a larger RM ambiguity. Although the six B2 sources analyzed in this section show the Laing-Garrington effect in the low-frequency DP, no asymmetric trend is found in $DP_{4.9}^{10.6}$. Depolarization is a low-frequency property. Since we have not found any clear RM - DP correlation except for the case of B2 1316+29, we can give some constraints.

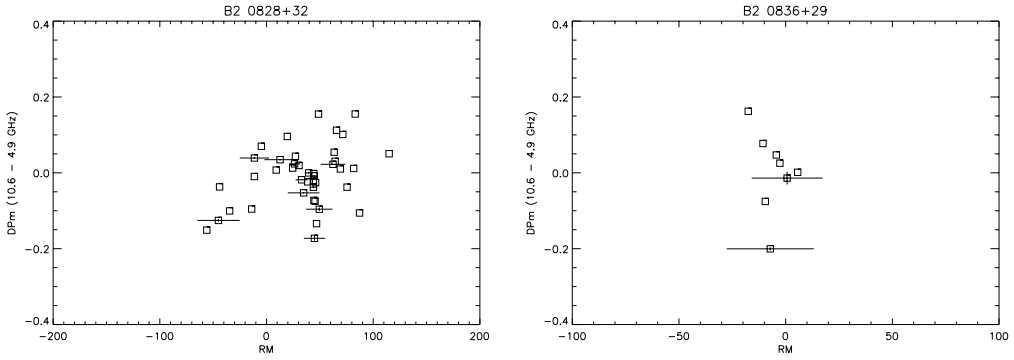

(a) B2 0828+32 (b) B2 0836+29

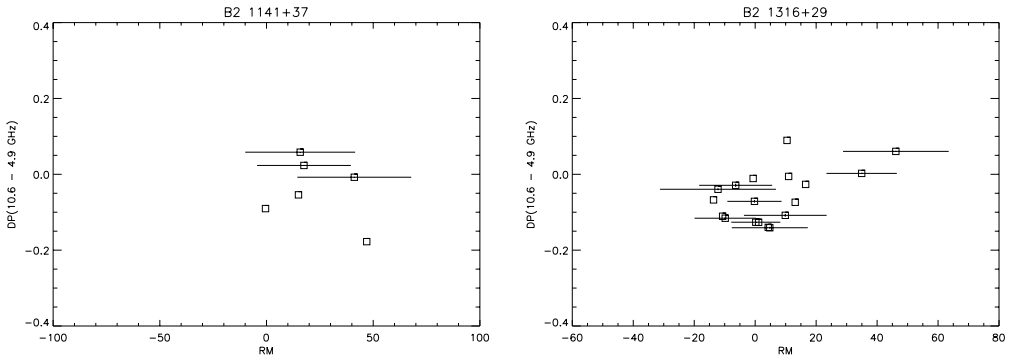

(c) B2 1141+37 (d) B2 1316+29

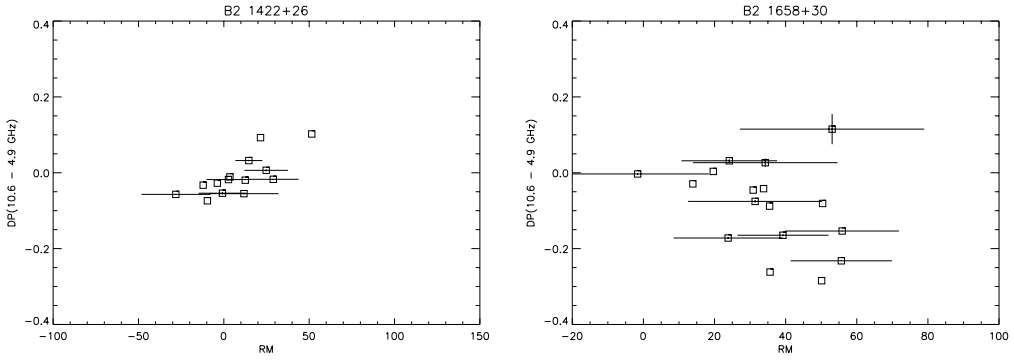

(e) B2 1422+26 (f) B2 1658+30

Figure 4.6: RM-DPm diagram of the six B2 galaxies.

The depolarization asymmetry at lower frequencies does not directly stem from the RM structure shown in this section. The depolarization asymmetry may come from a more omnipresent weak magnetic field with a shorter scalelength. This magneto-ionic medium could have a density distribution which roughly follows a King profile (Garrington & Conway, 1991). Alternatively, this Faraday medium can be sub-relativistic as discussed in the former chapter. If present, it must fill the environment following roughly a King's profile in order to produce the Laing-Garrington effect.

The RM structure is strongly suspected to be produced in the vicinity of the radio sources. Whether this is amplified through the interaction between radio galaxies and their environment Eilek & Owen (2002) or whether this is generated by the radio galaxies themselves (Daly & A., 1990), is an open question at this stage. In addition to the mean difference in the RM, there is also a difference in the scalelength of B2 radio galaxies and GRGs. The exact RM scalelength of B2 radio galaxies should be studied using better resolved sample.

Table 4.3: Positional information of 14 B2 radio galaxies

B2 name	z	r (Mpc)	RA(J2000)	DEC(J2000)	l	b
0034+25	0.031849	128	$00^h37^m05\overset{s}{.}5$	$+25°41'56''$	$118\overset{\circ}{.}881$	$-37\overset{\circ}{.}059$
0755+37	0.042836	171	$07^h58^m28\overset{s}{.}1$	$+37°47'12''$	$182\overset{\circ}{.}676$	$28\overset{\circ}{.}828$
0828+32	0.052700	203	$08^h31^m27\overset{s}{.}5$	$+32°19'26''$	$190\overset{\circ}{.}707$	$34\overset{\circ}{.}150$
0836+29	0.078900	316	$08^h39^m15\overset{s}{.}8$	$+28°50'39''$	$195\overset{\circ}{.}2904$	$34\overset{\circ}{.}985$
1141+37	0.115000	458	$11^h44^m27\overset{s}{.}2$	$+37°08'32''$	$173\overset{\circ}{.}436$	$72\overset{\circ}{.}684$
1243+26	0.087234	356	$12^h46^m21\overset{s}{.}9$	$+26°27'17''$	$243\overset{\circ}{.}398$	$88\overset{\circ}{.}682$
1316+29	0.072800	291	$13^h19^m04\overset{s}{.}2$	$+29°38'34''$	$57\overset{\circ}{.}027$	$83\overset{\circ}{.}424$
1357+28	0.062700	252	$14^h00^m00\overset{s}{.}8$	$+28°29'56''$	$42\overset{\circ}{.}081$	$74\overset{\circ}{.}787$
1422+26	0.036992	148	$14^h24^m40\overset{s}{.}5$	$+26°37'30''$	$36\overset{\circ}{.}891$	$69\overset{\circ}{.}232$
1441+26	0.062100	248	$14^h44^m06\overset{s}{.}3$	$+26°01'12''$	$36\overset{\circ}{.}867$	$64\overset{\circ}{.}836$
1455+28	0.141100	564	$14^h57^m53\overset{s}{.}8$	$+28°32'19''$	$43\overset{\circ}{.}276$	$62\overset{\circ}{.}087$
1528+29	0.084300	337	$15^h30^m10\overset{s}{.}3$	$+29°00'30''$	$45\overset{\circ}{.}519$	$55\overset{\circ}{.}096$
1643+27	0.101070	404	$16^h45^m27\overset{s}{.}5$	$+27°20'06''$	$47\overset{\circ}{.}514$	$38\overset{\circ}{.}492$
1658+30	0.034424	140	$17^h00^m45\overset{s}{.}2$	$+30°08'09''$	$51\overset{\circ}{.}928$	$35\overset{\circ}{.}899$

4.2 The second sample: a high-resolution sample

Based on the knowledge from the previous section, we investigate 14 B2 radio galaxies with better angular resolution, i.e. $15'' \times 15''$, but with a higher RM ambiguity. The sample includes six B2 sources from the former section, too. In Tab. 4.3, we present their positional information. The Galactic latitudes of the sources are quite high. The six sources that appeared in the former section have a lower Galactic latitude. Although this does not automatically imply that the remaining 8 sources have a small Galactic RM contribution, we nevertheless expect a small Galactic RM contribution, i.e. the small mean RM for the remaining 8 sources.

4.2.1 Sample description

Information about the sources is summarized in Tables 4.3 and 4.4. Since the 1.6 GHz data of Capetti et al. (1993) have a larger synthesized beam than the 5 GHz data of Morganti et al. (1997a), the latter were convolved to the angular resolution of the 1.6 GHz data using a Gaussian beam. The convolution was done with the task CONVL in AIPS. Since CONVL cannot handle any 'magic blanking values' in the I,U,Q maps, we assigned them a zero value (using task COMB/SUM) prior to the convolution. This replacement of the magic blanking value introduces an underestimate of $\sigma_{I,U,Q}$ in the 5 GHz data.

In constructing the polarized intensity maps, $I_p = \sqrt{Q^2 + U^2}$, we applied the 'hybrid' Ricean bias correction which we have introduced in Chap. 2. The two widely used solutions, Wardle & Kronberg (1974); Killeen et al. (1986), are acceptable when the fractional polarization, m, is obtained from the integrated flux densities, i.e. $m = \Sigma I_P / \Sigma I$. This has been done in the literature. Because of the integrations the so obtained m is 'structure dependent'. This means that if the sources possess dominant and bright polarized components, the integrated m will reflect the fractional polarization of these dominant components (e.g. hot spots, jets). This 'structure dependence' makes the Ricean bias of regions with low signal-to-noise (predominantly the lobes) unsignificant.

DP maps published in the literature should therefore be interpreted with care. Of-

Table 4.4: The convolved data of 14 B2 radio galaxies

B2 name	convl. beam	σ_I(mJy) 5GHz	σ_{I_p}(mJy)	σ_I(mJy) 1.6GHz	σ_{I_p}(mJy)	FR type
0034+25	$16\farcs6 \times 16\farcs6$	0.06	0.04	0.2	0.06	I
0755+37	$22\farcs2 \times 22\farcs2$	0.14	0.05	1.4	0.39	I
0828+32	$12\farcs5 \times 12\farcs5$	0.18	0.09	0.4	0.13	II
0836+29	$12\farcs5 \times 12\farcs5$	0.06	0.04	0.4	0.21	I-II
1141+37	$14\farcs0 \times 14\farcs0$	0.10	0.05	0.5	0.07	II
1243+26	$13\farcs1 \times 13\farcs1$	0.05	0.03	0.3	0.06	I
1316+29	$13\farcs5 \times 13\farcs5$	0.14	0.06	0.3	0.06	I
1357+28	$13\farcs6 \times 13\farcs6$	0.04	0.04	0.2	0.05	I
1422+26	$13\farcs7 \times 13\farcs7$	0.19	0.05	0.2	0.07	I
1441+26	$14\farcs2 \times 14\farcs2$	0.05	0.04	0.2	0.06	I-II
1455+28	$15\farcs6 \times 15\farcs6$	0.19	0.05	0.4	0.06	II
1528+29	$12\farcs9 \times 12\farcs9$	0.03	0.03	0.2	0.06	I-II
1643+27	$13\farcs7 \times 13\farcs7$	0.06	0.05	0.15	0.05	I-II
1658+30	$18\farcs4 \times 18\farcs4$	0.15	0.07	0.7	0.12	I-II

ten, they are presented down to $\sim 3\,\sigma_{I,obs}$ where the polarized flux density is $< 3\,\sigma_{I_p,obs}$. In addition to these under- or overestimates of the real I_P there is also the danger of mis-interprepation. Using the hybrid solution, the error in our estimate of the fractional polarization will be 2% at $3\,\sigma_{I_p,obs}$. Of course, the fluctuation due to the noise is inevitably the same as in Wardle & Kronberg (1974) and in Killeen et al. (1986). The values of DPm and DP in Tables 4.5 and 4.7 were computed from the areal means of the hybrid solution, i.e. $m = \Sigma(I_p/I)$. This was done using IDL.

Using the two-frequency data, we have estimated the RM of the sources. Since our RM is based on two frequencies only, the ambiguity is about 100 rad m^{-2}, which is too large to estimate the real RM. However, our RM may already be useful to estimate the fluctutaion in the RM structure, ΔRM. The DP and RM maps of the individual sources will be shown after the integral properties.

4.2.2 Integrated properties

DP and DPm

In this section, we present the results of the depolarization of 14 B2 radio galaxies in two ways, namely by their DP and DPm. Their definitions are

$$DP = \frac{m_{low}}{m_{high}}$$

and

$$DPm = \frac{1-DP}{1+DP},$$

where m_{low} and m_{high} are the fractional polarizations at low and high frequencies, respectively. DPm has its merit in terms of a better visualization, while the merit of DP is its direct connection to the Faraday depth. In Tables 4.5 and 4.7 we show both, DP and DPm.

The DP values in Tab.4.6 have been directly measured. In fact, the conversion values

Table 4.5: The integrated DPm of B2 sources. B2 1141+37, B2 1441+26 and B2 1455+28 have no jet. The jet side of Morganti et al. (1997a) is adopted.

B2 name	DPm_{int}	ΔDPm_{int}	Jet side	DPm_j	ΔDPm_j	DPm_{cj}	ΔDPm_{cj}
0034+25	0.11	0.28	E	0.35	0.19	-0.14	0.25
0755+37	0.11	0.26	E	0.19	0.24	0.02	0.25
0828+32	0.08	0.29	SW	0.07	0.27	0.08	0.31
0836+29	0.02	0.46	N	-0.01	0.56	0.18	0.33
1141+37	0.00	0.21	NE?	-0.03	0.14	0.12	0.23
1243+26	0.09	0.26	N	0.01	0.19	0.22	0.27
1316+29	0.08	0.27	E	0.10	0.26	0.08	0.21
1357+28	0.23	0.25	N	0.19	0.22	0.38	0.23
1422+26	0.14	0.25	W	0.08	0.19	0.24	0.26
1441+26	0.17	0.19	W?	0.11	0.21	0.18	0.18
1455+28	0.23	0.23	N?	0.21	0.22	0.26	0.24
1528+29	0.14	0.20	NE	0.15	0.19	0.14	0.20
1643+27	0.27	0.20	N	0.18	0.18	0.33	0.20
1658+30	0.18	0.20	SW	0.06	0.13	0.30	0.21

are more reliable than the direct DP measure. The reason is that depolarization has a finite value in DP between 0 to 1, but re-polarization has infinite values, from 1 to ∞. Therefore, the pixel integration of DP is not a promising practise. In 0828+32, 0836+29 and 1141+37, this problem is especially important. The last two columns in Table 4.8 are the numbers of field reversals in a lobe. The numbers will be very sensitive to the angular resolution.

Our newly estimated DP (and DPm) is to mainly probe the foreground magneto-ionic medium. Except for B2 0034+25 at [0.5, 1.3], the depolarization asymmetry is in general more pronounced in our new estimate than in Morganti et al. (1997a). Fig. 4.23 conveys how patchy the DP distributions in the lobes on the jet- and counterjet-side lobes are. The Laing-Garrington effect exists in B2 sources at low frequencies. Our new and statistically more reliable DP shows this effect more clearly than in the past. The integrated results are summarized in Tab. 4.7.

In the case of B2 0034+25 and B2 0836+29, which are wide-angle-tailed (WAT) sources, their opposite lobes reside in quite different environments, which cannot be due to King-profile type distributions of X-ray clusters; interaction with their environment seems to be important. In general, a DP asymmetry is visible in the sample. The distribution ofΔDP, which indicates the 'patchiness' of the DP structure, is asymmetric. The DP of the lobes on the jet-side is more patchy than that on the counterjet-side. Two sources which do not follow the general trends are WAT sources.

Rotation Measure data

In Tab. 4.8, the integrated RM properties of 14 B2 radio galaxies are summarized. The last two columns in Table 4.8 denote the number of field reversals in a lobe. These numbers are very sensitive to the angluar resolution. The sample includes the six B2 radio galaxies discussed in the previous section. In spite of the differences in the resolution and the frequency range used, the RM values estimated here are in good agreement. Fig. 4.7 shows that the RM of each B2 radio galaxy covers a very narrow range. Only B2 0828+32 shows signs of an ambiguity. At higher frequencies, the RM of B2 0828+32

Table 4.6: The integrated DP of B2 sources, measured

B2 name	DP_{int}	ΔDP_{int}	DP_j	ΔDP_j	DP_{cj}	ΔDP_{cj}
0034+25	0.97	0.75	0.56	0.36	2.72	0.62
0755+37	0.92	0.71	0.78	0.51	1.10	0.86
0828+32	1.08	1.01	1.14	1.23	1.01	0.62
0836+29	2.07	3.05	4.70	4.45	1.00	0.99
1141+37	1.10	0.50	1.11	0.34	1.10	0.58
1243+26	0.95	0.55	1.06	0.49	0.74	0.50
1316+29	0.98	0.53	1.00	0.59	0.97	0.39
1357+28	0.71	0.40	0.75	0.41	0.50	0.32
1422+26	0.85	0.49	0.92	0.43	0.68	0.41
1441+26	0.76	0.30	0.86	0.32	0.73	0.28
1455+28	0.69	0.35	0.71	0.34	0.66	0.36
1528+29	0.81	0.35	0.79	0.36	0.82	0.35
1643+27	0.62	0.29	0.75	0.31	0.54	0.26
1658+30	0.75	0.31	0.90	0.24	0.59	0.30

Table 4.7: The integrated DP of B2 sources, computed from DPm

B2 name	DP_{int}	ΔDP_{int}	DP_j	ΔDP_j	DP_{cj}	ΔDP_{cj}
0034+25	0.80	0.56	0.48	0.68	1.33	0.60
0755+37	0.80	0.59	0.68	0.61	0.96	0.60
0828+32	0.85	0.55	0.87	0.57	0.85	0.53
0836+29	0.96	0.37	1.02	0.28	0.69	0.50
1141+37	1.00	0.65	1.06	0.75	0.79	0.63
1243+26	0.83	0.59	0.98	0.68	0.64	0.57
1316+29	0.85	0.57	0.82	0.59	0.85	0.65
1357+28	0.63	0.60	0.68	0.64	0.45	0.63
1422+26	0.75	0.60	0.85	0.68	0.61	0.59
1441+26	0.71	0.68	0.80	0.65	0.69	0.69
1455+28	0.63	0.63	0.65	0.64	0.59	0.61
1528+29	0.75	0.67	0.74	0.68	0.75	0.67
1643+27	0.57	0.67	0.69	0.69	0.50	0.67
1658+30	0.69	0.67	0.89	0.77	0.54	0.65

Table 4.8: The integrated RM of 14 B2 radio galaxies

B2 name	$\overline{RM}$	ΔRM	RM_j	ΔRM_j	RM_{cj}	ΔRM_{cj}
0034+25	-41	4	-49	1	-48	1
0755+37	+15	9	+16	10	+14	7
0828+32	+38	10	+37	10	+31	25
0836+29	+26	12	+30	6	+25	14
1141+37	+4	6	+3	3	+5	6
1243+26	+18	10	+14	7	+22	12
1316+29	+11	6	+11	6	+11	5
1357+28	+17	18	+19	9	+1	17
1422+26	+15	12	+16	11	+13	13
1441+26	+16	4	+17	4	+15	3
1455+28	+1	12	0	11	+3	13
1528+29	+11	6	+10	6	+11	5
1643+27	+34	7	+30	6	+39	5
1658+30	+25	6	+22	7	+26	5

(Fig. 4.2[a]) has indeed a broader distribution than any other source in the sample.

4.3 The individual sources

B2 0034+25

B2 0034+25 is a wide-angle-tailed (WAT) source. The magnetic field is parallel to the total intensity ridge (Fig. 4.8). In this source, the core-to-lobe contrast is more pronounced than the lobe-to-lobe asymmetry.

B2 0755+37

Morganti et al. (1997a) reported that the integrated RM of B2 0755+37 calculated from three frequencies (2.7, 4.9 and 10.8 GHz) exceeds the ambiguity of our $RM_{1.6}^{4.9}$, with $RM_{int} = -70$ rad m^{-2}. The magnetic field morphology shown in Fig. 4.9[c] looks rather messy. The DP and RM structures are patchy (Fig. 4.9[a],[b]). If $\Delta RM = 10$ rad m^{-2} in Tab. 4.8 is real, the RM patchy structure can be real, but not as a result of a high RM.

B2 0828+32

The magnetic field direction shown in Fig. 4.10[c] is almost identical to that in Fig. 4.5. The DP and RM structures are patchy (Fig. 4.10[a],[b]).

B2 0836+29

B2 0836+29 is a WAT source. Similar to B2 0034+25, the fractional polarization in the lobes is very low. The magnetic field in the southern lobe is parallel to the total intensity ridge. The same trend is seen in Fig. 4.5.

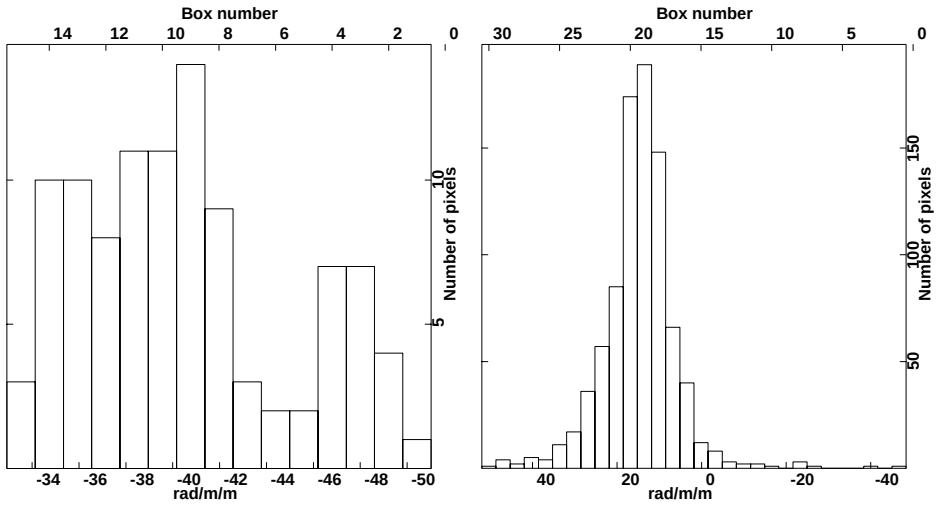

(a) B2 0034+25 (b) B2 0755+37

Figure 4.7: RM distribution of the 14 B2 sources. The histograms exhibit the $RM_{1.6}^{4.9}$ distribution in the 14 B2 sources.

B2 1141+37

B2 1141+37 is FR II type in morphology. DP and RM structure are smoothed (Fig. 4.12[a],[b]). The magnetic field in Fig. 4.12[c] is almost identical to the magnetic field in Fig. 4.5.

B2 1243+26

The spot at $\alpha = 12^h43^m52\overset{s}{.}8$ and $\delta = 26°42'32''$ is known not to belong to B2 1243+26 (Morganti et al., 1997a). This core is not linearly polarized. Therefore, this radio core was automatically excluded in the computation of the RM and DP maps (see Fig. 4.13[a][b]). The shape of B2 1243+26 is complex. DP asymmetry is obvious, also in ΔRM. As the result, the RM-DP diagram (Fig. 4.13[d]), shows an exemplary trend: the 5 most strongly polarized points have a much smaller dispersion in RM than the 5 most strongly depolarized ones. Despite the low integrated RM reported by (Morganti et al., 1997a), the magnetic field directions in Fig. 4.13[c] look rather messy.

B2 1316+29

B2 1316+29 has an S-shaped, bent two-sided jet. Fig. 4.14[a] shows the re-polarized core. The DP and RM distributions of the two lobes are patchy. The magnetic field structure in Fig. 4.14[c] is identical to that in Fig. 4.5. However, the RM - DP diagram does not exhibit any clear correlation (see Fig. 4.14[d]). The scalelength of the Faraday medium must lie between the spatial resolutions embraced by the observations at the low and high frequencies involved here.

B2 1357+28

B2 1357+28 exhibits an exemplary Laing-Garrington effect. The maps of DP and RM exhibit a smooth and asymmetric structure (Fig. 4.15[a] and [b)]. The magnetic field

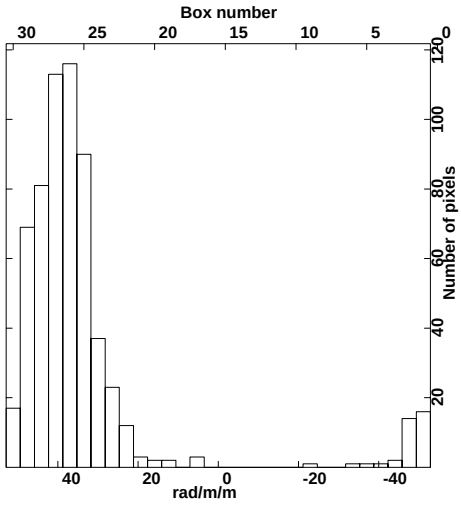

(c) B2 0828+32

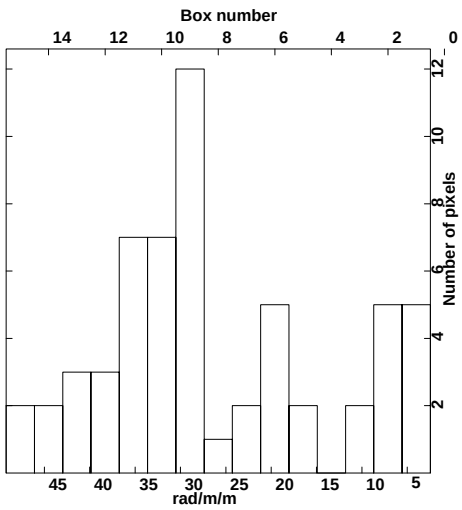

(d) B2 0836+29

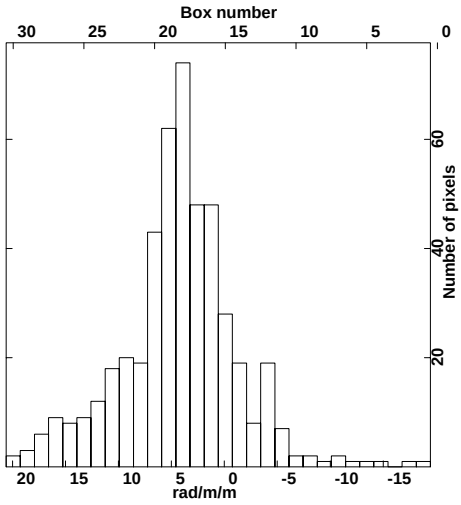

(e) B2 1141+37

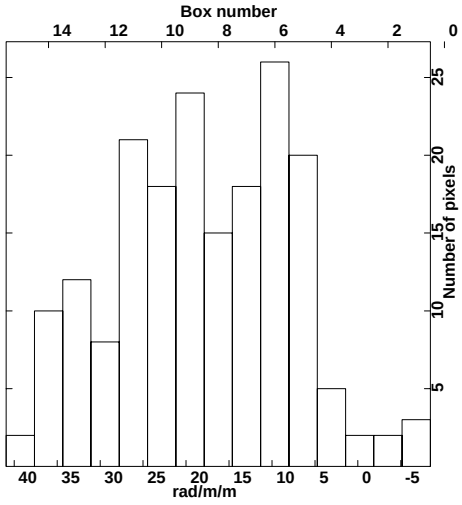

(f) B2 1243+26

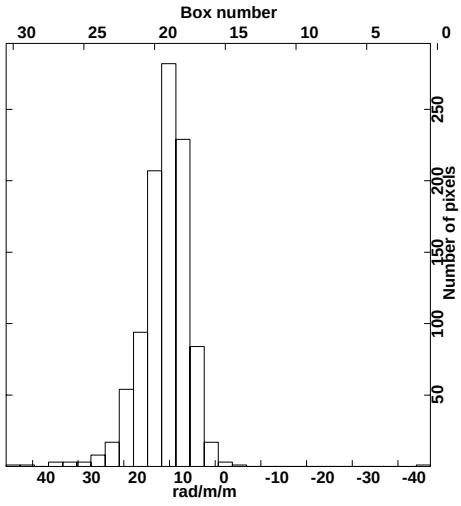

(g) B2 1316+29

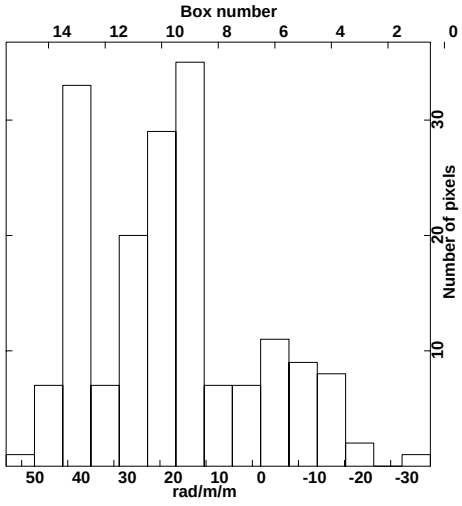

(h) B2 1357+28

Figure 4.7: RM histograms of the 14 B2 sources, continued.

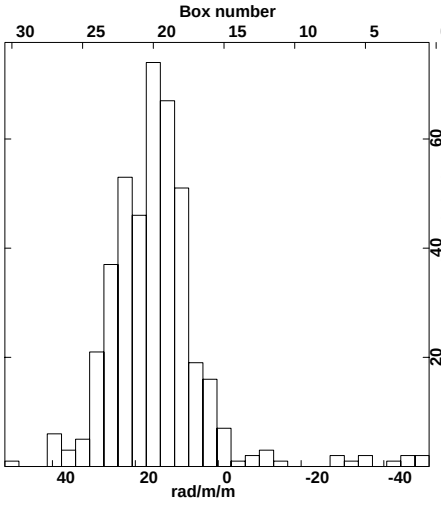

(i) B2 1422+26

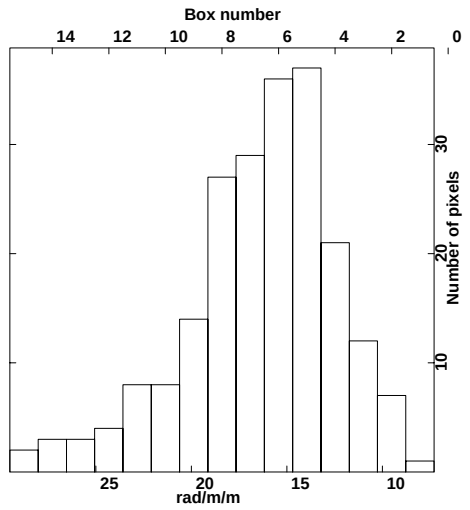

(j) B2 1441+26

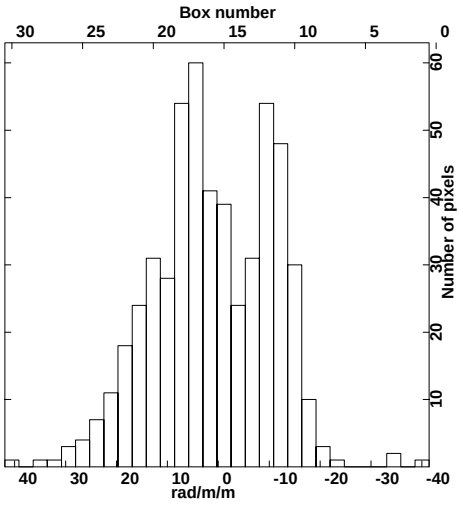

(k) B2 1455+28

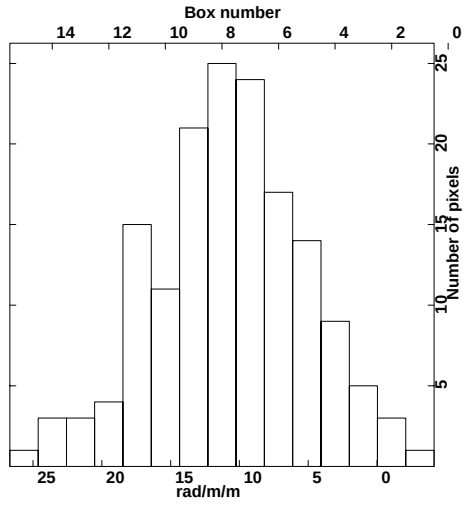

(l) B2 1528+29

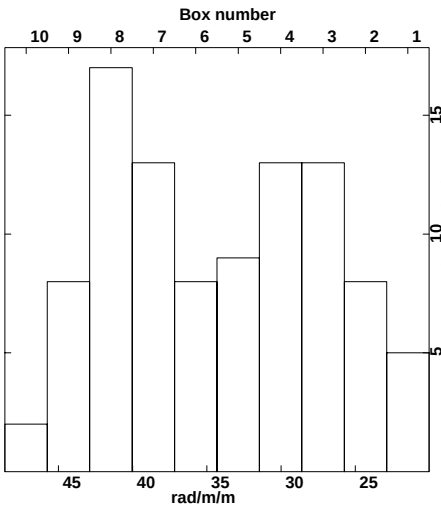

(m) B2 1643+27

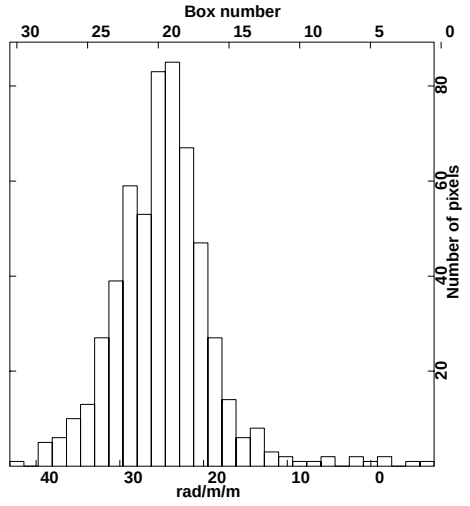

(n) B2 1658+30

Figure 4.7: RM histograms of the 14 B2 sources, cont.

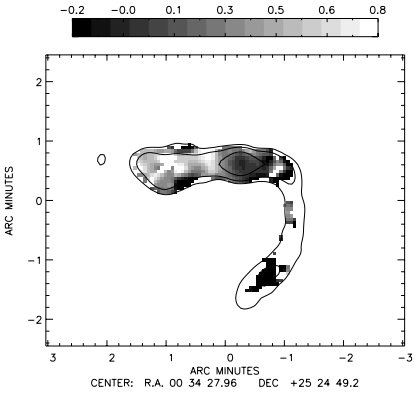

(a) DPm map

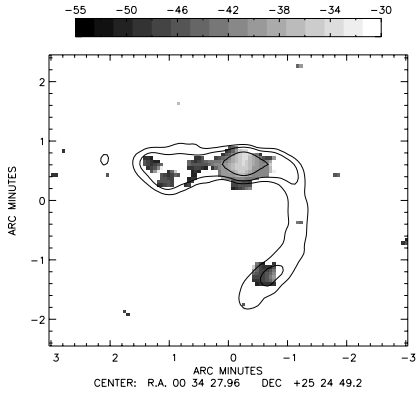

(b) RM map

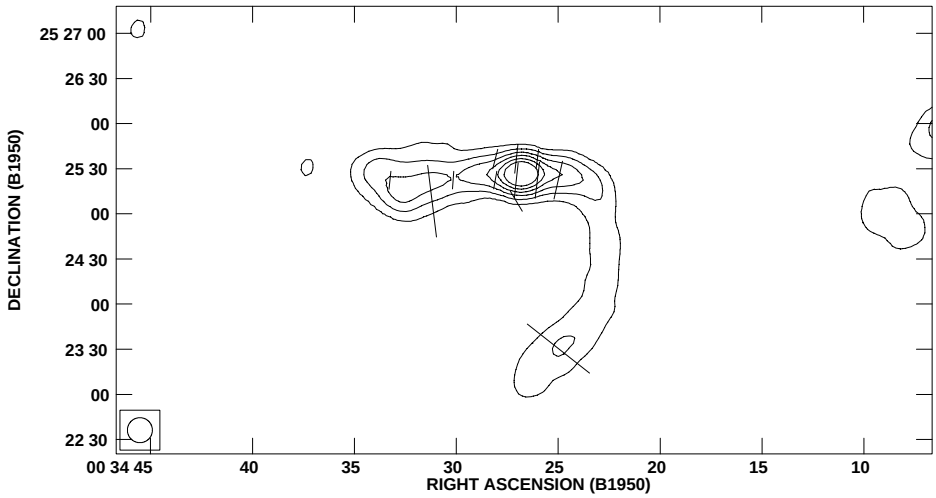

(c) polarization angle at $\lambda = 0$angle

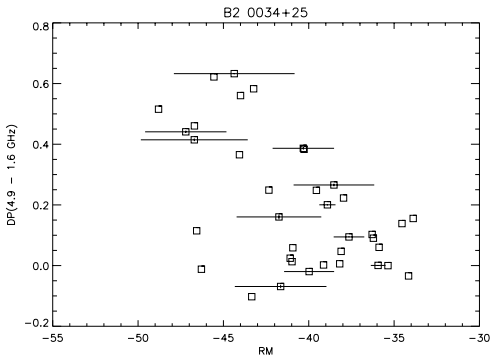

(d) RM-DPm

Figure 4.8: B2 0034+25. In [c] the contours represent the total intensity at 4.9 GHz. The contour lines are 3, 12, 27, 48 and $75\sigma_I$. The direction of the vectors represents E-vectors at λ_0. The length of the vectors indicates DP, where $DP = 1$ corresponds to 0.′5.

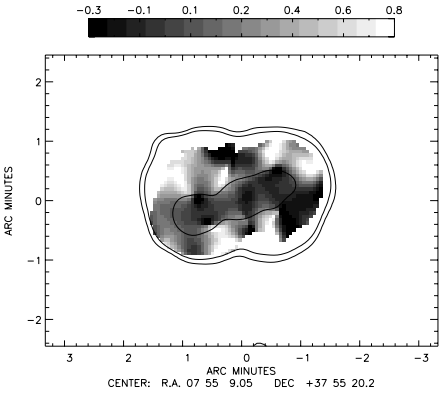

(a) DPm map

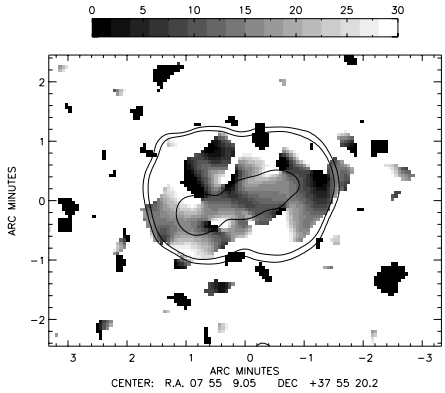

(b) RM map

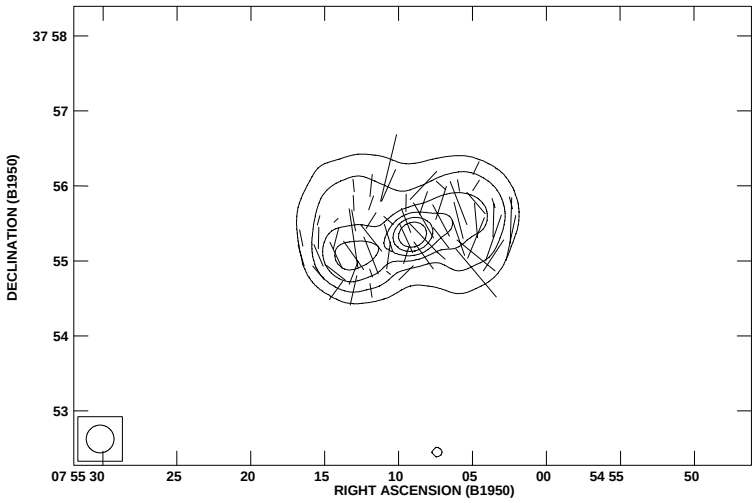

(c) polarization angle at $\lambda = 0$

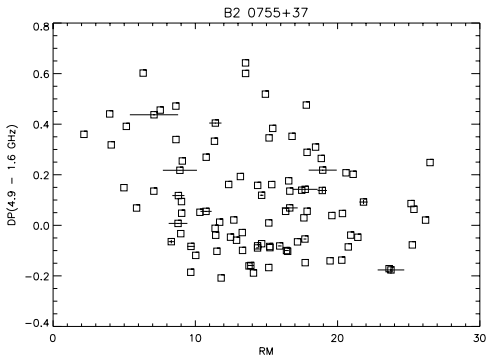

(d) RM-DPm

Figure 4.9: B2 0755+37. The layout is the same as in Fig. 4.8.

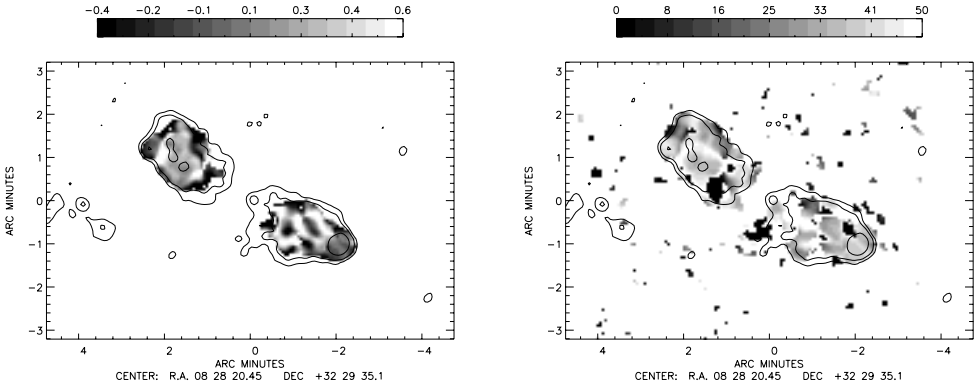

(a) DPm map

(b) RM map

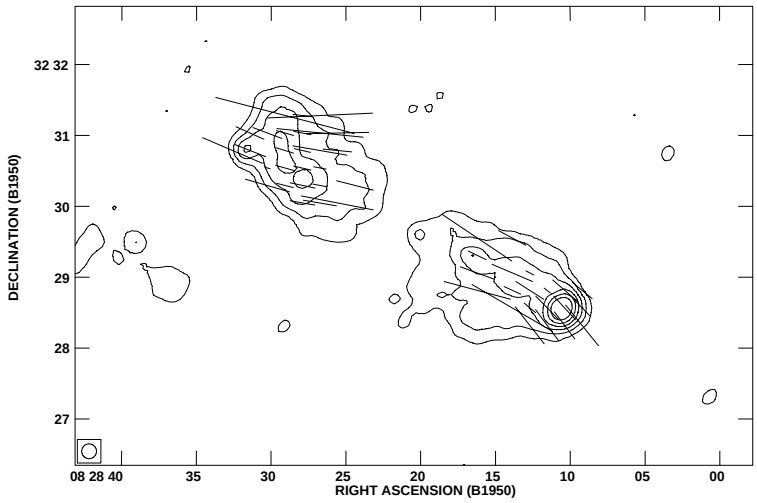

(c) polarization angle at $\lambda = 0$

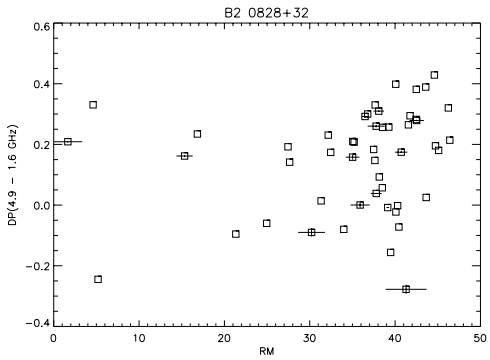

(d) RM-DPm

Figure 4.10: B2 0828+32. The layout is the same as in Fig. 4.8.

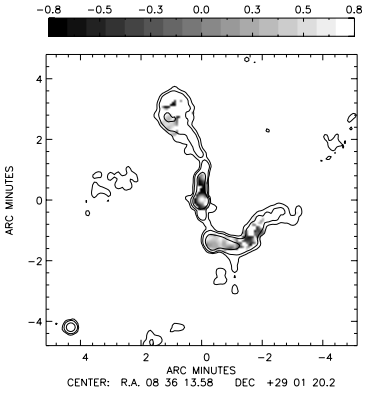

(a) DPm map

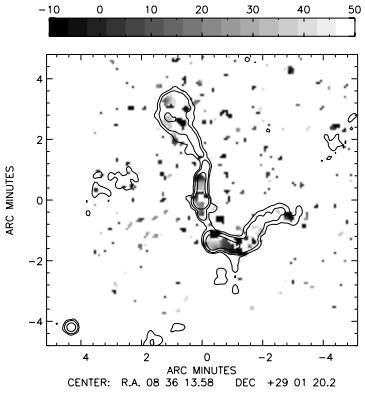

(b) RM map

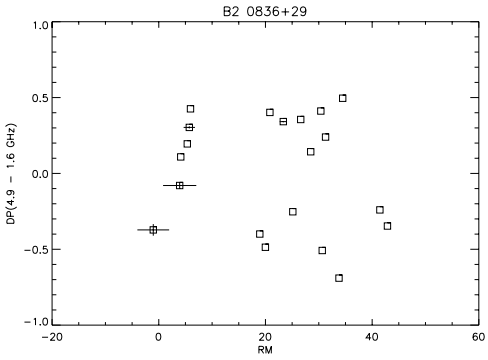

(d) RM-DPm

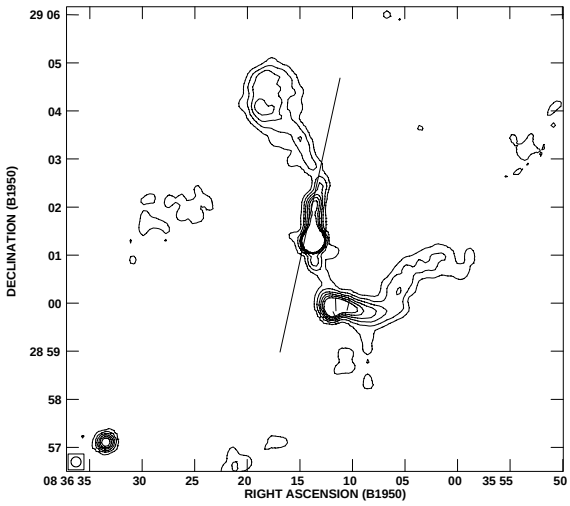

(c) polarization angle at $\lambda = 0$

Figure 4.11: B2 0836+29. The layout is the same as in Fig. 4.8.

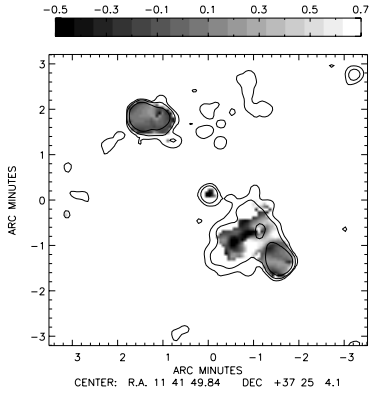

(a) DPm map

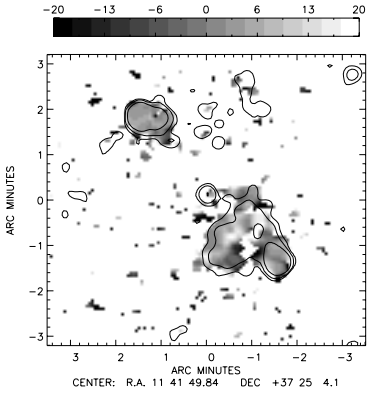

(b) RM map

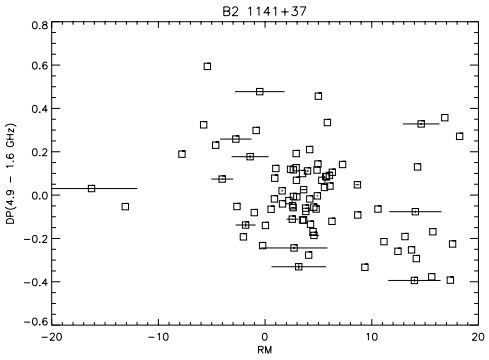

(d) RM-DPm

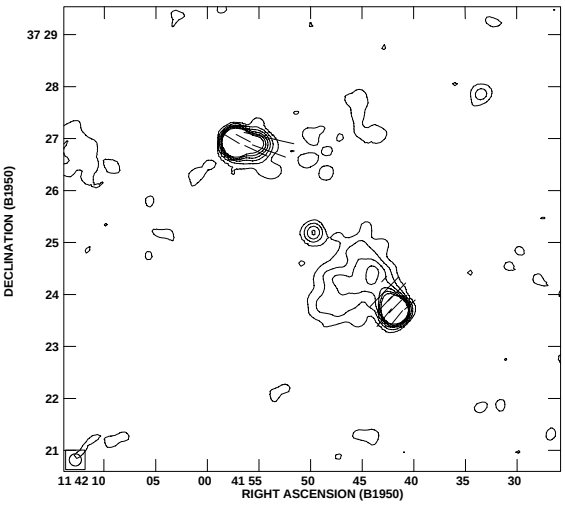

(c) polarization angle at $\lambda = 0$

Figure 4.12: B2 1141+37. The layout is the same as in Fig. 4.8.

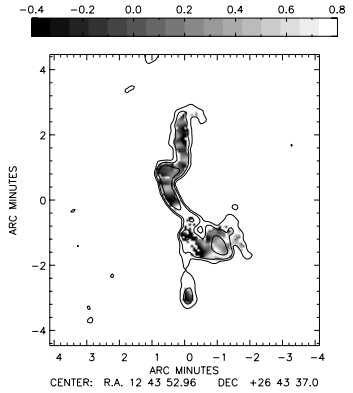

(a) DPm map

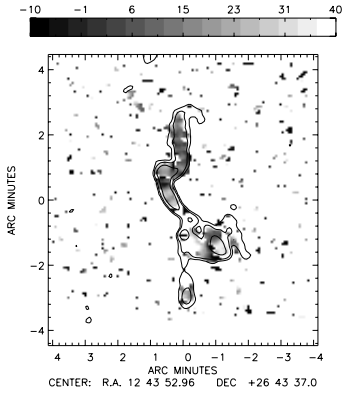

(b) RM map

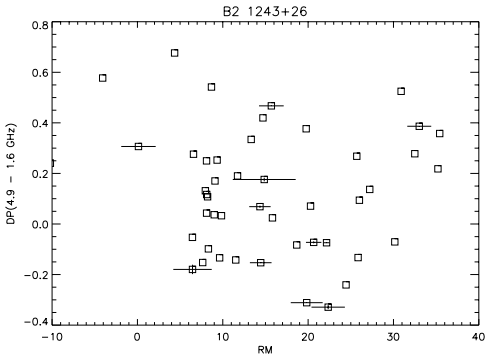

(d) RM-DPm

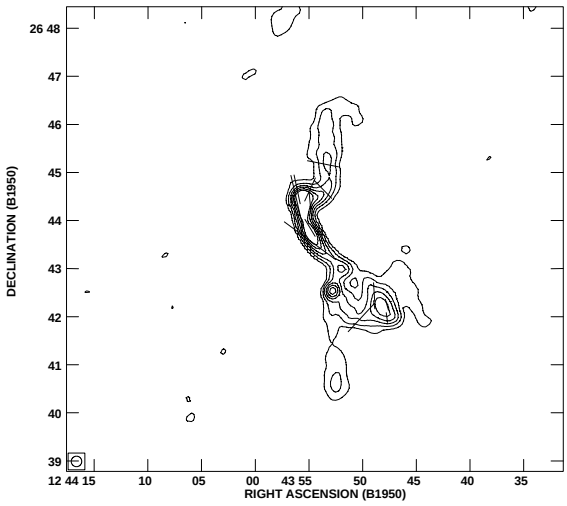

(c) polarization angle at $\lambda = 0$

Figure 4.13: B2 1243+26. The layout is the same as in Fig. 4.8.

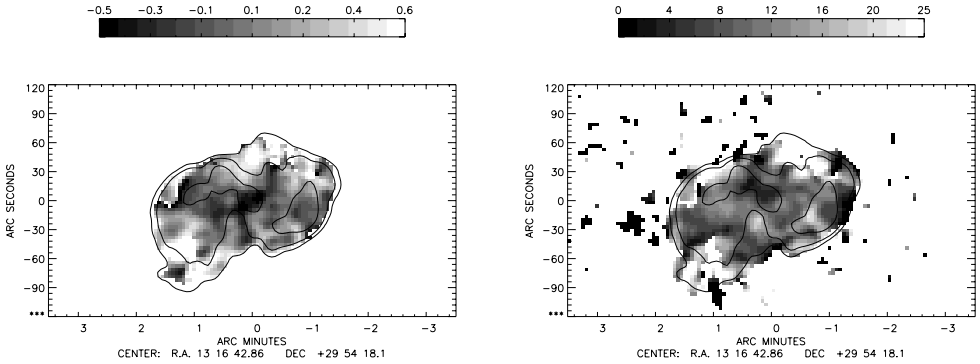

(a) DPm map

(b) RM map

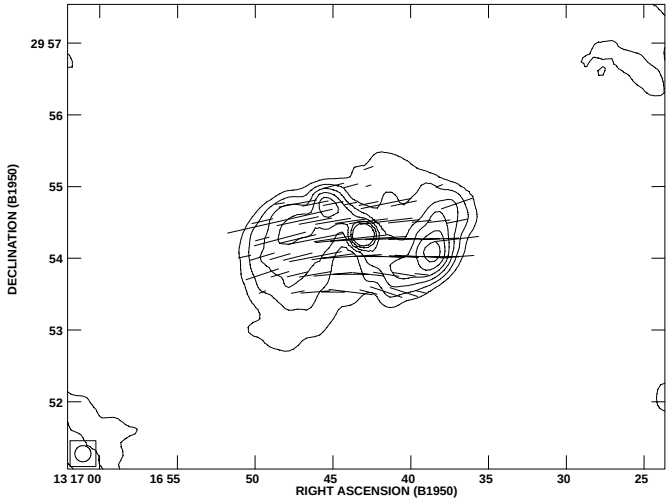

(c) polarization angle at $\lambda = 0$

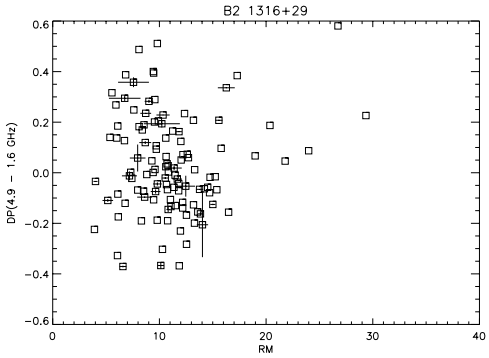

(d) RM-DPm

Figure 4.14: B2 1316+29. The layout is the same as in Fig. 4.8.

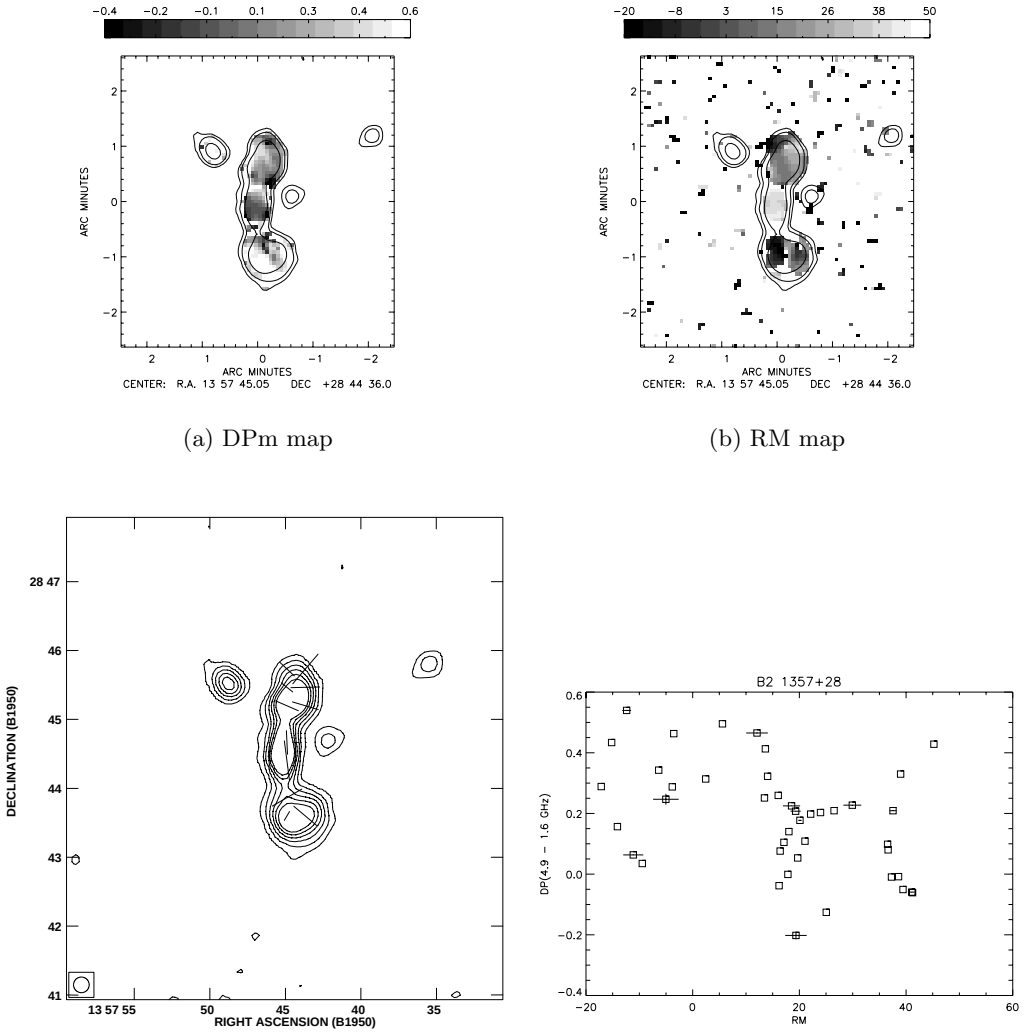

(a) DPm map

(b) RM map

(c) polarization angle at $\lambda = 0$

(d) RM-DPm

Figure 4.15: B2 1357+28. The layout is the same as in Fig. 4.8.

structure in Fig. 4.15[c] looks chaotic. The RM - DP diagram (Fig. 4.15[d]), exhibits a rather clear ΔRM - DP correlation Garrington & Conway (1991). The RM scalelength of B2 1357+28 is probably smaller than the resolution used here. If this is true, the RM scalelength varies from source to source, as B2 1357+28 is at an intermediate distance.

B2 1422+26

Tha maps of DP and RM of B2 1422+26 have a patchy structure without any clear asymmetry (Fig. 4.16[a] and [b]). The magnetic field structure in Fig. 4.16[c] is identical to that in Fig. 4.5. The RM - DP diagram (Fig. 4.16[d]) does not show any clear trend.

B2 1441+26

The results of Morganti et al. (1997a) imply that their integrated RM based on three frequencies (2.7 , 4.9 and 10.8 GHz) of B2 1441+26 exceeds the ambiguity of our $RM^{4.9}_{1.6}$,

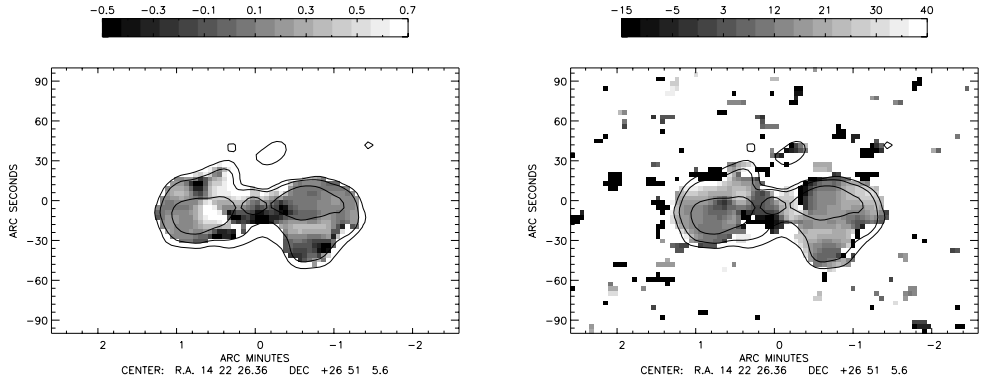

(a) DPm map

(b) RM map

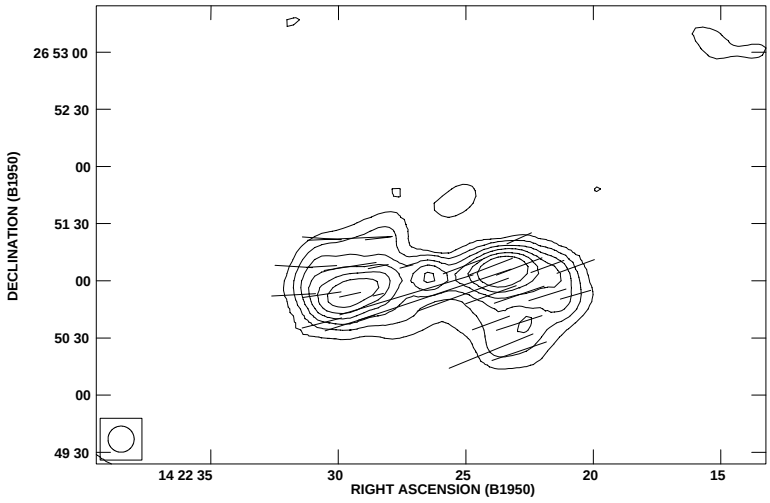

(c) polarization angle at $\lambda = 0$

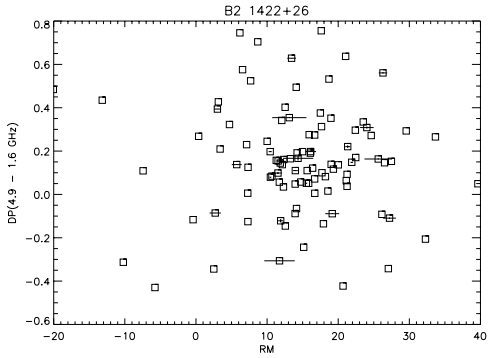

(d) RM-DPm

Figure 4.16: B2 1422+26. The layout is the same as in Fig. 4.8.

with $RM_{int} = +87$ rad m^{-2}. The sizes of the areas of the W (jet-side) and the E lobe are different. In the E lobe (which subtends the larger area), a patchy structure in the DP and RM maps is obvious. This is less clear for the W lobe, but the area is smaller than a patch 'cell' in the E lobe. Therefore, this is not conclusive (Fig. 4.17[a] and [b]). The magnetic field structure of B2 1441+26 looks rather messy (Fig. 4.17[c]). This is probably due to the high RM.

B2 1455+28

B2 1141+37 has a typical FR II morphology with advancing hotspots. The maps of DP and RM of B2 1455+28 have a patchy structure and are symmetric (Fig. 4.18[a] and [b]). The magnetic field structure is core-symmetric, but not parallel or perpendicular to the total intensity ridge (Fig.4.18[c]). In the RM - DP diagram, a correlation ΔRM - DP is seen between the lowest 5 and the highest 5 DP points (Fig. 4.18[d]). The region of high DP is well correlated with that of high $|RM|$.

B2 1528+29

No lobe-to-lobe asymmetry is seen in the DP and RM maps of B2 1528+2 (Fig. 4.19[a] and [b]). A patchy structure is seen in DP and RM. At the both extremities, the magnetic field is tangential. In the SW back lobe, the magnetic field is oblique as in B2 1455+28, but not symmetric in this case (Fig. 4.19[c]). A correlation of ΔRM - DP is seen in the extreme DPs (Fig. 4.19[d]).

B2 1643+27

The maps of DP and RM of B2 1643+27 exhibit an asymmetry in Fig. 4.20[a] and [b]. ΔRM is symmetric (see Tab.4.8). The magnetic field is oblique at the source extremity and perpendicular to the major axis in the inner part (Fig. 4.20[c]). The asymmetries in DP and RM cause a linear trend in the DP - RM diagram (Fig. 4.20[d]).

B2 1658+30

A DP asymmetry is already seen in the DP map (Fig. 4.21[a]). The SW lobe on the jet side is slightly depolarized and that on the counter-jet side is strongly depolarized, with a patchy structure. In contrast to that, the maps of RM and ΔRM do not show any clear asymmetry, but rather a patchy pattern (Fig. 4.21[b]; see also Tab. 4.8). Different from the other two 'fat doubles' in the sample, the magnetic field well follows the source structure, in that it is perpendicular to the major axis or the total intensity ridge in Fig. 4.21[c]. Despite the clear DP asymmetry, the RM - DP diagram does not exhibit any correlation, due to the lack of the ΔRM asymmetry.

4.3.1 DP-RM correlation?

The trends in the sources of the sample are rather varying. Even the sources which show morphological similarities, e.g. B2 0755+37 and B2 1658+30 or B2 1141+37 and B2 1455+30 or B2 1357+28 and B2 1643+27, show little resemblance in their DP and RM maps.

However, our pixel-to-pixel estimate of the depolarization measure confirms that the Laing-Garrington effect in the B2 sample is indeed visible (see Fig. 4.22). The solid line in the diagram indicates $DP_j = DP_{cj}$. On the whole, the new estimate indicates

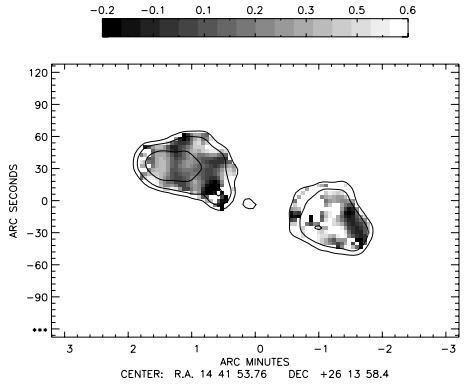

(a) DPm map

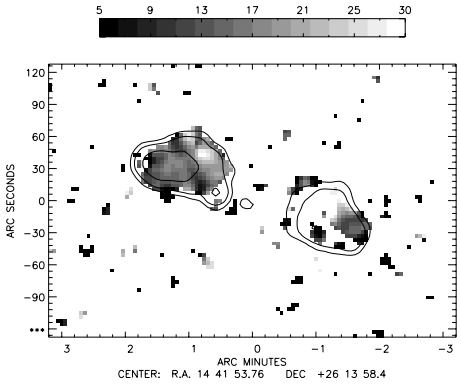

(b) RM map

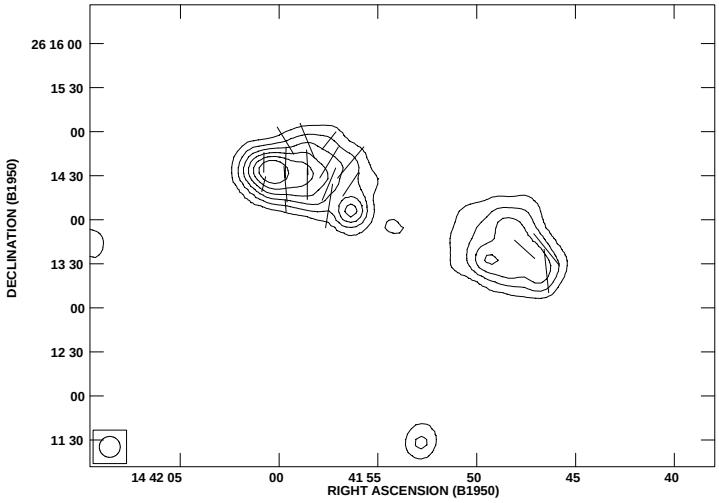

(c) polarization angle at $\lambda = 0$

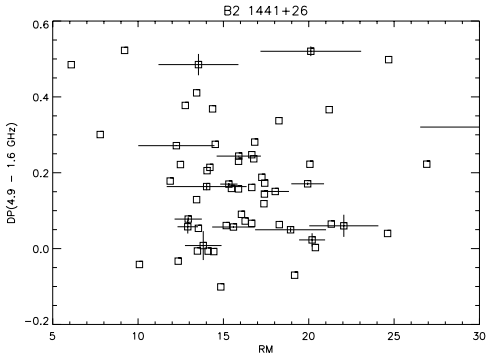

(d) RM-DPm

Figure 4.17: B2 1441+26. The layout is the same as in Fig. 4.8.

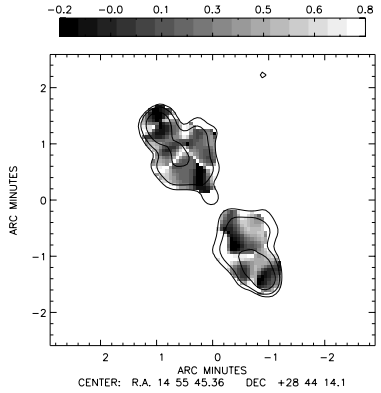

(a) DPm map

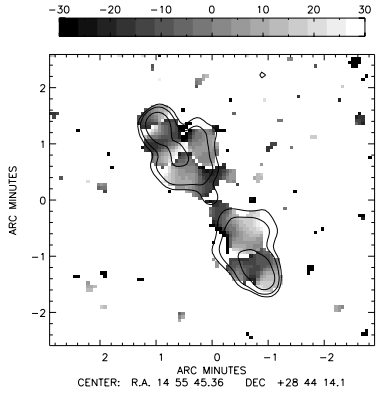

(b) RM map

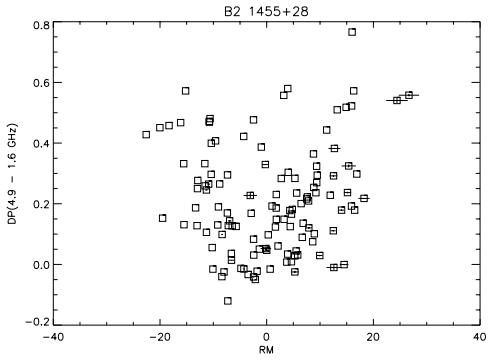

(d) RM-DPm

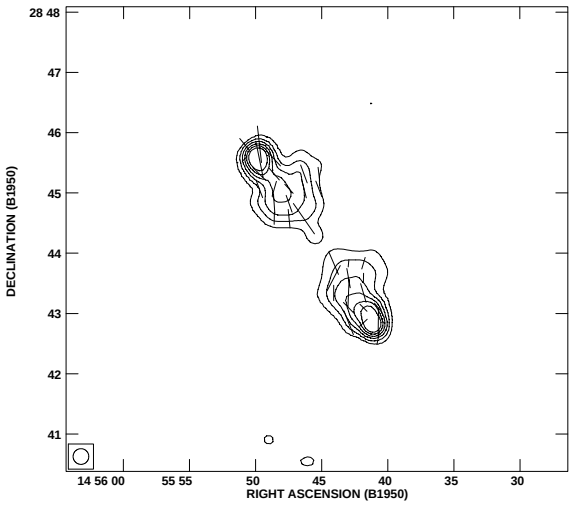

(c) polarization angle at $\lambda = 0$

Figure 4.18: B2 1455+28. The layout is the same as in Fig. 4.8.

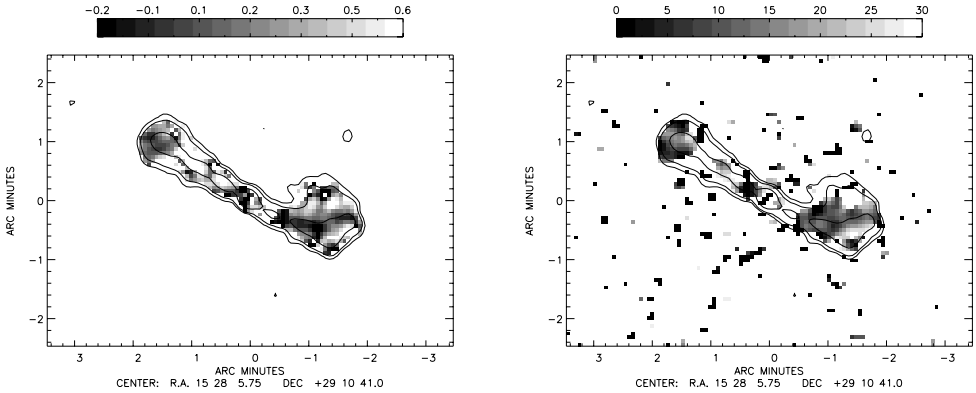

(a) DPm map

(b) RM map

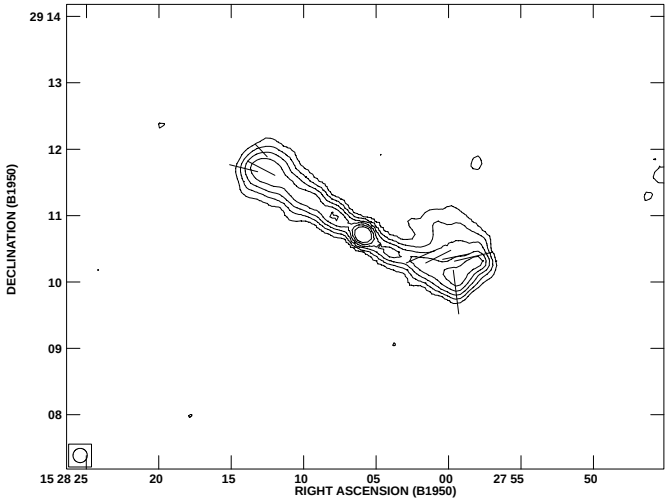

(c) polarization angle at $\lambda = 0$

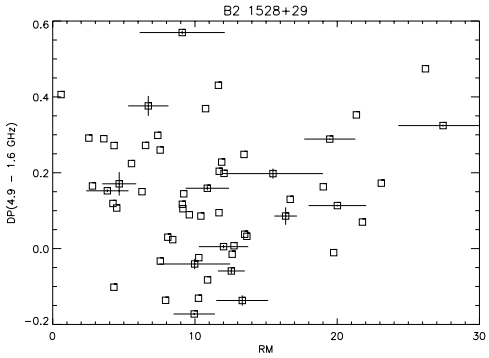

(d) RM-DPm

Figure 4.19: B2 1528+29. The layout is the same as in Fig. 4.8.

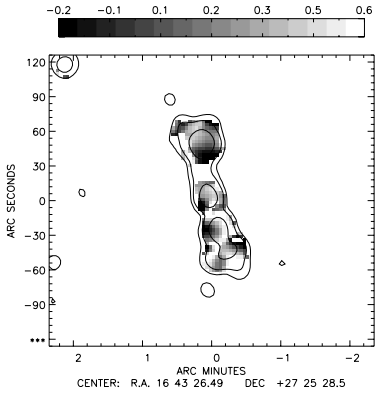

(a) DPm map

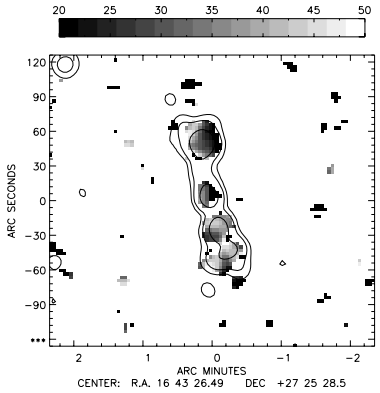

(b) RM map

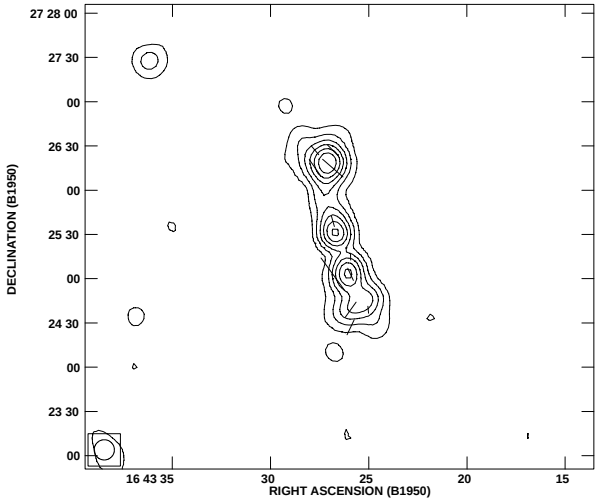

(c) polarization angle at $\lambda = 0$

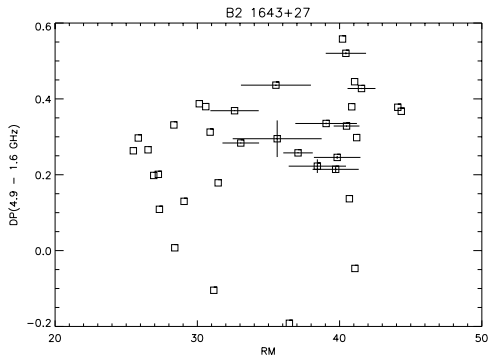

(d) RM-DPm

Figure 4.20: B2 1643+27. The layout is the same as in Fig. 4.8.

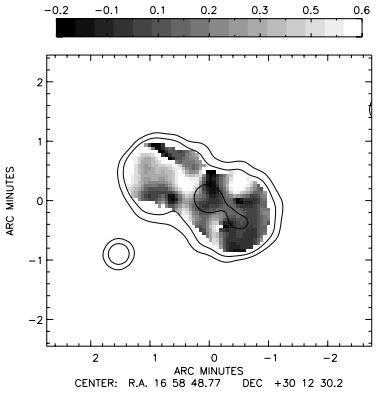

(a) DPm map

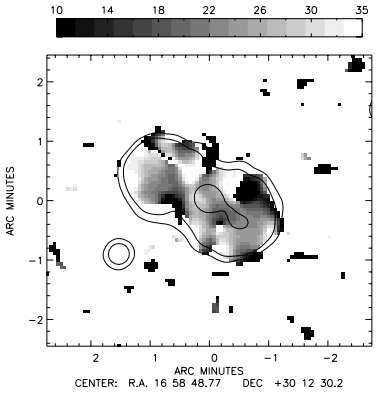

(b) RM map

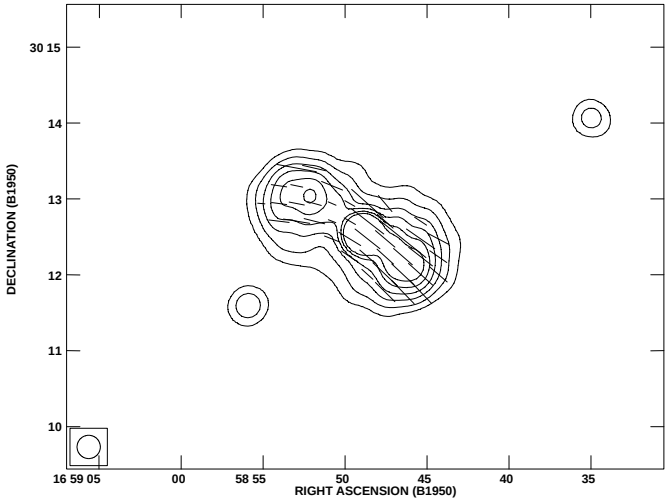

(c) polarization angle at $\lambda = 0$

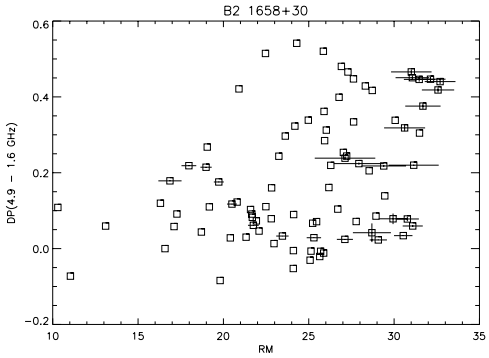

(d) RM-DPm

Figure 4.21: B2 1658+30. The layout is the same as in Fig. 4.8.

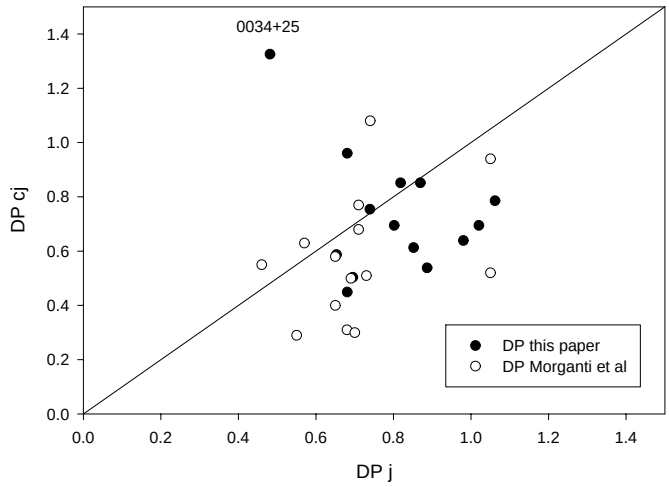

Figure 4.22: DP_j - DP_{cj} diagram of the 14 B2 sources. The two results are compared. The solid line indicates symmetric depolarization. The filled circles were obtained from $m = \Sigma(P/I)$. The open circles were obtained from $m = \Sigma P/\Sigma I$.

rather little depolarization. This is because our estimate is a pixel-to-pixel estimate and therefore, depolarized points are excluded this way which are included in the integrated estimate. The WAT sources, B2 0034+25 and B2 0836+29 show an 'anomaly' in the DP - ΔDP plane.

Fig. 4.23 shows that the DP patterns of the counterjet-side are slightly smoother than the those on the jet-side. This can be understood in the following way: the polarized radiation from the counterjet-side of the radio galaxies travels through more magneto-ionic cells than that of the jet-side. The distribution of the most probable DP values of the counterjet-side is smoother. On the jet-side, with the radiation traveling through fewer cells, the DP value more strongly depends on the property of each cell that the radiation has to pass.

In Fig. 4.24, we check if there is any intrinsic RM asymmetry between the jet-side and counter-jet side lobe. The dashed line is that of $RM_j = RM_{cj}$. The solid line is the simple linear least-squares fit to the data. The results show that the RM-related Faraday medium is quite symmetrically distributed in the sample sources. The RM is quite evenly distributed in both lobes in terms of $\overline{RM}$ (Fig.4.24). The distribution of ΔRM (Fig. 4.25), is more interesting than that of $\overline{RM}$, since a $ln(DP) \propto \Delta RM^2$ relation is expected in the presence of a Laing-Garrington effect (e.g. Garrington & Conway (1991); Johnson et al. (1995)). Fig. 4.25 shows the result. In Fig. 4.25, we further check the ΔRM asymmetry which has a more important meaning than RM with respect to the DP asymmetry ((Garrington & Conway, 1991; Johnson et al., 1995)). The dashed line represents $\Delta RM_j = \Delta RM_{cj}$. The solid line is the simple linear least-squares fit to the data.

We can see different trends etween the high-$\Delta RM > 7$ rad m^{-2}and the low-$\Delta RM \leq 7$ rad m^{-2} sources. In the low-ΔRM sources, the distribution of ΔRM is rather symmetric. In the high-ΔRM sources, the counterjet side lobes have definitely higher ΔRM

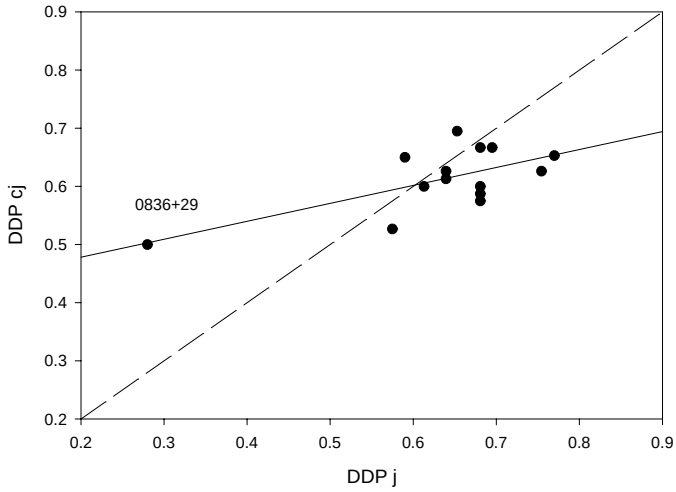

Figure 4.23: ΔDP_j - ΔDP_{cj} diagram of the 14 B2 sources. The dispersion in DP is marginally larger on the jet side. The dashed line indicates $\Delta DP_j = \Delta DP_{cj}$.

values. Fig. 4.26 exhibits the DP-to-ΔRM ratio, the least-squares fit indicates only a weak correlation between them.

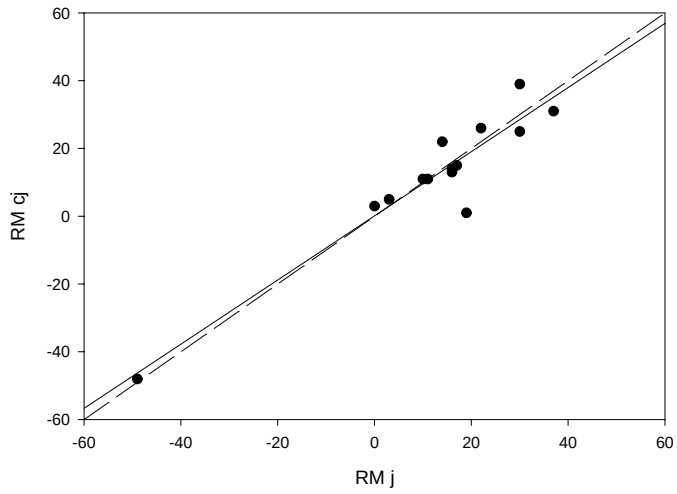

Figure 4.24: RM_j-RM_{cj} diagram of the 14 B2 sources. The dashed line indicates $RM_j = RM_{cj}$. The solid line is the simple least-squares fit to the points.

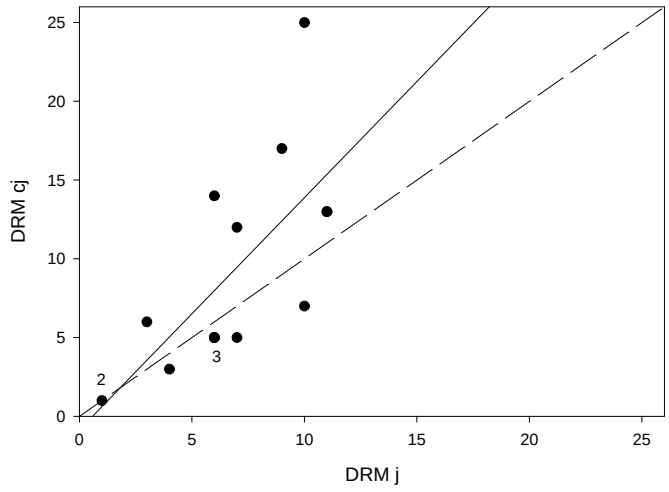

Figure 4.25: ΔRM_j - ΔRM_{cj} diagram. The RM dispersion is larger on the counterjet side. The dashed line indicates $\Delta RM_j = \Delta RM_{cj}$. The solid line is the simple least-squares fit to the points. Although $\overline{RM}$ is quite symmetric (Fig. 4.24) ΔRM becomes asymmetric. The trend becomes clear with increasing ΔRM.

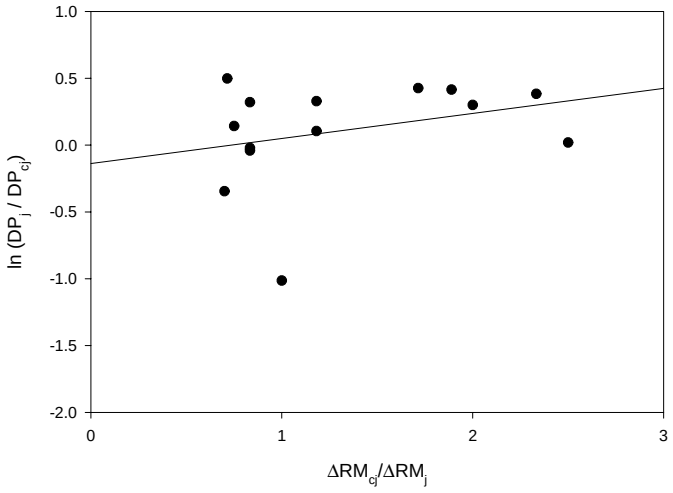

Figure 4.26: ΔRM - DP diagram. The solid line is the least-squares fit to the data. On the whole, there is weak correlation such that the counter-jet side is more depolarized and has a larger ΔRM.

Chapter 5

Discovery of high rotation measures in GRGs

5.1 Introduction

Through decades of observations of radio galaxies, it has been shown that the Faraday rotation of their polarization angles follows well a λ^2 relation throughout the radio regime, i.e.

$\Delta\chi \propto \lambda^{-2}$,

while its fractional polarization profile does not show any significant variation in the low-frequency regime. This indicates that the Faraday (magneto-ionic) medium and the relativistic electrons of radio galaxies (RGs) are spatially separated. Therefore, most of the detected Faraday rotation comes from the foreground medium. Since RGs are linearly polarized, their Rotation Measure (RM) is a useful tool to estimate the physical properties of their foreground medium. In order to yield a measurable RM, the foreground medium must consist of thermal electrons and ions. Electron-positron pairs must be ruled out, since the magnetized positrons are as effective as the electrons as a Faraday rotator, but in an opposite direction. Therefore, any Faraday rotation would be largely cancelled out.

Recently, carefully planned systematic studies by Clarke et al. (2001) and Eilek & Owen (2002) showed evidence for high RMs in the cores of clusters of galaxies. These results indicate that cooling flows in the cluster cores amplify the magnetic field strength in the Faraday medium, although the cooling flows themselves usually disappear through the heating by RGs. The fact that the field RGs exhibit Faraday rotation at a level of RM ~ 15 rad m^{-2} only, strongly supports the amplification theory Clarke et al. (2001). Eilek & Owen (2002) estimate that the energy contained in RGs is sufficient to explain the total magnetic field energy of the cluster core RGs, too. This energy budget must be the same for the field RGs. Therefore, this internal energy of RGs may not contribute significantly to the field amplification in the RG stage.

This situation may be different in GRGs which must have been normal RGs in past. During the expansion phase from RGs to GRGs, most of the internal energy of the pre-expansion stage of RGs will be released in the form of kinetic energy. A further interesting point of the expansion is the longer dissipation time through the expanded field. The (ohmic) dissipation time is related to the scale-length of the magnetic field, l_{RM} and the Alfven speed of the medium, v_A, $\tau_d \propto l_{RM}/v_A$. If the internal energy of RGs is released and transported to the environment and if τ_d is long enough, then the

Table 5.1: Mean RM and absolute mean RM of the GRGs. The values $\overline{RM_3}$ are the mean of the three nearest extragalactic objects found in Simard-Normandin et al. (1981).

Source	res. scale (kpc)	$\overline{RM}$	RM_{peak}	$\overline{RM_3}$
NGC 315	48	−225	−230	−53
DA 240	100	−135	+220/+140	−54
3C 236	261	+90	−160	+27
3C 326	256	−210	+55/+120	+38
NGC 6251	67	+180	−170/−260	−29

question may arise whether field RGs could possess high RMs. The study of the RM properties of GRGs will help to shed light on this question. We estimate the RM and its scale-length of five GRGs in this work.

5.2 Rotation measure data

We have compiled the rotation measure (RM) data of five GRGs. We have used measurements of the relevant Stokes parameters, I, Q, U at 10.6 and 4.8 GHz published by Mack et al. (1998), who obtained them with the Effelsberg 100-m telescope. The equation

$$RM = \Delta\chi/(\lambda_1^2 - \lambda_2^2)$$

indicates that the two-frequency estimate of RM has an ambiguity from −495 to +495 rad m^{-2}. Only RMs of RGs in cluster cores with strong X-ray cooling flows have higher RM values (Clarke et al., 2001; Eilek & Owen, 2002). The data reduction was done using the NRAO AIPS package and the IDL software. The polarization angles at each frequency were obtained with a 3σ cut in I and $\mathrm{I_p}\,(= \sqrt{U^2 + Q^2})$. In Tab. 5.1, we list the integrated estimates of the five GRGs. The $|\overline{RM}|$ of the GRGs clearly exceeds the $|RM_3|$ the mean of the three nearest extragalactic objects. That is the mean RMs of the GRGs exceed the 'field' RM (see Tab. 5.1) in all five GRGs. This indicates that the GRGs have systematically more foreground Faraday medium than the three nearest extragalactic objects. We report the discovery of high RMs in GRGs.

5.2.1 Correction for Galactic Faraday rotation

In order to correct the Galactic contribution to the RM, we have established and compared two correction methods. The first one includes a 'self controlled' term,

$$RM_1 = RM - \overline{RM}.$$

The second one is the classical method, namely,

$$RM_2 = RM - \frac{\overline{RM} + \overline{RM_3}}{2}.$$

The results are listed in Tab. 5.2. In RM_1, the whole $\overline{RM}$ is considered as the Galactic contribution. It is more natural to imagine that there is an intrinsic contribution to $\overline{RM}$ by our Galaxy. In RM_2, this idea is taken into consideration. Since the Galactic contribution towards the source of interest will be contained in $\overline{RM}$ of the source, rather

Table 5.2: Compiled physical parameters of the GRGs.

Source	RM_1	RM_2	L_{RM}(kpc)	$\overline{B_\parallel} \cdot n_e$ ($\mu G\, cm^{-3}$)
NGC 315	36	91	55	$2.0 \cdot 10^{-3}$
DA 240	42	122	110	$1.4 \cdot 10^{-3}$
3C 236	79	133	375	$4.4 \cdot 10^{-4}$
3C 326	45	42	1050	$4.9 \cdot 10^{-5}$
NGC 6251	36	91	70	$1.6 \cdot 10^{-3}$

than in the neighbouring values, we used a weighted mean between $\overline{RM}$ and the mean of three neighbouring measurements, $\overline{RM_3}$, as the most likely value for the source.

The scale length of the RM structure in Tab. 5.2, l_{RM}, was determined as follows. We estimated the total length of the RM structure, d_{RM}, which we divided by the number of field reversals, N_{RM}, along the major axis of GRGs. We then obtained $l_{RM} = d_{RM}/N_{RM}$. One can easily see the linear correlation between l_{RM} and the resolved length scale in Tab. 5.1.

Since the current X-ray telescopes do not yet have sufficient sensitivity to deliver the density of thermal electrons n_e over the full extension of GRGs, e.g. NGC6251 (Mack et al., 1997a; Kerp & K.-H., 2001), we get the product of $< \overline{B_\parallel} \cdot n > \mu G\, cm^{-3}$ from

$$RM = 810 \cdot \tfrac{l_{RM}}{kpc} \cdot < \tfrac{\overline{B_\parallel}}{\mu G} \cdot \tfrac{n_e}{cm^{-3}} > \ \mathrm{rad\,m^{-2}}.$$

5.3 Results

A frequently asked question when estimating magnetic field strengths is how many field reversals occur along the line-of-sight. We consider two cases, a single cell and a large number of cells. We assume that each cell is identical in size and magnetic field strength. The only difference is the direction of the magnetic field. There are two arguments against the case of a large number of cells. First, the increase of cells increases the magnetic field strength of each cell, $B_{cell} = \sqrt{N} \cdot \overline{B_\parallel}$, where $\overline{B_\parallel}$ results from the observed RM. Using the X-ray brightness, we derive $n =\leq 10^{-4}\, cm^{-3}$. Considering this low density and the strong magnetic field for the case of a large number of cells, the individual cells would not be pressure balanced and thus would not be stable (Eilek & Owen, 2002). The second argument is the patchy patterns of the RM images. In case of a large number of cells, the RM distribution will be a binomial one. The increase of the number (N) means that the number of degrees of freedom of the value of RM increases. Therefore, the resulting RM image should be strongly smoothed. Our results and data in the literature show that RM images of RGs are not in accord with this.

Because of these two arguments we favour the single-cell model for the further estimation of physical parameters in this work. The single-cell model is surely over-simplified. As shown below, the parameter obtained from this model is the 'minimum energy condition'.

5.3.1 Pressure balance estimate

In order to compile the components of the product $< \overline{B_\parallel} \cdot n >$, we have made the following considerations. Most RM values of the GRGs originate from the ($\sim$ Mpc) extended radio

lobes. On the other hand, estimates of the density of the hot gas in GRGs represent the density of their inner part ≤ 100 kpc, e.g. NGC 6251 by Mack et al. (1997a), NGC315 by Worrell & Birkinshaw (2000). The extrapolation of the densities of the X-ray emitting gas of the host galaxies and their halos yields a density of $\sim 3 \times 10^{-6}\, cm^{-3}$ at 500 kpc in the case of NGC 315.

This low density would require an unlikely strong magnetic field for the observed $< \overline{B_{\parallel}} \cdot n >$. In the single-cell model, this density calls for several hundred μG. Alternatively, if the field strength is at the μG level, then the cell must be an extended cylinder along the line-of-sight. The length of this cylinder must be hundred times longer than its radius. To maintain such a structure would be very hard, not to mention the increase of X-ray brightness. Furthermore, the RM values in the GRGs do not show any clear correlation with distance from their central cores, which is expected in the relaxed X-ray cluster.

Because of these reasons, we do not extrapolate the central density of the hot gas to estimate n_e. We rather assume pressure balance $p_m/p_g = 1$ for the estimate, where p_m and p_g are the magnetic and the gas pressure respectively. According to Eilek & Owen (2002), for NAT sources in the cluster centre the magnetic field strength $\overline{B_{\parallel}}$ of the single-cell model and the electron density n_e derived from X-ray observations are in good agreement, too, so that $p_m/p_g \sim 1$.

Using the total emitted bremsstrahlung $L_X = A \int n_e^2 T^{-0.5}\, dl$, we can compare the X-ray luminosity of this 'mantle' with that of an X-ray cluster of $l \sim 500\, kpc$ and of $n_e \sim 10^{-3}\, cm^{-3}$ at the same temperature. The total luminosity ratio, $l_{GRG}/l_{cl} = (100 \times 50^3 \times 10^{-8}\, kpc)/(500^3 \times 10^{-6}\, kpc)$, is about 10^{-3}. The projected area ratio is $(1.5 \times 10^5\, kpc^2)/(2.5 \times 10^5\, kpc^2) = 0.6$. Such a structure is too weak to be detected with current X-ray instrumentations. We have looked for extended X-ray emission in the hard band of the *ROSAT All-Sky Survey* [1]. We could not identify any significant extended X-ray structure which could be related to the GRGs' lobes. We should mention, however, that the extrapolated periphery should have weak X-ray emission, too.

Let us assume a scale length of $l \sim 50\, kpc$ and a temperature of T = 10^8 K. In order to 'wrap up' a 1 Mpc GRG, we would need at least a hundred of such single cells. From the obtained $< \overline{B_{\parallel}} \cdot n_e >$ and the pressure balance assumption, $B^2/8\pi = 2 n_e k T$, we obtain B and n_e. In this equation, we have assumed equal contributions from the electrons and ions to the thermal pressure. We estimate the total magnetic field strength B from $B = \sqrt{3} \cdot \overline{B_{\parallel}}$. The results are listed in Tab. 5.2. The results obtained for $\overline{B_{\parallel}}$ are in the same range as those for the cluster core sample (Eilek & Owen, 2002). The values of n are as low as expected from the periphery of X-ray clusters. Since we assume pressure balance, the magnetic field strength and the density of thermal particles are correlated. Three well-resolved sources (NGC 315, DA 240 and NGC 6251, see Figs. 5.1, 5.2 and 5.5) exhibit a stronger magnetic field and higher density than the two sources with the resolved scale $> 250\, kpc$ (3C 236 and 3C 326, see Figs. 5.3 and 5.4). The reason for this difference may be the over-estimate of l_{RM} in 3C 236 and 3C 326, due to the low resolution. The RM structures of 3C 236 and 3C 326 are smoother than those of the other three GRGs. Therefore, $\overline{B_{\parallel}}$ and n_e are likely to have been under-estimated in 3C 236 and 3C 326, due to the beam smearing effect.

[1] http://www.xray.mpe.mpg.de/cgi-bin/rosat/rosat-survey

Table 5.3: Estimates of the magnetic field strength, the electron density of the foreground medium and the dissipation time, based on the assumption of pressure balance. The first table assumes $T = 10^8\,K$, while the second one assumes $T = 10^7\,K$.

Source	$\overline{B_\parallel}\,(\mu\,G)$	$n_e\,(cm^{-3})$	$\tau_A\,(Myr)$
NGC 315	13.4	$2.6 \cdot 10^{-4}$	360
DA 240	11.9	$2.0 \cdot 10^{-4}$	730
3C 236	8.1	$9.4 \cdot 10^{-5}$	2500
3C 326	3.9	$2.2 \cdot 10^{-5}$	6900
NGC 6251	12.4	$2.2 \cdot 10^{-4}$	460

Source	$\overline{B_\parallel}\,(\mu G)$	$n\,(cm^{-3})$	$\tau_A\,(Myr)$
NGC 315	6.2	$5.6 \cdot 10^{-4}$	1100
DA 240	5.5	$4.4 \cdot 10^{-4}$	2300
3C 236	3.8	$2.0 \cdot 10^{-4}$	7800
3C 326	1.8	$4.7 \cdot 10^{-5}$	22000
NGC 6251	5.8	$4.8 \cdot 10^{-4}$	1500

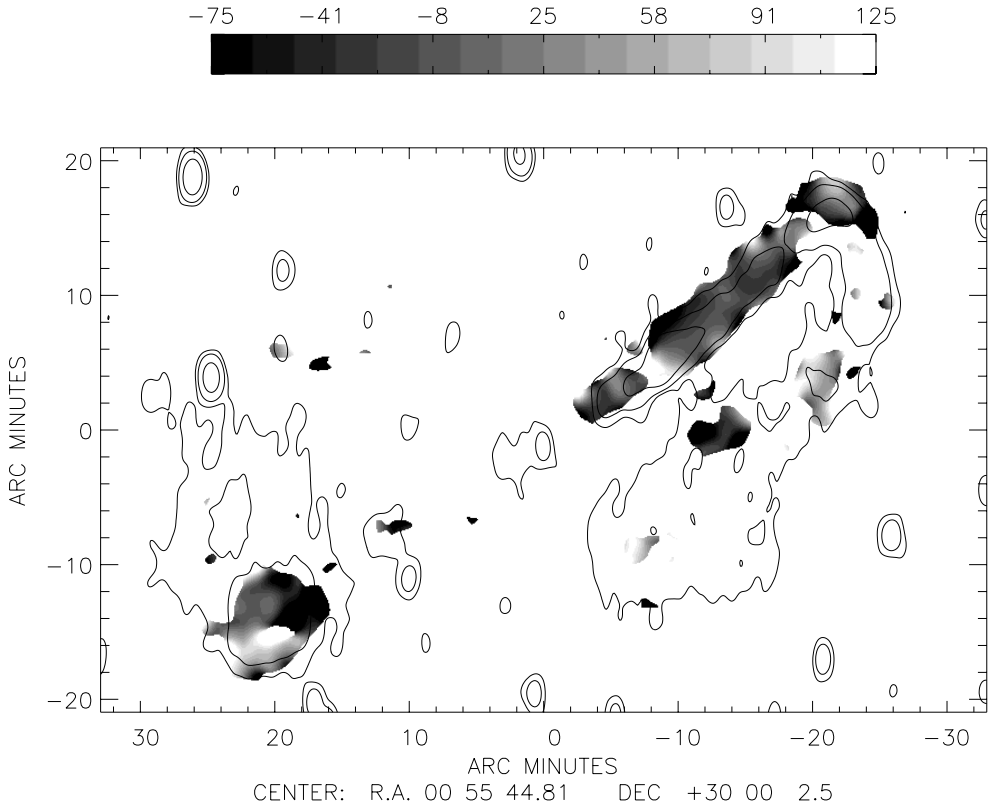

Figure 5.1: RM map of NGC 315.

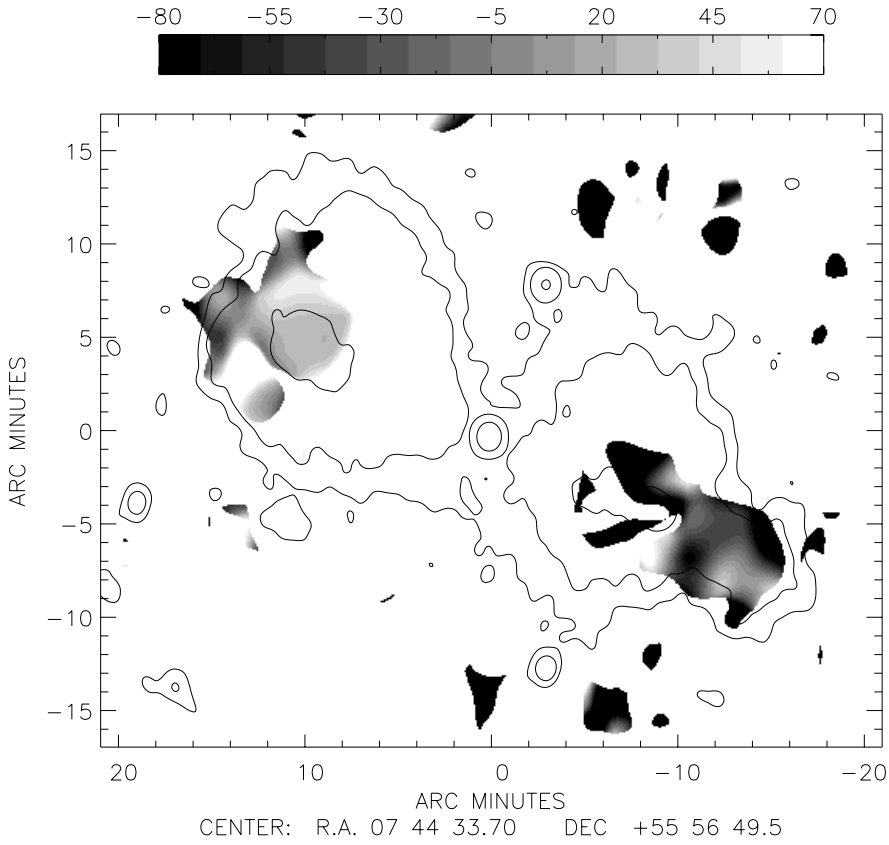

Figure 5.2: RM map of DA 240.

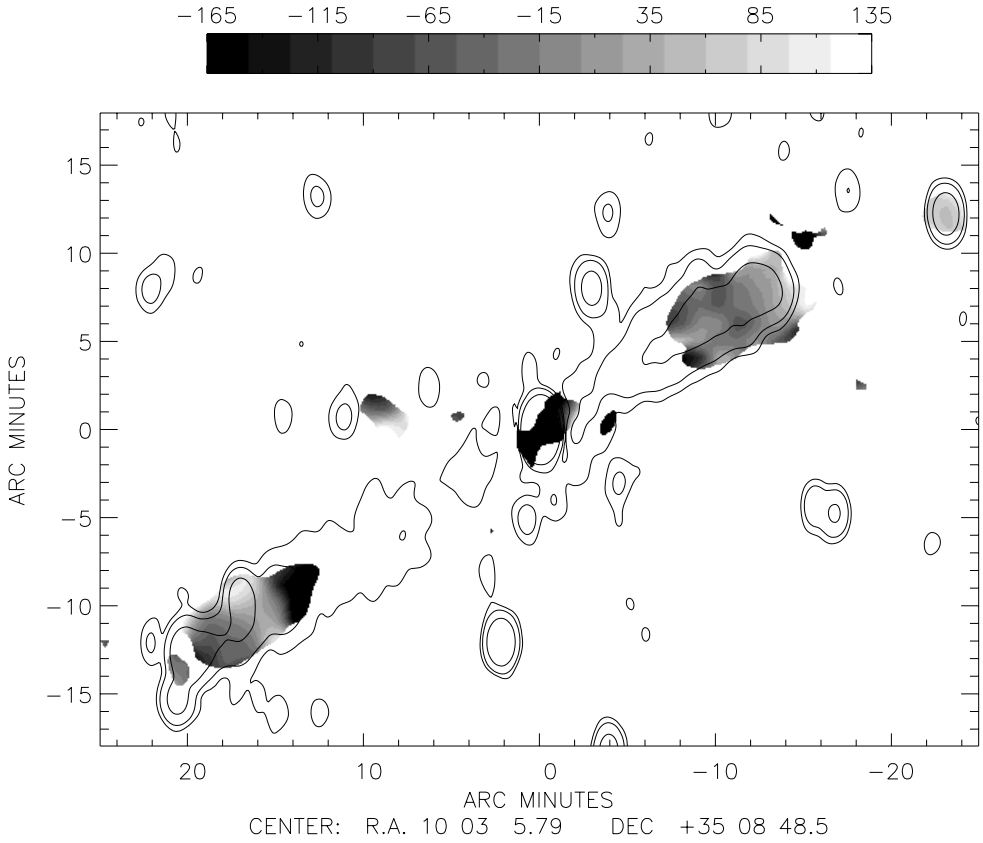

Figure 5.3: RM map of 3C 236. The RM in the central core region is an artifact.

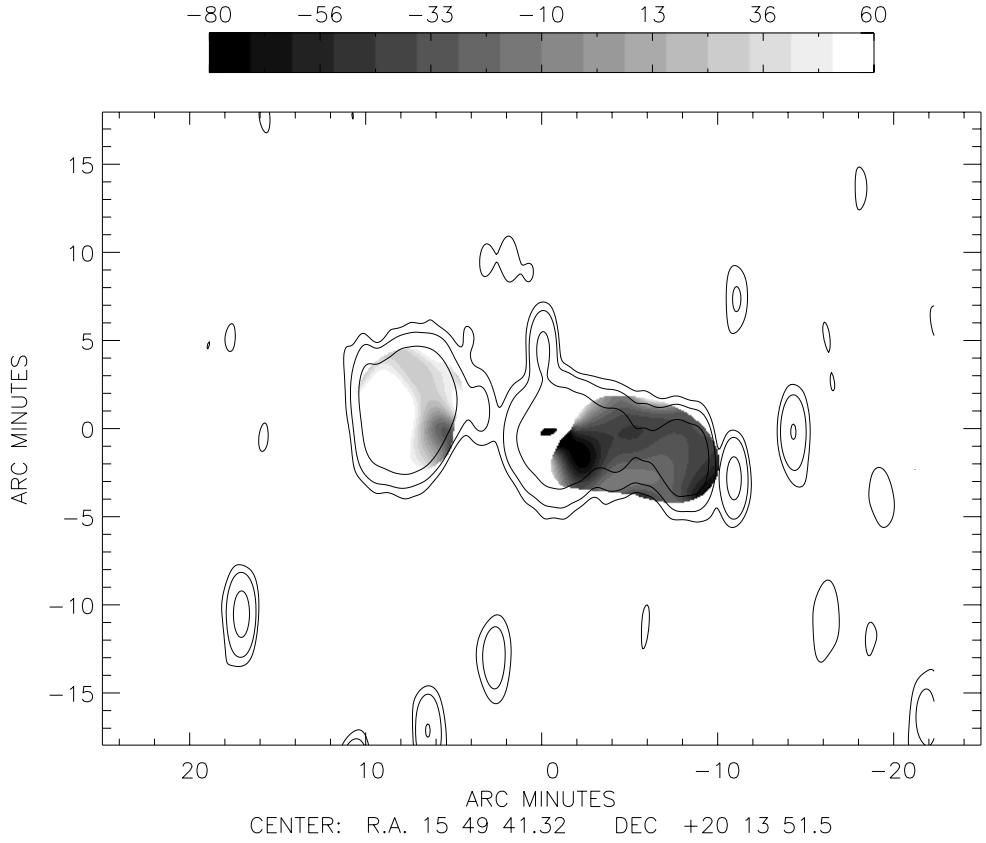

Figure 5.4: RM map of 3C 326.

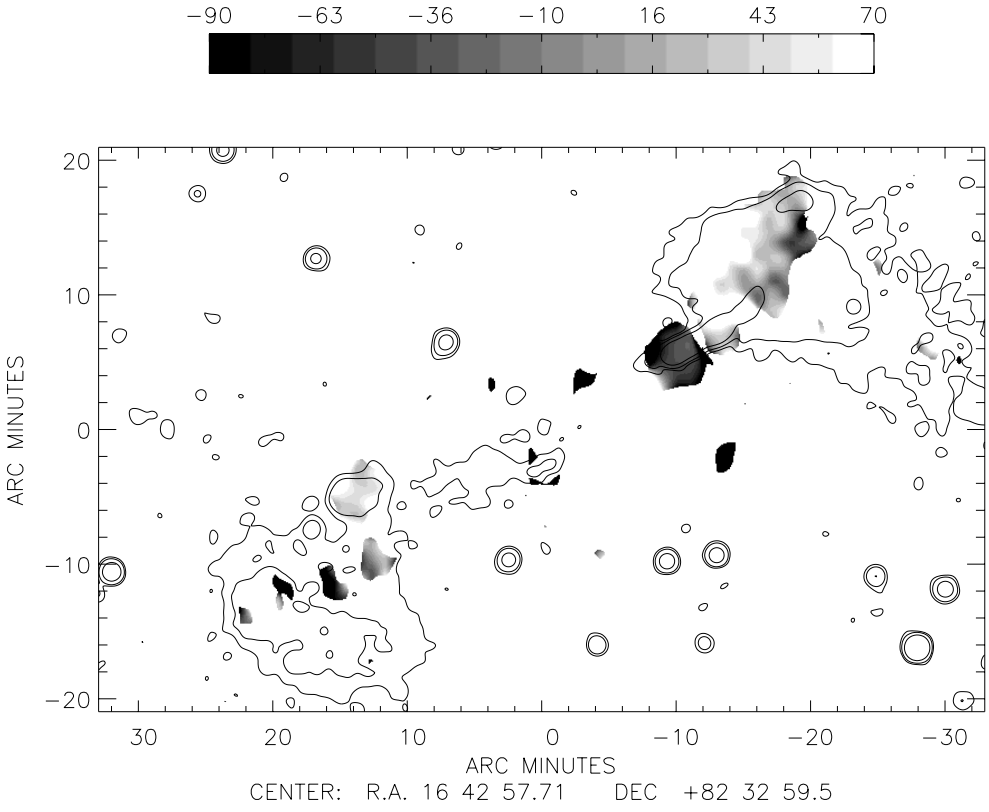

Figure 5.5: RM map of NGC 6251.

5.4 Discussion

In this section, we consider the stability of the magnetic fields in GRGs. In case of thermal energy equilibrium between electrons and protons, dissipation through reconnection will not occur within a source radiation lifetime. If most of the particle energy is in electrons, the dissipation time is comparable to the radiation lifetime. In contrast to cluster core sources (Clarke et al., 2001; Eilek & Owen, 2002), amplification mechanisms related to gravitation (mergers, cooling flows) are not attractive for GRGs; such scenarios would be in conflict with their linear sizes, their locations and their X-ray properties.

5.4.1 The total magnetic energy

We estimate the total magnetic energy contained in the Faraday-rotating medium. We further assume the validity of a single-cell model for the line-of-sight properties. For the observed $< \overline{B_{\parallel}} \cdot n_e >$, this is the minimum total magnetic energy for the assumed pressure balance condition. We assume single cells with sizes of 50 kpc in NGC 315, and a magnetic field strength of $\sqrt{3} \cdot 5\,\mu G$. A GRG should have ~ 100 of such cells surrounding it. Then the total magnetic energy is $E_B = 100 \times (50\,\mathrm{kpc})^3 \times ((\sqrt{3} \cdot 5)^2\,\mu G)/(8\pi) \sim 3.7 \times 10^{59}$ergs.

5.4.2 What could be the 'driver'?

We compare this result with the other energy estimates related to the GRGs.

Internal Driver The total radio luminosity of a GRG, $L_r = 10^{42} \cdots 10^{43}\,\mathrm{ergs\,s^{-1}}$. With a typical lifetime of 10^8 yr, the radiation energy input to the surrounding environment of a GRG could be $3 \times 10^{57} \cdots 10^{58}$ ergs. If we assume a conversion efficiency of 1% from the beam power of the AGN of the GRG to the luminosity of the GRG, the total energy input (heat, pressure) from the GRG to its surrounding environment will easily reach the order of the total energy in the RM structure that we estimated.

But how can this energy be transported to the Faraday screen? As mentioned in the previous chapter, adiabatic expansion can convert the internal energy of a radio galaxy to kinetic energy. Let us consider a GRG in its pre-expansion phase, with a volume of $(100\,\mathrm{kpc})^3$, and a number density of relativistic electrons of $10^{-8}\ cm^{-3}$, which is an order of magnitude higher than in a fully grown GRG. With a steep power-law distribution function of the particles, $N(\gamma) = N_0\gamma^{-p}$, where $p > 2$ and the $\gamma_{cut} = 1000$, the total energy in the relativistic particles is

$$E_{tot} = V \times n_{rel} \times \gamma \times m_e \times c^2,$$

which yields $2.4 \cdot 10^{59}$ ergs.

External Driver Large-scale flows due to shock waves, e.g. (Enßlin et al., 2001), can produce a comparable amount of energy. If GRGs are the 'weather stations' of the intra-cluster flows (Burns, 1998), the shock wave energy could be accumulated in the surrounding medium of the GRGs. With a surface area of $150\,\mathrm{kpc} \times 1.25\,\mathrm{Mpc}$ of an assumed single-cell, the input power of the large-scale shock wave flow proposed by (Enßlin et al., 1998, 2001) is $5 \cdot 10^{42} \cdots 10^{43}$erg s^{-1} for a ($\sim 0.5$ Mpc)^2 impact

area. If this flow has a time scale of $\sim 10^8$ yr for the source age, the upper range of the accumulated energy, $1.5 \cdot 10^{59}$ ergs, will reach the order of magnitude of the energy in the RM structure. Concerning the scale length of superclusters, $\sim 10^8$ pc, this time scale is not unusual.

5.5 Rotation Measures of GRGs and B2 sources

In Fig. 5.6, we indicate the location of 11 radio galaxies (5 GRGs and 6 B2 RGs) in the map of collected RMs of Simard-Normandin et al. (1981). As seen in the figure, all sources are at high Galactic latitudes. The five GRGs are NGC 315, DA 240, 3C 236, 3C 326 and NGC 6251 (Mack et al., 1998). The six B2 sources are 0828+32, 0836+29, 1141+37, 1316+29, 1422+26 and 1659+30 (Mack et al., 1994; Klein et al., 1995; Morganti et al., 1997a). The angular resolutions are $150''$ and $69''$ for the GRGs and the B2 sources, respectively.

In the RM histograms, two different properties between the RM of the GRGs and of the B2 RGs can be noticed.

- The B2 sources have their RM peaks in the lower RM range, < 100 rad m^{-2}, compared to the GRGs which have their peaks at a few 100 rad m^{-2}.
- Four of the five GRGs show multi-component distributions in the RM histograms. Three of them (DA 240, 3C326 and NGC 6251) show bimodal distributions. The other one, NGC 315, has a broad RM wing. Such trends are not found in the B2 sources. It is these multi-components which give rise to the large RM variation across the GRGs, $\Delta\mathrm{RM} > 100$ rad m^{-2}.

There is no evidence for any correlation of the observed RMs with their Galactic coordinates; in particular, neighbouring sources have typically lower RMs. The high RMs of the five GRGs rather seem to be intrinsic. Furthermore, the bimodal distributions of the RM in the GRGs imply high variations ΔRM across the GRGs (see Fig. 5.7). Such high values of RM and ΔRM have only been found in the vicinity of cluster cores so far (Clarke et al., 2001; Eilek & Owen, 2002).

5.5.1 Relation between ΔRM and DP

The variation ΔRM of the B2 sources and the GRGs is shown in Fig. 5.7. The depolarization DP of the B2 sources was obtained between 10.6 and 4.9 GHz (filled triangles) and between 4.9 and 1.6 GHz (open circles). The vaue of DP of the GRGs (filled circles) was obtained between 10.6 and 0.6 GHz. The value of ΔRM (14 B2 sources) were obtained between 4.9 and 1.6 GHz (open circles) and have an angular resolution of $12'' \cdots 16''$. The angular resolution and the RM ambiguity of the six B2 sources (filled triangles) and the five GRGs (filled circles) are the same as in Fig. 5.6.

5.5.2 Test of Burn's law

With the assumption that the structure of the Faraday foreground medium is unresolved, we can calculate DP from ΔRM:

$$DP = \exp\left[\Delta RM^2_{high} \cdot \lambda^4_{high} - \Delta RM^2_{low} \cdot \lambda^4_{low}\right],$$

where we assume that $\Delta RM_{high} \sim \Delta RM_{low}$. This assumption comes from the idea that Faraday rotation remains roughly linear in the observed frequency range. We obtain $\Delta RM = 5 \cdots 15$ rad m^{-2} for the B2 sources. Then for the low-frequency sample (open circles), the range of $\ln DP$ is $-3 \cdot 10^{-4} \cdots -0.08$, while for the high-frequency B2 sample (filled triangles) it is $-0.03 \cdots -0.26$. The observed DP of the low-frquency sample is lower than that of the high-frequency sample. On the contrary, the observed DP is stronger in the low-frequency sample than predicted.

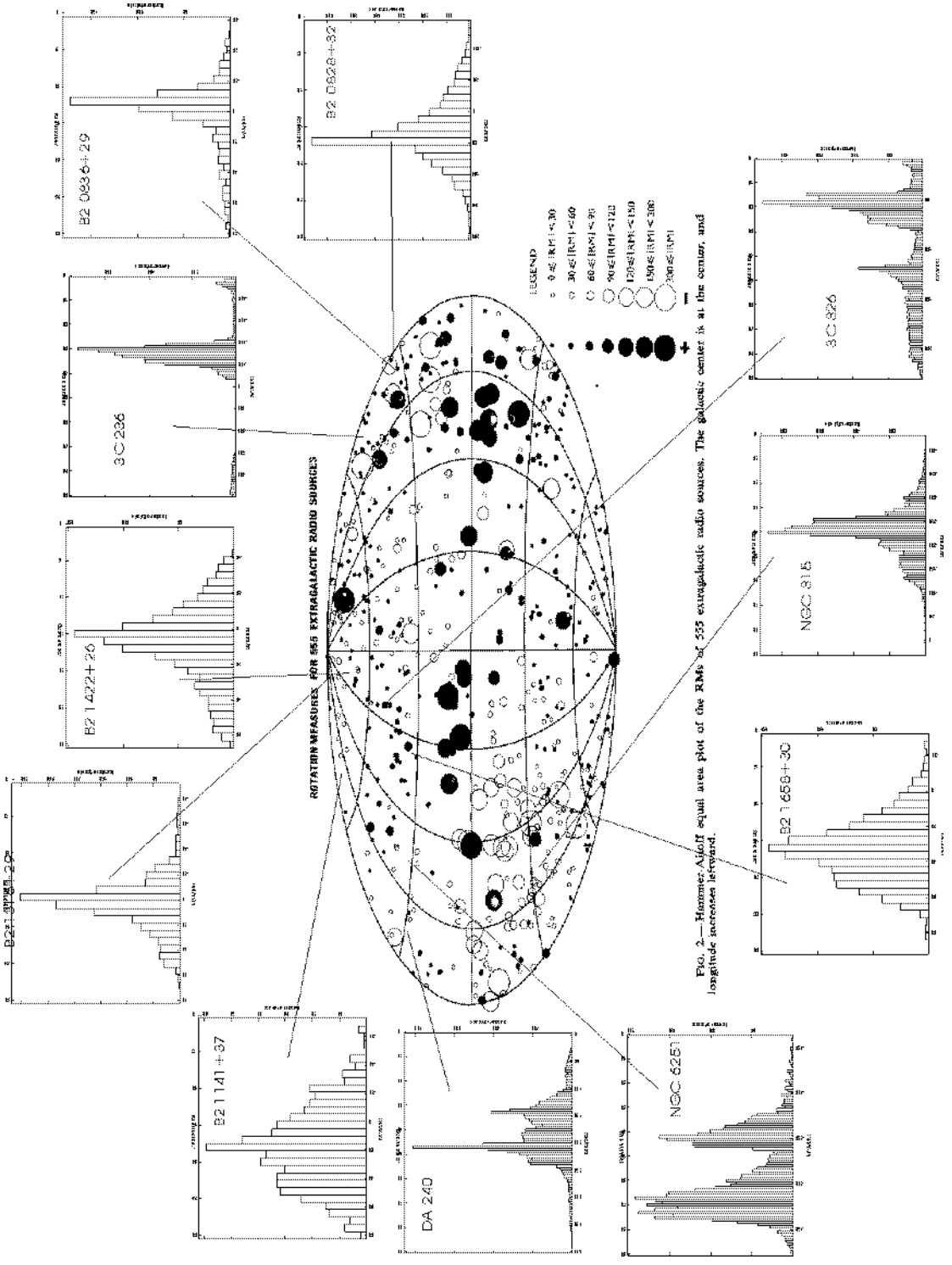

Figure 5.6: RMs of 11 radio galaxies in Galactic coordinates. The RMs of five GRGs and of six B2 radio galaxies which were observed at 10.6 and 4.8/4.9 GHz are included in the plot produced by Simard-Normandin et al. (1981).

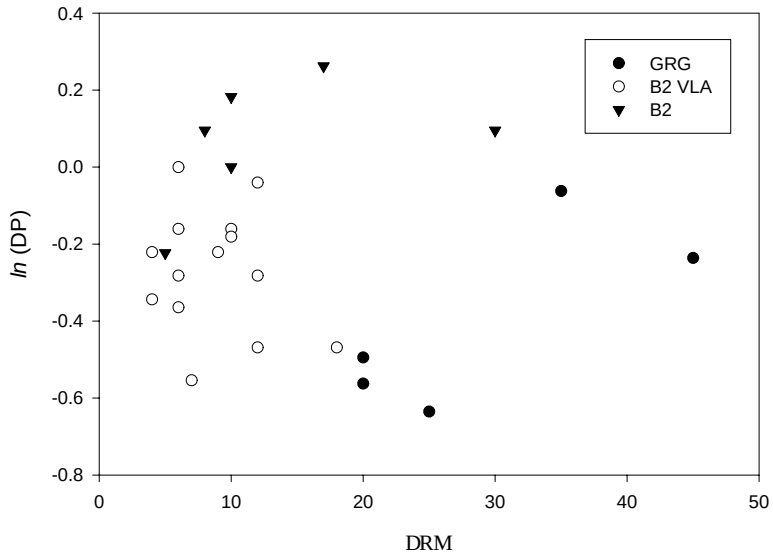

Figure 5.7: Integrated ΔRM - DP diagram of B2 RGs and GRGs. All radio galaxies studied in this thesis are plotted. The ordinate is the depolarization measure, DP, plotted here logarithmically, since Burn (1966)'s law predicts $DP = \exp\left[\Delta RM^2_{high} \cdot \lambda^4_{high} - \Delta RM^2_{low} \cdot \lambda^4_{low}\right]$. The abscissa corresponds to ΔRM (see text for more information.)

In the GRG sample, the observed range of ΔRM is $20 \cdots 40$ rad m^{-2}. Then the range of $\ln DP$ calculated from the Burn's law is $-23 \cdots -9000$. The frequency dependence is obvious in DP, but not as strong as predicted by Burn's law. The simplest answer to this discrepancy is that the Faraday foreground towards the GRGs is at least partially resolved. We probably need a more complicated description of the Faraday medium as suggested by Tribble (1991). In the B2 sample, the observed trend is marginally in agreement with Burn's law.

Part II

Spectral asymmetry in radio galaxies

Chapter 6

Spectral curvature in GRGs

6.1 The spectral-curvature parameter

6.1.1 Introduction

Spectra of synchrotron sources from the radio through the X-ray regime reflect the energy distribution of relativistic particles, i.e. electrons whose energy distributions obey a power-law. In general, the synchrotron emissivity also follows a power-law (Pacholczyk, 1970). While the conventional spectral indices only provide the spectral slope between the two observing frequencies, a multi-frequency data set can also disclose spectral curvature over a larger frequency range. The significance of the shape of synchrotron spectra has been underlined early on by Kardashev (1962); Pacholczyk (1970); Pacholzcyk (1997); Jaffe & Perola (1973), who were among the first to describe and apply synchrotron loss models to flux densities obtained at several frequencies.

It is obvious that the information on the spectral shape of a source under the effects of ageing, adiabatic expansion etc. provides an important tool for understanding source evolution. If the injection of relativistic particles following a power-law is restricted to a certain region – the cores and/or hot spots of radio galaxies – and if the observation is performed with appropriate resolution, one can detect regional variations of spectral curvature resulting from the above-mentioned physical processes. Since synchrotron and Inverse Compton losses are the main energy dissipation processes in radio galaxies, in particular at high and intermediate radio frequencies (> 1 GHz), large efforts have been made to explain the variation of spectral curvatures – often by modeling two-frequency data – of radio galaxies with the synchrotron ageing theory (e.g. Alexander & Leahy, 1987; Alexander, 1987; Klein et al., 1995; Feretti et al., 1998; Murgia et al., 1999). A proper determination of parameters like the injection spectral index $\alpha_{\rm inj}$ (the spectrum of the electron distribution immediately after acceleration, $N(E) \propto E^{-p}$, $\alpha_{\rm inj} = (p-1)/2$) or the break frequency $\nu_{\rm br}$ (the frequency at which spectral steepening occurs) can be obtained with a spectral ageing analysis (e.g. Carilli et al., 1991; Mack et al., 1998; Murgia et al., 1999). This requires, however, the fitting of appropriate models with several parameters, thus high-quality measurements at many fequencies with a good signal-to-noise ratio are essential.

In order to fit synchrotron and Inverse-Compton losses, three models are widely used: the continuous injection (CI) model (Pacholczyk, 1970) assumes a mixture of electron populations of various synchrotron ages. In this model, permanent replenishment of fresh particles is assumed so that the injection spectral index steepens to its final value of $\alpha_{inj} + 0.5$ beyond the break frequency. The Kardashev-Pacholczyk (KP)

model (Kardashev, 1962; Pacholczyk, 1970) merely includes a single injection of power-law distributed electrons. The pitch angles of the electrons are assumed to be constant with time. The high-frequency slope in this model is $\frac{4}{3}\alpha_{\rm inj} + 1$. The Jaffe-Perola (JP) model (Jaffe & Perola, 1973) incorporates – similar to KP – a single injection but permits permanent pitch angle isotropization. Beyond the break frequency this model leads to an exponential steepening of the high-frequency spectrum. A sketch of the different tracks of the various ageing models in the classical $\log(S) - \log(\nu)$ space can be found in the work of Carilli et al. (1991, see their Fig. 1).

In many cases the spectral ageing analysis yielded significant results. However, high-resolution multi-frequency studies of two prototypical nearby radio galaxies – 3C 449 (FR I-type) by Katz-Stone & Rudnick (1997) and Cygnus A (FR II-type) by Carilli et al. (1991), show trends that cannot be explained by the synchrotron ageing theory alone. The first problem is that jets and lobes (3C 449), and hot-spots and lobes (Cygnus A) have different injection spectra. The second problem to be dealt with is that of the microscopic physical conditions. While possible physical conditions such as turbulent magnetic fields and inverse-Compton scattering by cosmic microwave background photons favour the pitch-angle isotropized (JP) model, the observational results appear to support the constant pitch angle (KP) model. This could mean that the nature of the spectral curvature is more complex than expected from the synchrotron ageing theory alone.

Carilli & Barthel (1996) have pointed out the necessity of an appropriate empirical analysis that is not tied to any theoretical model in order to find the real trends in sources. Here we present a new method which can fulfill this requirement. It also aims at a quick determination of the injection spectral index and the best suited model to fit the observed spectrum. It fills the gap between the simple spectral index study and the much more complex spectral ageing analysis. It is also suited to provide first guesses of the parameters to be fitted in a spectral ageing analysis, therefore making the fit procedure less susceptible to local minima in the error space.

6.2 The spectral curvature parameter-α diagram

This method is based on the so-called spectral curvature parameter (SCP). It is defined as

$$SCP \equiv \frac{\alpha_{high} - \alpha_{low}}{\alpha_{high} + \alpha_{low}}.$$

When displayed as a function of the spectral index α, with

$$I_\nu \propto \nu^{-\alpha},$$

the SCP indicates how the spectrum evolves, starting from its pure power-law. As α_{high} is more sensitive to both spectral steepening and spectral flattening than α_{low} (Pacholczyk, 1970; Eilek & Hughes, 1991; Carilli et al., 1991), we employ α_{high} as the counter axis of SCP. Though the classical $log(S_\nu)$ - $log(\nu)$ diagram is the best way to test ageing models for a single-spectrum population, it is not a straight-forward tool to unveil different trends in an extended source. It is here where the SCP - α diagram has its power. Each spectrum is represented by a point in the SCP - α plane, and a lot of spectra from an extended source can be drawn in this plane.

Fig. 6.1 illustrates the schematic tracks of the power-law spectra undergoing syn-

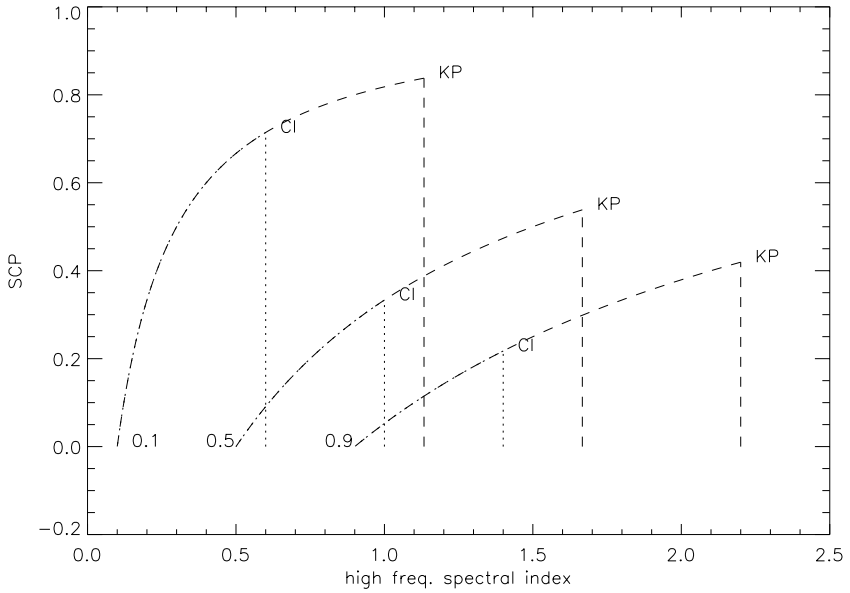

Figure 6.1: Schematic SCP– α_{high} diagram of power-law injection spectra, $\alpha_{inj} = 0.1, 0.5, 0.9$, undergoing synchrotron losses. The numbers represent the injection spectral index of each line. Along the solid curves, all models, i.e. CI, KP, and JP are possible. At the maximum SCP values of the CI models the tracks between CI (dotted lines) and KP/JP (dashed lines) *bifurcate* at the points marked 'CI'. Along the dashed curves both, the KP and JP models are possible. At $\mathrm{SCP_{max}}$ of the KP model (marked 'KP') the KP (dashed straight lines) and JP models (imaginary curves approaching SCP = 1) take separate tracks. The break frequency, ν_{br}, reaches the low-frequency regime such that $\nu_1 \geq \nu_{br} \geq \nu_2$, where ν_1, ν_2 are the frequencies used for the estimate of α_{low}. The KP spectra will fall vertically to $SCP = 0$, since $\alpha_{high} = \alpha_{KP,br} = 4/3\alpha_{inj} + 1$. The JP high-frequency tail falls off exponentially beyond the break frequency in the $log(S_\nu)$ - $log(\nu)$ diagram. Therefore, the track will approach asymptotically SCP = 1 in the SCP-α_{high} regime. Tracks of these most common synchrotron ageing models in the $log(S_\nu)$ - $log(\nu)$ parameter space have been sketched by Carilli et al. (1991).

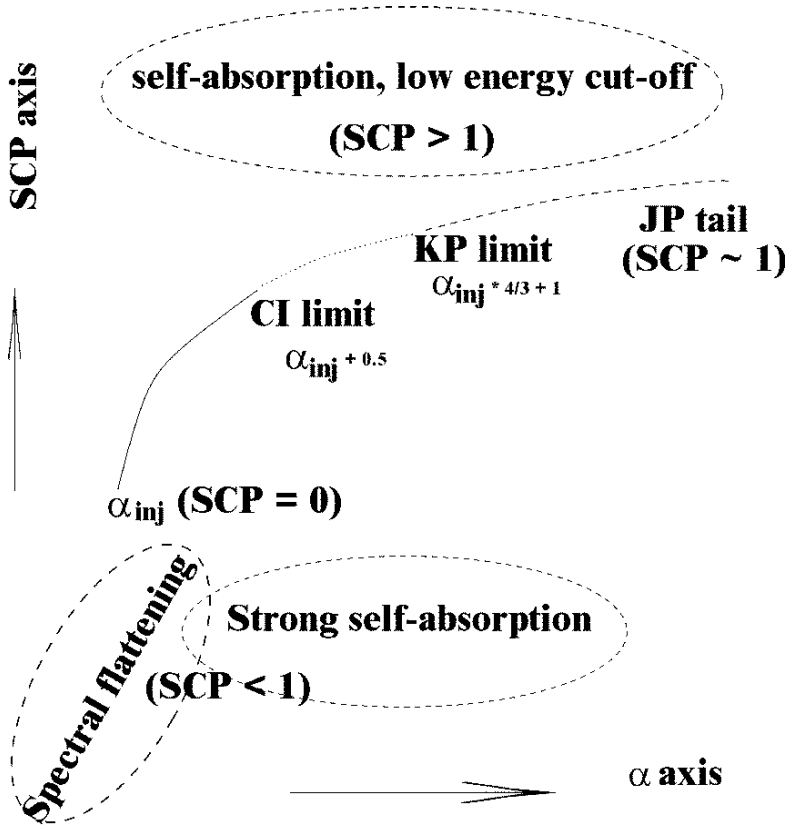

Figure 6.2: Schematic diagram of a synchrotron source with a given injection spectrum and with various processes that affect the spectral curvature. In this sketch, the classical pitch angle models, i.e. KP and JP are considered.

chrotron ageing. More realistic simulations of the SCP–α diagram including the Inverse Compton equivalent field of Cosmic Microwave Background radiation, i.e. B_{CMB}, are presented in what follows. The solid curved lines represent tracks where the break frequency has not yet reached the low-frequency regime (i.e. where α_{low} is determined). The CI, KP and JP models produce different SCP ranges. This makes it easy to distinguish between the different models in the SCP-α_{high} plane. Different injection spectral indices also follow different tracks.

Since both the CI and the KP model predict a power-law spectrum also beyond the break frequency, namely the so-called broken power-law (Eilek & Hughes, 1991), we can calculate the maximum SCPs in these cases. For $\alpha_{inj} = 0.5$, these are $SCP_{CI,max} \sim 0.33$ and $SCP_{KP,max} \sim 0.54$. In contrast, the high-frequency part of the JP model has a non-power-law curvature, viz. an exponential one. Therefore, the tracks of JP spectra asymptotically approach SCP= 1.0. In any case, $\alpha_h > (\frac{4}{3}) \cdot \alpha_{inj} + 1$ is predicted by the JP model only.

6.2.1 SCP - α and colour-colour diagram

An advantage of the SCP - α diagram with respect to the colour-colour diagram (C-C diagram), is seen when the source has multiple values of α_{inj}. As predicted by the particle ageing (i.e. synchrotron) theory, the track of an aged α_{inj} does not leave immediately the $\alpha_{low} = \alpha_{high}$ line (see Fig. 6.3). Because of the overlap of the $\alpha_{low} =$

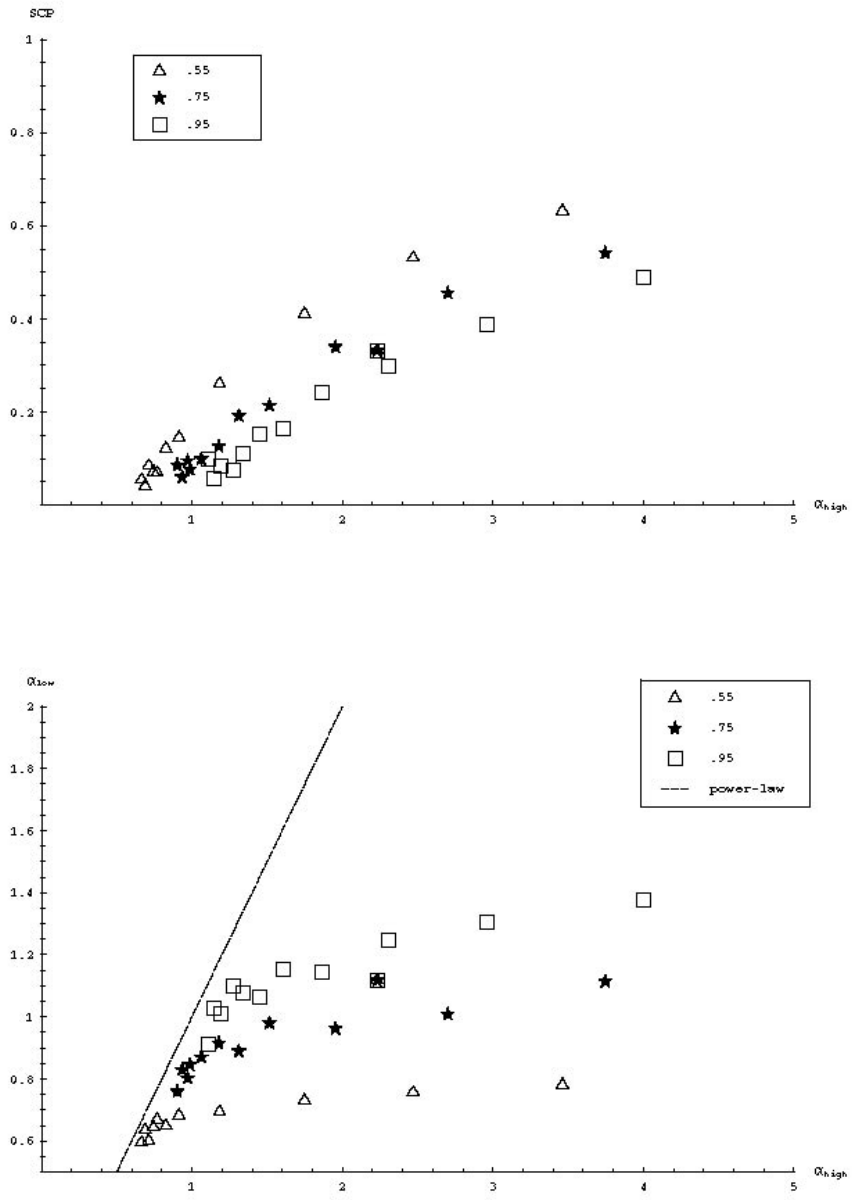

Figure 6.3: Comparison between the SCP - α and colour-colour diagram with $B_{sync} = 6.0\ \mu G$, $B_{CMB} = 3.2\ \mu G$ and the JP model. The frequency intervals were selected to be similar to standard observing frequencies in the classical radio regime. Open triangles represent $\alpha_{inj} = 0.55$. Filled stars designate $\alpha_{inj} = 0.75$. Open squares show $\alpha_{inj} = 0.95$. The dotted line in the Colour-Colour diagram corrresponds to the line $\alpha_{low} = \alpha_{high}$, i.e. a pure power-law, while in the SCP-α diagram this corresponds to SCP = 0.

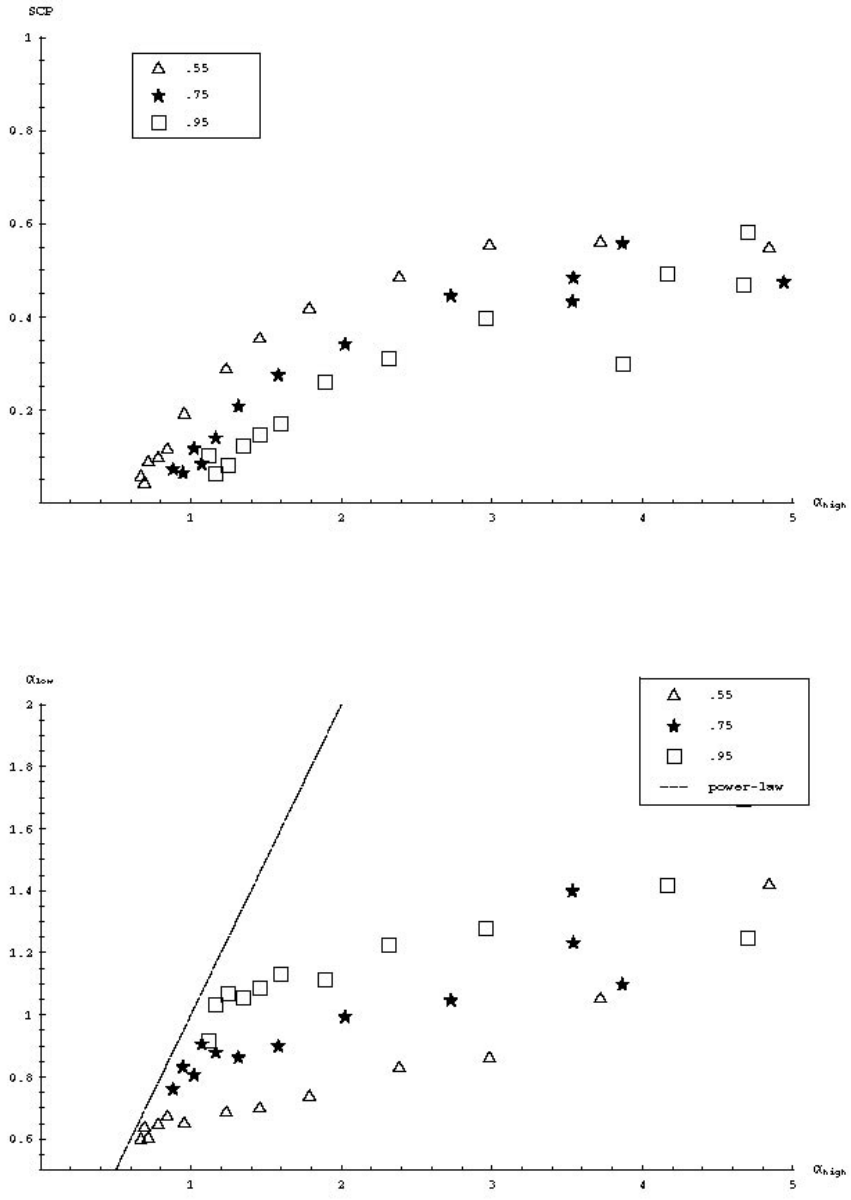

Figure 6.4: Comparison between the SCP - α and colour-colour diagram with $B_{sync} = 6.0\ \mu G$, $B_{CMB} = 3.2\ \mu G$ and the KP model (see the mixing of aged points from different values of α_{inj}). This becomes more serious with increasing B_{sync} in the KP model.

α_{high} line and the spread of points parallel to it in the C-C diagram, trends in the source cannot be easily identified. We emphasize that there are model dependent aspects in the spectral tomography or the classical synchrotron ageing analysis, (e.g. Alexander & Leahy, 1987; Murgia et al., 1999).

For example, the synchrotron ageing analysis can hardly permit a pixel-to-pixel study. The synchrotron ageing analysis is therefore done in a way with certain subdivided integration areas. As a property of the integration, the obtained α_{inj} is strongly biased by bright structures in these areas. The spectral tomography aims at solving this problem. This technique isolates a 'different' component from an assumed or known α_{inj} component. The value of α_{inj} deduced from this 'different' component is not directly obtained in the spectral tomography. The spectral tomography with multiple values of α_{inj} could be much more complex than the classical synchrotron ageing analysis. The tool suggested here will extract α_{inj} without the bias due to bright structures and without complex tomographical mapping. It can serve as a 'precensor', such as to select the area of integration in the synchrotron ageing analysis correctly, thus providing quite reliable physical parameters.

The two clear bifurcations between CI and KP/JP and between KP and JP provide a further strength of the SCP - α diagram in that sense. In both cases, i.e. CI and KP, straight vertical lines arise, while in the KP/JP and JP case the original curves are maintained. This fact makes the selection of the proper ageing model easier than for the C-C diagram. Of course, under the influence of the CMB, this last argument is only true if B_{sync} is (much) stronger than B_{CMB}. The weak point of both, the C-C diagram and the SCP - α diagram is the loss of positional information of the spectra. In order to compensate for this weakness, we present the SCP - α diagram and the SCP map together. In this way, the position information of spectra can be restored. Some first results of this exercise will be shown in the next section.

6.3 Application to radio galaxies

In this section, we present SCP - α diagrams of three GRGs and of a sample of CSS sources. The integrated spectra have been analyzed by Mack et al. (1998) for the GRGs and by Murgia et al. (1999) for the CSS sources with synchrotron ageing models. The error bars in the diagrams represent σ_{scp} and σ_α. These are estimated as follows:

$$\sigma^2_{scp} = \frac{4(\alpha^2_{high}+\alpha^2_{low})}{(\alpha_{high}+\alpha_{low})^4}(\alpha^2_{high}\cdot\sigma^2_{\alpha_{high}} + \alpha^2_{low}\cdot\sigma^2_{\alpha_{low}})$$

$$\sigma_\alpha = \frac{1}{\log(\lambda_2/\lambda_1)}\sqrt{(\sigma^2_{I,1}/I^2_1) + (\sigma^2_{I,2}/I^2_2)}\ .$$

α_{low} and α_{high} are the spectral indices ($I_\nu \propto \nu^{-\alpha}$), obtained at low (e.g. < 1 GHz) and high (e.g. > 1 GHz) frequencies, respectively. Since two independent spectral indices are needed for the SCP, observations over at least three different frequencies are necessary.

6.3.1 Giant Radio Galaxies

These objects are classified by their projected linear sizes. The measurements used here have been performed by Mack et al. (1997b) at frequencies between 326 and 10.6 GHz. We use four frequencies in our analysis, viz. 326, 610, 4.8 and 10.6 GHz. We compute $\alpha^{610\mathrm{MHz}}_{326\mathrm{MHz}}$ as α_{low}, and $\alpha^{10.6\mathrm{GHz}}_{4.8\mathrm{GHz}}$ as α_{high}. All maps were convolved to a common

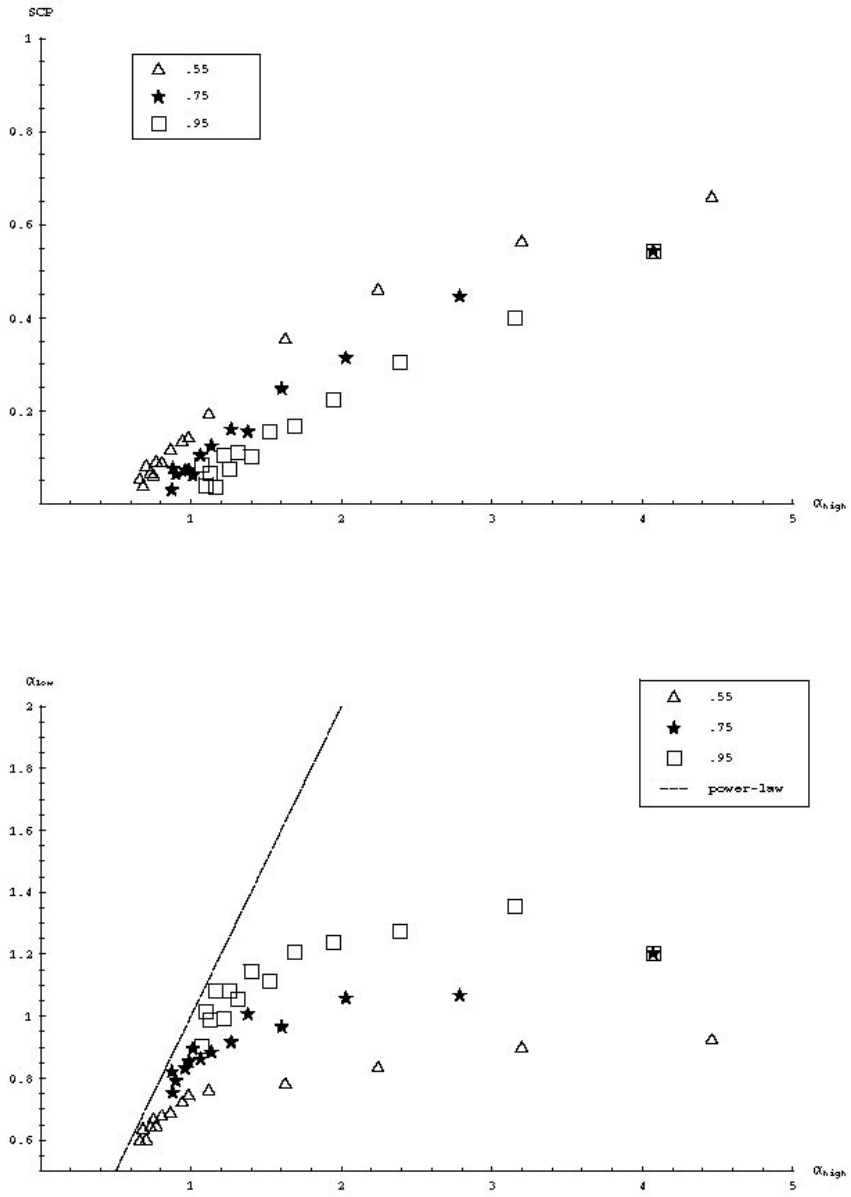

Figure 6.5: Comparison between SCP - α and the colour-colour diagram with $B_{sync} = 3.0\ \mu G$, $B_{CMB} = 3.2\ \mu G$ and KP model.

resolution of $150'' \times 150''$, SCP - α diagrams were produced for brightness levels above $\sim 3\sigma$. In general, the low-frequency spectral indices in the lobes of all three sources remain relatively constant, $\alpha_{low} \sim \alpha_{inj}$. This means that neither ageing processes nor synchrotron self-absorption play an important rôle at low frequencies in the regions of interest. In what follows, we shall discuss the results for the three GRGs investigated here in detail. For the best performance, if needed, the cubic convolution interpolation method with a value of -0.5 is used when regridding (Park & Schowengerdt, 1983). The linear convolution interpolation shows only a marginal difference.

DA 240

The radio morphology of DA 240 is symmetric at low frequencies, but becomes increasingly asymmetric towards higher frequencies (Mack et al., 1997b). At 326 MHz, DA 240 is seen as a 'fat double'. The SW fat lobe has disappeared at 10.6 GHz, forming an elongated edge-darkened FR-I-type lobe. On the contrary, the NE lobe maintains its 'fat round' shape up to 10.6 GHz.

A fit to the SCP-α diagram yields steep injection spectra, $\alpha_{inj} \sim 0.82$ (NE lobe) and ~ 0.94 (SW lobe). These unusually steep and asymmetric injection spectra have already been reported by Mack et al. (1998), viz. 0.76 and 0.97 for the NE and SW lobe respectively. Those authors used the synchrotron ageing technique. The difference of the injection spectral indices is relatively large in the NE lobe, since the region with SCP< 0 of the NE lobe (Fig. 6.6) is included in the integrated synchrotron ageing calculation. Including this flatter-spectrum region, $\alpha_{high} = 0.5 \ldots 0.85$ makes the synchrotron ageing estimate uncertain. On the whole, our intuitive rapid estimate shows good agreement with their result.

Besides this asymmetry of the injection spectral indices, the two lobes reveal quite different trends in the diagram. Using the synchrotron ageing theory, the KP and JP models well describe the trend in the SW lobe (Fig. 6.7). On the other hand, the majority of the SCP values in the NE lobe are well below zero. This is a clear case of spectral flattening. The remaining points with SCP> 0 are best fitted by the CI model. In the NE lobe α_{high} commences with 0.5, then increases to 0.8 below SCP< 0. This is indicative of a non-relativistic strong shock as discussed in the last section. Since there is no indication of any bifurcation (see Fig. 6.1) in the SCP-α diagram, we can not definitely prefer any model to the others, except for region CI mentioned in Fig. 6.7.

NGC 315

Spectral flattening is present over the whole source. The value $\alpha_{inj} \sim 0.58$ in the NW lobe is consistent with the estimate of Mack et al. (1998), who obtained $0.54 \ldots 0.59$. On the other hand, we cannot properly estimate the injection spectral index of the SE lobe, due to the small number of points with $SCP > 0$ and the large uncertainties. The general trend in the SE lobe implies a steep injection spectrum, $\alpha_{inj} \sim 1.0$. The trends in the two lobes are neither symmetric nor asymmetric, but rather symmetric w.r.t the minor-axis (Fig. 6.9). At the southern ends of the two lobes, the spectral upturn is striking. After that, towards the north, a gradual steepening follows.

The tracks of the NW and the SE lobe are well separated, which implies different injection indices, although the error is quite large. The reason for the extremely flat and even upturning curvature in the NW is unclear. Unresolved background sources or relativistic shocks could be the explanation. Enßlin et al. (2001) suggest that the

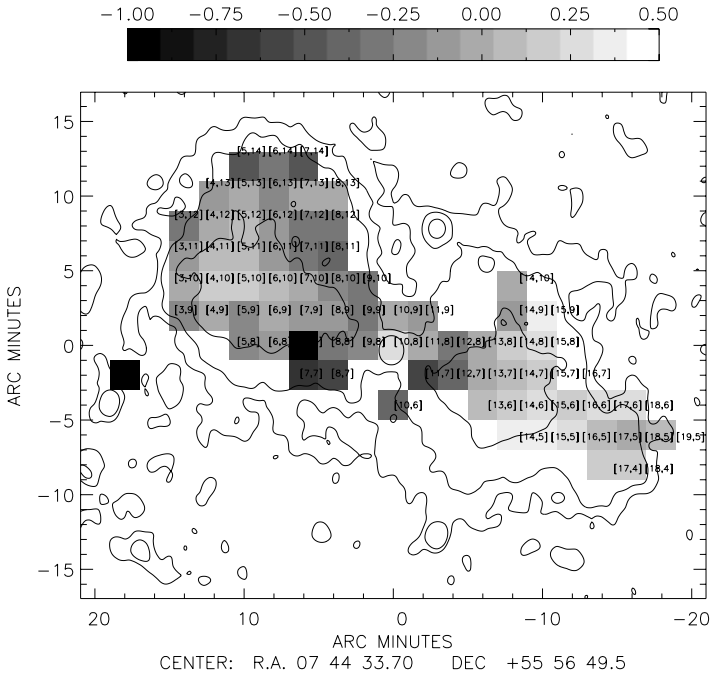

Figure 6.6: SCP map of DA 240. The contours show the total intensities at 326 MHz Mack et al. (1997b). Contour levels are 3, 10 and $50\sigma_I$. The SCP map shows an asymmetry. The spectral curvature of the NE lobe is nearly a power-law in the vicinity of its bright centre [5,10]. The envelope of the NE lobe shows spectral flattening. This implies an effective *in situ* acceleration, possibly through the interaction with a surrounding thermal magneto-ionic medium whose existence is detected via its rotation measure. The SCP values of the SW lobe are in a range which is expected by the particle ageing theory. The SW lobe lacks a well-defined envelope at high frequencies. Its SW extremity shows spectral flattening with respect to its bright centre. The fact that all of DA240's extremities have a SCP flatter than their brightness centres implies that the interaction (i.e. re-acceleration) with its environment is an essential mechanism for the growth of this GRG.

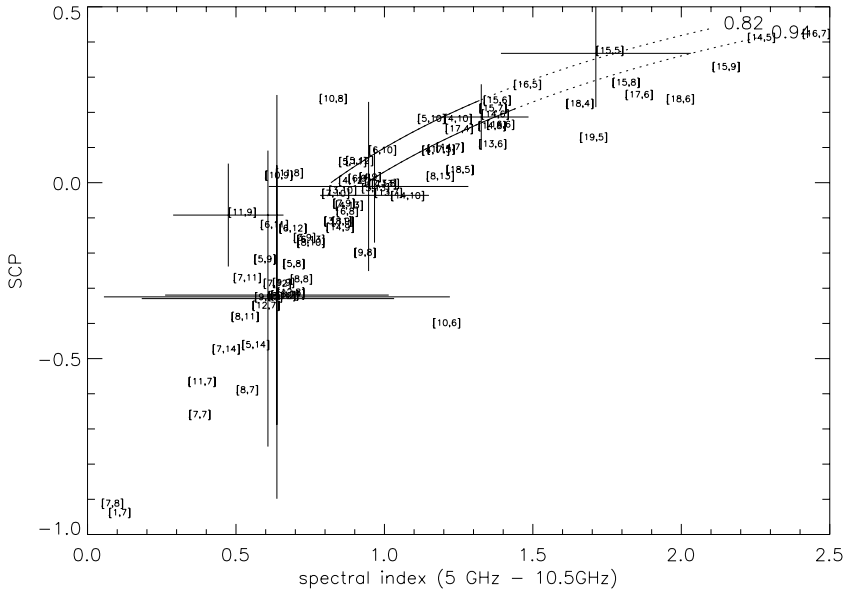

Figure 6.7: SCP-α diagram of DA 240. The error estimation is described in the text. Two lines represent the best fit to the SW lobe and the NE lobe, respectively. For the fitting procedure, only points with SCP> 0 of each lobe were used. In the SW lobe, two interesting trends are visible. If we confirm the drop at the end of the CI track, with $\alpha_{inj} \sim 0.82$, inspite of the large error of SCP and α_{high}, this can be interpreted as the CI bifurcation in Fig. 6.2. If this bifurcation is real, it implies that B_{sync} in the CI region is much stronger than B_{CMB}. The second point is the spread of data in the KP/JP range. Again inspite of the error bar, the trend visible here resembles the evolution of KP spectrum (see Fig. 6.20), and B_{sync} may be several times stronger than B_{CMB}.

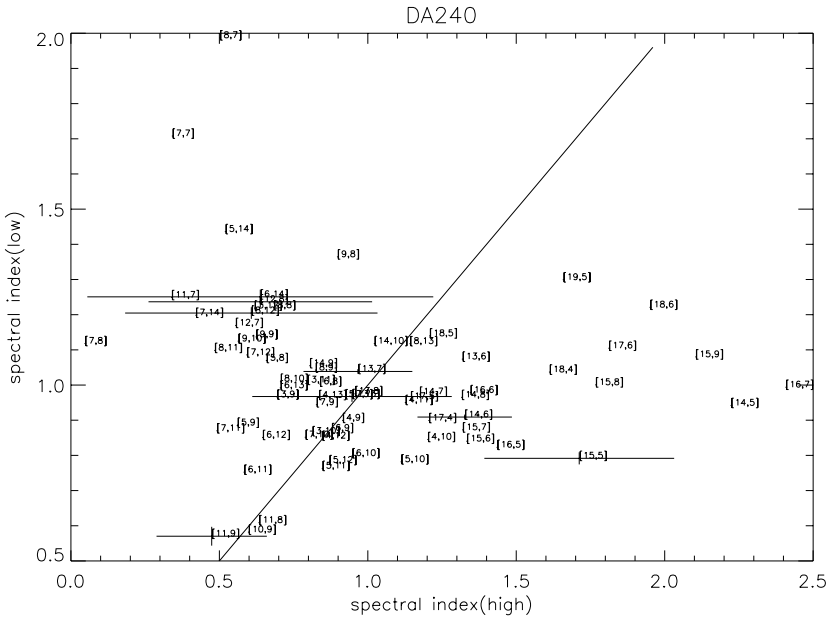

Figure 6.8: C-C diagram of DA 240. The straight line corresponds to a pure power-law. The area to its left is populated by points of spectral flattening, the area to its right contains points which show spectral steepening.

relic NW tail of NGC 315 is re-accelerated by a cosmological shock wave. Our analysis demonstrates that the particles in both lobes have been re-accelerated. If the re-acceleration scenario is true, the spectral flattening implies that the energy threshold of this acceleration and/or B_{sync} of this region are higher than those of the injection spectrum. Spectral flattening plus an upturn are independent of possible problems of missing short spacings inherent to the 610 MHz WSRT data, since it would be detectable via the Effelsberg single dish multi-frequency observations at 2.6, 4.8 and 10.6 GHz (Mack et al., 1998) alone. However, the prominence of the points with $SCP < 0$ could be related to the angular size of the 610 MHz data. It can be speculated that this is a viable explanation for the prominence of $SCP < 0$ in NGC315, which is by far the largest source in terms of angular size, $\Phi \sim 1°$. On the other hand, a value α of our SCP–α diagram is also obtained from single-dish 4.8 and 10.6 GHz data and shows $\alpha < \alpha_{inj}$. The spectral flattening in NGC 315 is mainly due to a low α_{high}.

3C 236

This source is the largest known GRG, with $d \sim 4.5$ Mpc. It has a typical FR II morphology. Our value of α_{inj} of 0.7 in the SE lobe (Fig. 6.13) is in the range of the integrated synchrotron ageing estimate of 0.5 to 0.7 derived by Mack et al. (1998). In the NW lobe, we obtain a steep α_{inj} of 1.10. The integrated spectral index from synchrotron ageing theory for this lobe is 0.7.

The spectral flattening shown at the extremity of the SE lobe is due to a known background source (Mack et al., 1997b). In the NW lobe, we find two different values of α_{inj}, without any significant flattening. One of them is well fitted by a steep spectrum, $\alpha_{inj} \sim 1.10$. The trend of these data clearly shows the synchrotron ageing in the lobe. In the backflow or so-called bridge region, $\alpha_{inj} \sim 0.7$ yields the best fit. Such an injection

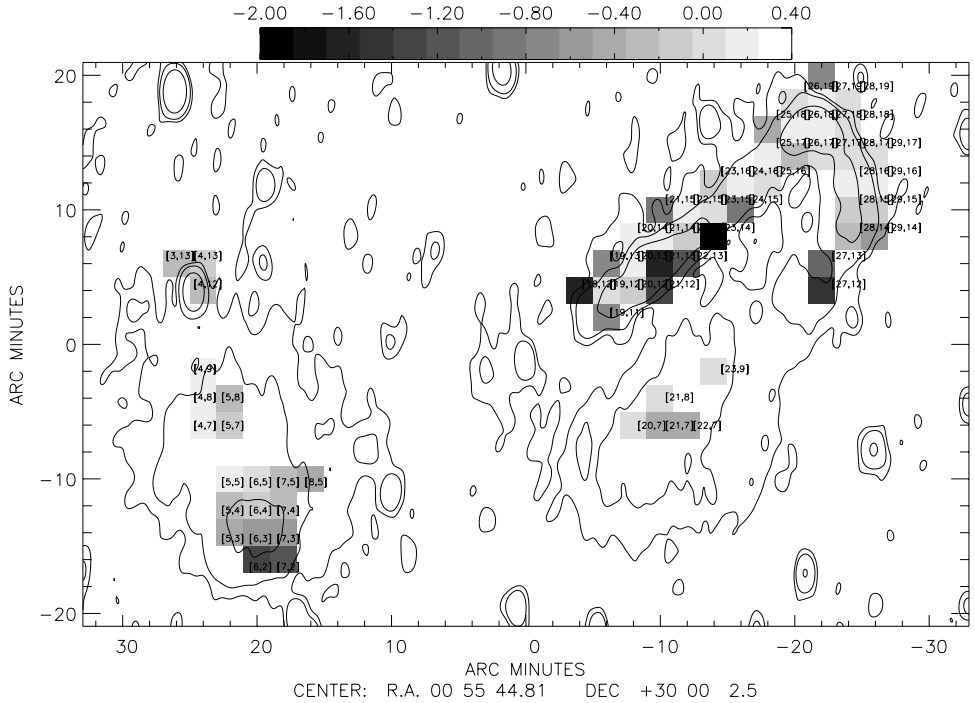

Figure 6.9: SCP map NGC 315. Contours show the total intensities at 326 MHz published by Mack et al. (1997b). Contour levels are 3, 10 and 50 σ_I. Although its morphology is highly asymmetric, there is no significant spectral asymmetry along the jet major axis. Along the minor axis, in the SW to NE direction, the spectral curvature exhibits a gradual steepening. This is clear in the whole SEern lobe and in the bow structure of the NWern lobe. The relic tail of this structure also has a flat spectral curvature.

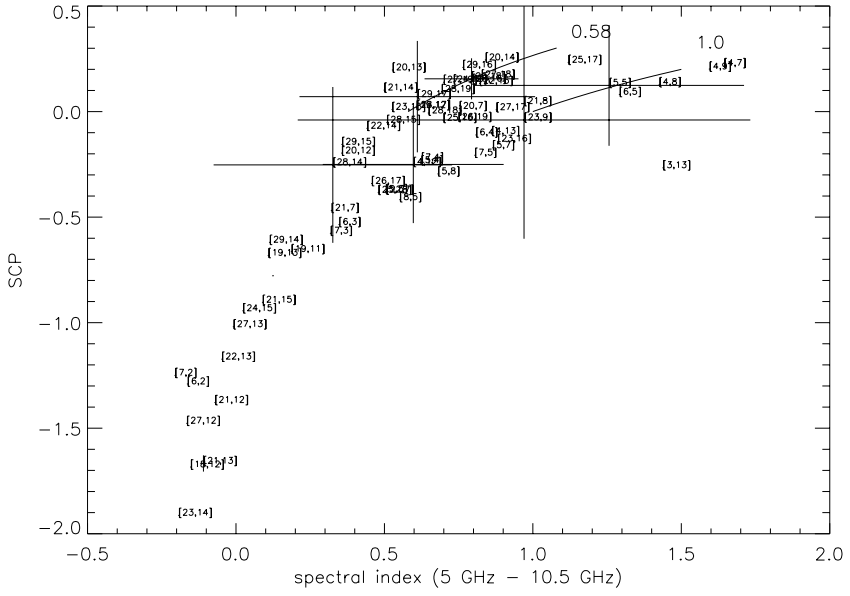

Figure 6.10: SCP-α diagram of NGC 315. The SCP values are curiously flat in the source. The main jet to the NW end has a low injection index, $\alpha_{inj} \sim 0.58$, while α_{inj} of the NWern relic tail and the SEern lobe is rather high, ~ 1. The NWern relic and the SEern lobe possibly have the same particle re-acceleration history.

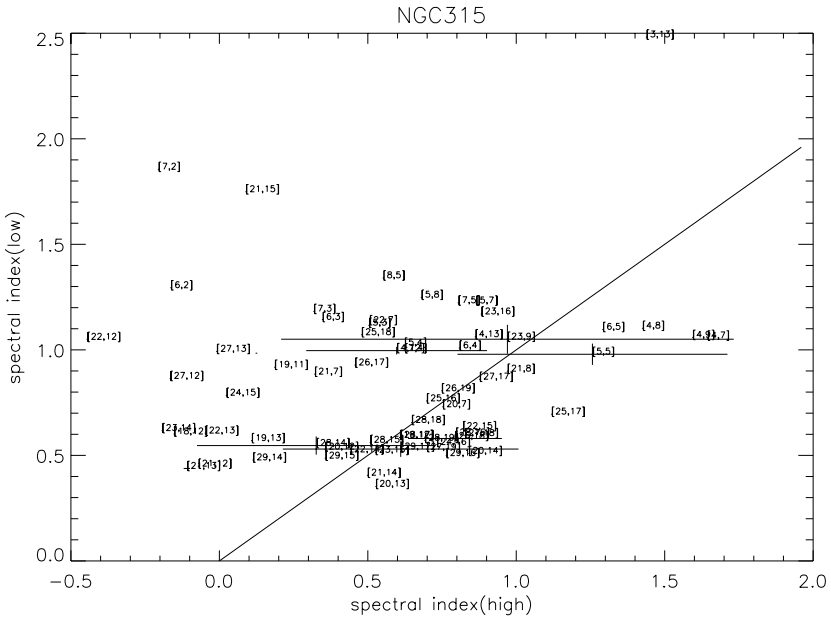

Figure 6.11: C-C diagram of NGC 315. See Fig. 6.11.

discrepancy between hot-spots and lobes has been reported for Cygnus A (Carilli et al., 1991). The injection spectral indices of the hot spots and lobes of Cygnus A are 0.5 and 0.75, respectively. The difference $\Delta\alpha_{inj} \sim 0.4$ here is larger than in Cygnus A. In Cygnus A, the hot-spots have $\Delta\alpha_{inj} \sim 0.25$ flatter than their lobes, i.e. their backflows. 3C 236 has a steeper spectrum (α_{inj}) in the advancing region. An explanation for this α_{inj} discrepancy (Carilli & Barthel, 1996) has not been found so far.

6.3.2 CSS sources

SCP - α diagrams can also be used for the analysis of samples of sources for which only integrated flux densities are given. As an example we present the application of our method to a sample of 47 compact steep spectrum (CSS) sources. Murgia et al. (1999) who have analyzed the flux densities of a sample of CSS sources in a thorough synchrotron ageing study show that these sources have moderate spectral steepening, i.e. a difference of $\Delta\alpha \sim 0.5$ between low- and high-frequency spectral indices, which is predicted by the continuous injection model (CI). We have used this sample to test the SCP behaviour, which provides an alternative method for a quick analysis of synchrotron spectra. In essence, four frequencies 408 (327) MHz, 1.4, 4.9 (5.0) and 10.7 (10.6, 8.1) GHz, were used. When no data were available at these frequencies, the total intensity at the frequencies given above in brackets were taken.

The points are found in the region where α_{high} does not exceed $\alpha_{inj} + 0.5$. The obtained range of values of α_{inj} is rather wide. This confirms the results of Murgia et al. (1999). The fact that α_{inj} shows more scatter in the SCP - α analysis than in the synchrotron model estimate is due to synchrotron self-absorption. There is a clear trend that the sources with stronger B_{eq} and with smaller projected sizes have flatter α_{inj}. These are the compact GHz-peaked spectrum (GPS) source candidates, since due to their extreme compactness $d \leq 1$ kpc, synchrotron self-absorption is likely to be effective. The sample does not show any correlation with redshift. This implies that

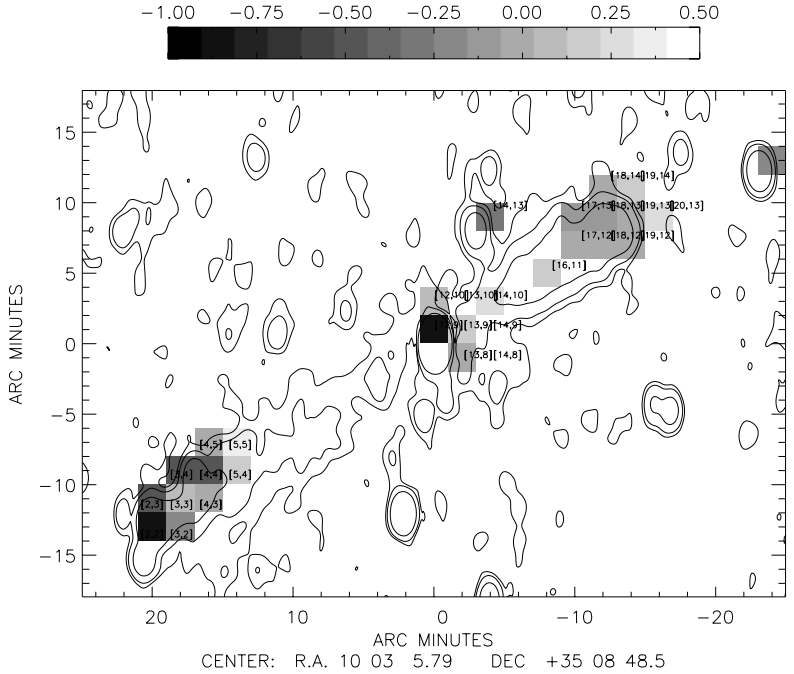

Figure 6.12: SCP diagram of 3C 236. The contours show the total intensities at 326 MHz Mack et al. (1997b). Contour levels are 3, 10 and 50 σ_I. Two lines are the best fit results for the NW lobe and the SE lobe, respectively. The very flat SEern extremity of SCP is due to a background source (Mack et al., 1998). The central core undergoes strong self-absorption, $SCP < 0$. In general, SCP is symmetric in 3C 236.

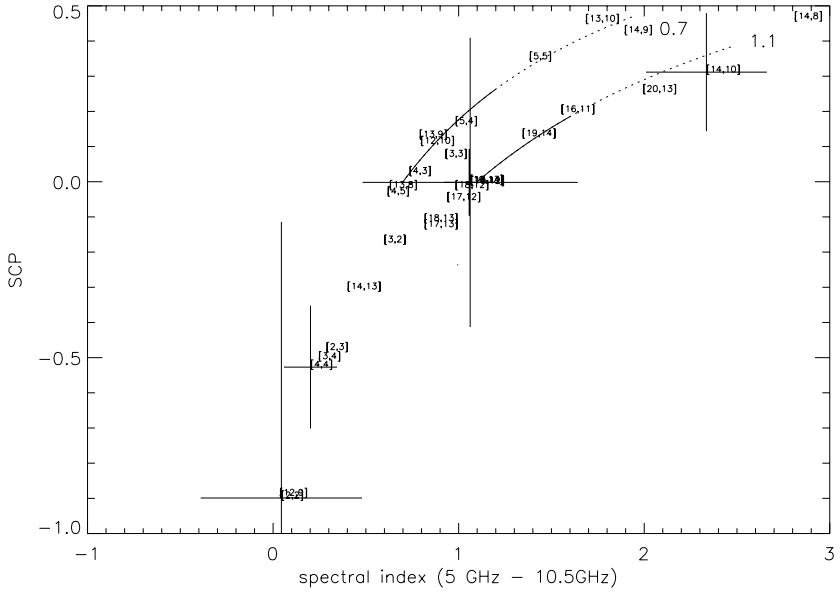

Figure 6.13: SCP - α diagram of 3C 236. Except for the central core and the background source, the points are well fitted by two values of α_{inj}. The SE lobe has $\alpha_{inj} \sim 0.7$. In the NW lobe, two values of α_{inj} are seen. The bridge has $\alpha_{inj} \sim 0.7$ close to the core, just like the SE lobe. The NW outer lobe has a much steeper value $\alpha_{inj} \sim 1.1$.

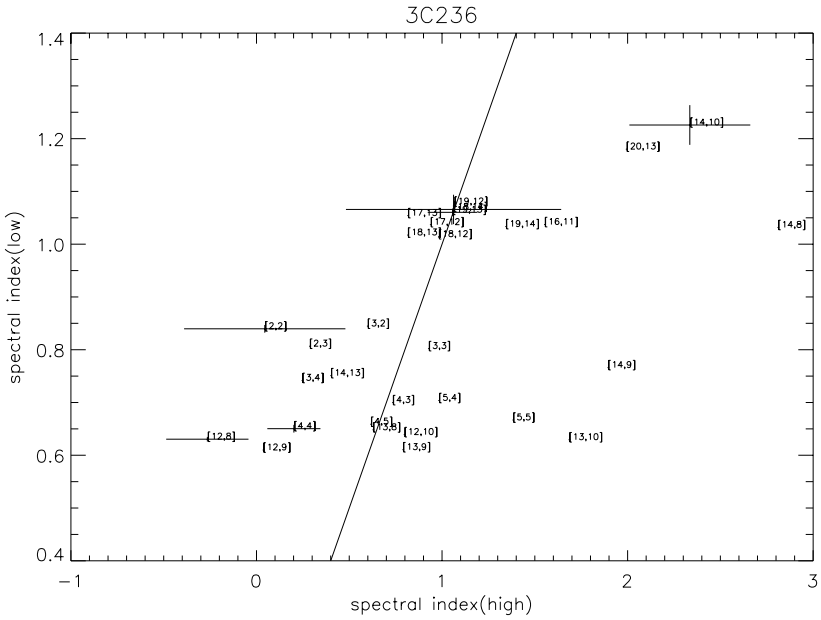

Figure 6.14: C-C diagram of 3C 236 (see Fig.6.8).

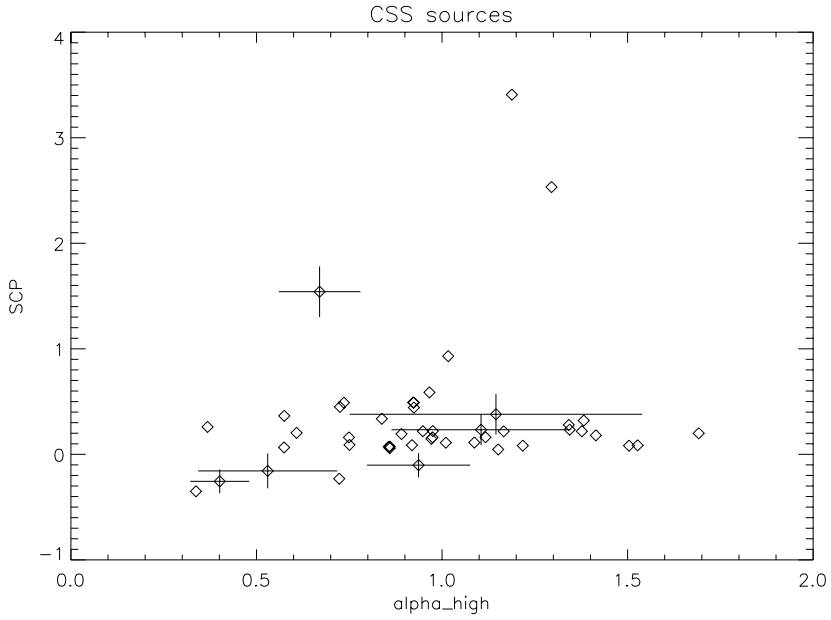

Figure 6.15: SCP - α diagram for 47 CSS sources. 40 sources have SCP values between 0 and 1. SCP > 1 clearly implies synchrotron self-absorption (see Fig. 6.2) at low frequencies. 3 out of 47 sources have SCP > 1. Because of the apparent synchrotron self-absorption at low frequencies, these sources were excluded from the further analysis in this work.

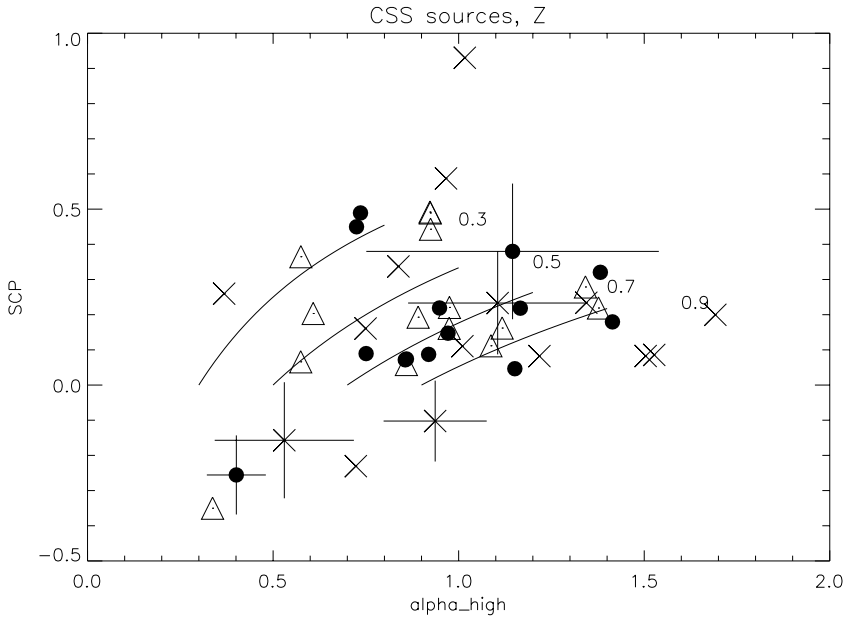

Figure 6.16: Filled circles are CSS sources with $z < 0.5$. Open triangles are CSS sources with $0.5 \leq z < 1.0$. Crosses are CSS sources with $z \geq 1.0$. The sample does not show any trend with redshift in the SCP-α diagram.

the intrinsic magnetic fields proponder by far over the magnetic field equivalent to the cosmic microwave background.

6.4 Discussion

The above analysis implies that all studied sources have a complex history. Now we discuss some possibilities. Before attempting any physical interpretation, we check again whether $SCP \sim -1$ could be generated by the problem of missing short spacings at 610 MHz. If anything, the possible missing short spacings at 610 MHz will steepen our α_{low}, which is already > 0. Then,

$$SCP = \frac{\alpha_{high} - \alpha_{low}}{\alpha_{high} + \alpha_{low}} \sim -1,$$

$$\alpha_{low} > 0.$$

This is possible if $\alpha_{low} \gg \alpha_{high}$ or $\alpha_{high} \sim 0$. $\alpha_{low} \gg \alpha_{high}$ is not known. The $SCP < 0$ trend can be emphasized when $\alpha_{low} > \alpha_{high}$ and $\alpha_{high} < 1$ are working together. But again, the measured α_{low} alone cannot explain the flattening up to $SCP \sim -1$. The trends in the sources are mainly caused by the high-frequency curvature, α_{high}.

6.4.1 Expansion losses, Energy Cut–off and Synchrotron Self–absorption

Adiabatic expansion losses may play an important rôle as an energy loss process of synchrotron sources. However, as Carilli et al. (1991) already pointed out, although adiabatic expansion will shift the spectral break to lower frequencies, the expansion does not change the spectral curvature. Therefore, expansion losses will not affect the

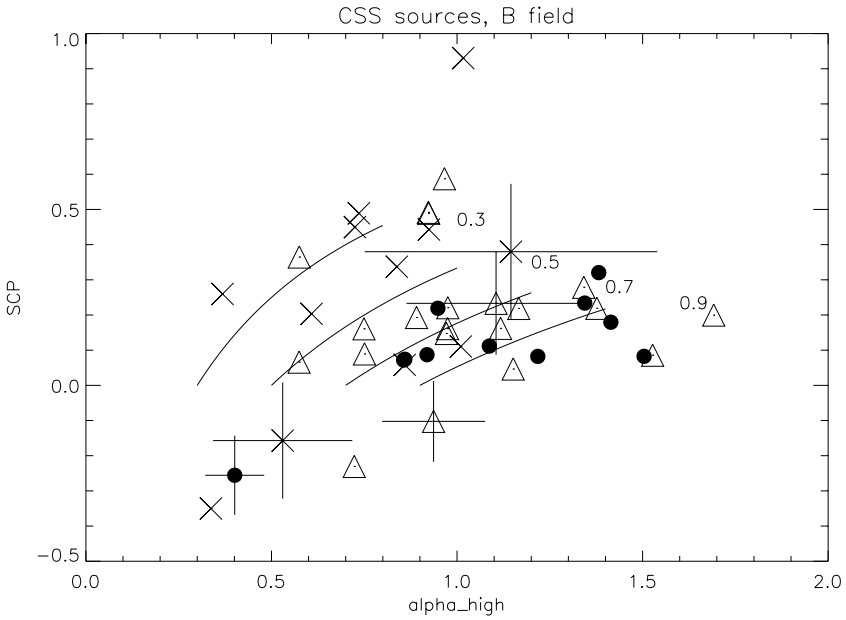

Figure 6.17: Filled circles are CSS sources with $B_{eq} < 5 \cdot 10^2 \mu G$. Open triangles are CSS sources with $5 \cdot 10^2 \mu G \leq B_{eq} < 10^3 \mu G$. Crosses are CSS sources with $B_{eq} \geq 10^3 \mu G$. Sources with $B_{eq} \geq 10^3 \mu G$ have a flatter spectral curvature than CSS sources with a weaker B_{eq}. $B_{eq} \sim 10^3 \mu G$ is a typical value for GPS sources. GPS sources have their turn-over (due to synchrotron self-absorption) at GHz frequencies. Their values of α_{low} are flat, $\alpha_{low} < \alpha_{inj}$, since they are estimated around about < 1 GHz. The lines in the diagram were drawn assuming $\alpha_{low} \geq \alpha_{inj}$. As a result, GPS sources tend to have a flat α_{inj}, < 0.5. Some CSS sources have a flat α_{inj} (Murgia et al., 1999) indeed, but these are not directly related to GPS sources, and none of them has any extremely flat $\alpha_{inj} < 0.3$.

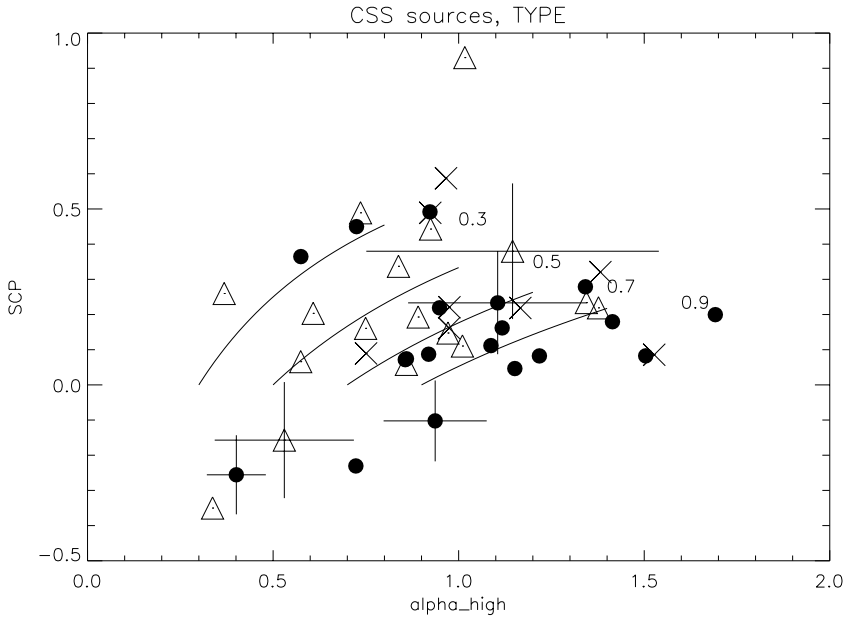

Figure 6.18: Filled circles are *lobe dominated* CSS sources, open triangles are *core dominated* ones. Crosses are uncertain types of CSS sources. There is no clear trend to distinguish the three classes in the diagram. This can be partly due to the fact that CSS and GPS sources are not a proper definition of source morphology, but rather represent an evolutonary stage (visible in their spectrum). Relatively nearby GPS sources can be resolved and defined as *lobe dominated*, while distant CSS sources can be unresolved and defined as *core dominated*. Alternatively, some 'frustration scenario' could be working. A definite answer would be only possible with the improvement of VLBI imaging.

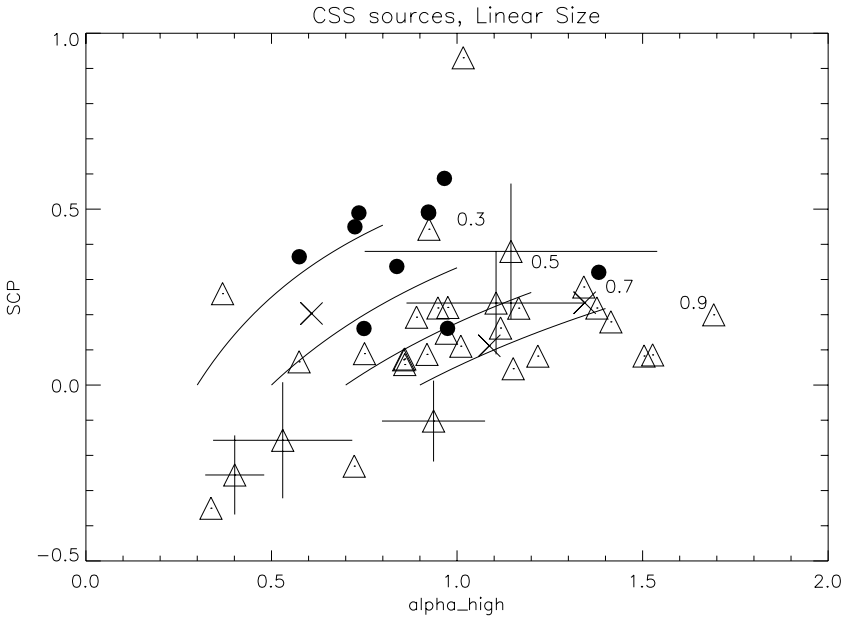

Figure 6.19: Filled circles are $d < 1\,kpc$ sources. Open triangles are $1 \leq d < 10\,kpc$ sources. Crosses are $d \geq 10\,kpc$ sources. Projected linear size, d, classes exhibit a clear grouping of CSS sources as in the classification according to B_{eq}. $d < 1\,kpc$ i s the typical size of a GPS source.

tracks of SCP - α.

At low frequencies, there are also other physical processes that give rise to spectral curvature, such as spectral turn–overs by synchrotron self–absorption in regions of high particle densities, or by a low–energy cut–off in the particle distribution. In the SCP - α_{high} plane (Fig. 6.2), the low-frequency turn-over produces SCP > 1, which cannot be produced by any ageing processes. Strong self-absorption can even produce SCP < 0 and will be important in the central core regions, if $|\alpha_{low}| > |\alpha_{high}|$. Since α_{low} will eventually approach $-5/2$ in the Rayleigh–Jeans limit, this will be possible. The spectra of the GRGs have $SCP \geq 0$

6.4.2 Re-acceleration

All three GRGs exhibit spectral flattening in some parts. In particular, NGC 315 even shows signs of a spectral upturn at high frequencies, and the majority of SCP points falls below 0. Let us consider the case where the power-law injection spectrum is already established,

$$N(E) \propto E^{-p}, \alpha_{inj} = (p-1)/2$$

and where Fermi acceleration is working. By the Fermi process, the particles in each energy bin will be re-accelerated such as to yield a power-law of the form $N(E) \propto E^{-q}$. For the non-relativistic strong shock, $q = 2$. The final shape of these two power laws is described by the following integration:

$$N(E) \propto E^{-q} \int_{E_0}^{E} E'^{-p} E'^{q-1} dE',\ q > 1, p > 1$$

where E_0 is low energy cut off. This can be approximated (Blandford & Eichler, 1987; Eilek & Hughes, 1991).

(i) for $q < p$, $N(E) \propto E^{-q}$, $\alpha = (q-1)/2$

(ii) for $p < q$, $N(E) \propto E^{-p}$, $\alpha = (p-1)/2$

In case (i), spectral flattening and $SCP < 0$ is expected (Fig. 6.2). An interesting result is that not every effective Fermi process results in a spectral flattening. In case (ii), the source will just look younger than indicated by its kinematic age, inferred from the shift of the break frequency towards higher frequencies (Parma et al., 1999). There is no flattening, since the energy distribution of the re-accelerated particles follow $N(E) \propto E^{-p}$, not E^{-q}.

Since GRGs are extraordinarily extended, they should have a weak magnetic field, $B_{sync} \leq B_{CMB}$ (Mack et al., 1998) and/or undergo re–acceleration processes during in their lifetime.

6.4.3 (Equivalent) Magnetic fields

The magnetic field B_{sync} and the equivalent field of the cosmic microwave background, B_{CMB} determine the curvature beyond ν_{br}. In some models (e.g. Eilek & Arendt (1996)) magnetic fields produce a power-law spectrum when they are ordered in a power-law form. However, we restrict our discussion to the curvature beyond ν_{br}, and to a simple homogeneous magnetic field B_{sync}, plus B_{CMB}. Many radio galaxies as well as GRGs have weak magnetic fields (Feretti et al., 1998; Mack et al., 1998; Parma et al., 1999), assuming that the equipartition estimation yields the strength of the magnetic field of the radiation region, $B_{eq} = B_{sync}$. The JP model becomes more appealing since it allows for pitch angle isotropization on a much shorter time scale than the radiation lifetime, $\tau_{iso} \ll \tau_{sync}$. However, KP 'like' spectra are observed (e.g. Carilli et al. (1991)). In order to explain such KP spectra, variable B_{sync} fields were introduced (Tribble, 1993; Eilek et al., 1997). In Tribble's model, the magnetic field has a Maxwellian distribution, while in Eilek's model, magnetic fields are filamented, therefore have approximately two components, B_{strong} and B_{weak}. But again, any of these models requires that some portion of their B fields is stronger than the equivalent B_{CMB}, such as to produce the KP-like spectrum.

In any case, KP-like spectra are only possible when there is a magnetic field that is strong compared to B_{CMB}. Therefore, the existence of KP spectra indicates that synchrotron radiation is the most important energy loss process in the region considered here. Furthermore, the variation of B_{sync}, if any, will cause a broadening of the spectral turn-over at low frequencies.

6.5 Summary and conclusions

We have investigated an alternative and very efficient method for the analysis of synchrotron spectra. We apply it both, to extended sources (like GRGs) and to the integrated flux densities of a sample of CSS sources. For all of them a thorough synchrotron ageing study has been performed which can be used for comparison. The information obtained from the spectral curvatures is manifold. The hotspots and jets possess pure power-law spectra, with particle ageing as expected. The spectral curvatures of the lobes exhibit both, spectral steepening and flattening.

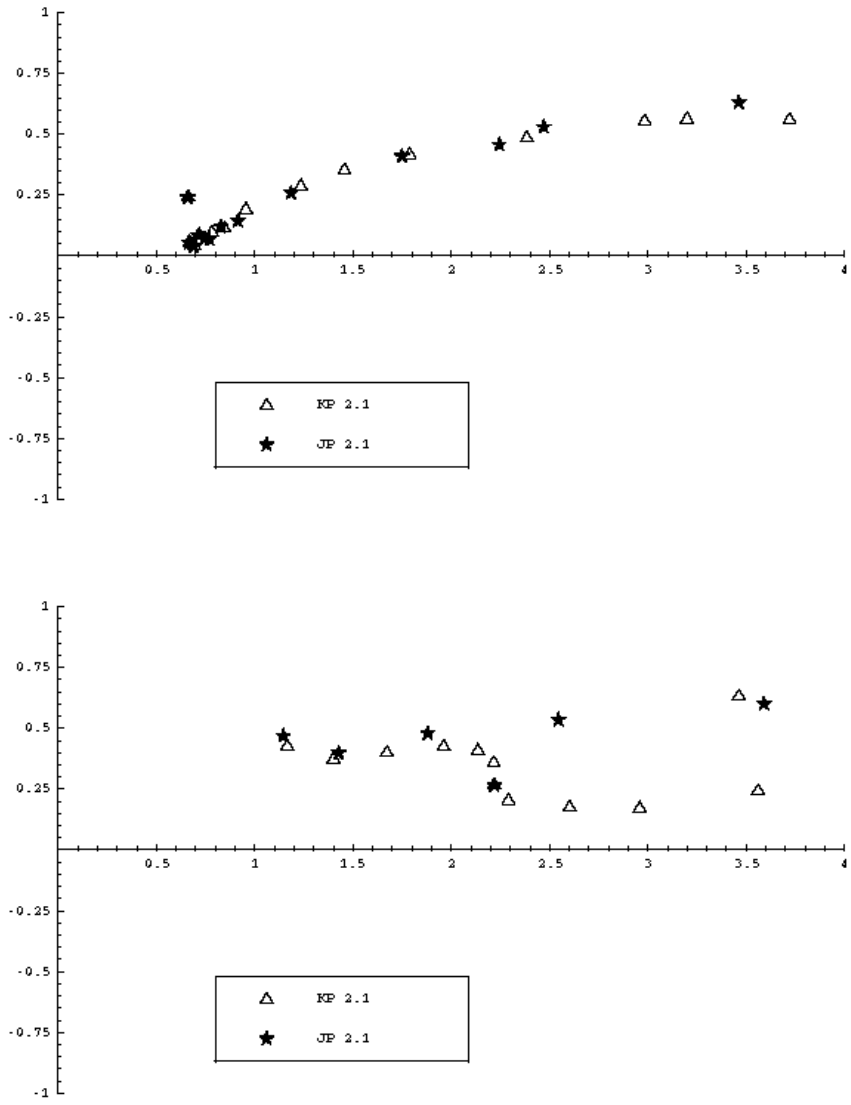

Figure 6.20: Comparison of KP and JP spectra under $B_{CMB} = 3\ \mu G$. The ordinate is α_{high} and the abscissa is SCP. The frequency intervals were selected to be similar to the observating frequencies of the GRGs. In the simulated synchrotron losses, IC losses and slight energy cut-off effects are considered. From top to bottom, the magnetic field B_{sync} is given as 6 μG and 15 μG. Age, power index, $p = 2.1$ ($\alpha_{inj} = 0.55$), and $B_{CMB} = 3.18\ \mu G$ are the same in all three diagrams. The pitch angle argument which makes the KP and the JP spectrum different is only valid when B_{sync} is significantly stronger than B_{CMB}. The bifurcation predicted in Fig. 6.1 is seen in the $B = 15\ \mu G$ diagram, while beyond that KP also has an asymptotic tail, since in the end the effect of B_{CMB} appears. This will happen at a very steep $\alpha_{high} > 2.5$.

In DA 240, there are CI spectra at the SW extremity, while KP/JP spectra show up around the bright core of the SW lobe. We cannot find any bifurcation in the diagram, which serves as the definite distinction between the KP and the JP model. More sensitive and/or higher-frequency observations are needed to reveal the bifurcation between the KP and JP models as shown between CI and KP/JP in DA 240. If a KP bifurcation is seen, it can be interpreted as an identification of the existence of a strong B_{sync}, i.e. $B_{sync} > B_{CMB}$. As seen in Fig. 6.20, KP spectra can be identified. Otherwise, they would look like JP spectra, due to the influence of the isotropic nature of B_{CMB}.

The high-frequency spectral indices start at values of around 0.5, which is indicative of non-relativistic strong shock acceleration. A possible origin of the shock could be the interaction of radio galaxies with their surrounding IGM/ICM (e.g. Enßlin et al., 2001). Adiabatic expansion, the other significant energy loss process, does not affect the SCP - α diagram. The results demonstrate that the SCP provides crucial parameters for the continuum spectrum of synchrotron radiation, without the more complex modeling.

Three characteristics that we have found in GRGs are not yet explained. The first is the origin of the asymmetry of the injection spectra of the radio lobes. Second, the physical explanation of the systematic flattening of α_{high} compared to α_{inj} is unknown. Third, there is a critical change of the re-acceleration efficiency showing up in the low- and high-frequency regime. We will investigate the environments of GRGs to find the possible reason.

In conclusion, it can be stated that the SCP - α diagram proves to be an efficient method to derive important properties of synchrotron spectra which otherwise can be determined only with the much more complex synchrotron ageing analysis. The SCP - α diagram and SCP map are especially useful tools to analyze a large number of sources and a large number of locations in a source. In such cases, the complex spectral analysis will provide better estimates. However, this alternative tool provides fast estimates without losing any significant accuracy and provides an overview, which is important to understand synchrotron sources. Compared to the C-C diagram, the SCP-α diagram extracts injection spectral indices and possible synchrotron ageing models in a source more efficiently.

6.6 Spectral curvature and polarization

In this section we shall discuss the question whether spectral curvature and polarization are correlated for the GRG sample. The situation for the GRG sample is as follows: we have shown that the RM and DP in GRGs do not show any clear correlation. The DP asymmetry is statistically certain, though this asymmetry does not show any clear Laing-Garrington effect (e.g. the jet-side lobe is less depolarized) in the GRG sample. Despite the low angular resolution, clear patchy structures are detected in the DP and SCP maps. The analysis of spectral curvature shows that the spectral variation in GRGs is not only due to particle ageing, but also to a multiple-injection spectrum, α_{inj}. The DP - RM correlation has been checked in Chapt. 2. Now we check any possible DP - SCP and $|RM_c2|$ - SCP relations.

NGC 315

A steep SCP favours depolarization, while a flat SCP favours repolarization (Fig. 6.21[a]). The RM dispersion does not show any trend that can be related to the SCP value in Fig. 6.21[b].

DA 240

The regions with the steepest SCP are located in the SW lobe. When they are included, the steep SCP favours depolarization, while the flat SCP favours repolarization (Fig. 6.22[a]). There is a marginal trend of the points with the flattest SCP to have a smaller RM dispersion (Fig. 6.22[b]).

3C 236

The flat-SCP points represent the hotspots which are less depolarized. The back lobes have steep SCP values and are more depolarized (Fig. 6.23[a]). The RM dispersion does not show any trend, which can be related to the SCP value (Fig. 6.23[b]).

3C 326

The connection of steep SCPs and high DPs as well as that of flat SCPs and low DPs is seen in 3C 326 (Fig 6.24[a]), too. The $\overline{RM}$ of 3C 326 and the RM of the three neighbouring extragalactic sources are relatively similar. Therefore, the corrected $|RM|$ is concentrated towards a zero value. A marginal trend that the flattest SCP points have a smaller RM dispersion is also seen (Fig. 6.24[b]).

NGC 6251

The SCP - DP connection is not as clear as in the other four GRGs (Fig. 6.25[a]). In the core and the inner jet region, $|RM| > 100$ rad m^{-2}, while in the hotspot and outer-jet region, $|RM| < 100$ rad m^{-2} , i.e. they have completely different trends (Fig. 6.25[b]).

6.6.1 Summary

The GRG sample exhibits a correlation in the sense that steep SCPs appear to be connected with high DPs, and flat SCPs with low DPs. In the case of foreground depolarization which is dealt with and proved in this thesis, the coupling of SCP and

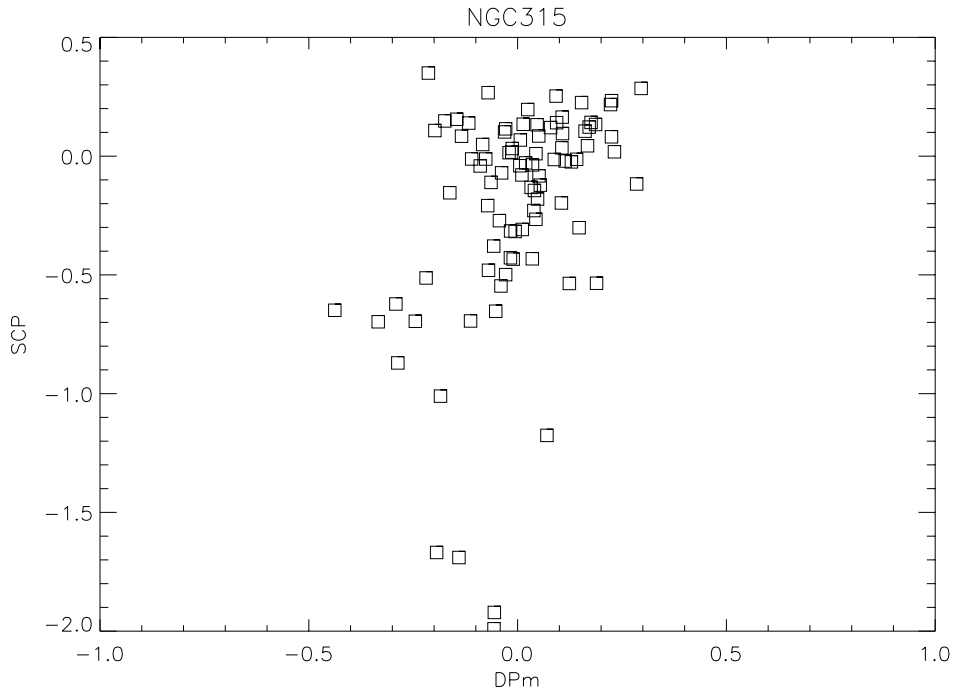

(a) DP-SCP

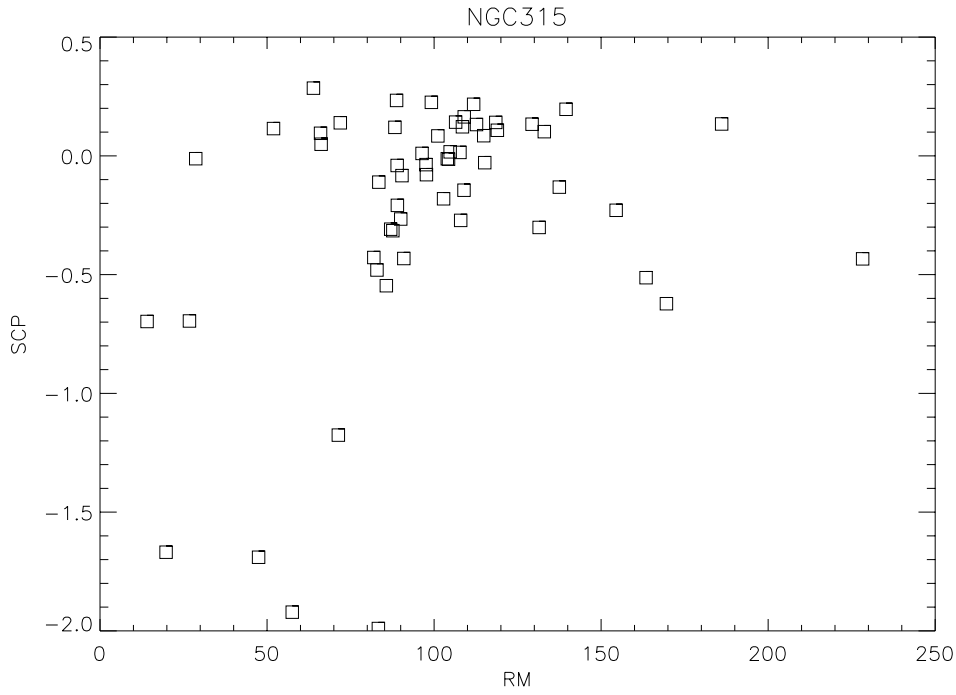

(b) RM-SCP

Figure 6.21: DP - SCP diagram of NGC 315

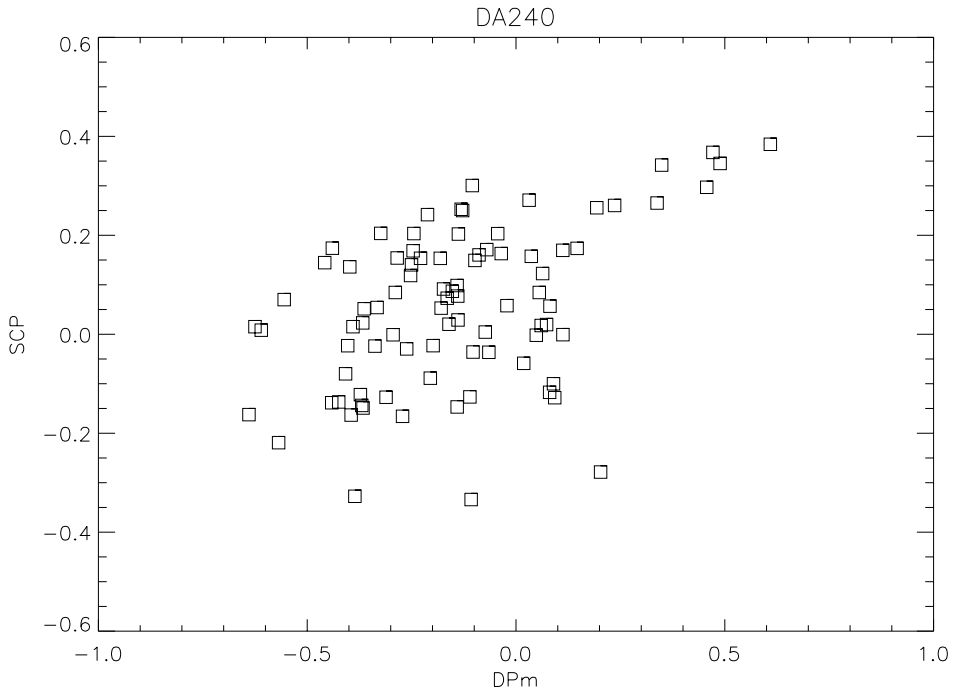

(a) DP-SCP

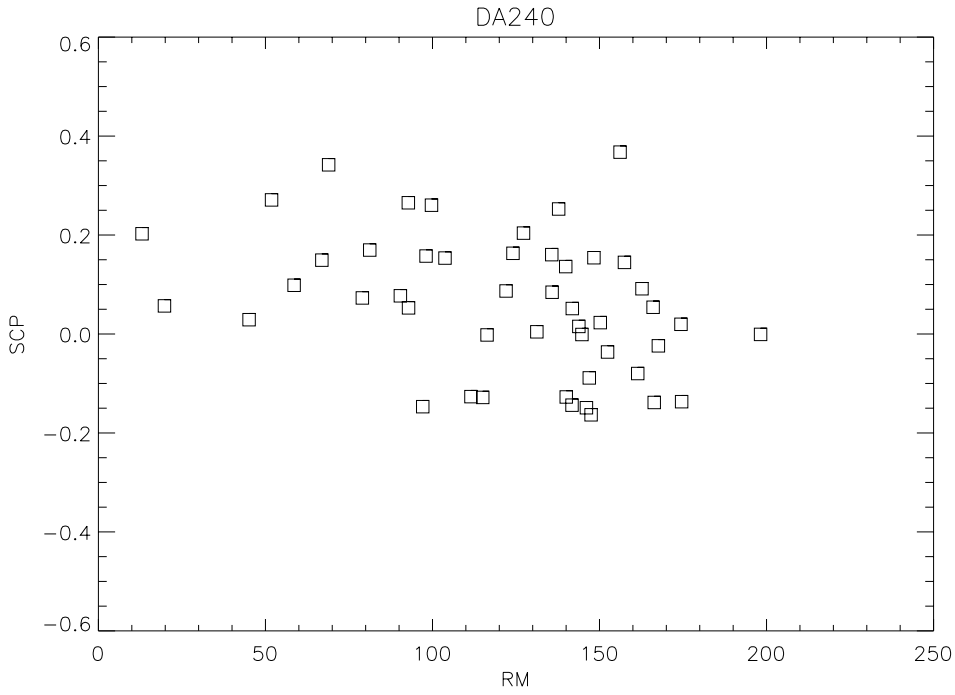

(b) RM-SCP

Figure 6.22: DP - SCP diagram of DA 240

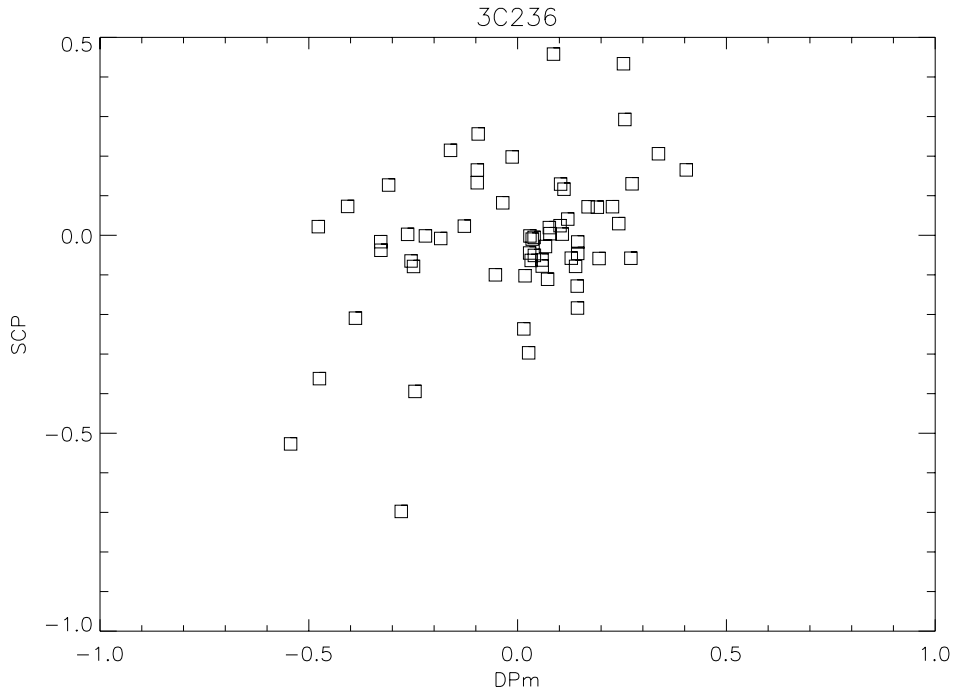

(a) DP-SCP

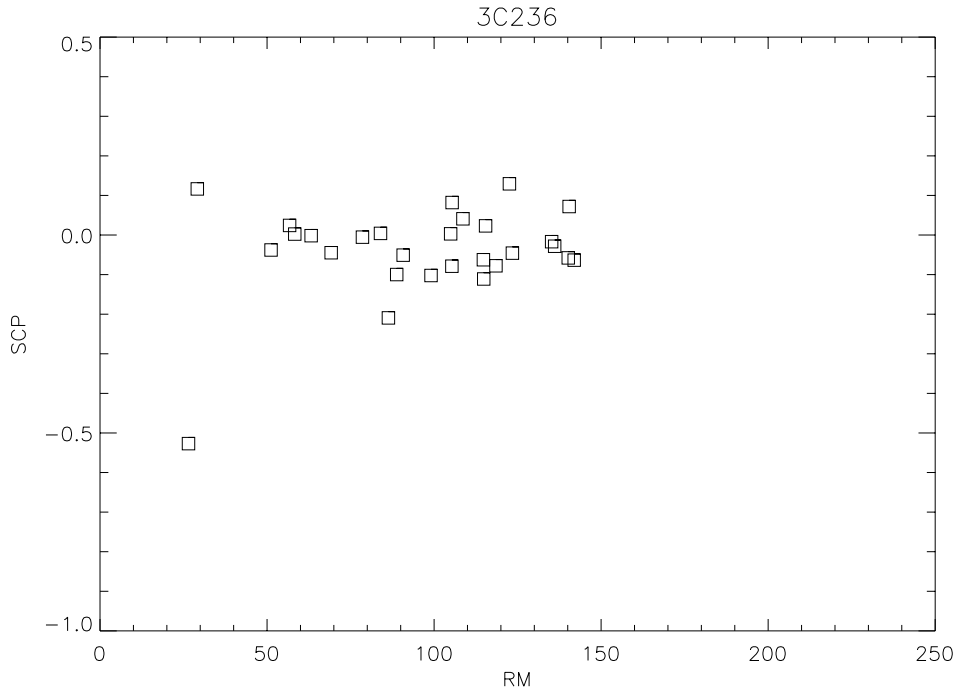

(b) RM-SCP

Figure 6.23: DP - SCP diagram of 3C 236

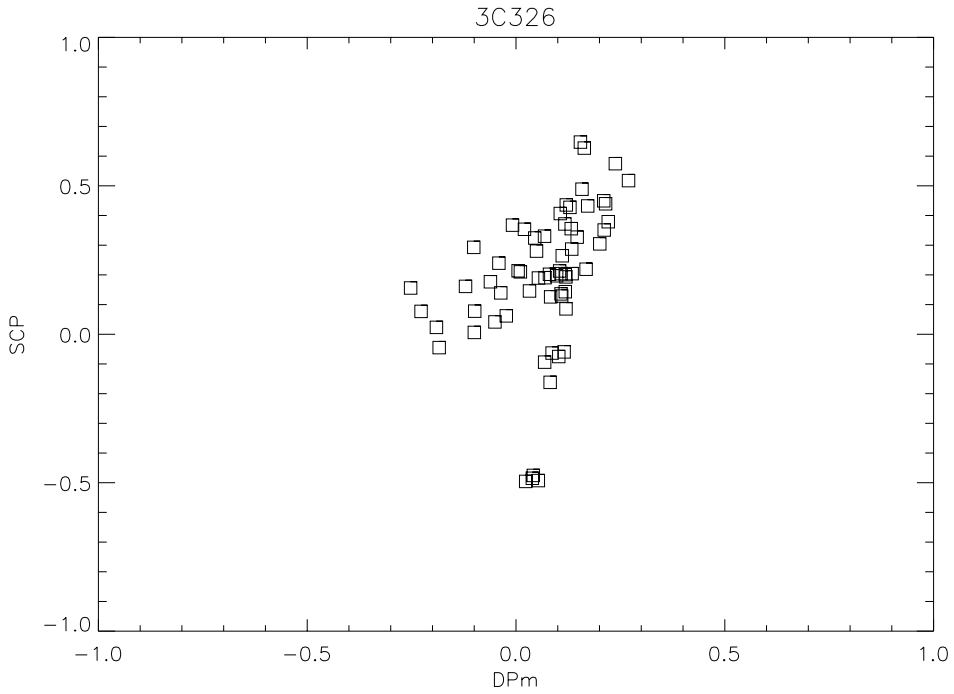

(a) DP-SCP

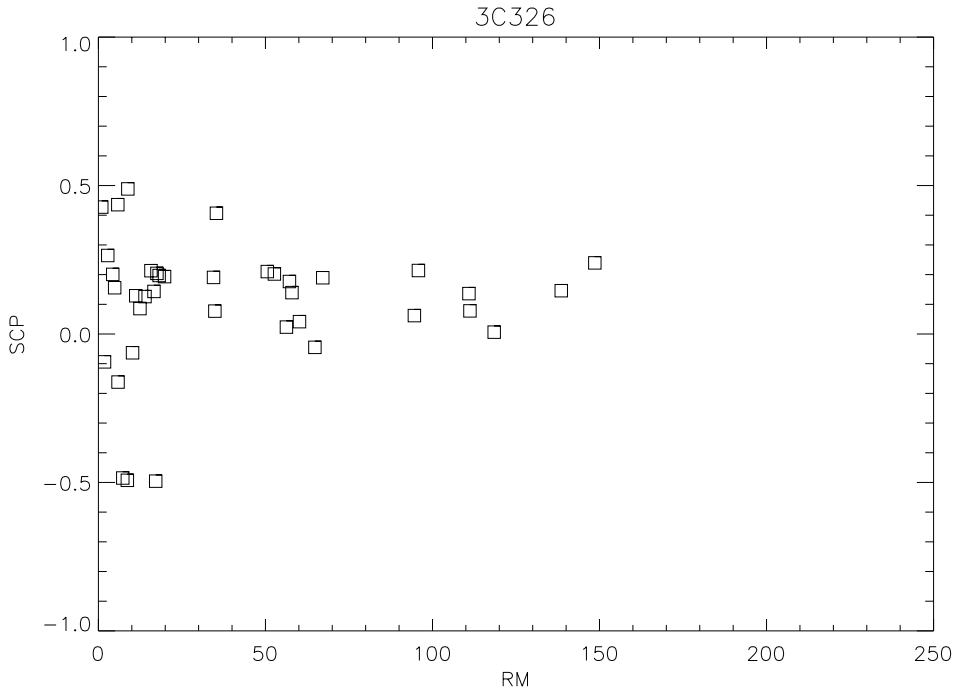

(b) RM-SCP

Figure 6.24: DP - SCP diagram of 3C 326

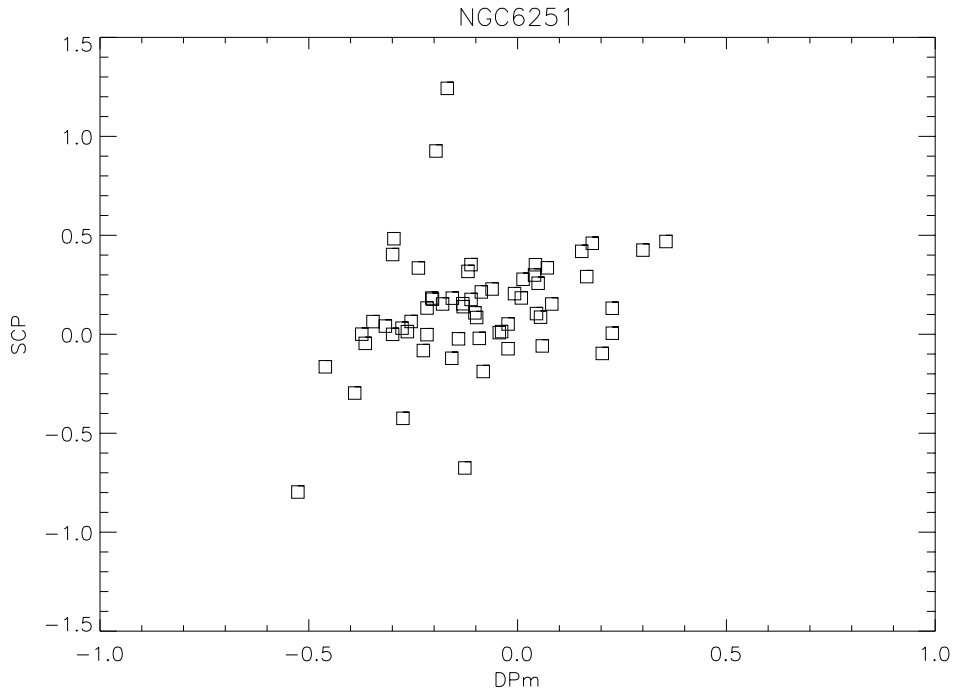

(a) DP-SCP

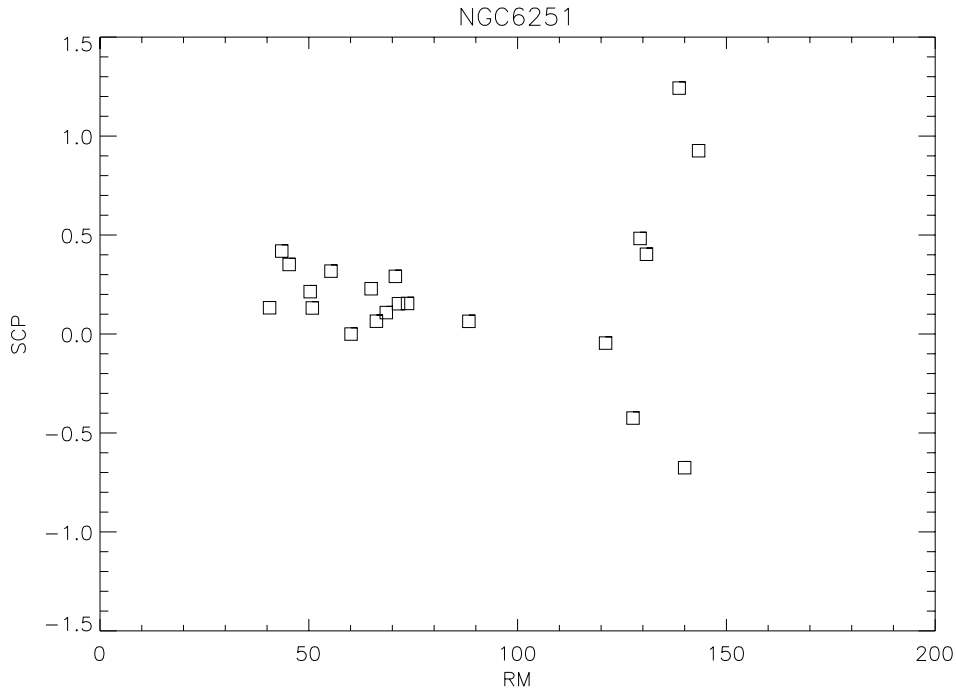

(b) RM-SCP

Figure 6.25: DP - SCP diagram of NGC 6251

DP in the GRGs indicates co-evolution of the GRGs and their environments: the well ordered foreground magneto-ionic medium with a low DP seems to be responsible for the flat, sometimes upturning, SCP – probably through shocks. With temporal evolution, the interaction between the foreground medium and the GRGs becomes less important when there is no further energy supply from the inside or from the outside. While the spectrum ages, the SCP steepenes and the magnetic fields in the foreground medium will be disturbed, e.g. through Alfven waves, and the DP will increase.

This scenario is well matched by the high RM of the GRGs found in the previous chapter. The GRGs might be the result of the complex and subtle interaction between the older RGs and their environments. This could be the reason why GRGs are so rare.

Chapter 7

Summary and outlook

In this work, we have studied the asymmetries of radio galaxies which are known to be related to the jet-asymmetry. They are the depolarization asymmetry and the spectral index asymmetry.

The first part of the thesis is concerned with the polarization asymmetry in GRGs and B2 RGs. After the introductory chapter, we discuss the Ricean bias in the fractional polarization and suggest a hybrid solution in the second chapter. The merit of this new solution is the enhanced reliability of the pixel-to-pixel fractional polarization. Using this hybrid solution, we present DP maps of the five GRGs at the end of the chapter. We conclude that the five GRGs are highly depolarized at low radio frequencies, but the depolarization is not as significant as Burn's law predicts. NGC 315 shows an interesting characteristic in that the source is NOT depolarized.

The subject of the third chapter is the rotation measure of the five GRGs. After correction for the Galactic contribution to the RM, the GRGs exhibit a few hundred $\mathrm{rad\,m^{-2}}$ of the Faraday medium. This must be due to field reversals or to changes of the field strength on a scale length of 50 to a few hundred kpc. This result indicates that the Faraday media of the GRGs are well resolved, despite the relatively large beam size used.

In the fourth chapter, we study the depolarization asymmetry of the B2 sources. Using the hybrid solution of the second chapter, we confirm the result of Morganti et al. (1997b) who discovered the 'Laing-Garrington' effect in the B2 sources. The RM of the B2 sources is estimated using a frequency range similar to that of the GRG sample, but with better angular resolution. The measured RM is about an order of magnitude lower than that of the B2 sources. We test the correlation between the depolarization asymmetry and the asymmetry of the RM dispersion, ΔRM. There is a trend that the more DP–asymmetric source is the more ΔRM–asymmetric. Again, the trend is not as strong as the prediction of Burn's law.

The fifth chapter is concerned with the high RM that we found in the GRG sample. We discuss the possible processes producing the high RMs. Since the GRGs with a symmetric morphology, e.g. 3C 236, also exhibit a high RM, we favour an 'internal' mechanism. Our estimate shows that expansion losses can support the amount of magnetic energy in the Faraday media. However, an external process such as large-scale shock flows may also play a role as we saw in the case of NGC 315, where the RM becomes even higher.

The sixth chapter deals with the spectral asymmetry. In FR II sources, there are conflicting results as to this asymmetry. Liu & Pooley (1991); Garrington et al. (1991) find a systematic asymmetry where the jet-side spectra are flatter in a sample of FR IIs.

In contrast to these results, Dennett-Thorpe et al. (1999) do not find any systematic asymmetry in a representative FR II sample.

Our concern was that the spectral asymmetry could occur not only through the spectral ageing effect but also through the difference in the injection spectral index. This idea may be more relevant for FR I sources and GRGs than for FR II sources, since the latter have a highly symmetric morphology, hence similar physical conditions are expected in both double lobes. Katz-Stone & Rudnick (1997) reported that there are possibly two injection spectra in the lobes of the FR I-type radio galaxy 3C 449, based on an analysis of the colour-colour diagram.

We develop a new analysis, the SCP - α diagram, in order to easily distinguish different injection spectra. We apply this technique to the GRG sample for which we have multiple frequency data at our disposal. The results show that there exists more than just one injection spectrum in the individual sources. Furthermore, we test this SCP - α diagram for a sample of 47 CSS sources whose injection spectra had been thoroughly analyzed by Murgia et al. (1999). This test proves that the SCP - α analysis is highly reliable. In the GRG sample we find multiple injection spectra using our new SCP - α analysis.

On the whole, the subject of this thesis is rather the study of the analysis of the asymmetries, rather than the asymmetries themselves. The behaviour of the two known systematic (jet-asymmetry related) asymmetries is studied. We might verify these results in another way. Recently, RGs were recognized as a promising tool for the process of cosmic structure formation. The linear polarization property of RGs enables us to probe the magneto-ionic intergalactic or intracluster medium. The theory of cosmic particle acceleration is largely based on the observation of the radio spectra of RGs. It will be interesting to investigate a larger and representative sample of RGs with the improved analysis methods suggested in this work.

Bibliography

AIPS Cookbook. 1999, *AIPS Cookbook* (N.R.A.O.)

Alexander, P. 1987, MNRAS, 225, 27

Alexander, P. & Leahy, J. P. 1987, MNRAS, 225, 1

Blandford, R. D. & Eichler, D. 1987, PhR, 154, 1

Blandford, R. D. & Rees, M. J. 1974, MNRAS, 169, 395

Blundell, K. M. & Alexander, P. 1994, MNRAS, 267, 241

Bolton, J. G., Stanley, G. J., & Slee, O. B. 1949, Nature, 164, 101

Burbidge, G. R. 1966, ApJ, 124, 416

Burn, J. P. 1966, MNRAS, 133, 67

Burns, J. O. 1998, Sci, 280, 400

Capetti, A., Morganti, R., Parma, P., & Fanti, R. 1993, A&AS, 99, 407

Carilli, C. L. & Barthel, P. D. 1996, A&A Rev., 7, 1

Carilli, C. L., Perley, R. A., Dreher, J. W., & Leahy, J. P. 1991, ApJ, 383, 554

Clarke, T. E., Kronberg, P. P., & Böhringer, H. 2001, ApJL, 547, 111

Daly, R. A. & A., L. 1990, ApJ, 364, 451

Dennett-Thorpe, J., Bridle, A. H., Laing, R. A., & Scheuer, P. A. G. 1999, MNRAS, 304, 271

Eilek, J. A. & Arendt, P. N. 1996, ApJ, 457, 150

Eilek, J. A. & Hughes, P. A. 1991, *Beams and Jets in Astrophysics* (Cambridge Univ. Press)

Eilek, J. A., Melrose, D. B., & Walker, M. A. 1997, ApJ, 483, 282

Eilek, J. A. & Owen, F. N. 2002, ApJ, 567, 202

Enßlin, T. A., Biermann, P. L., Klein, U., & Kohle, S. 1998, ApJ, 332, 395

Enßlin, T. A., Simon, P., Biermann, P. L., Klein, U., Kohle, S., Kronberg, P. P., & Mack, K.-H. 2001, ApJ, 549, L39

Feretti, L., Giovannini, G., Klein, U., Mack, K.-H., Sijbring, L. G., & Zech, G. 1998, A&A, 331

Garrington, S. T. & Conway, R. G. 1991, MNRAS, 250, 198

Garrington, S. T., Conway, R. G., & Leahy, J. P. 1991, MNRAS, 250, 171

Garrington, S. T., Leahy, J. P., Conway, R. G., & Laing, R. A. 1988, Nature, 331, 147

Jaffe, W. J. & Perola, G. C. 1973, A&A, 26, 423

Johnson, R. A., Leahy, J. P., & Garrington, S. T. 1995, MNRAS, 273, 877

Kardashev, N. S. 1962, Soviet Astr.-AJ., 6, 317

Katz-Stone, D. M. & Rudnick, L. 1997, ApJ, 488, 146

Kerp, J. & K.-H., M. 2001, in *Two Years of Science with Chandra* (Washington)

Killeen, N. E. B., Bicknell, G. V., & Ekers, R. D. 1986, ApJ, 302, 306

Klein, U., Mack, K.-H., Gregorini, L., & Parma, P. 1995, A&A, 303, 427

Laing, R. A. 1985, Physics of Energy Transport in Extragalatic Radio Sources (NRAO, Green Bank)

—. 1988, Nature, 331, 149

Liu, R. & Pooley, G. 1991, MNRAS, 249, 343

Mack, K.-H., Gregorini, L., Parma, P., & Klein, U. 1994, A&AS, 103, 157

Mack, K.-H., Kerp, J., & Klein, U. 1997a, A&A, 324, 870

Mack, K.-H., Klein, U., O'Dea, C. P., & G., W. A. 1997b, A&AS, 123, 423

Mack, K.-H., Klein, U., O'Dea, C. P., Willis, A. G., & Saripalli, L. 1998, A&A, 329, 431

McCarthy, P. J., van Breugel W., & Kapahi, V. 1991, ApJ, 371, 478

Morganti, R., Parma, P., Capetti, A., Fanti, R., & de Ruiter, H. 1997a, A&AS, 126, 335

Morganti, R., Parma, P., Capetti, A., Fanti, R., de Ruiter, H. R., & Prandoni, I. 1997b, A&A, 326, 919

Murgia, M., Fanti, C., Fanti, R., Gregorini, L., Klein, U., & Mack, K.-H. 1999, A&A, 345, 769

Pacholczyk, A. G. 1970, *Radio Astrophysics* (Freeman, San Francisco)

Pacholzcyk, A. G. 1997, *Radio Galaxies* (Pergamon press, Oxford)

Park, S. & Schowengerdt, R. 1983, Graphics & Image Processing (Journal), 23, 256

Parma, P., Murgia, M., Morganti, R., Capetti, A., de Ruiter, H. R., & Fanti, R. 1999, A&A, 344, 7

Perley, R. A., Bidle, A. H., & Willis, A. G. 1984, ApJS, 54, 291

Rees, M. J. 1971, Nature, 229, 312

Rottmann, H. 2001, PhD thesis, Univ. Bonn

Scheuer, P. A. G. 1974, MNRAS, 166, 513

—. 1995, MNRAS, 277, 331

Shklovskii, I. S. 1953, Astron. Zh., 30, 15

Simard-Normandin, M., Kronberg, P. P., & Button, S. 1981, ApJS, 45, 97

Tribble, P. C. 1991, MNRAS, 273, 877

—. 1993, MNRAS, 261, 57

Tsien, S. C. 1982, MNRAS, 200, 377

Vinokur, M. 1965, Ann. d'Ap., 28, 412

Wardle, J. F. C. & Kronberg, P. P. 1974, ApJ, 194, 249

Worrell, D. M. & Birkinshaw, M. 2000, ApJ, 530, 719

Danksagung/ Acknowledgments/ 감사의 글

The completion of my thesis leaves me with many people to appreciate.

Zuerst mchte ich Herrn Prof. Dr. Uli Klein danken fr die Themenstellung, fr die langjhrige Betreuung meiner Arbeit und insbesonders fr die gedulige und freundliche Hilfe.
Mein Dank gilt Herrn Prof. Dr. Ulrich Mebold fr die bernahme des Koreferats und fr seine Hilfsbereitschaft in den ersten Jahren.
Ich danke RAIUB, der Internationalen Astronomischen Union und der Korean Astronomical Observatory fr die Fianzierung meiner Wissenschftlichen Hilfskraftstelle und fr die Bereitstellung von Reisemitteln.
Ich danke Herrn Dr. A. Zensus, Herrn Dr. A. Witzel und Max-Planck Gesellschaft fr das Stipendium in den letzten Phase der Arbeit.
Ich bedanke mich allen Mitarbeitern am RAIUB.
Vor allem gilt es fr die zwei Mitglider der Radiogalaxiengruppen. Ich bedanke mich herzlich Herrn Dr. K.-H. Mack fr die GRGs Daten sowie Effelsberg 100 m Telescope Daten von B2 Quellen und fr die vielen guten Ratschlge rund um die Arbeit und seine Freundschaft. Von Herrn Dr. H. Rottmann lernte ich eine Menge ber Datenreduktion und Beobachtungsverfahren.
Meinen alten und neuen Zimmerkollegen Herrn Dr. N. Neinninger, Frau Dr. M. Neinninger und Herrn J.-E. Pradas Simn bin ich dankbar fr die optimale Arbeitsatmosphre und fr vielen guten Rat.
Herrn Dr. T. Fritz, Herrn Dr. A.Weiss und Herrn Dr. P. Richter danke ich fr ihre Hilfe bei Posterarbeit.
Ich danke Herrn Dr. J. Kerp und Herrn Dr. H. Falke fr die Diskussion ber X-ray Astronomie und Teilchenbeschleunigung.

I am grateful to Dr. R. Morganti for friendly providing her FR I data at 1.4 GHz & 5 GHz and to Dr. M. Murgia for generously allowing to use his CSS data.
I thank Prof. Dr. J. Eilek, Prof. Dr. R. Laing and Prof. Dr. P. Leahy for answering my questions and for their comments on my work.

Last but not least,
논문의 완성을 가장 기뻐하실 부모님과 착한 동생들에게 감사 드리고, 오랜 학업기간 동안 마음 졸인 아내 성원이와 아들 유탁이에게 고맙다는 말을 전하고 싶습니다.